Thèse de Doctorat

Mention Chimie
Spécialité Chimie des Solides et Science des Matériaux

présentée à ***l'Ecole Doctorale en Sciences Technologie et Sante (ED 585)***

de l'Université de Picardie Jules Verne

par

Sorina Creţu

pour obtenir le grade de Docteur de l'Université de Picardie Jules Verne

Study of All-solid-state Li-ion Batteries based on LAGP electrolyte using Multiscale Imaging Techniques

Soutenue le 26 janvier 2023, après avis des rapporteurs, devant le jury d'examen :

Muriel Veron	**Prof. Grenoble-INP Phelma, France**	**Président**
Montserrat Casas-Cabanas	**Dr. CICEnergigune, Spain**	**Rapporteure**
Claire Villevieille	**Dr. DR-CNRS Grenoble-INP, France**	**Rapporteure**
Matthew McDowell	**Assoc. Prof. Georgia Tech, USA**	**Examinateur**
Martial Duchamp	**Asst. Prof., NTU, Singapore**	**Examinateur**
Christian Masquelier	**Prof. UPJV University, LRCS France**	**Examinateur**
Loic Dupont	**Prof. UPJV University, LRCS France**	**Directeur de thèse**
Arnaud Demortière	**Dr. CR-CNRS, LRCS/RS2E France**	**Co-Directeur de thèse**

To my family,

Acknowledgements

I am very grateful to jury members Dr. Montserrat Casas Cabanas, Dr. Claire Villevieille, Prof. Matthew McDowell and Prof. Muriel Veron for their interest in this study, providing examination and advice on this work.

I would like to thank you to laboratory direction, Dr. Mathieu Morcrette and Prof. Christian Masquelier for hosting me in LRCS and for the care with which they manage the laboratory. I want to say how much I appreciate that they provide for all the students all the equipment required to perform their studies. There has been no moment during my thesis when I wanted to perform an experiment and the laboratory didn't provide us the materials. More than that, I appreciate that they constantly invest in their student by organizing exceptional seminars and classes. They created a nice environment in the laboratory where working has been a pleasure.

I would like to express my gratitude towards my supervisors, Dr. Arnaud Demortière, Dr. Martial Duchamp and Prof. Loic Dupont for offering me this PhD thesis, proving me guidance, and offering me advice for this work. I want to thank you Dr. Arnaud Demortière for his kindness and strong moral support offered during those years, especially when mine was low and the patience with which he treated me during those years. I have always appreciated the way he encourages his students performing lab experiments, and mostly the way he treats his students when lab mistakes are done, he takes them as lesson and never discourage them from performing another experiment. I want to thank you Dr. Martial Duchamp for the rugosity with which he corrected and criticized my work. I also extremely appreciate the moments when he made time to explain me science. I want also to thank to him for the moments when he let the scientific decisions to me to develop my critical thinking, even if those times felt hard on the moment, today are highly appreciated for bringing a high contribution to my development as a scientist. I want also to thank you to Prof. Loic Dupont for the help provided to me during almost those 4 years. I also always appreciated and admired the speed with which he reacted all the time when something was required.

I also would like to thank you to Prof. Ovidiu Ersen from University of Strasbourg for inspiring me to pursue a PhD and specially for the moral support he offered me during those four years. His kindly mails with moral support always come in the difficult moments and always had a strong contribution on my moral support.

I am grateful to all the collaborators that have made this work possible, for their contributions and valuable scientific discussions. I want to thank you to Prof. John V. Hanna

and David G. Bradley (University of Warwick) for Nuclear Magnetic Resonance spectroscopy measurements and analysis, and for their critical comments on my work which improved my study. Thank you, David Troadec (IEMN, Lille) for the hard work and providing me such perfect FIB lamellas which without an important part of my studies wouldn't have been possible. I am grateful to Eric Maire, Justine Papillon and Jérôme Adrien (MATEIS, Lyon) for proving us time at the X-ray micro-CT device and to Nynke Krans**,** Rainer Straubinge, Mathias Mosig (Protochips) for the support they gave us by borrowing us equipment in order to perform the in-situ electrochemical TEM experiment. I would like to thank you also to people from Cameca for their SIMS analysis.

Those four years that I spent in LRCS, Amiens and NTU, Singapore would have not been the same without the amazing and kind people that I met on the way. There has been always someone next to me to encourage, to offer support and to have scientific discussions. I want to thank you to Jean-Noel Chotard, Vincent Seznec, Arash Jamali, Carine Davoisne and Virginie Viallet from LRCS for all the help and scientific contributions they provided to my work. I am also grateful to Nathalie Saulnier, Anne Charbonnier and Daphne Boursier for their help with the administrative work.

All my LRCS colleagues, you have made the cloudy and rainy days of Amiens to be so beautiful and always joyful. I want to thank you all (Briseis, Adolfo, Eunike, Ulas, Laura, Ronan, Theo, Ilda, Jia, Fenu, Noura, Solveig, Arina, Mariana, Marina, Jenny, Cedric, Waad, Julien, Darcy, Neelam, Matheus, Nicolas, Zeliang, Tuan Tu and many others who probably name I forgot to mention) for the nice activities we always organize. I have always enjoyed the time spent with you. I appreciated so much the kindness I met in my colleagues at LRCS and the support they offer when you are in need. It will be hard leaving such a nice work environment. I also want to thank to Helene, Ali, Clement, and Scott for always for creating such a nice atmosphere, it was a pleasure sharing the office with you. My time in Singapore wouldn't have been the same without my office colleague, Liza who always found time to offer help or grab a drink with me.

I would like to acknowledge Université de Picardie Jules Verne (UPJV) and Nanyang Technological University (NTU) for providing the finding for this study. I would like also to thank you Platform de Microscopie Electronique (PME – UPJV/RS2E) and Facility for Analysis, Characterisation, Testing and Simulation (FACTS) for equipment supports.

Lastly, I would like to thank my family, specially to my parents, Dorin and Olimpia for all the support they offered to me during my studies, without them I couldn't have arrived here.

Publications during the PhD thesis

1. *Oxidative decomposition products of synthetic $NaFePO_4$ maricite: nano-textural and electrochemical characterization* Fabrice Brunet, Camille Crouzet**,** **Sorina Cretu**, Rénald David, Matthieu Courty, Arnaud Demortière, Nadir Recham, **European Journal of Mineralogy,** 2019, 10.1127/ejm/2019/0031-2885

2. *X-ray Nanocumputed Tomography in Zernike Phase Constrast for Studying 3D Morphology of Li-O_2 Battery Electrode*, Zeliang Su, Vincent De Andrade, **Sorina Cretu**, Yinghui Yin, Michael J Wojcik, Alejandro A Franco, Arnaud Demortière, **ACS Aplied Energy Materials,** 2020, 10.1021/acsaem.9b02236

3. *In-situ TEM cycling of Semi-Solid State Micro Battery in Liquid Electrolyte*, Ankush Bhatia, Maxime Hallot, **Sorina Cretu**, Maxime Berth, David Troadec, Pascal Roussel, Jean Pierre Pereira-Ramos, Rita Baddour-Hadjean, Christophe Lethien, Arnaud Demortière, **ECS Meeting Abstracts,** 2021

4. *In-situ Liquid Electrochemical TEM Investigation of Semi Solid State LMNO Micro-Battery*, Ankush Bhatia, Maxime Hallot, **Sorina Cretu**, Nicolas Folastre, Maxime Berthe, David Troadec, Pascal Roussel, Jean-Pierre Pereira-Ramos, Rita Baddour-Hadjean, Christophe Lethien, Arnaud Demortière **Microscopy and Microanalysis**, 2021, 10.1017/S1431927621003949

5. *Under Pressure: Mechanochemical Effects on Structure and Ion Conduction in the Sodium-Ion Solid Electrolyte Na_3PS_4*, Theodosios Famprikis, O Ulas Kudu, James A Dawson, Pieremanuele Canepa, François Fauth, Emmanuelle Suard, Mohamed Zbiri, Damien Dambournet, Olaf J Borkiewicz, Houssny Bouyanfif, Steffen P Emge, **Sorina Cretu**, Jean-Noël Chotard, Clare P Grey, Wolfgang G Zeier, M Saiful Islam, Christian Masquelier, **Journal of the American Chemical Society,** 2020, 10.1021/jacs.0c06668

6. *In Situ Liquid Electrochemical TEM Investigation of LiMn1.5Ni0.5O4 Thin Film Cathode for Micro-Battery Applications*- Ankush Bhatia, **Sorina Cretu**, Maxime Hallot, Nicolas Folastre, Maxime Berthe, David Troadec, Pascal Roussel, Jean-Pierre Pereira-Ramos, Rita Baddour-Hadjean, Christophe Lethien, Arnaud Demortière, **Small Methods**, Volume 6, 2021, 10.1002/smtd.202270013

7. *Structural details in Li_3PS_4: Variety in thiophosphate building blocks and correlation to ion transport*- Ömer Ulaş Kudu, Theodosios Famprikis, **Sorina Cretu**, Benjamin Porcheron, Elodie Salager, Arnaud Demortiere, Matthieu Courty, Virginie Viallet, Thierry Le Mercier, Benoit Fleutot, Marc-David Braida, Christian Masquelier, **Energy Storage Materials**, Volume 44, 168-179, 2022, 10.1016/j.ensm.2021.10.021

8. The Impact of Inter-grain Phases on the Ionic Conductivity of LAGP Solid Electrolyte Prepared by Spark Plasma Sintering- **Sorina Cretu**, David G. Bradley, Omer Ulas Kudu, Li Patrick Wen Feng, Linh Lan Nguyen, Tuan Tu Nguyen, Arash Jamali, Jean-Noel Chotard, Vincent Seznec, John V. Hanna, Arnaud Demortière, Martial Duchamp, in **submission ACS Energy Letters**, 2022

9. *In-situ electrochemical TEM experiments to study all-solid-state Li-ion battery using LAGP as solid electrolyte*: **Sorina Cretu**, Nicolas Folastre, David Troadec, Arash Jamali, Nynke Krans**,** Rainer Straubinge, Martial Duchamp, Arnaud Demortière, *in preparation.*

10. What comes first? Dendrites or cracks? Degradation mechanism of $Li_{1.5}Al_{0.5}Ge_{1.5}(PO_4)_3$ using x-ray micro-CT- **Sorina Cretu**, Justine Papillon, Zeliang Su, Jérôme Adrien, Vincent Seznec, Loic Dupont, Eric Maire, Martial Duchamp, Arnaud Demortière, *in preparation.*

Conferences

1. Poster- Operando TEM Studies of The Structural Evolution of All-solid-state Li-ion battery: **Sorina Cretu**, Vincent Seznec, Loic Dupont, Lea Nicoletti, Martial Duchamp, Arnaud Demortière, Electron Microscopy Summer School, *Canadian Center of Electron Microscopy*, Hamilton, Canada, Juin 2019

2. Oral talk- Local studies of the evolution of the structural properties of Li solid-state battery by STEM Operando: **Sorina Cretu**, Vincent Seznec, Loic Dupont, Lea Nicoletti, Arnaud Demortière, Martial Duchamp, *ICMAT*, Singapore, Juin 2019

3. Poster- Insights in to the Li1.5Al0.5Ge1.5(PO4)3 solid electrolyte using FIB-SEM tomography: **Sorina Cretu**, Linh Lan Nguyen, Vincent Seznec, Loic Dupont, Martial Duchamp, Arnaud Demortière, *XVIIeme Colloque de la Société Française des Microscopies*, July, Reims, 2021

4. Oral talk- What comes first? Dendrites or cracks? Degradation mechanism of LAGP solid electrolyte using X-ray micro CT: **Sorina Cretu**, Justine Papillon, Zeliang Su, Jérôme Adrien, Vincent Seznec, Loic Dupont, Eric Maire, Martial Duchamp, Arnaud Demortière, *MRS Fall Boston (Virtual)*, December 2021

Workshops

1. Advanced Electron Microscopy School on Aberration-corrected microscopy and EELS organized by the Canadian Centre for Electron Microscopy (10th edition), Toronto, 2019

2. HyperSpy workshop organized by Diamond Light Source, (Virtual), 19-23 April 2021

Collaborations

1. University of Warwick, UK- John V. Hanna and David G. Bradley for Nuclear Magnetic Resonance spectroscopy measurements on the LAGP sintered pellets at various sintering temperatures

2. MATEIS laboratoire, Lyon, France- Eric Maire, Justine Papillon and Jérôme Adrien for the *ex-situ* analysis and *in-situ* electrochemical experiments of Li/LAGP/Li using X-ray micro-CT

3. Protochips- Nynke Krans**,** Rainer Straubinge, Mathias Mosig for providing us the in-situ electrochemical holder during a DEMO session to perform the *in-situ* electrochemical experiment on a solid-state battery

4. Institut d'électronique de microélectronique et de nanotechnologie, Lille, France- David Troadec for FIB lamella preparation for STEM analysis and microbatteries for *in-situ* electrochemical experiments

5. CAMECA, Paris, France- Image analysis of (electro)chemical reaction between LAGP and Li metal using IMS 7f-Auto device

Chapter I 13
General introduction 13
1.1 General context & global warming 13
1.2 The necessity of energy storage devices: Li-ion batteries 15
1.3 Mechanism principle of a Li-ion battery 16
1.4 Materials science and engineering of Li-ion batteries 17
1.5 Solid-state LiB technology 19
1.6 Types of solid electrolytes 21
1.7 Solid electrolyte manufacturing strategies 23
1.8 Solid-state Li-ion batteries performances 24
1.9 Main limitations of solid-state Li-ion batteries 26
1.10 Usual techniques used for ASSB characterizations 32
Chapter II 37
Impact of microstructural properties on ionic conductivity in LAGP solid electrolyte 37
2.1 Introduction 37
2.2 LAGP synthesis and sintering process 39
2.3 Ionic conductivity 41
2.4 Morphological properties and tortuosity 43
2.5 Chemical and structural properties analysis 47
2.6 Conclusions and perspectives 54
Appendix A 58
Chapter III 66
LAGP interface with Li metal 66
3.1 Introduction 66
3.2 Ionic transport in LAGP pellets 68
3.3 Chemical stability of LAGP versus Li metal 71
3.4 Electrochemical stability window of LAGP 74
3.5 Current density influence on LAGP 75
3.6 Protection layer of the solid electrolyte 83
3.7 Conclusions and perspectives 87
Appendix B 90
Chapter IV 92
***In-situ* electrochemical X-ray µ Computed Tomography** 92
4.1 Introduction 92

4.2 Cell design and experimental methods 94
4.3 Results and discussions 95
4.3a Initial state 95
4.3b Monitoring the lithium plating and stripping 97
4.4 3D analysis of LAGP lithium plating and stripping 102
4.5 LAGP/Li metal degradation mechanism 105
Conclusions and perspectives 106
Appendix C 109
Chapter V 113
Oxide all-solid-state battery using Li metal as anode 113
5.1 Introduction 113
5.2 First cycling results of the solid-state battery 115
5.3 Parameters optimization of the solid-state battery 118
5.4 Electrochemical performances of improved SSBs 120
5.5 Degradation mechanism of the solid-state battery 122
Conclusions and perspectives 128
Appendix D 131
Chapter VI 133
***In-situ* electrochemical TEM experiments** 133
6.1 Introduction 133
6.2 All solid-state Li-ion battery system 135
6.3 Ex-situ cycling of all solid-state battery 137
6.4 Solid-state battery preparation for *in-situ* electrochemical TEM 140
6.5 Study of the pristine FIB lamellas 143
6.6 *In-situ* electrochemical TEM cycling 146
6.7 Post-mortem studies of the FIB lamellas 149
Conclusions and perspectives 153
Chapter VII 158
Conclusions and perspectives 158
References 167

List of Abbreviations

ACOM	Automated crystal orientation mapping
AM	Active materials
ASSB	All-solid-state batteries
ASSLMBs	All-solid-state Li metal batteries
ALD	Atomic layer deposition
BE	Backscattering electrons
CV	Cyclic voltammetry
CT	Computed tomography
CCD	Critical current density
DMC	Dimethyl carbonate
DFT	Density functional theory
EV	Electric vehicles
ED	Electron diffraction
EELS	Electron energy loss spectroscopy
EDX	Energy Dispersive X-ray analysis
EIS	Electrochemical Impedance Spectroscopy
EC	Ethylene carbonate
FIB	Focused Ion Beam
GHG	Greenhouse gases
GIS	Gas Injection System
GCPL	Galvanostatic Cycling with Potential Limitation
HAADF	High Angle Annular Dark Field
KSI	Kinetically stable interphase
LAGP	$Li_{1.5}Al_{0.5}Ge_{1.5}(PO_4)$
LATP	$Li_{1+x}Al_xGe_yTi_{2-x-y}(PO_4)_3$
LLTO	$Li_{3x}La_{(2/3)-x}TiO_3$
LLZO	$Li_7La_3Zr_2O_{12}$
LGPS	$Li_{10}GeP_2S_{12}$
LFP	$LiFePO_4$
LCO	$LiCoO_2$
LVP	$Li_3V_2(PO_4)_3$

LiB	Li-ion batteries
$LiPF_6$	Lithium hexafluorophosphate $LiPF_6$
MAS	Magic-angle spinning
MCI	Mixed conductive interface
NMC	$LiNi_xCo_yMn_{1-x-y}O_2$
NMR	Nuclear Magnetic Resonance
OPLA	$Li_9Al_3(P_2O_7)_2(PO_4)_3$
PEIS	Polyvinylidene Fluoride
PVdF	Polyvinylidene Fluoride
PVDF-TrFE	Poly(vinylidene fluoride-*co*-trifluoroethylene
PEO	Poly(ethylene oxide)
RT	Room temperature
SEM	Scanning Electron Microscopy
SIMS	Secondary ions mass spectroscopy
SE	Solid electrolyte
SEI	Solid electrolyte interface
SPE	Solid polymer electrolyte
STEM	Scanning transmission electron microscopy
SSBs	Solid-state batteries
SSLBs	Solid-state Li-ion batteries
SPS	Spark plasma sintering
TEM	Transmission electron microscopy
XCT	X-ray computed tomography
XRD	X-ray diffraction
XPS	X-ray photoelectron spectroscopy
µ-CT	µ computed tomography

Chapter I 13
General introduction 13
1.1 General context & global warming 13
1.2 The necessity of energy storage devices: Li-ion batteries 15
1.3 Mechanism principle of a Li-ion battery 16
1.4 Materials science and engineering of Li-ion batteries 17
1.5 Solid-state LiB technology 19
1.6 Types of solid electrolytes 21
1.7 Solid electrolyte manufacturing strategies 23
1.8 Solid-state Li-ion batteries performances 24
1.9 Main limitations of solid-state Li-ion batteries 26
1.10 Usual techniques used for ASSB characterizations 32

Chapter I

General introduction

1.1 General context & global warming

The development of Human civilization is closely related to its ability to harness energy from different sources such as Sakai powered by horses or oxen in ancient Egypt, windmill, or water wheel in more recent times as well as coal, petrol, and gas in the last two centuries. The easy accessibility of carbonated sources of energy have led the Human civilization to have a direct impact on the earth climate. Nowadays, due to various human activities such as burning fossil fuels, transportation, building construction and industrial processes, the amount of greenhouse gases (GHG) [1] emitted into the atmosphere, *i.e.* CO_2, CH_4, N_2O and fluorinated gases[1], are constantly increasing and cause significant changes in the climate. The amount of CO_2 emissions (**Figure 1.1**[2]) increased drastically in time and today we have more than 35 gigatons CO_2 emissions per year. The global emissions of CO_2 tripled from 1960 to 2010 and is expected to quintuple by 2040[3,4] whether we continue this actual pace, and no changes are implemented. As a result of the rise concentration of GHG emissions we have now hotter temperatures with wildfires that start and spreads faster, more severe storms which leads to flooding and increased drought expanding the desert[4].

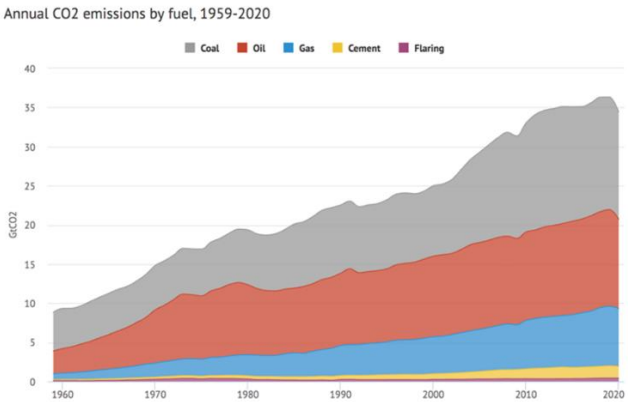


Figure 1.1 Historical trends of greenhouse gas emissions. Reproduced from the source[5].

An overview on the human activities sources that increase the GHG (**Figure 1.2**) shows that the main contribution comes from the energy sector followed by agriculture, industry, and waste[5]. The highest improvement needs to be implemented in the energy

sector where probably the fossil fuel will remain the significant source of energy for the following years, but great progress towards nuclear and clean renewable energy is recorded. Wind and solar energy are among the most abundant and potentially readily renewable energy sources available but remain intermittent sources with varying levels of energy produced. Therefore, energy storage devices remain a necessary sustainable solution to store the excess of energy generated during daily peaks and to redistribute it during days or nights when the wind is not blowing, or the sun has set[6].

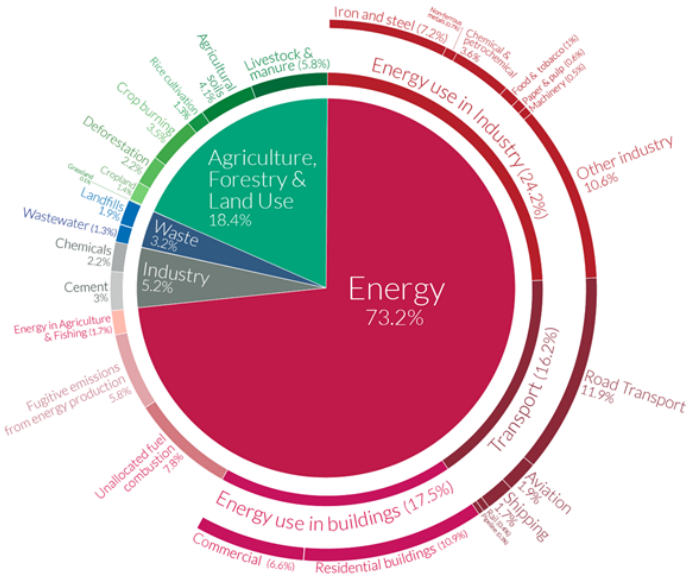


Figure 1.2 Global greenhouse gas emission per capita by sector in 2016. Source[5]: Our World in Data CO_2 and Greenhouse gas emissions.

To protect the environment, a reduction target of greenhouse gasses in the atmosphere was settled for the following years. A target of 55% GHG reduction by 2030 compared to 1990 was proposed (COP-21, Paris), followed by an ambitious path of achieving the climate neutrality by 2050. The goal is to limit global warming well below 2° C, aiming for a maximum of 1.5 °C which may be the threshold to avert catastrophic damages.

Energy storage devices need to be reliable with a long calendar life (*i.e.* >15 years), long cycle life, low cost, to require low maintenance and provide high safety requirements. Potential candidates as supercapacitors present high efficiency and high power, but their main drawbacks are represented by low energy density. Electrochemical storage technologies as batteries caught great attention due to their possibility to back-up the fluctuating sources of renewable energy as they respond very rapidly to load changes, present high energy efficiency (60%-95%) and have low standby loses[7,8]. Another sector, in which the reduction of GHG emission is crucial, is the transportation sector where the

replacement of gasoline vehicle by electric vehicle (EV) is essential and this technology demands batteries with high energy density, fast charging and low cost[9]. All those requirements for performant energy storage devices reveal the importance of developing suitable batteries for today necessities.

1.2 The necessity of energy storage devices: Li-ion batteries

Batteries are energy storage devices that store electric energy within active crystal hosts using an electrochemical reaction involving a charge carrier ion.[4,10,11]. A battery is an assembly of several electrochemical cells connected in series, in parallel, in which each cell is composed of two porous electrodes separated by an electrolyte. Connecting the two electrodes, electric current (external) and a charge carrier ion (internal) will pass from one electrode to another resulting in the discharge of the battery if it was in a charge initial state. Once the process of discharging is completed, applying a reverse current the cell will be charged[12].

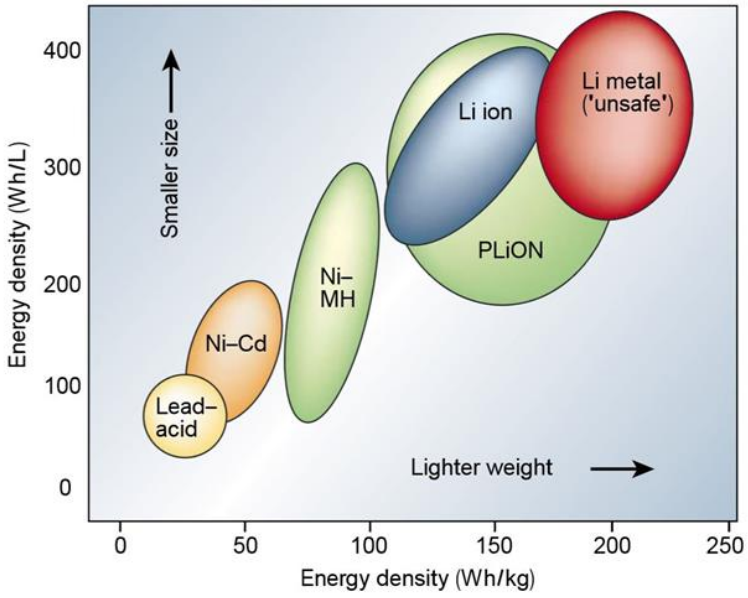


Figure 1.3 Comparison of energy densities and specific energy of different rechargeable batteries. Reproduced from the source[17].

Various batteries technologies[13] as lead-acid, nickel-cadmium or sodium-sulfur batteries were developed since 1850, but unfortunately, they possess limitation in size and weight for integration in portable electronic products (*i.e.* laptops, phones, tablets) where small and lightweight rechargeable batteries are desired [14]. Moreover, they contain toxic metal components which can harm the environment[15,16].

In the early 1970 rechargeable Li-ion batteries (LiB) were firstly discovered by S. Whittingham and then further developed in the early 1980 by A. Yoshino and J.

Goodenough[14] (2021 Nobel price). Today, LiB technology has almost totally replaced the old generation of batteries thanks to their great advantages as high energy density, high power density, long cycle life and affordable cost [11,18–22]. Such attractive properties of high energy density coupled with lighter weight and smaller size of LiB compared with the previous batteries (**Figure 1.3**) leaded to a domination and fast integration of the LiB in all the portable electronic devices triggering the transformation of our lifestyle in a digital nomad.

The first LiB technology was based on lithium metal as negative electrode due to its high theoretical capacity and low reduction potential (-3.045 V vs. standard hydrogen electrode) allowing to obtain high energy densities. Unfortunately, when lithium metal is used together with the liquid electrolyte, the formation of lithium dendrites is observed generating a short-circuit, leading to severe security issue as fires[23]. To overcome this issue, lithium metal has been replaced with Li intercalation anode in which lithium is only presented as ions (Li^+) in a host material, not as metallic lithium anode, (*i.e.* graphite carbon) limiting the dendrite formation in the cell and leading to the first LiB commercialized in 1991 by Sony company[24].

1.3 Mechanism principle of a Li-ion battery

A conventional Li-ion battery consists of a negative electrode (anode) and positive electrode (cathode) isolated physically by a porous separator immersed in a liquid electrolyte. The electrolyte is a solution containing dissociated salts that will enable the movement of Li^+ ions and isolates the movement of electrons (**Figure 1.4**)[25]. In a Li-ion battery, electrochemical reactions are occurring simultaneously in both electrodes. Based on the application of the electrochemical potential during the discharge process, an oxidation reaction occurs at the negative electrode and a reduction reaction occurs at the positive electrode. During the charge the opposite reactions will occur at the electrodes. The two electrodes present different electrochemical potential and there will be a thermodynamic driving force for Li ions to move from the high potential material to the low potential material. A mediator, an electrolyte (ionic conductor medium and electronic insulator) is placed between the two electrodes that allows the movement of Li ions through it. As the electrolyte allows Li^+ diffusion, but oppose the electrons movement, an external connection is placed between the anode and the cathode which allows the passage of electrons generating electric current for power various devices. Host materials in anode and in cathode will accommodate their crystalline structures to assure the diffusion of Li-ions in bulk leading to deformation and volume extension of active materials.

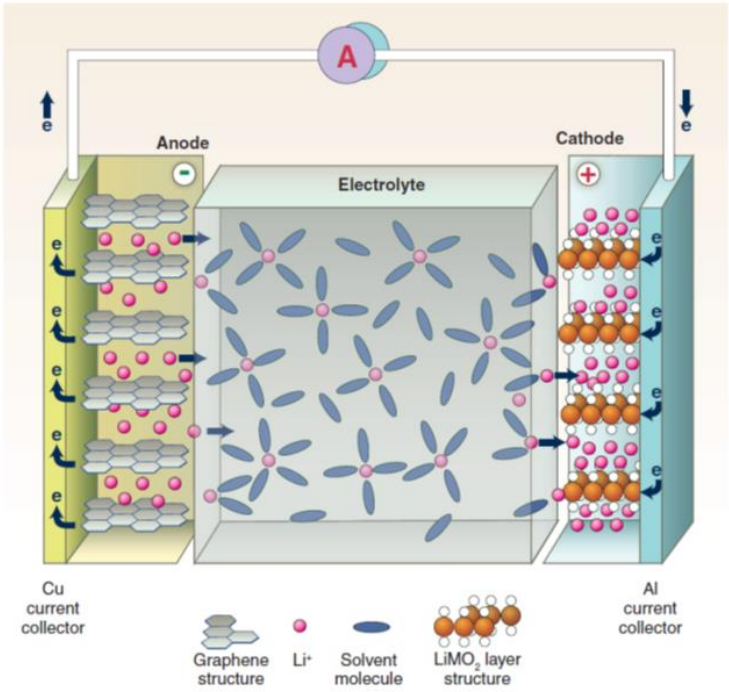


Figure 1.4 Schematic representation of conventional Li-ion battery in which graphitic carbon is the negative electrode whereas the positive electrode is represented by a Li-intercalation compound ($LiMO_2$)[25].

In the typical example of the Li-ion battery presented in the **Figure 1.4**, the working principle during discharge consists of de-insertion of lithium ions while releasing electrons from the graphite layer structure material (anode), meanwhile insertion of lithium-ion into the $LiMO_2$ layers is occurring at the cathode side. During the charge process, the reverse phenomena take place. Redox reactions are occurring simultaneously at both electrodes.

Positive electrode: $LiMO_2 \leftrightarrow Li_{(1-x)}MO_2 + x\ Li^+ + x\ e^-$

Negative electrode: $C_6 + x\ Li^+ + x\ e^- \leftrightarrow Li_xC_6$

Overall reaction: $LiMO_2 + C_6 \leftrightarrow Li_{(1-x)}MO_2 + Li_xC_6$

1.4 Materials science and engineering of Li-ion batteries

Energy density value defines how much electrochemical energy can be stored inside a battery device. It determines the product of the cell potential (V) and the capacity (Ah) of the electrode depending on the materials science and engineering. If the energy density refers to the energy in comparation with the mass, it is called gravimetric energy density ($Wh.kg^{-1}$) and if it refers to the amount of energy compared to the volume, it is called volumetric energy density ($Wh.L^{-1}$). A wide variety of battery technologies is created to meet the requirements of different applications with high energy density in terms of mass or volume.

The Li-ion battery electrodes are a mixture of 3 components: (a) active materials (AM) usually in secondary particle form, (b) conductive carbon (C45, VGCF) to create electronic conductivity percolation network and (c) processing additives as binder (Polyvinylidene Fluoride (PVdF)) to guaranty a good mechanical retention of the electrode[26]. Typically, the cathode is built on a current collector (thin aluminum foil) that hold the electrode mixture (slurry).

The AM in the positive electrodes (high potential material versus Li/Li^+) could be classified in two group: transitional metal oxide intercalation materials and conversion materials. The transitional metal oxide intercalation active materials are further classified based on their lithium-ion diffusion channel as following:

(a) One diffusion channel as in olivine phosphate ($LiFePO_4$) [27];

(b) Two-dimensional lithium-ion diffusion pathway as with layered oxide ($LiCoO_2$) [28];

(c) Three-dimensional lithium-ion transportation space as in spinel oxide ($LiMn_2O_4$)[29].

$LiFePO_4$ discovered by Goodenough presents quite low ionic diffusion coefficient and capacity (170 $mAh.g^{-1}$), but long cycle durability, low cost and high safety making it today one of the main candidates of cathodes for batteries. $LiCoO_2$ (LCO) is one of the most successful commercial cathode materials with a theoretical capacity of 275 $mAh.g^{-1}$, good cycling performances, high discharge voltage, low self-discharge, but high cost. $LiMn_2O_4$ with a theoretical capacity of 148 $mAh.g^{-1}$ has a high operating voltage (4.7 V), low cost, high ionic conductivity, and good thermal stability, but challenges arrive from rapid capacity decay and poor cycle life, especially at high temperatures[30–34].

The electrolyte needs to exhibit good ionic conductivity allowing high mobility of Li-ion between the electrodes and to ensure the electronic isolation, low melting and high boiling point and must present a good electrochemical stability, especially at high potential. The commercial liquid electrolyte is a mixture of linear and cyclic carbonates (diethyl carbonate (DEC), dimethyl carbonate (DMC) and ethylene carbonate (EC)) and a lithium salt (lithium hexafluorophosphate ($LiPF_6$))[35].

The negative electrode is a low potential material versus Li/Li^+ and based on the type of reaction mechanism, three types of anode materials can be defined:

(a) Intercalation/de-intercalation such graphitic carbon[18], hard carbon[36,37], synthetic graphite[38], metallic lithium[39], $Li_4Ti_5O_{12}$[40]

(b) Alloying/dealloying materials as silicon-based materials[41], Ge[42], SnO_2[43]

(c) Conversion materials as CuO[44], Cu_2O[45], Fe_xO_y[46], NiO[47], Mn_xOy[48]

Today LiB technology most relies on graphite as anode material due to its balance between low cost, long cycle life, good energy density (theoretical gravimetric capacity (372 $mAh.g^{-1}$)) and power density[49,50]. They are ideal for small scale devices (*i.e.* laptops, phone,

tablets) in which the energy density and cycling life of the battery matches with the device life. The demand for electric vehicle applications is increasing dramatically and requires batteries, first with a higher energy density to be able to drive them longer, then with a higher power density to be able to charge them faster, and then, with longer life because the life expectancy of a car is much higher than small electronic devices[51]. Silicon anodes were intensively studied as they present higher theoretical capacity values and were considered to replace the graphite anode (ten times higher theoretical capacity than graphite) but their high-volume expansion occurring during the cycling process (400%) impede them yet from commercialization[52]. Lithium metal is the most desired anode material to be inserted in a LiB as it can increase the energy density values due to the low potential values (-3.045 V vs. standard hydrogen electrode) and high gravimetric capacity (3860 $mAh.g^{-1}$). Unfortunately, the use of lithium metal together with the liquid electrolyte leads to undesirable chemical reactions occurring at the electrode-electrolyte interface where products as LiF, Li_2CO_3, Li_2O are formed which aggregate and leads to the formation of a large solid electrolyte interface (SEI)[53–55] and lithium dendrites[56–58] inducing short-circuit and fire of the battery.

The demand for electric vehicles (EV) increased dramatically, but batteries that provides a higher energy density are required and seems that the current technology based on liquid electrolyte touched their limits as very few improvements were done in the past years. The implementation of lithium metal as anode will satisfy the high energy density requirements, but the flammable nature of the liquid electrolyte [59] and the hazardous effects produced when used together with lithium metal is a real lock. There is no doubt that safety must represents one of the prime requirements for EV batteries and another solution must be found to further improve safety, sustainability, and batteries performances.

1.5 Solid-state LiB technology

A potential solution for the battery technology that needs to be implemented in the electrical vehicles could be the use of solid-state Li-ion batteries (SSLBs) technology[60–62] where a solid electrolyte[63,64] (SE) replace the liquid electrolyte (**Figure1.5**). By replacing the liquid electrolyte that contains flammable organic compounds with a solid electrolyte (non-flammable), the safety hazard will be removed making them a reliable technology for EV application. Furthermore, SSLBs opens the possibility to use lithium metal as anode in which a stable interface between the SE and Li metal is formed (with appropriate choice for SE) delivering higher energy density which represents another important requirement for EV applications.

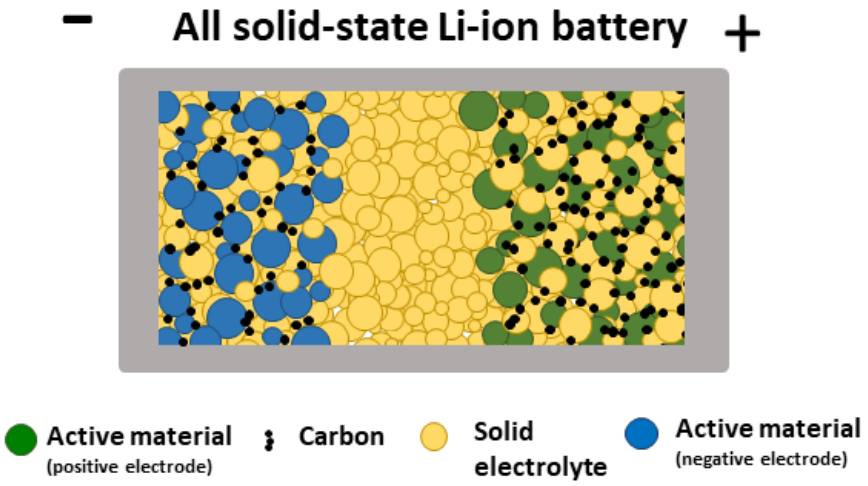


Figure 1.5 Illustrative representation of the architecture of a solid-state battery technology.

SSLBs technology could bring other advantages as wider electrochemical stability window which allows to use higher voltage cathode materials. The operating temperature window can be broadened, present quite low electronic conductivity compared to liquid electrolytes limiting the self-discharge (discharge at open circuit when the battery is not connected to a device). The industrial fabrication process will then be facilitated as SSLBs could be packed in a single package by alternating the solid electrolytes and bipolar electrodes (the anode material of one cell and the cathode of the next cell will be linked to the same current collector) reducing the weight and the volume of the package[51,60,63,65–69].

However, plenty of challenges remains to be solved in the SSLBs such as too low ionic conductivity, poor interfacial stability, often incompatibility between the electrodes and the SE, instability against lithium metal and large-scale production[65]. Nevertheless, essential requirements for the solid electrolyte are necessary to be used in a future battery technology[70]:

(a) possess ionic conductivity higher than 10^{-3}S.cm^{-1} at RT.
(b) have a large electrochemical stability window (at least 4-5V).
(c) negligible electronic conductivity.
(d) good mechanical properties.
(e) good contact at the electrode-electrolyte interface.
(f) ideally stable against Li metal.

1.6 Types of solid electrolytes

Today, two main classes of Li-ion solid electrolytes (**Figure1.6**) are intensively studied as a possible solution in future to replace the liquid electrolyte[71]: Inorganic solid electrolytes (oxides, sulfides, halides) and solid polymer electrolytes (SPEs).

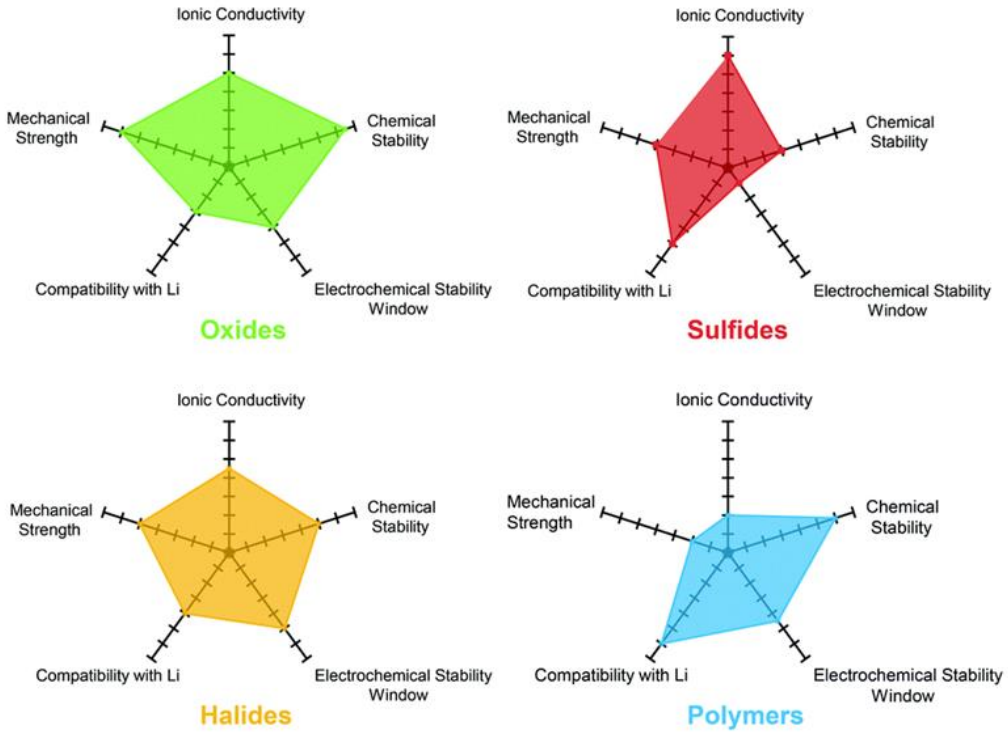


Figure 1.6 Chart representation of the main classes of solid electrolytes[71] (a) oxides, (b) sulfides, (c) halides, (d) polymers.

(a) Oxides based solid electrolytes can be further divided in various classes: NASICON (LATP, LAGP)[72], Garnets (LLZO)[73], Perovskite (LLTO)[74], Anti-perovskite (Li_3OCl, Li_3OBr)[75], LISICON[76] and thin films LIPON[77]. The greatest advantages of the oxides based solid electrolytes are represented by their high stability in the air, good chemical compatibility with high potential electrodes materials and large electrochemical stability window (LAGP and LLZO)[23]. Their total ionic conductivity reaches values up to 10^{-4} $S.cm^{-1}$ at RT (LAGP), but the grain boundaries are limiting for higher values[72,78]. Unfortunately, the most detrimental points are their low stability versus lithium metal generating a large interphase layer and the high mechanical strength (are very rigid making them susceptible for large cracks during operation, difficult for the mass production of electrolyte sheets and assembly in the battery)[79].

(b) Sulfides are the most promising candidate for the next generation of batteries as their ionic conductivities values are the highest among all the SEs candidates (12 $mS.cm^{-1}$

at RT for LGPS and 3.9 mS.cm^{-1} at RT for the Li_6PS_5Cl)[80,81]. Mechanical properties represent one of their advantages as they are ductile and presenting a lower grain boundaries resistance and contribute to a facile production process of the battery (*i.e.* cold pressing)[82]. The main limitations of the sulfides are due to their narrow electrochemical stability window, low chemical stability with electrode materials and the most important, their severe air instability[83,84].

(c) Halides based solid electrolytes attracted their attention with their good ionic conductivity values (between 10^{-3}-10^{-4} S.cm^{-1} for Li_3YCl_6 and Li_3YBr_6), good compatibility with oxides cathode materials and possible water synthesis strategies[85]. However, halides present a poor reduction stability with metal elements due to the existence of high valence state metal elements (reduction potential of halides is >0.6 V vs. Li^+/Li) and contain expensive metals in the structure which hindered their applicability [86].

(d) Solid polymers electrolytes (SPEs) are intensively investigated due to their good compatibility with metallic lithium (poly(ethylene oxide) (PEO) based SPEs) where only a stable passive layer is formed making them a very good candidate for a protection layer between the solid electrolyte and lithium metal[87]. Their other advantages include good mechanical properties (they are highly flexibles) and excellent thermal stability[88,89]. Unfortunately, their stability at high potential is quite weak (limit of 3.8 V vs Li^+/Li) and the total ionic conductivity is relatively low at RT (bellow 10^{-5} S.cm^{-1} for the PEO) , but it reaches acceptable values at higher temperature when they become viscous (10^{-3} S.cm^{-1} at 80 °C)[90] which succeeded with their commercialization (Autolib by Bolloré company with more than 4000 vehicles in circulation) [91].

Ideally, the next generation of solid electrolytes needs to present an ionic conductivity as high as the sulfides, a good stability in the air as the oxides and a good compatibility with lithium metal as the polymers based solid electrolyte. Mechanical properties represent another crucial step in the fabrication of the SSLBs and the next generation of the solid electrolyte will be ideally a combination between the hard ceramics and soft polymers allowing to accommodate the volume changes during electrochemical cycling without contact loss between electrode and solid electrolyte. Giving all advantages from various class of solid electrolytes, is likely that the next successful solid electrolyte in the SSBs will be probably a composite of various types of SEs (*i.e.* sulfides and polymers, oxides and polymers) making the research in all the classes to be highly important.

1.7 Solid electrolyte manufacturing strategies

Battery manufacturing represents one challenging process of solid-state batteries (SSBs) and currently there is a huge difference between laboratory scale facilities for producing SSBs for various studies and the desired design for their industrial production. In a laboratory scale, the most common way for obtaining SSBs is to use applied hot or cold pressure (**Figure 1.7a**) to form pellets[92–94]. This is one of the easiest ways to produce pellets, intensively used for sulfide based SSBs, but sometimes the different mechanical properties between the solid electrolyte and electrodes makes it difficult to obtain a proper interface and a sustainable solid-state battery.

Spark Plasma Sintering (SPS) it is another way to obtain compact SSBs[95–99]. The sintered sample is placed in a die (typically graphite, but stainless steel, WC or SiC could also be used) which is connected by two pistons that apply a pulsed electric current together with a uniaxial force achieving high temperatures and pressures in a few minutes (**Figure 1.7b**). SPS technique allows to obtain in a very short period high compact pellets with a good interphase contact between the solid electrolyte and electrodes.

Another method for manufacturing SEs (LIPON, Li_3PO_4,) at the laboratory scale is atomic layer deposition (ALD)[100] used intensively to produce thin solid-state micro-batteries[101]. ALD method is also used for coating components in the battery as they present an improved stability and ionic conductivity at the SSBs interfaces. LIPON layer presents good stability towards lithium metal and added at the interface between solid electrolyte showed improved battery performances[102]. Other emerged methods used for manufacturing SSBs are physical vapor deposition[103] and 3D printing[104].

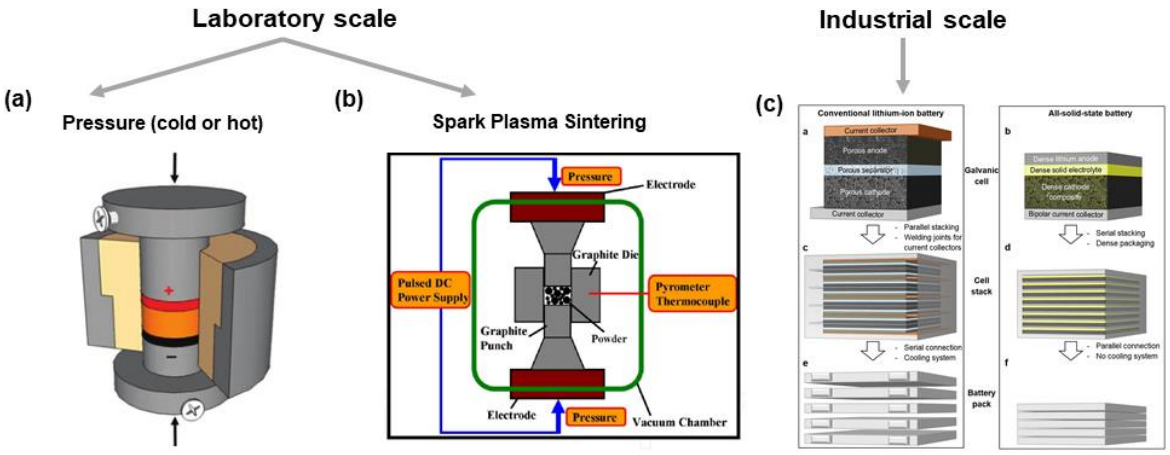


Figure 1.7 Commons procedures of obtaining compact solid-state batteries in laboratory scale: (a) cold or hot pressure, (b) spark plasma sintering and (c) a proposed protocol for industrial scale.

In the industrial scale, the manufacturing research is quite in the early stage. Various strategies are proposed for the manufacturing process of the solid electrolyte such as hot pressing suitable for oxide and sulfide based solid electrolytes or rolling, suitable only for sulfides SSE as oxides hard particles will be difficult to consolidate. The cathode most likely will be obtained using a slurry cast composite and the Li metal thin anode will be obtained by evaporation[105]. A schematic representation of a possible manufacturing process of SSBs is represented in the **Figure 1.7c**.

1.8 Solid-state Li-ion batteries performances

The performances of solid-state batteries are strongly advancing every year with the high research investment in the field and more companies are close to SSBs commercialization. Bollore (Blue Solutions, France) developed their own SSBs based on lithium metal polymer technology and LFP as cathode, batteries which are already present on the market in car sharing and bus sector (BlueCar, BlueBus). The battery operates at temperatures ranging from 50°C to 105°C (SE polymers exhibit low ionic conductivity at low temperatures) and does not require a cooling system, making it suitable for transportation vehicles that are in continuous operation as battery must be activated before running [106].

Solid Power (Louisville, US) started a pilot manufacturing for SSBs designed for EV application. Their technology is based on a high-content silicon anode, sulfide SE and NMC as cathode. They will begin providing at the end of the year batteries for Ford and BMW for testing and if everything goes well in 2024 a mass production of batteries could begin[107]. Another company working on developing SSBs based on sulfide solid electrolyte for hybrid electric vehicles is Toyota (leader in patents for SSBs with more than 1000) [108].

Quantum Scape (San Jose, California) is considered as one of the leaders in the field of SSBs. Their technology is based on an oxide solid electrolyte and the battery design is “anode-free” during the manufacturing process (discharge state), the lithium metal anode being formed *in-situ* during the first charge[109]. There are many other companies working in the field of solid-state batteries as Samsung, Nissan-Renault-Mitsubishi, CATL, LG Chem, Northvolt and the race for producing the most performant SSB is very tight.

High investments in the research of SSBs by industrial partners is pushing for a fast development in the field and currently the knowledge of SSBs is slightly more advanced in industry compared to academia, but important studies that shows the performances of SSBs are published constantly and is worth to mention a few[105].

Most of the studies that presents SSBs performances focus on the sulfide SE and lithium metal as anode due to an increase of 70% in the volumetric energy density in this system compared to the graphite anode lithium-ion batteries[110]. Various sulfide SE such as

Li_6PS_5Cl, Li_3PS_4, LGPS were considered, but recently most of the studies focus on Li_6PS_5Cl as SE due to their high ionic conductivity and limited interfacial decomposition process during SSBs operation[111]. Remarkable results were obtained in SSBs using a thin layer of Li_6PS_5Cl and polar poly(vinylidene fluoride-*co*-trifluoroethylene) (P(VDF-TrFE)) as SE, lithium-indium as anode and a composite cathode of $LiNbO_3$ coated $LiNi_{0.8}Co_{0.1}Mn_{0.1}O_2$ and Li_6PS_5Cl. The SSB showed a capacity retention of 92% after 1000 cycles and 71% after 20 000 cycles with a current of 1.0 $mA.cm^{-2}$ at RT[112].

In 2021, another highly performant SSB system was published using Li_6PS_5Cl solid electrolyte, µSi as anode and lithium nickel cobalt manganese oxide (NMC 811) as cathode, the battery was able to cycle for more than 500 cycles in a temperature range from -20 °C to 60 °C, the cell achieving a capacity retention of 80% and an average columbic efficiency of 99.9%[110]. The use of silicon as anode is highly desired as it is the second most abundant element in Earth and has a specific capacity exceeding 3500 $mAh.g^{-1}$, but poor interfacial stability against liquid electrolyte and large volumetric expansion during battery operation (>300%) which results in new interfaces growth with Li^+ consumption which hindered its commercialization. By using µSi as anode in SSBs, the generation of new interfaces is limited as even lithiation in the interfacial contact area between the SE and µSi is reduced to a 2-dimensional plane, contrary to conventional liquid where it permeates throw the electrode[113]. Their study combined 2 desired technologies, silicon anode and SSBs opening new possibilities for SSBs commercialization.

Oxides solid-state batteries[114,115] have been intensively studied due to their high stability in the air and high electrochemical window which allows the use of high voltage cathode materials, but their main limitation is the ionic conductivity at room temperature which is limited by the grain boundaries[116]. $Li_7La_3Zr_2O_{12}$ (LLZO) has been one of the most studied oxide solid electrolytes in SSBs and performances such as a discharge capacity of 160 $mAhg^{-1}$, maintained at 137 $mAhg^{-1}$ for 100 cycles at room temperature in an ultrathin Li/LLZO/$LiFePO_4$ were obtained[117]. Such performances could be attributed to the fact that the solid electrolyte layer was a very thin prepared as a slurry after ball milling reaction compared to classic thick pellets sintered at high temperatures.

LAGP has been also studied for SSBs applications due to its high stability in the air[118,119]. Unfortunately, LAGP alone is not stable against lithium metal, the valence state of Ge is reduced resulting in the formation of an interphase layer at the interface between SE and Li metal which consequently leads to rapid capacity loss [120,121]. Introducing a buffer layer with high stability against lithium metal as PEO at the interface between SE and Li metal anode improved the cycling results of LAGP. In a SSB with LAGP-PEO solid

electrolyte, protected lithium metal and $LiFePO_4$ cycled at 0.1C, the battery presented a cycling stability with an initial discharge of 147.2 $mA.g^{-1}$ and a retention of 96% after 200 cycles[122].

1.9 Main limitations of solid-state Li-ion batteries

SSBs showed essential advantages that are required for the future energy storage devices compared to conventional LiB, but as being an early technology new challenges are faced and should be solved to make from SSBs a sustainable future efficient battery.

A schematic illustration of a Li metal anode SSB (**Figure 1.8**) shows the current limitations encountered in the cell: loss of contact between the lithium metal anode and SE that appears during cycling process, the formation of an interface due to (electro)chemical reaction inducing high resistance in the system, dendrites and cracks formation promoting the short-circuit, improper interface contact between the cathode and SE due to their different mechanical properties, low (electro)chemical stability between the SE and the electrodes and weak ionic conductivity limitations (oxides and polymers).

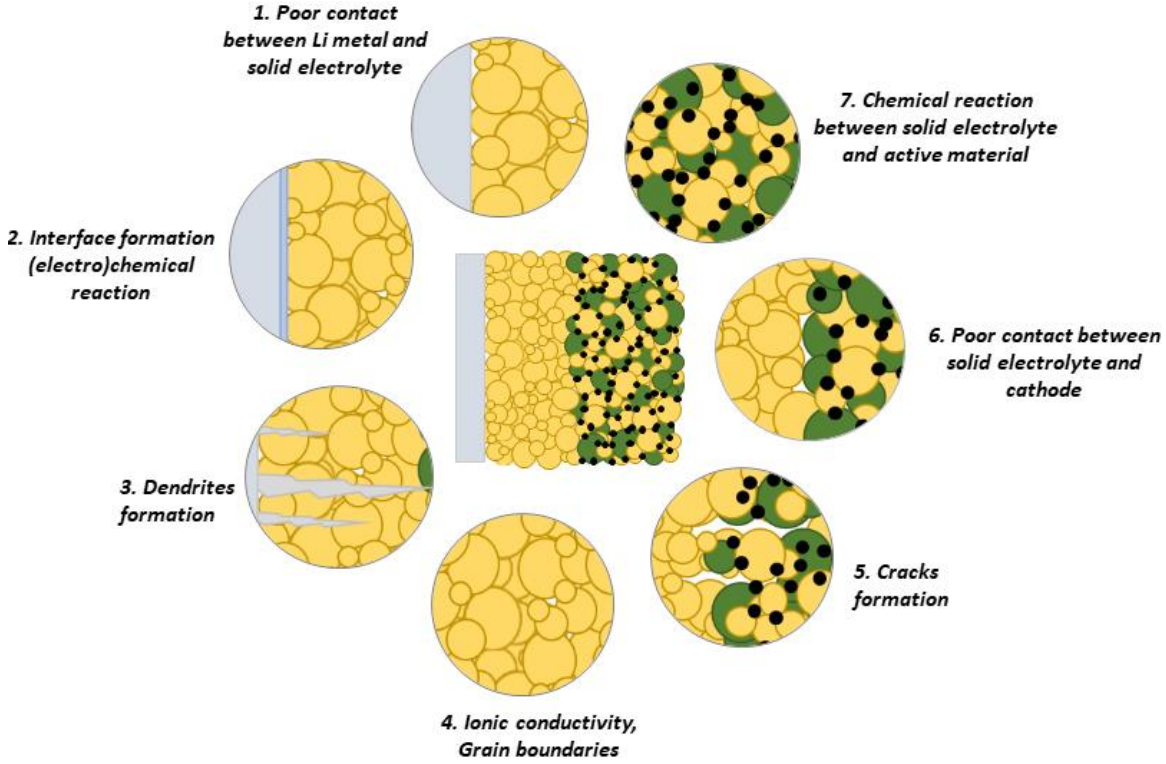


Figure 1.8 Schematic illustration of the main limitation encountered in solid-state batteries.

a) Interfaces in SSBs

Compared to conventional LiB where the liquid electrolyte infiltrates into the pores facilitating Li^+ transport, in SSBs the physical contact between batteries components is

ensured by solid-solid interfaces (anode-electrolyte, cathode-electrolyte and interparticle interface) which can present high interfacial resistance, limiting the performances of SSBs.

One of the SSBs advantages is represented by the higher energy density that could potentially provide, but for this the insertion of Li metal as anode and high operating voltage cathode materials is required. One of the criteria required for an efficient long-lasting SSBs is that the SE should present a larger electrochemical stability window to resist the oxidation and reduction processes. Although the electrochemical stability window is an intrinsic property of the SE, it impacts the interfaces stability as this is the place where electrochemical decomposition usually occurs. The calculated electrochemical stability windows values (**Figure 1.9a**) of the most encountered electrolytes shows that fluorides present the largest electrochemical window including high potentials, oxides present quite a large electrochemical stability window with SEs stable at low or high potential values and sulfides present the narrowest electrochemical stability window limiting their compatibility with electrodes[84,123–125].

Regarding the interface between Li metal and solid electrolyte it should be noted that Li metal is very electropositive and reactive which leads to a spontaneous reaction with the SE at RT. Depending on the reactivity of the SE, the formed interfaces could be classified as the following[126]:

1) Stable interface; the solid electrolyte is thermodynamically stable with lithium metal (no SEI formation), it is the ideal case of interface.

2) Mixed conductive interface (MCI); the reduction of solid electrolyte is spontaneous, and an interface is formed that shows high electronic and ionic conductivity. The reduction of the solid electrolyte by lithium metal is continuous triggering its degradation. This kind of interphase is encountered for solid electrolytes such as: LAGP[127], LATP[128] and LGPS[129].

3) Kinetically stable interphase (KSI) where the reduction of the interphase is also spontaneous, but the formed interphase is electronically insulative and the further degradation of the solid electrolyte is stopped. This interphase was displayed for solid electrolytes such as LPS[130], LLZO[129], Li_6PS_5X[131].

Experimentally, XPS (**Figure 1.9b**) is the most studied method for investigating the interfaces between SE and Li metal. In the case of LAGP only after few cycles the reduction of 3d Ge^{4+} to Ge^{3+} was observed which promoted a continuous corrosion of the solid electrolyte [127]. LLTO showed a similar behavior regarding the interphase formation where Wenzel et al. noticed after 300 minutes of deposition the reduction of Ti^{4+} from the pristine sample to Ti^{3+}, Ti^{2+}, Ti^{0} and an increase area of the peaks after 900 minutes of deposition

[130]. Argyrodite, sulfide-based SE when placed in contact with lithium metal also showed a reduction to Li_2S, Li_3P and LiX (X=Cl, I, Br)[131].

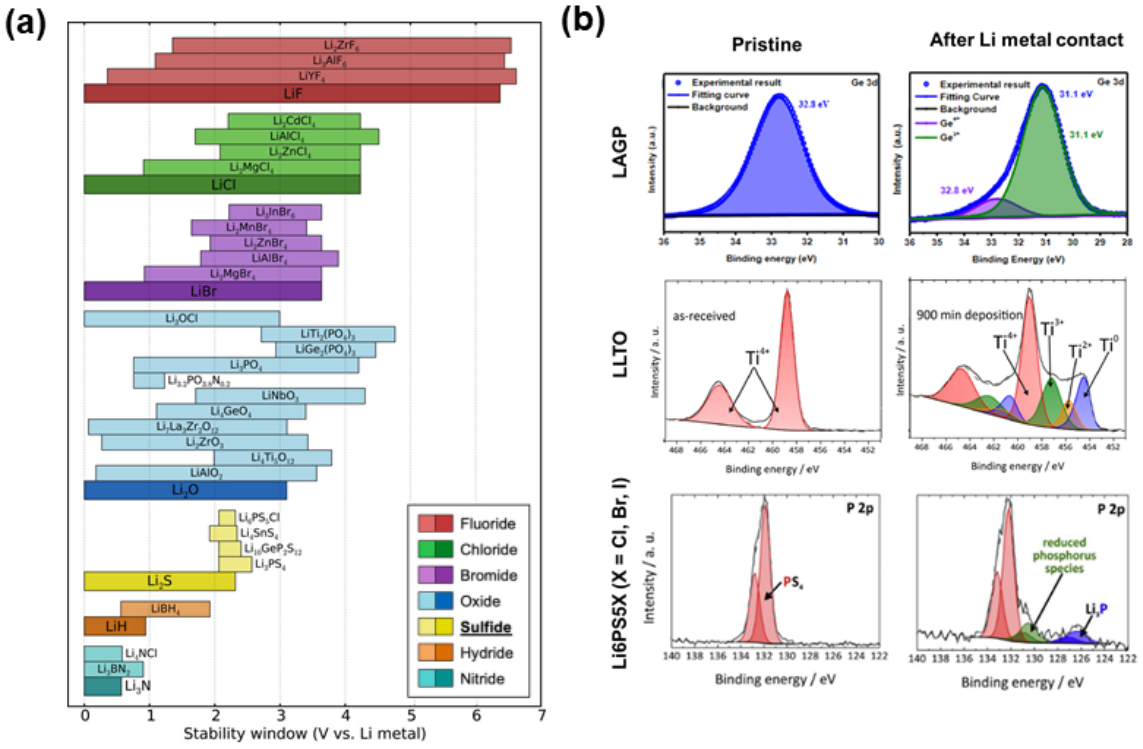


Figure 1.9 (a) Electrochemical stability windows of SEs determined computationally by predicted anodic and cathodic reactions[84] and (b) XPS spectra showing the formation of an interphase between the solid electrolyte and lithium metal for LAGP, LLTO and LPSCl.

Regarding the chemical stability at the interface between the SE and the cathode it was reported that oxide-based SEs are more stable with oxide cathodes compared to sulfide-based SEs that present an instable interface as sulfide species are more polarizable (more readily reduce the transitional metals to a lower oxidation state)[132,133].

b) Lithium dendrites formation

The high energy density required for rechargeable battery in the electric vehicles makes the use of lithium metal as anode to be mandatory due to its high theoretical specific capacity (3860 $mAh.g^{-1}$), lowest electrochemical potential (-3.04 V vs standard hydrogen electrode) and low density[39,134]. Studies, in which lithium metal was used as anode, were done years ago using conventional liquid electrolyte, but as the temperature of the battery increased, the formation of a solid electrolyte interphase (SEI) was noticed leading to short-circuit and finally combustion of the battery[57].The short-circuit of the battery is caused by the lithium metal nucleation and growth (**Figure1.10a**) as-called dendrites.

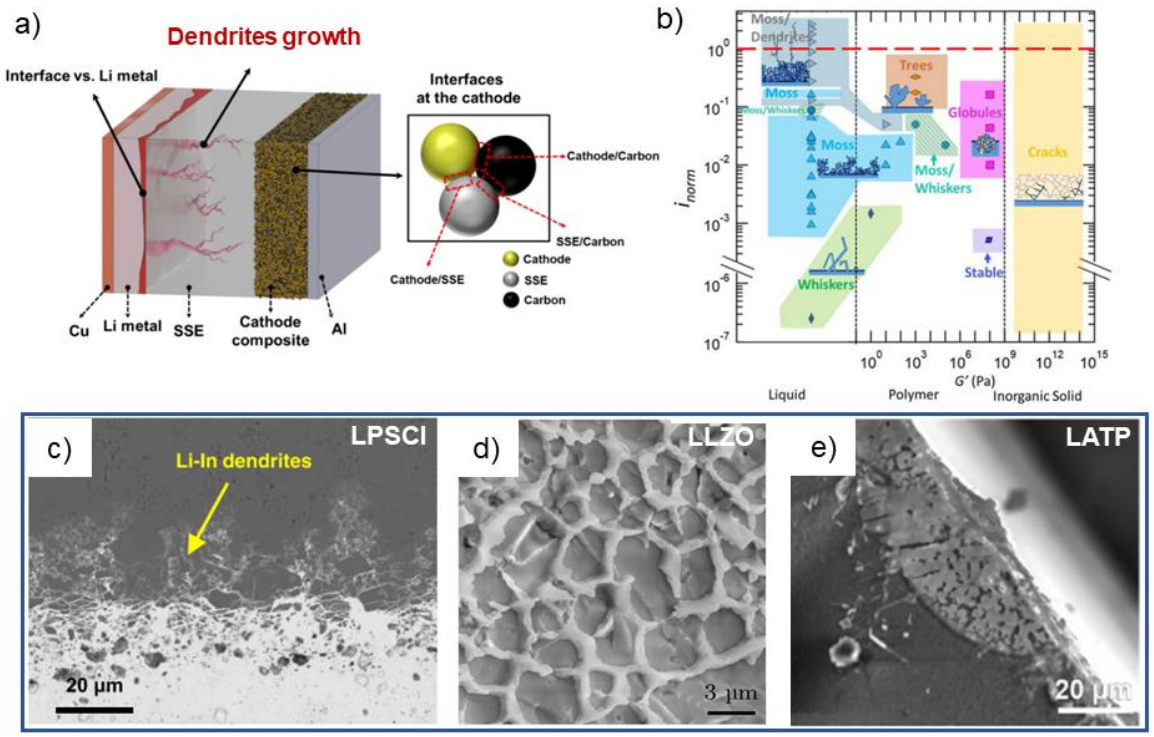


Figure 1.10 (a) Schematic representation of lithium dendrites growth inside the solid electrolyte layer in a solid-state battery[84]; (b) morphology representation of lithium dendrite growth in liquid, polymer and solid electrolyte as a function of the current density normalized, I norm, and storage shear modulus, G[56]; SEM images of the Li/ Li-In dendrites growth in (c) argyrodite[135], (d) LLZO[136] and (e) LATP[137] inorganic solid electrolytes.

The development of SEs opened again the possibility to safely use lithium metal as anode. Indeed, initially the dendrites were considered as being non-existent in the solid electrolyte due to their hard mechanical properties. Based on Monroe-Newman model it was presumed that SEs with high shear moduli, at least double compared to lithium metal, will suppress lithium metal dendrites [137,138]. In the case of the inorganic solid-state electrolytes, storage shear moduli are in a range between 10^9 and 10^{15} Pa and at this value a free dendrites solid electrolyte was expected. The advancements in the research prove it wrong, the formation of dendrites in solid electrolytes being possible, despite their high mechanical strength.

The morphology of lithium metal is affected by various factor such as current density, salt concentration where lithium is plating, temperature, pressure, and mechanical properties of electrolyte[139,140]. It can be noticed (**Figure 1.10b**) that in liquid electrolyte lithium metal grows in various shapes such as whiskers and moss. In polymers, (storage shear moduli values are between 10 and 10^9 Pa) the dendrites grow under the form of globules or trees[56,57]. In the case of solid-state electrolyte, lithium dendrites are present

under the form of small tips that promotes cracks formation which are growing in the solid electrolytes[141].

Post-mortem SEM images (**Figure 1.10c-e**) showed the presence of dendrites in SSBs using various solid electrolytes such as LPSCl, LLZO and LATP [135–137,142,143]. The fact that storage shear moduli was not enough to suppress the dendrites from the SEs indicated that various causes lead to its formation and the mechanism is much more complex. Possible other identified causes for lithium dendrite growth are the high electronic conductivity,[144] the grain boundaries and the preexisting voids and pores[145].

A solution widely investigated for lithium dendrites suppression was lithium-indium alloy due to their (electro)chemical stability. Recent study compared LPSCl/NMC cells versus lithium metal and lithium-indium alloy, both showing the presence of dendrites and finally, short circuit. In the case of lithium metal, the dendrites grew vertically, perpendicular to anode-electrolyte interface and caused severe crack propagation. In the case of lithium-indium anode the dendrites grew laterally in stripes, denser and uniform forming also a thin interphase layer (15 nm)[135]. Another solution for dendrites suppression involved: grain boundary modification, an increase in the relative density, lowering the electronic conductivity, reducing the number of preexisting defects and cracks and to apply a relaxation period during the cycling, which made the short-circuit to disappear[145,146].

c) **Cracks formation**

The hard mechanical properties of the SEs generate extra stress in the materials during the Li-ion transport and cracks are formed, producing irreversible mechanical damages in the battery[147]. Using X-ray computed tomography, J. Tippens et al.[144] investigated lithium and plating degradation mechanism in the LAGP and observed cracks formation in the SE during cycling (**Figure 1.11a**). The applied current density on the cell plays an important role as cracks formation and propagation in the SE were producing more damages when higher values were applied[148]. Cracks propagation during lithium plating and stripping process of Li_3PS_4 was investigated by M. Otoyama et al.[149] and S. Hao et al. (**Figure 1.11b**)[150] and concluded that the mechanism leading to the short-circuit of the battery consists of small cracks formation filled with lithium metal in the initial stage followed by a faster propagation of the cracks on the entire SE. At the end, lithium metal will start filling the cracks and reach the cathode and promoting a short-circuit in the battery. In the case of Li_6PS_5Cl (**Figure1.11c**)[151] the cracks formation is less violent, one possible reason for the lower intensity of cracks propagation could be related to a thin interface (around 15 nm) formed between lithium metal and SE, which does not propagate further as in the case of LAGP.

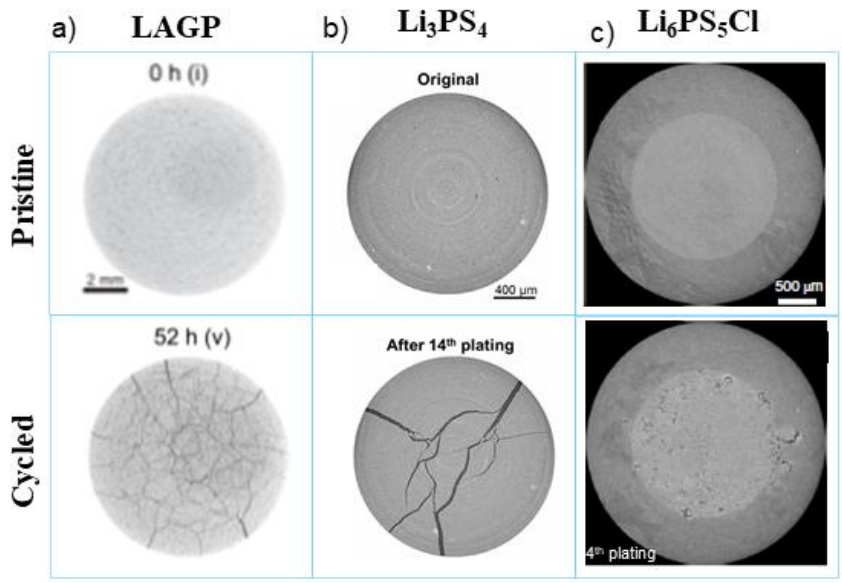


Figure 1.11 X-ray tomography images of lithium plating and stripping process in the (a) LAGP, (b) Li_3PS_4 and (c) Li_6PS_5Cl solid electrolyte.

The apparition of the cracks in the battery did not impede its functionality; the batteries are still operating even after the cracks crossed the entirely battery (the short-circuit of the battery takes place when Li metal reaches the cathode)[151,152]. However, some part of the battery can be disconnected after crack formation inducing a capacity loss and favoring dendrites formation. Possible solutions for the crack formation involve the mixture of an inorganic solid electrolyte with hard mechanical properties with a polymer based solid electrolyte, which presents very soft mechanical properties[153,154] creating a composite electrolyte with less rigidity.

d) Ionic conductivity, grain boundaries, contact quality between SE and electrodes

Ionic conductivity is known to be one of the historical challenges which limited the practical performances of SSBs [155–159] . The low RT ionic conductivity values limited the practical use of SSBs to operate at high temperatures or under the form of thin films. Since the discovery of $Li_{10}GeP_2S_{12}$ (LGPS)[80], SEs field was revitalized, sulfide-based SE presenting higher ionic conductivity (10^{-2} $S.cm^{-1}$), at RT. The continuous development in the field contributed to the generation of new SEs that currently exhibit ionic conductivity close to liquid electrolyte at RT. Unfortunately, in the case of oxide, polymers and halides, the ionic conductivities values at RT (a value of 10^{-3} $S.cm^{-1}$ at RT is required for the battery to operate) are below the current conventional batteries with liquid electrolyte. The main limiting factor that restricts the ionic conductivity in the case of oxides solid electrolytes is represented by the grain boundaries[152–156] as Li-ion diffuse with more difficulty at the grain boundaries compared to bulk [116].

Maintaining an intimate solid-solid contact between solid electrolyte and electrodes represents another challenge that needs to be resolved to improve the performances of SSBs. The difference between the mechanical properties of batteries materials results in the difficulty of maintaining a physical contact. Imperfect contacts between SE and electrodes could be formed during cell fabrication and then further promoted during the cycling process [132,160,161]. For example, at the interface between lithium metal and SE (LLZTO[162] and LIPON[161]) it was reported that during cycling process, voids are generated resulting a nonuniform interfacial contact between the two. Such effect promotes battery degradation due to the high contact resistance area and results in a capacity drop[163,164]. Possible solution for ameliorating the generation of contact loss during cycling includes the introduction of an organic buffer layer to stop the undesirable reactions or a coating layer on the solid electrolyte or active material particles[165,166].

1.10 Usual techniques used for ASSB characterizations

To overcome the challenges that SSBs face in its way to a sustainable efficient technology, is essential to understand the fundamentals governing the degradation mechanism by gaining insights into different aspects. Various characterization techniques (*ex-situ, in-situ, operando*) were used for a deeper comprehension of the kinetics and thermodynamics in the SSBs. **Figure 1.12** summarize diverse characterization techniques used for the determination of lithium metal dendrites inside the SSBs[145].

Imaging techniques such as X-ray computed tomography (XCT) and scanning electron microscopy (SEM) are used for the morphological characterization at the microscale, while (Scanning) Transmission electron microscopy ((S)TEM) is used for a better understanding of the phenomena at the nanoscale. In 2002, M. Dolle *et al.*[167] detected for the first time using *in-situ* SEM the formation of lithium dendrites in a polymer battery while cycling. He observed that with an increase in the current density, Li evolved from mossy to dendritic shape, moreover the growth process was continuing even after the tip was no longer in contact with the solid electrolyte. Later in 2016, C. L. Tsai *et al.* noticed using HR-TEM and EELS the presence of the lithium metal and a mixture of Li_3N, Li_2CO_3 and LiO_x phases at the grain boundaries of LLZO solid electrolyte. Advanced characterization techniques such as X-ray CT were used to understand the failure mechanism of LAGP solid electrolyte based on the evolution of cracks network[168,169].

X-ray diffraction (XRD), electron diffraction (ED) and Nuclear Magnetic Resonance (NMR) are used for a comprehension of the crystal structure battery materials. In 2019 Marbella *et al.*[170] used 7Li NMR chemical shift imaging and electron microscopy to track the microstructural growth of lithium metal into Garnet solid electrolyte and confirmed the

short-circuit of the battery. *In-situ* space X-ray diffraction combined with *in-situ* phase contrast X-ray computed tomography (XCT) was used to investigate the cracks and lithium propagation in the SE during plating[151]. They showed that cracks propagate in the SE far ahead than lithium metal and when the cracks transverse completely the SE no short-circuit is occurring until lithium fills the cracks.

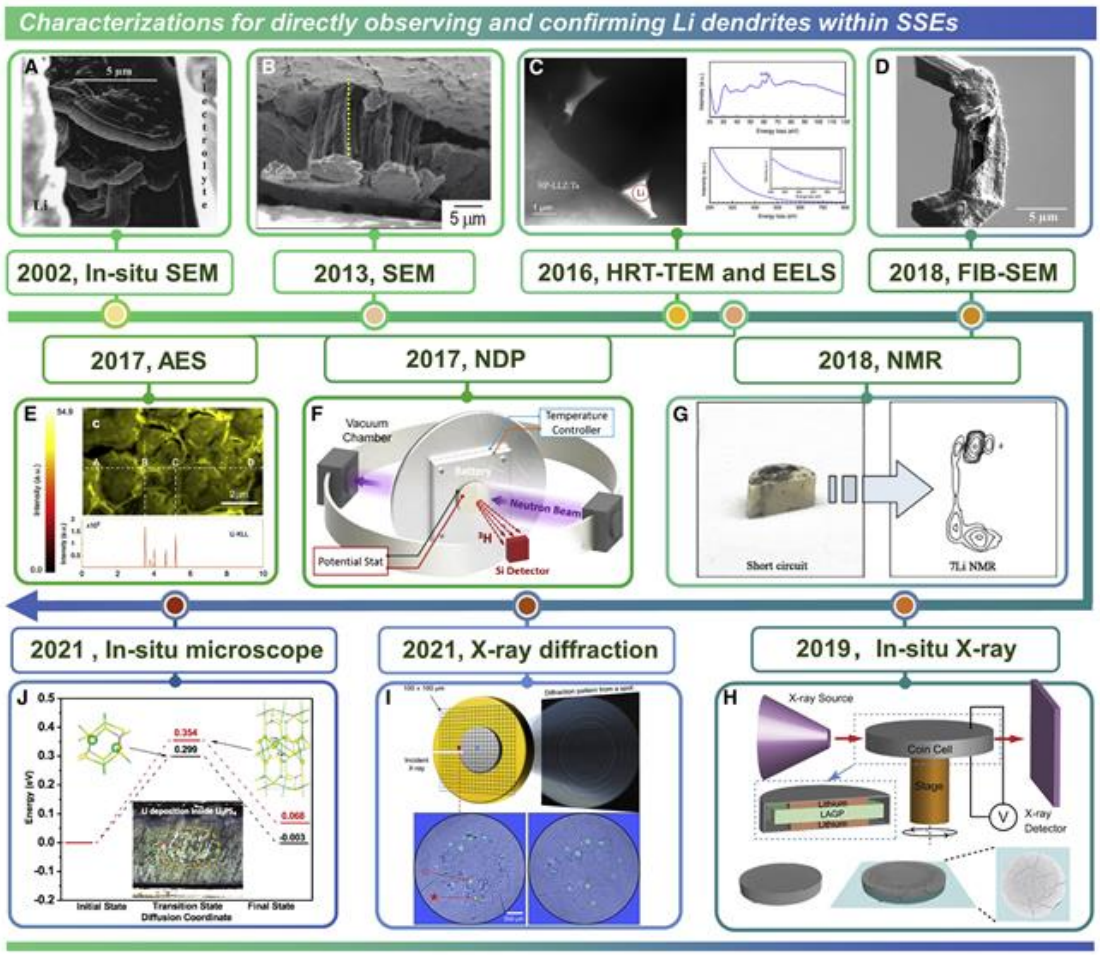


Figure 1.12 Summary of various characterization techniques as: (a-b) SEM, (c) HRT-TEM and EELS, (d) FIB-SEM, (e) AES, (f) NDP, (g) NMR (j) in-situ microscope (i) X-ray diffraction (h) In-situ x-ray used for the dendrites/cracks observations inside the SSBs.

In this thesis, we are interested in understanding the challenges that LAGP need to overcome to become sustainable solid electrolyte for the future generation of batteries. Understanding the fundamentals governing the degradation mechanism of oxide solid-state batteries is essential to improve the next generation of batteries. A comprehension of the oxides solid-state batteries during operation starting from microscale to nanoscale and combining with analytical methods will provide deeper insights on the degradation mechanism. During this work, we are using numerous characterization techniques such as FIB-SEM tomography, *In-situ* X-ray tomography, *in-situ* (S)TEM, XRD, NMR and EIS to understand deeply the fundamentals that triggers the degradation mechanism of oxide solid-state batteries.

The structure of the thesis manuscript:

Chapter 2 "Impact of microstructural properties on the ionic conductivity of LAGP" presents our study on the synthesis of LAGP oxide solid electrolyte, and its characterization, followed by the SPS procedure to obtain pellets with high density and ionic conductivity. Our investigation to get a better insight into the inter-grain nature, the limiting factor for the ionic conductivity, pushed us for further characterization such as FIB-SEM tomography, SEM-EDX and MAS-NMR analysis to understand the impact between ionic conductivity, morphology, and structure of the grain boundaries. Our investigation showed the presence of an inter-grain phase ($Li_4P_2O_7$ and $Li_9Al_3(P_2O_7)_2(PO_4)_3$) as one of the detrimental points that are impacting the total ionic conductivity of LAGP.

Chapter 3 "Li metal interface with LAGP**"** focus on the most challenging solid-state battery limitation, the interface between the solid electrolyte and the lithium metal. We investigated the interface formation in function of the applied current density using various imaging analysis techniques such as SEM, SIMS and X-ray tomography. Our investigation showed an immediate chemical degradation between LAGP and Li metal leading to an interphase layer and cracks generation. During an electrochemical reaction, the formation of a stronger interphase layer was noticed, and cracks penetrated deeper inside the solid electrolyte as the applied current density value increased.

Chapter 4 "*In-situ* electrochemical X-ray µ-computed tomography**"** focus on the dynamics at the interface between lithium metal and solid electrolyte. Using *in-situ* X-ray tomography imaging coupled with EIS analysis, we investigated the lithium plating and stripping process within LAGP. This study demonstrated the presence of an interphase layer and a reduction layer at the interface. As the reaction progressed, the reduction layer propagated and covered the entirely surface interface. The formation of dendrites in the form of spallation was also spotted.

Chapter 5 "Oxide all-solid-state battery using Li metal as anode" presents the one of the most challenging parts of this thesis, cycling a solid-state battery without any liquid electrolyte. We will share our contributions on the path that we followed in order to obtain such a working oxide solid-state battery. Parameters as thickness of electrode and solid electrolyte, temperature of cycling, electrode composition and mixing conditions were considered to improve the cycling performances. The degradation mechanism of the solid-state battery investigated using SEM revealed the presence of large cracks which penetrated the entirely battery and lithium that penetrates inside the SE using "medusa arms dendrites".

Chapter 6 "*In-situ* electrochemical STEM experiments" presents our most ambitious goal during this project, to realize *Operando* TEM measurement on a working all-solid-state battery. We will present our strategy to obtain a micro-battery that will contain the three layers of the battery (positive electrode, solid electrolyte, negative electrode) within 50 µm. Our study uses various characterization methods (STEM-EDX, 4DSTEM and EELS analysis) and offers insightful results about the degradation mechanism at the nanoscale. We observed using STEM the appearance of large cracks in the solid electrolyte, LAGP particle shrinkage and the formation of large grain boundaries.

Chapter II 37

Impact of microstructural properties on ionic conductivity in LAGP solid electrolyte 37

2.1 Introduction 37

2.2 LAGP synthesis and sintering process 39

2.3 Ionic conductivity 41

2.4 Morphological properties and tortuosity 43

2.5 Chemical and structural properties analysis 47

2.6 Conclusions and perspectives 54

Appendix A 58

Chapter II

Impact of microstructural properties on ionic conductivity in LAGP solid electrolyte

2.1 Introduction

Solid-state batteries[60,171,172] (SSBs) have attracted great attention in the last decade due to their higher energy density possibility as may enable the use of Li metal[173] and high potential cathode materials[174,175]. Solid electrolytes[63,74,172] (SEs), the key component of SSBs, have experienced a rapid development in the last years due to their non-inflammable nature making them ideal for electric vehicle (EV) applications. Within the range of available material for the SEs, oxides solid electrolytes have a high stability in the air, low cost, wide electrochemical window, and improved chemical stability with oxide cathode materials[79,114].

One of the promising Li-ion conducting oxides SEs are the NASICONs (Na-super-ionic-conductive), first reported in 1976 by Goodenough and Hong[176]. At first, NASICON materials were described as Na superionic conductors where their structure was composed of a rigid substructure, $[Zr_2Si_xP_{3-x}O_{12}]^-$ and Na as a charge carrier that was moving within the interconnected pathways[177]. Later, the list of chemicals elements included in the charge carrier and skeleton developed and today NASICON materials can be represented by the general formula $A_{1+x}M_2(BO_4)_3$[72]. The charge carrier "A" is represented by Li^+, Na^+ or K^+ ions, "M" is a tetravalent cation (Zr, Ti, Ge, Hf, Sn) or its combination with a trivalent cation (Al, Fe, In, Y, Ga) or a bivalent cation (Sr, Ca, Mg) and "B" is generally P^{5+} or Si^{4+} combination[178].

$Li_{1+x}Al_xGe_{2-x}(PO_4)_3$ abbreviated as LAGP is one of the most intensively studied Li-ion conducting NASICON materials.[179,180] LAGP structure is composed of $LiGe_2(PO_4)_3$ as the main phase where Al^{3+} ions partially replace Ge^{4+} ions. In the $LiGe_2(PO_4)_3$ phase a 3D network is built from the GeO_6 octahedra and PO_4 tetrahedra creating cavities where Li ions reside and bottlenecks through which Li ions pass. LAGP forms a rhombohedral unit cell where the partially replacement of Ge^{4+} ions by Al^{3+} ions reduce the unit cell dimensions resulting in higher density and enhanced ionic conductivity[72]. It should be noted that LAGP presents one of the highest ionic conductivities from the oxides SEs group (~10^{-4} –10^{-3} $S.cm^{-1}$ at room temperature)[78], but despite their improved ionic conductivity, the values are notably reduced compared to sulfide SEs[82,155] due to their grain boundaries (GB)

resistance[116]. GB resistance has been reported already in various types of oxides SEs and it was suggested that the reduced ionic conductivity is due to structural or chemical changes that occurs at GBs and may disrupt the diffusion pathways of Li-ions[181,182].

Different strategies have been proposed to decrease GB resistances in oxide SEs, such as the introduction of B_2O_3 as a microstructure modifier to facilitate the grain growth and to reduce the number of grain boundaries[183] or the incorporation of a secondary lithium compounds such as Li_3BO_3, Li_3PO_4, Li_2O, $Li_4P_2O_7$ which segregate at the grain boundaries and subsequently inducing lower grain boundary resistance[183–185]. Nevertheless, the total ionic conductivity of oxide-based SEs is still an order of magnitude lower in comparison to its sulfide SEs counterparts[82].

Previous studies, showed that NASICON-type SEs sintered at high temperature results in a partial decomposition at the grain boundaries, leading to the formation of secondary phases creating an inter-grain region[186–188]. Studies performed on $Li_{1+x}Al_xTi_{2-x}(PO_4)_3$ (LATP) at higher sintering temperatures than 900 °C showed the formation of secondary phases at the grain boundaries (inter-grain region) probably due to high lithium loss content during the sintering process[188]. The formation of an inter-grain region was also reported after Si doping in LATP where $LiTiOPO_4$ phase segregated at the grain boundaries suppressing the abnormal growth of the grains resulting in an improved ionic conductivity[186]. LAGP synthetized using excess Li showed an enhanced total ionic conductivity due to lithium segregation at the grain boundaries, which subsequently increases the concentration of charge carriers, leading to an increase in grain boundary conductivity[189,190].

Despite their importance, the structure and the composition of the inter-grain region are still not fully understood and prevent further development of LAGP-based SSBs. To unambiguously pin down the origin of the ionic conductivity losses at the inter-grain region, this work aims to correlate the inter-grain region composition with LAGP ionic conductivity by varying the sintering temperature of LAGP in Spark plasma sintered (SPS) pellets. A more complete understanding of the inter-grain microstructure is obtained using complementary macroscopic techniques (compactness and impedance measurements), longer range/periodic structural techniques such as XRD, and short-range/local characterization achieved by SEM-EDX, 3D FIB-SEM tomographic reconstruction and solid-state MAS NMR coupled with materials modelling.

2.2 LAGP synthesis and sintering process

$Li_{1.5}Al_{0.5}Ge_{1.5}(PO_4)_3$ (LAGP) can be obtained by various synthesis methods such as solid-state synthesis, melt quenching, microwave assisted sintering, coprecipitation and sol-gel technique, but the latest allows to obtain highly conductive solid electrolyte pellets at lower sintering temperature[191–193]. In this study, LAGP powder was synthesized using sol-gel method (See **Appendix A** for more details). The synthetized powder characterized using Scanning Electron Microscopy (SEM) (**Figure 2.1a**) showed that the obtained powder displays a tetragonal morphology with a particle size distribution spanning a 0.175 − 3 µm range with LAGP particles agglomerated in the groups of tens of microns (**Figure 2.1b**).

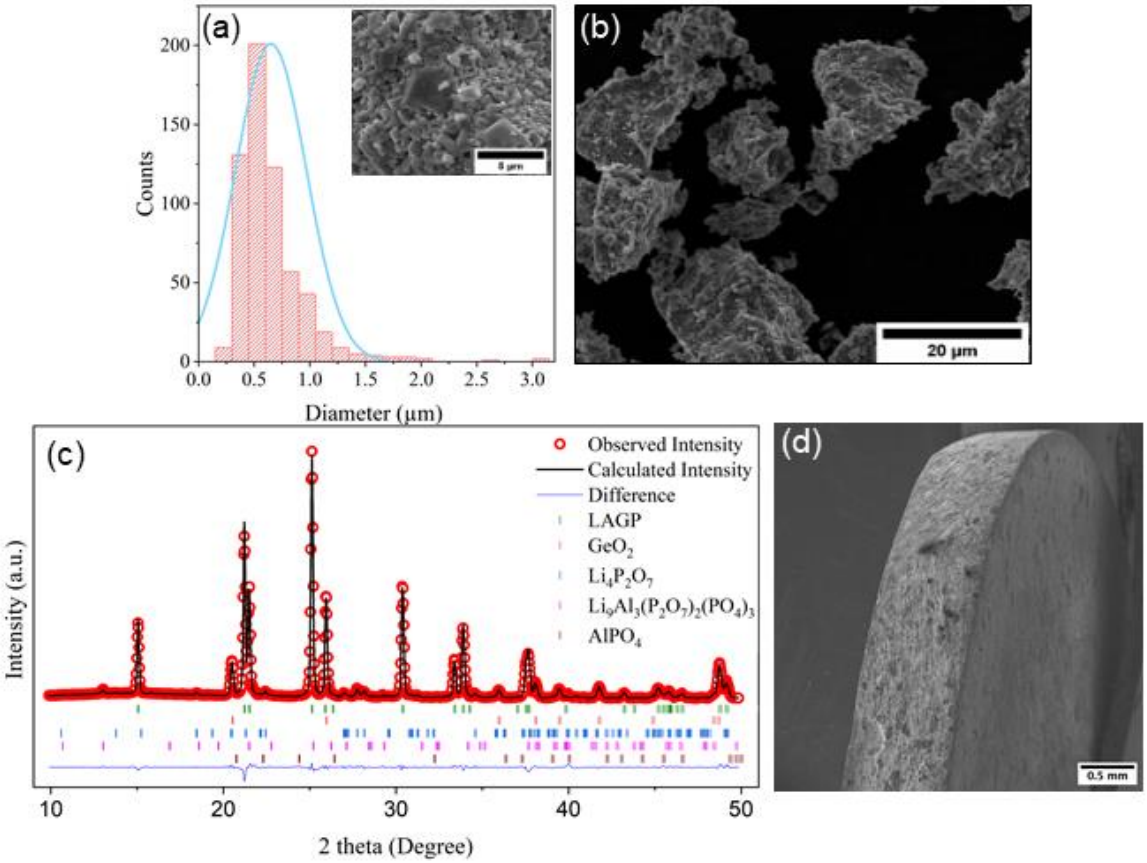


Figure 2.1 (a) Secondary electrons images and size distribution of the $Li_{1.5}Al_{0.5}Ge_{1.5}(PO_4)_3$ powder obtained by sol-gel method. The pink line is the histogram (N=612 particles) of the particle size distribution and in blue line is the normal fit of the size distribution (mean of 0.649 (±0.317) µm). (b) Secondary electron SEM image and (c) XRD Rietveld refinement analysis of synthetized $Li_{1.5}Al_{0.5}Ge_{1.5}(PO_4)_3$ using sol-gel method (d) Cross-section secondary electron image of LAGP made pellet using Spark Plasma Sintering.

The Rietveld refinement XRD pattern of sol-gel synthesized solid electrolyte (**Figure 2.1c**) showed that the main phase is LAGP phase (R3-c group phase) (81.35 wt %). Small secondary phases such as GeO_2 (7.02 wt %), $Li_4P_2O_7$ (10.11 %), $Li_9Al_3(P_2O_7)_2(PO_4)_3$ (1.17 wt %) and $AlPO_4$ (0.36 wt %) are also presented, encountered, and reported very often during the synthesis of this solid electrolyte[72,194].

Oxides SEs requires high temperatures to get densified and obtain pellets with high ionic conductivity[79]. The most common methods used in a laboratory scale are cold pressing followed by an annealing high temperature treatment[92] and Spark Plasma Sintering[95,195]. Unfortunately, in the case of oxide SEs, cold pressing technique doesn't promote good solid-solid interfaces with acceptable ionic conductivity without annealing at high temperature[96]. SPS represent one of the most efficient methods to obtain in a short period of time (couple of minutes) highly dense pellets (**Figure 2.1d**) which improves the ionic conductivity[196]. This method was used successfully for the sintering of various solid electrolytes such as LLZO, LLTO, LAGP or even complete solid-state batteries[98,99].

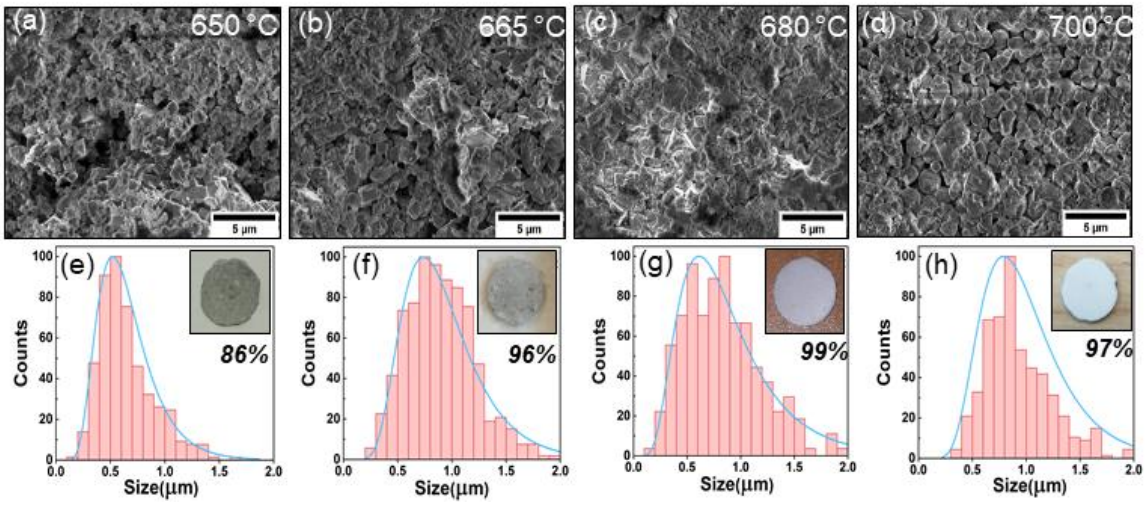


Figure 2.2 SEM Secondary electron images of LAGP surface pellets sintered at (a, e) 650 °C, (b, f) 665 °C, (c, g) 680 °C, (d, h) 700 °C and their associated particle size distribution histogram. The compacity values of each pellet is given in % in the insets.

During this project, we used SPS technique to obtain densified LAGP solid electrolytes pellets. (See **Appendix A, Figure A1** for methods). SPS temperature was varied (650, 665, 680 and 700 °C) to get different compacity values and optimize the ionic conductivity of the pellets. **Figure 2.2a-d** displays the optical images of the solid electrolyte pellets and the top view secondary electron SEM images of sintered LAGP grains at different temperature. It can be observed that the lower sintering temperature pellets (650 and 665 °C) displayed a change of color from white to light gray after the sintering process, a possible hypothesis for this effect being related to graphite diffusion inside the solid electrolyte from the SPS die. Moreover, based on top surface SEM images it can be observed that pellets obtained at a lower sintering temperature exhibits higher porosity compared to pellets sintered at higher temperature (680 and 700°C). Average particle size distribution measured from the SEM images (FIJI software) increased from 0.65 µm for synthetized LAGP grains to a spanning 0.66 – 1 µm ± 0.49 µm range in the sintered pellets;

with an average particle size distribution increasing with the sintering temperature (**Figure 2.2e-h**).

The compacities of the pellets are directly linked to the ionic conductivity values as higher compacity will theoretically provide a better solid-solid contact between solid electrolyte particles and should generate less grain boundaries. The compacity of the sintered pellets were calculated using **Eq. 1**.

$$\textbf{\textit{Compacity}} = (m * \rho)/(\pi * r\text{^}2 * h) \qquad \textit{(Eq. 1)}$$

where: h: thickness (cm), m: mass of the pellet (g) and ρ: density (g/cm)

The compacity values of sintered LAGP are in the 85 to 99 % range (**Figure 2a-d**), increasing from its lowest value for a sintering temperature of 650 °C up to its highest value for a sintering temperature of 680 °C, before decreasing again at higher sintering temperatures.

2.3 Ionic conductivity

The ionic conductivities of the four sintered pellets at different SPS temperatures were measured using electrochemical impedance spectroscopy (EIS) in a temperature range spanning -30 − 60 °C (See **Appendix A** for methods). The obtained Nyquist plots of the four pellets recorded at room temperature (RT) are shown in the **Figure 2.3a.** Each Nyquist plot is composed of two semicircles (at higher frequencies) followed by a linear tail (at low frequencies). The linear tail corresponds to electrode polarization from the gold protection layer added on pellet surface to ensure a proper contact with cell electrodes. A Brick-Layer model[197,198] can be used to fit the impedance data (**Figure 2.3a**) which consists of an instrumental resistance (R_1), two parallelly connected resistance/CPE (constant phase element) couples connected in series representing the bulk and the inter-grain region with grain boundaries, and a CPE representing the capacitive effect at the blocking electrodes (CPE4). The first high frequency semicircle (repressed by R2 and CPE2) was attributed to Li^+ motion in the bulk, whereas the second semicircle (repressed by R3 and CPE3) was attributed to Li^+ motion in the inter-grain region with grain boundaries[155,192,193]. The ionic conductivities of bulk and inter-grain (σ_b and σ_{ig+gb}) were calculated using **Eq. 2** based on the obtained fit resistances values and total ionic conductivity represents the sum of the bulk and inter-grain region + grain boundaries ionic conductivity.

$$\sigma_b / \sigma_{ig+gb} = \frac{1}{Rb/R\ ig+gb} \left(\frac{t}{A}\right) \qquad \textit{(Eq. 2)}$$

where: t= thickness of the pellet and A=surface area of the pellet

Arrhenius plots of the bulk and inter-grain region ionic conductivity vs 1/T shows the bulk conductivity (**Figure 2.3b**) remains constant for all the pellets regardless their sintering temperature, but the inter-grain region ionic conductivity (**Figure 2.3c**) increases until 680 °C, then slightly decreases at 700. As a result, the total ionic conductivity values (**Figure 2.3d**) increased monotonically until 680 °C, then reduced at 700 °C. **Figure 2.3e** displays the compacity and the RT ionic conductivity values of the pellets in function of their sintering temperature. The resistance values at RT resulted from the fit using Brick-Layer model and thickness/surface rapport values are presented in **Table1**. The RT impedance data of **Figure 2.3e** show that pellets sintered at 650 and 665 °C have larger inter-grain resistivities (1,155.4 and 1,074.9 ohm.cm, respectively) in comparison to the pellets sintered at higher sintering temperature, 680 and 700 °C counterparts (195.7 and 322.6 ohm.cm, respectively), with the 680 °C pellet demonstrating the lowest inter-grain resistivity.

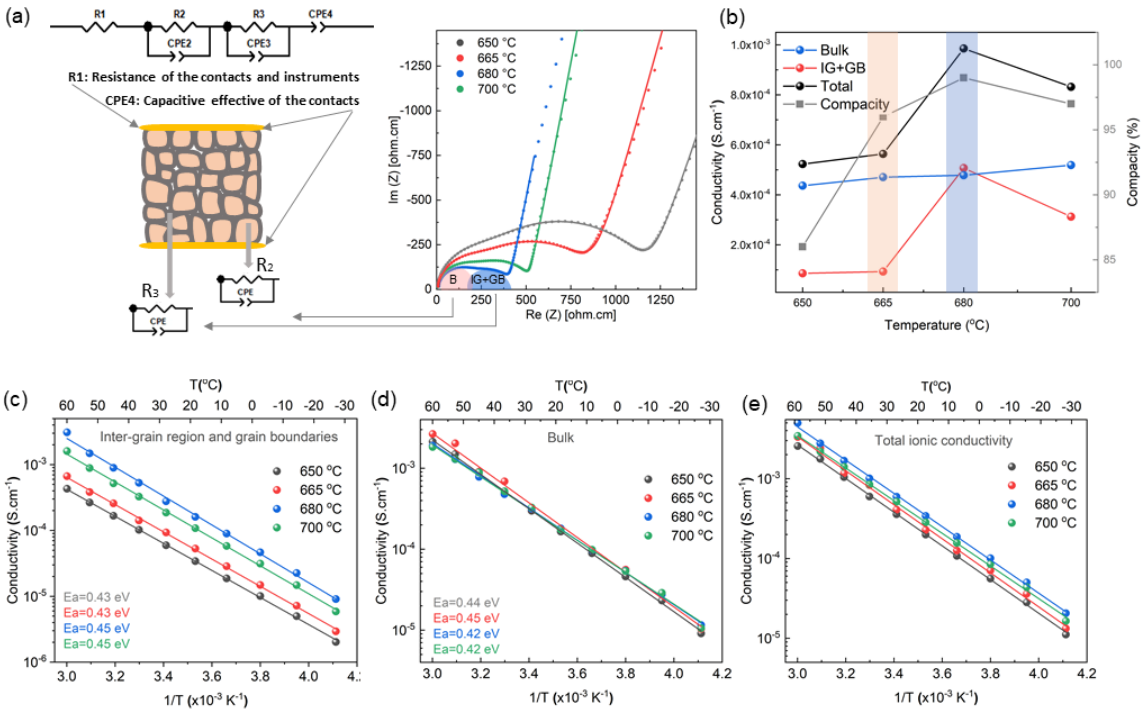


Figure 2.3. (a) Schematic representation of the Brick-Layer model and of the grain structure within LAGP film and room temperature Nyquist plots of the pellets sintered at 650 °C, 665 °C, 680 °C and 700 °C; the fitted semi-circles of the grain and inter-grains regions are displayed. (b) Compacity and room temperature ionic conductivity of grain, inter-grain and pellet values versus sintering temperatures (c-e) Arrhenius plots of the (c) inter-grains and grain boundaries region, (d) bulk and (e) total ionic conductivity values. The resistance and conductivity data are normalized by the specimen geometrical dimensions of the pellets.

The highest total ionic conductivity value was observed for the pellet that presented the lowest inter-grain region resistance and the highest compacity (680 °C). It was observed that generally, the ionic conductivity increased with the compacity values. However, the pellets sintered at 650 and 665 °C presented similar inter-grain region ionic conductivity, but the latest displayed a higher total ionic conductivity, most likely due to a

higher compacity in the pellet. Moreover, despite similar compacity values registered for the 665 and 700 °C samples, the latest exhibited a higher total ionic conductivity value. An increase in the total ionic conductivity of 700 °C pellet was induced by a higher inter-grain region ionic conductivity (**Figure 2b**). Such increase in the total ionic conductivity despite the same compacity could be attributed to morphology and compositional changes at the inter-grain region.

Table 1. Resistance values of the bulk and inter-grain region obtained after the fit with Brick-Layer model for the RT measurement and thickness/surface area rapport values of sintered pellets.

	650 °C	**665 °C**	**680 °C**	**700 °C**
R bulk (ohm)	218.1	156.7	227.3	237.7
R inter-grain (ohm)	1060	762.4	206	435.9
t/A (cm)	1.09	1.41	0.95	0.74

The slopes of the σT vs 1/T Arrhenius plots allow to extract the activation energies of the ionic transport through the inter-grain region and bulk (LAGP grains) network. The activation energies of grain network at high sintering temperatures (680 and 700 °C) displays marginally lower value of ~0.42 eV compared to grain activation energy of ~0.44 eV at lower sintering temperatures (650 and 665 °C), indicating that the ionic conduction through the bulk experience lower energy barriers for higher sintering temperature samples. At the opposite, for the ion migration through inter-grain region, marginally lower activation energies values were observed for the sample sintered at lower sintering temperatures, indicating a less disturbed ionic migration through the inter-grain region.

2.4 Morphological properties and tortuosity

As inter-grain region plays an important role on the total ionic conductivity of LAGP pellets, FIB-SEM tomography experiments were carried out (See **Appendix A** for methods) to investigate their local morphology. FIB-SEM tomography provides a 3D representation at the micrometer scale of the inter-grain and grain morphology, and allows a quantification of the phase fractions, tortuosity, and local connectivity[199,200]. Moreover, as the difference level of contrast in the backscattering-electrons-SEM (BE-SEM) images is based on the atomic number Z, a segmentation of the BE-SEM 3D volumes enables to associate a contrast with a given phase and allows to quantify and determine the spatial distribution of each phase present inside the SE.

A representative BE-SEM image collected during the FIB-BE-SEM tomography acquisition of the pellets sintered at different temperatures (offers a cross section view) is shown in the **Figure 2.4a-d**. It can be noticed that all the analyzed solid electrolyte pellets reveal the presence of pores and voids (darker gray contrast) and an inter-grain region

(light gray contrast). The image series acquired during the FIB-BE-SEM tomography analysis were aligned, 2D multi-phase segmented with Trainable Weka Segmentation[201] package (FIJI, Random Forest algorithm) and then further 3D reconstructed using DragonFly software. From the reconstructed 3D-FIB-BE-SEM analysis it was observed that the inter-grain region forms a connected network around LAGP grains which can strongly impact the ionic conduction. Most likely, the main reason for a lower grain boundaries ionic conductivity in the pellets sintered at lower temperature is represented by the presence of such an inter-grain region located between the LAGP grains. The reconstructed 3D-FIB-BE-SEM volumes of the different phases (LAGP, inter-grains region and pores) associated with the 680 °C sintered pellet are displayed in the **Figures 2.4e-i**. The presence of the inter-grain region was noticed in all the analyzed LAGP pellets (**Figures 2.4j-m**) and generates a network inside the SE. The 3D volumes of the different phases (LAGP grains, inter-grain regions, voids, germanium oxide and $AlPO_4$) of all the SE pellets are shown in the **Figure 2.5**.

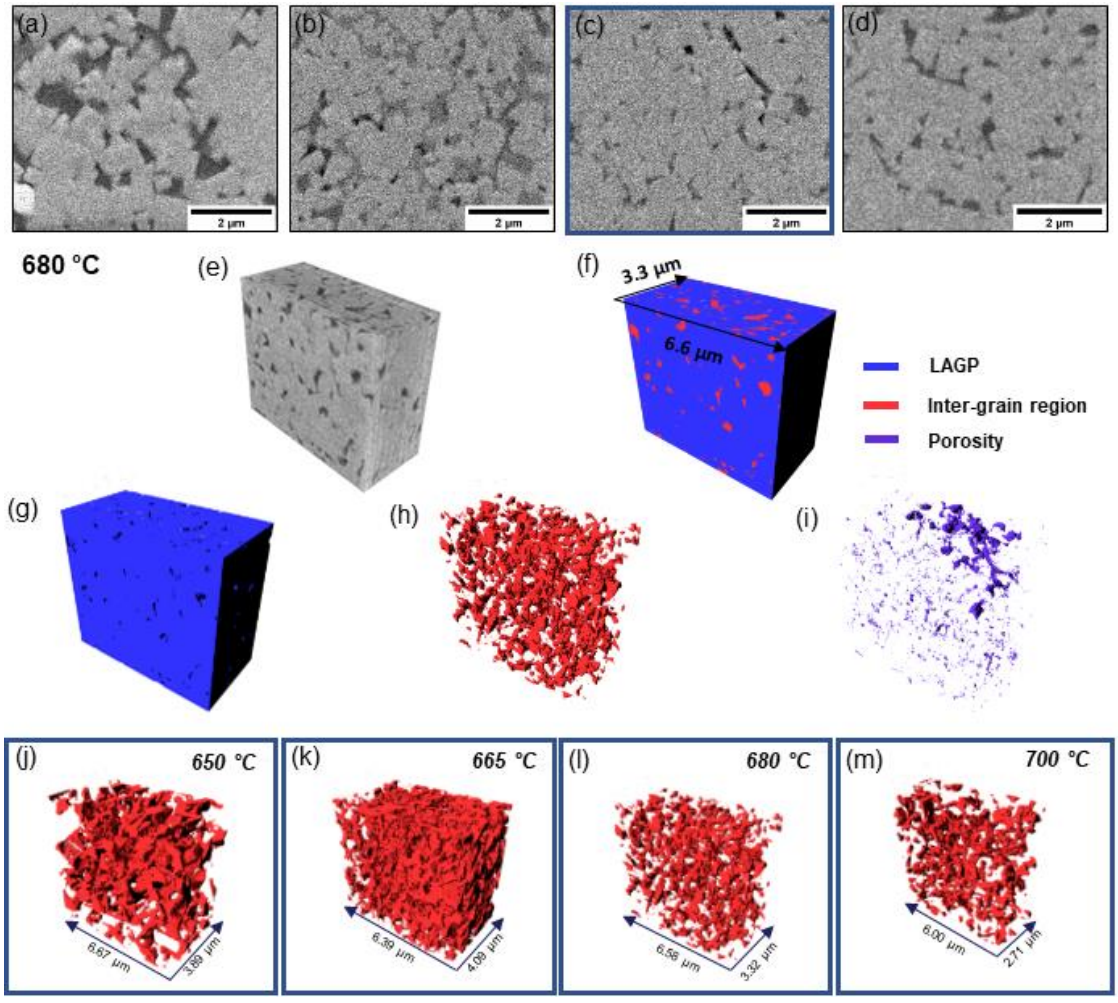


Figure 2.4. Backscattering electrons images from the FIB-SEM tomography of the pellets sintered at (a) 650 °C, (b) 665 °C, (c) 680 °C, (d) 700 °C. FIB-SEM tomography on the solid state electrolyte pellet prepared by SPS at 680 °C where it shows (e) 3D volume reconstructed from a series of BE electron images, (f) 3D

volume after segmentation, based on BE electron images of the three phases shown in g to i, (g) LAGP grains, (h)Inter-grain region, (i) pores and voids. Reconstructed 3D volumes of inter-grain phase from LAGP pellets sintered at (j) 650 °C, (k) 665 °C, (l) 680 °C and (m) 700 °C.

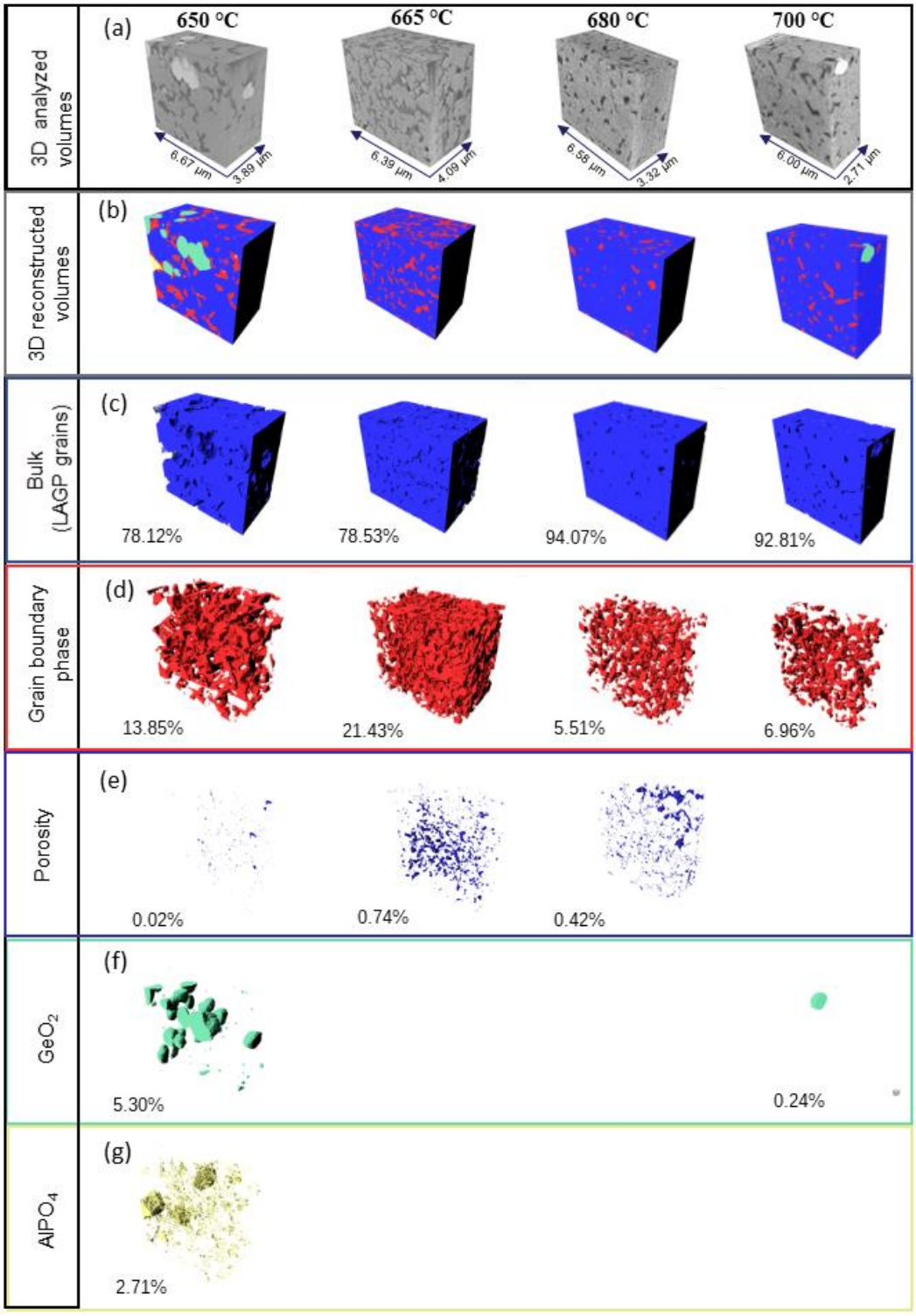


Figure 2.5 FIB-SEM tomography on the solid state electrolyte pellets prepared by SPS at 650 °C, 665°C, 680 °C and 700 °C where it shows (a) 3D volumes reconstructed from a series of BE electron images, (b) 3D reconstructed volumes after segmentation based on BE electron images of the five phases presented in the SE (c) LAGP grains, (d) Inter-grain phase, (e) pores and voids), (f) germanium oxide and (g) $AlPO_4$.

The phase fraction of each phase inside the SE can be extracted from the 3D segmented phases volumes. Based on the 3D-FIB-BE-SEM analysis a higher fraction ration of inter-grain region was observed for the low sintering temperature (spanning 13.8 − 21.4 % range) compared to high sintering temperature (spanning 5.5 – 6.9 % range). The pellets sintered at lower temperature presented higher resistance at the inter-grain region. The lowest fraction ration of the inter-grain region was observed in the 680 °C SE pellet, which also presented the highest inter-grain ionic conductivity. This observation suggests a link between the fraction ratio, morphology of the inter-grain region and total ionic conductivity.

The tortuosity values of the grain and inter-grain region are extracted from the 3D volumes of each phase to understand better the ionic pathways in the solid electrolyte. The tortuosity represents how 'direct' the 3D pathway is from one point to another in the volume. In terms of ionic conductivity, a tortuosity value of 1 represents a direct path, meanwhile a larger tortuosity value indicates a less direct paths (more tortuous) between the two sides of the pellets[202]. The tortuosity maps calculated based on a selected volume from the 3D-FIB-BE-SEM analysis using TauFactor are given in **Figure 2.6** and their values in **Table 2** with the associated phase fraction.

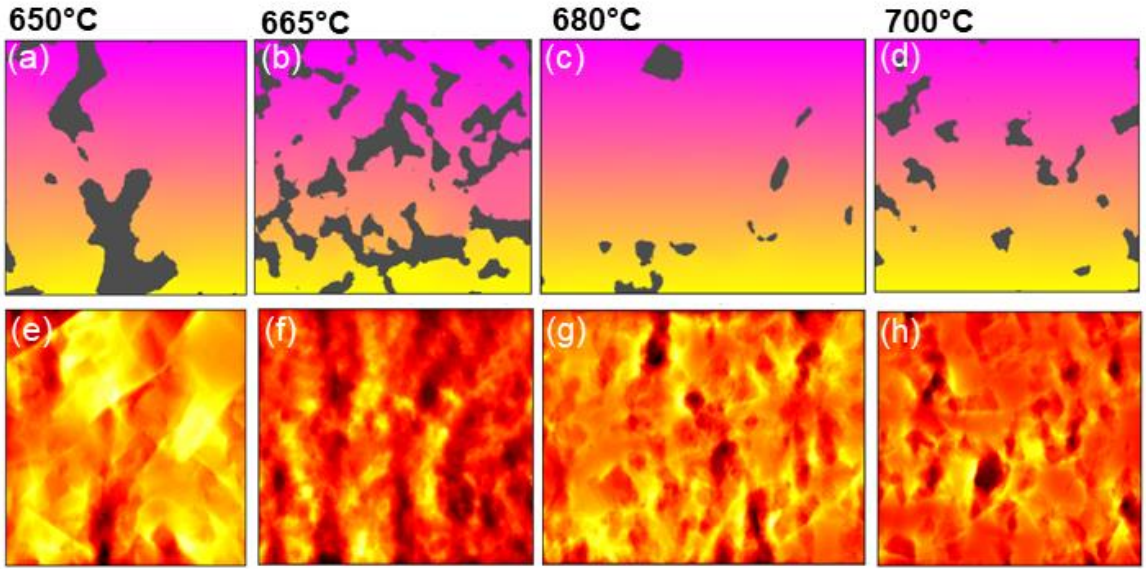


Figure 2.6. Tortuosity analysis (Flow through approach from TauFactor) on the four sintered pellets by Spark Plasma Sintering using the 3D volumes representation obtained by FIB-SEM tomography.

LAGP grains exhibited similar tortuosity with values close to 1 in all the sintered pellets, with a slightly increase for the 665 °C pellet. The increased tortuosity value for the 665 °C may be explained by the increase of fraction ratio of the inter-grain network, preventing a continuous connection of the LAGP grains. The inter-grain region tortuosity values decreased from 6.15 to 2.22 when the sintering temperature increased from 650 °C to

665 °C and become infinite at higher sintering temperatures. A finite value indicates the presence of a continuous pathway in the inter-grain regions at lower sintering temperatures, meanwhile the infinite values indicate the inter-grain region does not form a continuous path for the conduction of Li^+ at higher sintering temperatures.

Table 2: Phases fractions, tortuosity and compacity values for the four pellets sintered at 650 °C, 665 °C, 680 °C and 700 °C.

Sintering temperatures	**650 °C**	**665 °C**	**680 °C**	**700 °C**
Grain phase fraction (%)	78.12	78.53	94.07	92.81
Inter-grain phase fraction (%)	13.85	21.43	5.51	6.96
Voids fraction (%)	0.02	0.74	0.42	0.00
Others phase fraction: GeO_2 & $AlPO_4$ (%)	8.01 (5.3+2.71)	0.00	0.00	0.24
Tortuosity : Grain	1.09	1.44	1.03	1.04
Tortuosity : Inter-grain	6.15	2.22	inf	Inf
Compacity (%)	86	96	99	97

The similar obtained tortuosity value of the grains is put in relation with the similar calculated activation energy measurements for the grains. The lower tortuosity values of the 650 °C and 665 °C pellets might explain the lower activation energies measured for the inter-grain regions. We hypothesize that a more continuous inter-grain pathway may decrease the energy barrier for the Li^+ to propagate through the inter-grain network. The tortuosity explains the difference between the activation energies but fails to explain the increase of the ionic conductivity in the pellet sintered at 680 °C.

2.5 Chemical and structural properties analysis

A combined approach using SEM-EDX, XRD and solid-state NMR/modelling was carried out to provide an in-depth analysis of the structure and composition of inter-grain region that impacts the total ionic conductivity.

To investigate the chemical composition of the inter-grain phase, BE-SEM images, and EDX-SEM mapping analysis (**Figure2.7** and **Figure2.8**) were performed at the end of the FIB-SEM tomography process allowing a cross-section view inside the solid electrolyte. Using the BE-SEM images formed from a signal proportional to the locally averaged atomic number (Z) of the analyzed area in combination with the EDX-SEM dataset acquired at the same location, a given composition can be attributed to each level of contrast presented in the BE-SEM image.

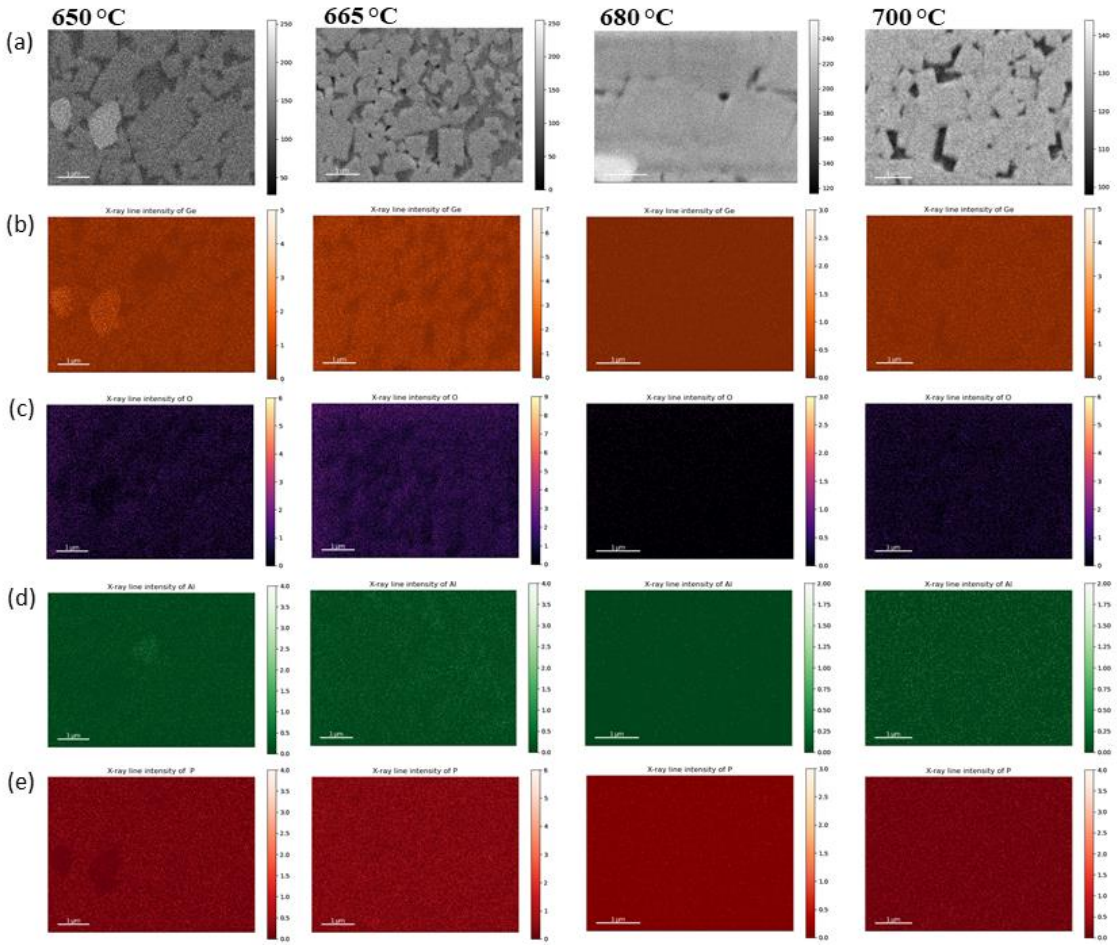


Figure 2.7 Cross-section SEM-EDX analysis performed on the solid-state electrolyte pellets prepared by SPS at 650 °C, 665°C, 680 °C and 700 °C where it shows (a) the BE image corresponding the analyzed area and the X-ray line intensities of (b) germanium, (c) oxygen, (d) aluminum and (e) phosphorus.

Based on the BE-SEM images, a segmentation process was carried out (**Figure A2**) to separate the different phases present in the pellet based on their contrast using a python segmentation code (See details in **Appendix A**) which allowed us to obtain the average atomic percent of each phase present in the pellet (**Table A2**). Thus, the five levels of contrast presented in the BE-SEM image (**Figure A2, Appendix A**) were attributed to pores and voids, inter-grain region, $AlPO_4$, LAGP and GeO_2 with decreasing level of intensity from black to white. This analysis allowed us to obtain an average at % of each element (except Li) in the grains and inter-grain region, listed in **Table 3**.

In all the analyzed pellets, germanium concentration was found in a significantly lower value for the inter-grain phase compared to the grains where its values were closer to the theoretical LAGP. The normalized average EDX spectra of the grain (orange) and inter-grains region (blue) are displayed in the **Figure 2.8**. The normalized average EDX spectra confirmed that germanium is found in a lower concentration for the inter-grain phase (blue).

Phosphorus concentration values were higher for the inter-grain region compared to grains. Interestingly, for the grain region, phosphorus values were found in a lower concentration in all the analyzed pellets, meanwhile the inter-grain region (higher values than the grains) showed comparative values to the theoretical ones.

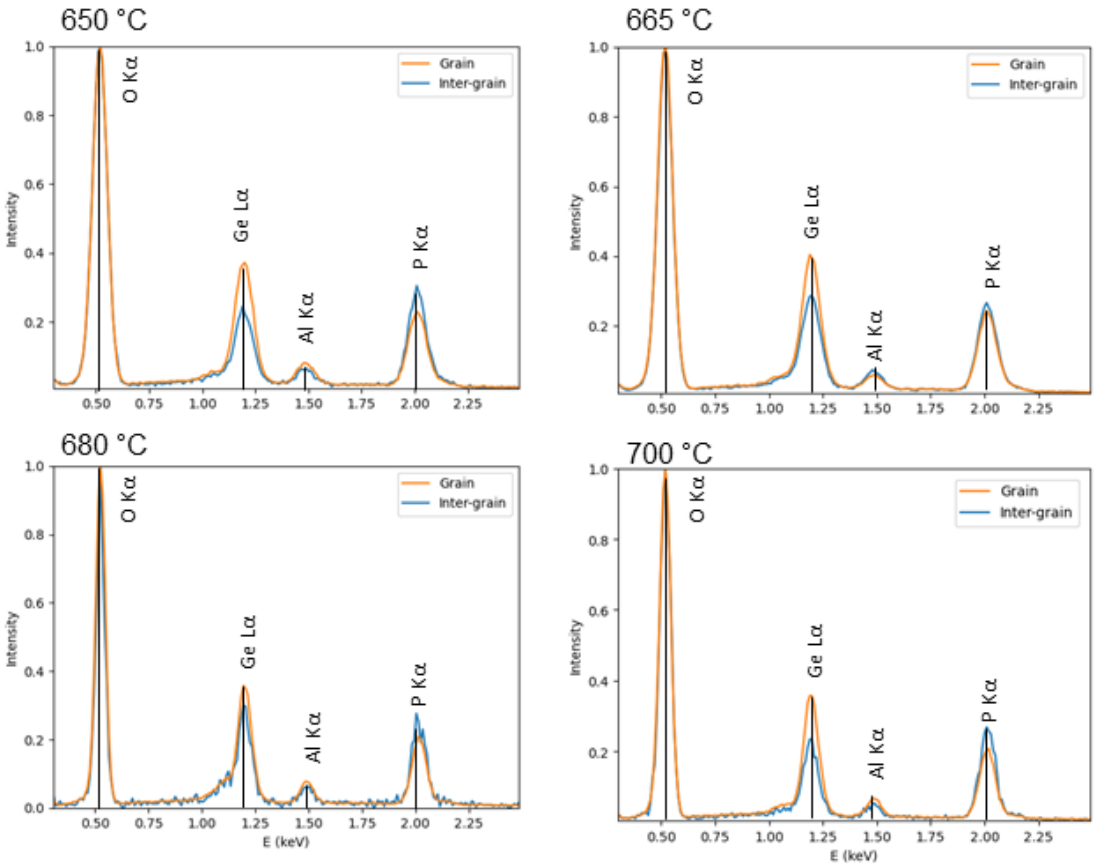


Figure 2.8 Normalized average EDX (based on oxygen intensity) spectra of grains and inter-grain phase obtained after a segmentation process where phases were separated based on their contrast.

Table 3: Atomic percent of Ge, Al, O and P detected by SEM-EDX for the grain and inter-grain phase

Phase	at % Ge	at % Al	at % O	at % P
Theoretical LAGP	8.81	2.92	70.60	17.65
650 °C grain	6.95	2.04	76.63	14.38
650 °C inter-grain	4.61	2.09	78.56	14.74
665 °C grain	8.03	1.56	78.25	12.16
665 °C inter-grain	5.83	2.54	77.97	13.66
680 °C grain	8.37	3.22	76.96	11.45
680 °C inter-grain	7.66	2.57	73.92	15.85
700 °C grain	7.92	2.43	78.29	11.36
700 °C inter-grain	5.04	1.81	78.07	15.07

According to the sintering temperature, aluminum concentration exhibited high variations in the grains and inter-grain region. Similar aluminum concentrations were found in grains and at the inter-grain region for the 650 °C pellet. A higher concentration of aluminum was observed for the inter-grain region compared to grains for the 665 °C sample. When the sintering temperature increased to 680 and 700 °C aluminum concentration was detected in a higher percent for the LAGP grains. Local Li^+ composition may be affected by these changes and can alter the Li^+ conductivity, which could explain the significant differences in the inter-grain resistivities in pellets sintered at different temperatures. A higher oxygen concentration than LAGP theoretical values was found in both grains and inter-grain region.

Using XRD, the different crystalline phases present in the pellets were identified on a millimeter scale pellets (**Figures 2.9**); the relative composition of each phase was calculated by Rietveld refinement and were given in **Table 4**. Depending on the sintering temperature the Wt % of the main phase, LAGP, varied from 73 to 82 %. GeO_2 was identified as the second most dominant phase, about 10 %. Based on the BE-SEM images this phase has been identified as micrometer-scale grains (**Figure A3, Appendix A**). Aside from its impact on the tortuosity pathway, as GeO_2 phase is present on the form of non-conducting islands is neither expected to contribute or be detrimental to the ionic conductivity and do not impact the overall conduction pathways[203]. $AlPO_4$ phase, like GeO_2 has been as well identified on the form of non-conducting islands.

$Li_4P_2O_7$ was the third most dominant phase with variations from ~10 % for pellet sintered at 650 °C to less than ~4 % for the 680 °C sintered pellet. An increase in the ionic conductivity by two order higher was reported to be induced by the presence of $Li_4P_2O_7$ in a mixture with another solid electrolyte such as in Li_3PO_4[184]. Neither $Li_4P_2O_7$ or $Li_9Al_3(P_2O_7)_2(PO_4)_3$ despite being identified by XRD measurements at obtained concentration up to 10.2 and 4.8 % wt. was not observed by BE-SEM or EDX-SEM analysis.

Table 4. Rietveld analysis on the SPS sintered pellets at different temperatures.

	LAGP % wt.	**GeO_2 % wt.**	**$Li_4P_2O_7$ % wt.**	**$AlPO_4$ % wt.**	**$Li_9Al_3(P_2O_7)_2(PO_4)_3$ % wt.**	**R_p**	**R_{wp}**	**R_{exp}**	**Chi 2**
Powder	81.35(0.2)	7.02(0.1)	10.11(0.1)	0.36(0.1)	1.17(0.0)	14.5	15.1	3.55	18.3
650 °C	73.33(0.8)	13.45(0.1)	10.20(0.4)	0.50(0.1)	2.52(0.2)	22.1	17.3	7.54	5.28
665 °C	74.43(1.1)	10.19(0.2)	7.78(0.9)	2.82(0.1)	4.77(0.2)	20.4	12.8	10.76	1.42
680 °C	82.27(0.2)	10.30(0.1)	3.83(0.1)	3.61(0.1)	0.00(0.0)	10.2	10.4	2.15	23.5
700 °C	81.06(0.3)	9.82(0.1)	5.57(0.2)	3.55(0.1)	0.00(0.0)	13.5	13.3	2.42	30.0

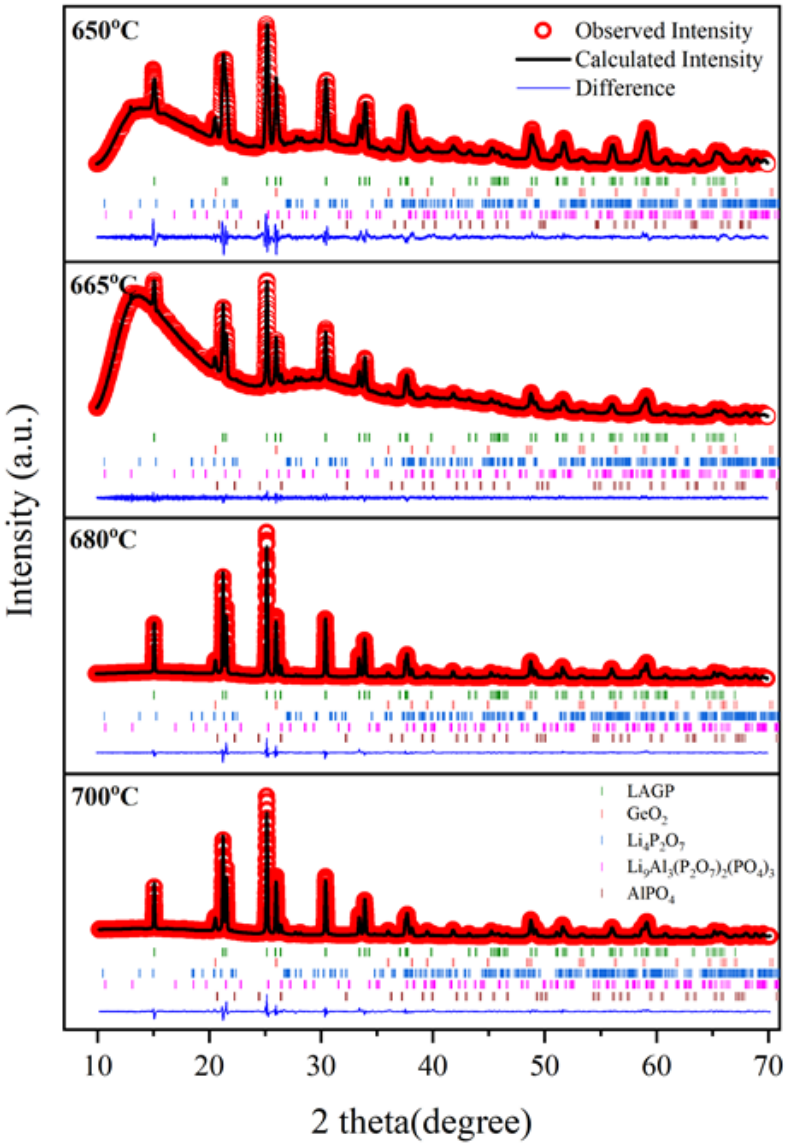


Figure 2.9. Rietveld refinement analysis of the four sintered pellets obtained by Spark Plasma Sintering.

Figure 2.10 displays the solid state ^{31}P and ^{27}Al MAS NMR data which confirm the variety of phases present within the SPS prepared pellets at various temperatures, including the predominant LAGP phase ($Li_{1.5}Al_{0.5}Ge_{1.5}(PO_4)_3$), OPLA ($Li_9Al_3(P_2O_7)_2(PO_4)_3$), the triclinic and trigonal polymorphs of $Li_4P_2O_7$, GeO_2 and $AlPO_4$. **Table A1** summarize the deconvoluted ^{31}P NMR parameters for each sintering temperature. ^{31}P MAS NMR data were acquired using 5 × the longest ^{31}P T_1 values (*i.e.* those of the $Li_4P_2O_7$ polymorphs) thus the relative intensities provide accurate quantitative estimates of the P speciation. The measured NMR parameters for the $Li_4P_2O_7$ and $AlPO_4$ polymorphs are confirmed by previous studies of Raguž *et al.*[204] and Müller *et al.*[205], respectively. LAGP and $Li_9Al_3(P_2O_7)_2(PO_4)_3$ phases observed chemical shifts are in good agreement with the previously reported data[206–208], but a detailed structural characterization and assignment of the numerous ^{31}P OPLA resonances has not yet been reported. GIPAW DTF calculations

of the NMR parameters using structure files confirms All ^{31}P and ^{27}Al chemical shifts reported in **Table A4.**

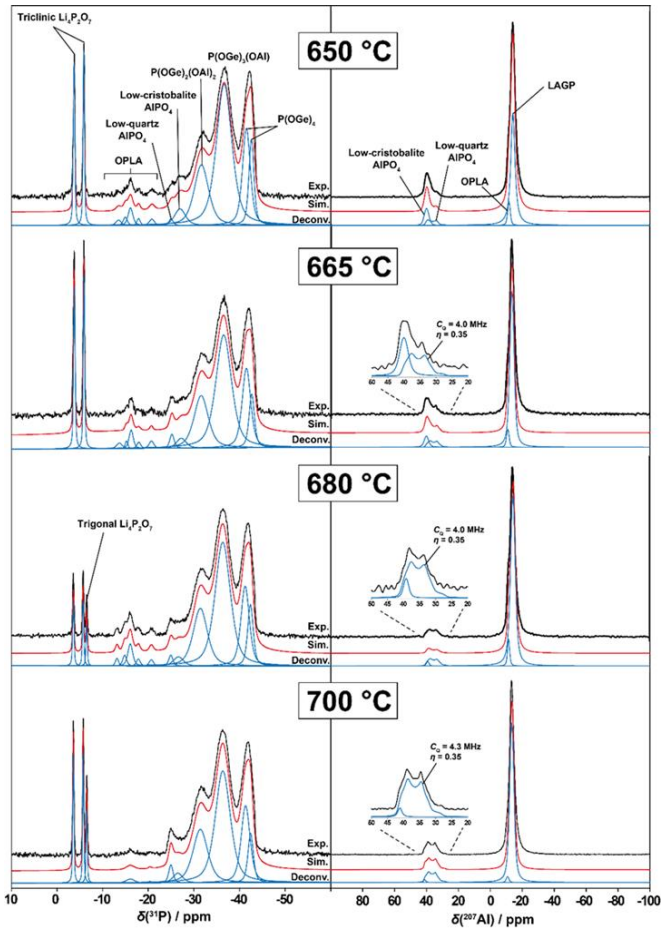


Figure 2.10 The solid state ^{31}P MAS NMR data (left, ν_0 = 130.3 MHz, ν_r = 30 kHz) and ^{27}Al MAS NMR data (right, ν_0 = 202.4 MHz, ν_r = 20 kHz) measured using single pulse methods from the four LAGP systems SPS sintered at temperatures of 650, 665, 680 and 700 °C. The long relaxation delays employed for the ^{31}P MAS NMR data ensures that P speciation is quantitatively estimated.

Figure A4 presents a quantitative analysis of the ^{31}P MAS NMR data shown in **Figure 2.10** and **Table A1** revealing that between the 650 and 665 °C sample only minor differences in composition are observed for grain and inter-grain region (< 2% variation for each phase quantity). A significant increase in the LAGP phase is observed starting with the 680 °C sample corresponding to an increase in the bulk grain phase and decrease in the inter-region phase. Furthermore, the 680 °C sample indicated a significant decrease in the $Li_4P_2O_7$ phase and an increase in the $Li_9Al_3(P_2O_7)_2(PO_4)_3$, these changes to inter-grain speciation for the 680 °C preparation coincide with the lowest inter-grain resistance and highest conductivity.

A close inspection in the ^{31}P MAS NMR spectrum, five resonances spanning a δ ~13 - ~21 ppm range representing the $Li_9Al_3(P_2O_7)_2(PO_4)_3$ system can be observed, but highly ordered $Li_9Al_3(P_2O_7)_2(PO_4)_3$ crystal structure possesses only two chemically distinct P

species with very similar GIPAW DFT predicted ^{31}P chemical shifts occurring at δ –16.1 and –16.2 ppm (see **Table A1**). This observation suggests that the $Li_9Al_3(P_2O_7)_2(PO_4)_3$ formed in the LAGP inter-grain regions under SPS conditions is highly disordered. Attempts to model the disorder using DFT calculations demonstrated that arrangements involving the loss of Li_2O (via the removal of adjacent Li^+ and O^{2-} atoms in the crystal structure) thus forming Li and O vacancies are energetically favourable. The calculated results showed a ^{31}P chemical shift distribution ranging from δ –12.6 - –22.8 ppm which is in excellent agreement with the experimental ^{31}P MAS NMR data.

(1) $Li_9Al_3(P_2O_7)_2(PO_4)_3 \xrightarrow{\Delta E} Li_9Al_3(P_2O_7)_2(PO_4)_3$ (O vac.) $+Li_2O$ (ΔE = +4.9 eV)

Other descriptions of disorder creating Li deficiency involved the substitution of Ge^{4+} for Al^{3+} accompanied by the removal of an adjacent Li^+ atom to maintain charge balance which predicted a distributed ^{31}P chemical shift range of δ –12.1 - –35.3 ppm which was not in agreement with the experimental data.

(2) $Li_9Al_3(P_2O_7)_2(PO_4)_3 + GeO_2 \xrightarrow{\Delta E} Li_9Al_3(P_2O_7)_2(PO_4)_3$ (Ge subs.) $+LiAlO_2$ (ΔE= +1.2 eV)

The presence of disordered/Li-deficient $Li_9Al_3(P_2O_7)_2(PO_4)_3$ may improve the ion migration through the inter-grain regions, consequently reducing the inter-grain resistance leading to an increase in the inter-grains and overall ionic conductivities. The presence of $Li_9Al_3(P_2O_7)_2(PO_4)_3$ at the inter-grain region was accompanied by a significant reduce of the $Li_4P_2O_7$ phase. Moreover, a partial phase transformation from $Li_4P_2O_7$ triclinic to the trigonal polymorph is also observed in a ratio of triclinic: trigonal ≈ 2 : 1. The ^{31}P T_1s of these $Li_4P_2O_7$ polymorphs are extremely long (>650 s) and the very narrow linewidth-at-half-height indicates long ^{31}P T_2s and high short range and long range structural order. These observations suggest low Li ion migration through the $Li_4P_2O_7$ polymorphs within the room temperature regime, thus delivering an inefficient relaxation mechanism(s) to the P speciation within the frameworks shown in **Figure A5**. A higher content in $Li_9Al_3(P_2O_7)_2(PO_4)_3$ at the inter-grain region for the 680 °C sample may offset the inefficient Li ion migration through the co-existing $Li_4P_2O_7$ phases and induce higher conductivity.

The presence of Al speciation as LAGP, OPLA and $AlPO_4$ phases are confirmed by the 1D ^{27}Al MAS NMR data shown in **Figure 2.10** (all samples) and the 2D ^{27}Al MQMAS NMR data presented in **Figure 2.11** (680 °C sample only). The contours 2D ^{27}Al MQMAS NMR data of LAGP phase displayed broad distributions along both the chemical shift (*CS*) and quadrupolar induced shift (Q_{IS}) axes. This suggests large dispersions in both isotropic chemical shifts (δ_{iso}) and quadrupolar coupling constants (C_Q) resulting from this disorder. In contrast, a highly ordered environment where a single second order quadrupole

broadening influences the ^{27}Al resonance was observed for the $AlPO_4$ (low quartz polymorph) as only a horizontal contour was observed.

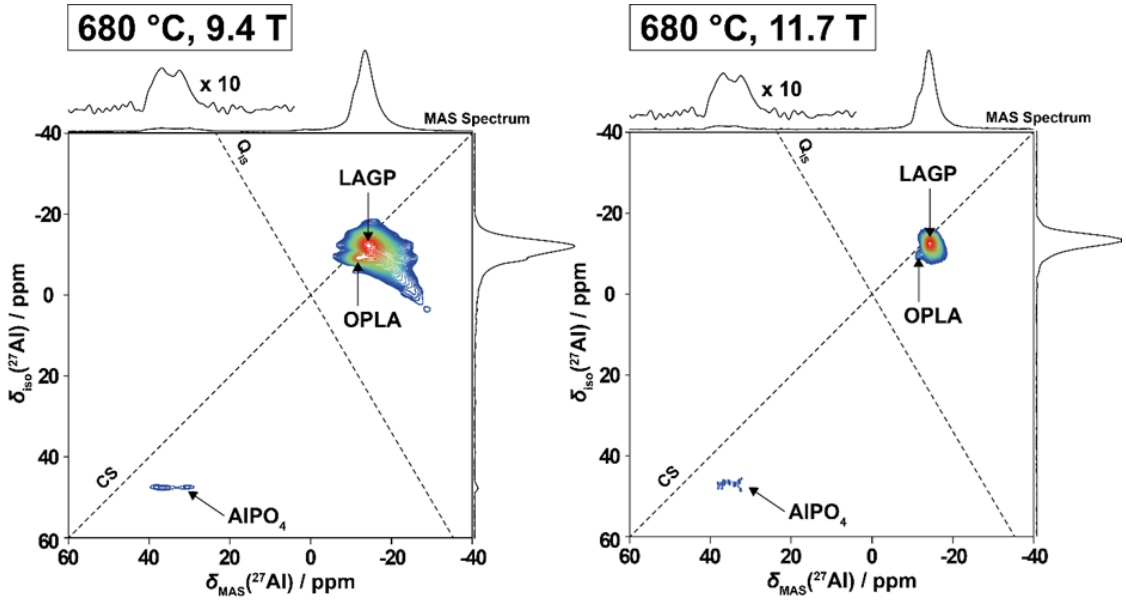


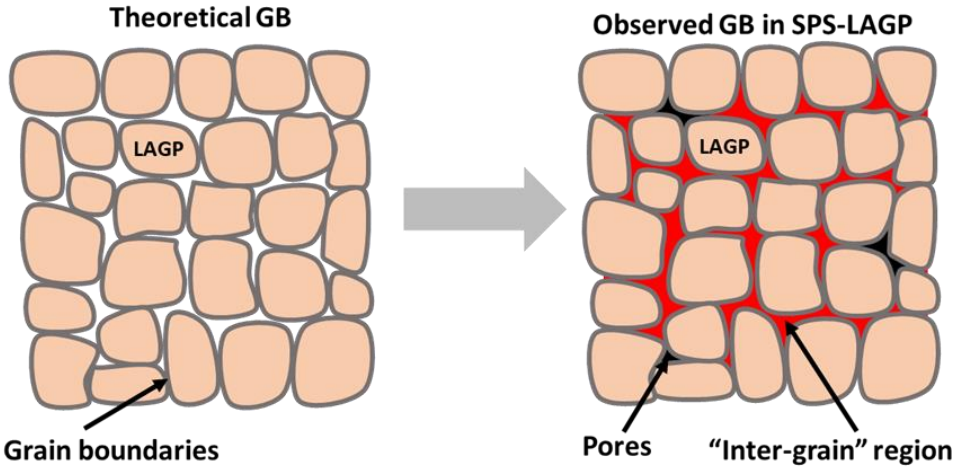
Figure 2.11 ^{27}Al MQMAS NMR data for the 680 °C sample acquired at magnetic field strengths of 9.4 T (left) and 11.7 T (right).

In some instances, structural disorder induces featureless resonances from quadrupolar nuclei, and no direct simulation of the resonance is possible to measure NMR parameters such as δ_{iso}, C_Q and η_Q. In this case, graphical methods as variable field MAS NMR measurements can be used to elucidate NMR parameters such as isotropic chemical shift, and the quadrupole product $P_Q = C_Q\sqrt{(1 + \eta_Q^2/3)}$ which is a close approximation of the quadrupole coupling constant C_Q. **Figure A6** displays the results of this analysis showing very little change in the quadrupole parameters for the LAGP, $Li_9Al_3(P_2O_7)_2(PO_4)_3$ and $AlPO_4$ phases is induced by the SPS sintering temperature. Minimal structural change within each specific phase (**Figure A6**) is suggested as the quadrupole parameters are very sensitive indicators of structure and structural change. The prominent changes that separate the 680 °C pellet from the other samples are the amount of $Li_9Al_3(P_2O_7)_2(PO_4)_3$ generated in the inter-grain region as reported by the quantitative ^{31}P MAS NMR.

2.6 Conclusions and perspectives

LAGP was successfully synthetized using sol-gel method and further sintered using Spark Plasma to obtain highly compact and densified pellets with high ionic conductivity. To investigate the role of morphologies and compositions of the grains and inter-grain region on the ionic conductivity a range of sintering temperatures (650, 665, 680 and 700 °C) have been implemented. The Nyquist plots analysis displayed two semicircles, the

semicircle located at high frequencies being attributed to the grain ionic conductivity and the semicircle at lower frequencies to the inter-grain region ionic conductivity. A higher resistance at the inter-grain region, therefore a lower ionic conductivity it was observed for the pellets sintered at a lower sintering temperature (650 and 665 °C) compared to pellets produced at higher sintering temperatures (680 and 700 °C). The total ionic conductivity of the pellets was observed to increase with the sintering temperature until 680 °C, followed by a small decrease at 700 °C. Moreover, it was found that the bulk ionic conductivity is constant throughout the different sintering temperatures and the predominant difference in the total ionic conductivity was induced by the ionic conductivity at the inter-grain region.



LAGP pellet which exhibited the highest ionic conductivity also present the highest compacity indicating a possible direct relationship between the compacity and ionic conductivity. Even though 665 and 700 °C samples showed similar compacity values, the later had higher overall ionic conductivity indicating that morphological and compositional changes in the inter-grain region influence the ionic conductivity. The presence of an inter-grain region, creating a network around the LAGP grains was revealed using 3D-FIB-BE-SEM tomography. The 3D reconstructed volumes indicated a higher presence of the inter-grain phase for the lower sintered temperatures pellets compared to the pellets sintered at higher temperatures with 680 °C sample exhibiting the lowest inter-grain region volume and the highest ionic conductivity. Moreover, the tortuosity of the inter-grain region calculated based on the reconstructed FIB volumes decreased from 6.15 for the 650 °C to 2.22 for the 665 °C and become infinite for the higher sintering temperatures. This indicates a non-continuous network of the inter-grain phase at higher sintering temperatures and a minimum impact on the inter-grain region ionic conductivity compared to lower sintered temperatures where a continuous network is formed limiting grains conductivity.

The chemical composition and crystal structure of the inter-grain region can also explain the observed difference in the ionic conductivity. Cross-section SEM-EDX analysis unveil a significantly lower germanium concentration and slightly higher phosphorus concentration in the inter-grain region compared to LAGP. $Li_4P_2O_7$ and OPLA ($Li_9Al_3(P_2O_7)_2(PO_4)_3$) phases were detected in the overall pellet using XRD and ^{31}P MAS NMR analyses; however, despite their presence in concentrations up to ~10.2% and ~4.8 %, respectively; both phases were not explicitly identified by the BE-SEM or EDX-SEM analyses on the sintered pellets, indicating their presence in the inter-grain region. We concluded that the inter-grain phase presented like a network around the LAGP grains is a mixture of $Li_4P_2O_7$ and OPLA phases based on the 3D-FIB-BE-SEM tomography analysis, SEM-EDX, XRD and ^{31}P MAS NMR analysis. Based on the ^{31}P MAS NMR measurements the optimal ionic conductivity for the LAGP system was achieved for the 680 °C SPS pellet when the disordered OPLA phase dominates the inter-grain region composition with reduced contributions from the highly ordered $Li_4P_2O_7$ phases. If the apparition of the grain boundary phase is related to the sintering SPS method is not clear and needs to be further investigated.

Main takeaways:

During this study, spark plasma sintering has been employed to sinter $Li_{1.5}Al_{0.5}Ge_{1.5}(PO_4)_3$ (LAGP) powder at different sintering temperatures (650, 665, 680 and 700 °C) to obtain compact pellets with high ionic conductivity.

EIS analysis showed that the bulk ionic conductivity was constant in all the sintered pellets and the main difference in the total ionic conductivity was due to the contribution of the grain boundaries. 3D FIB-SEM tomography analysis revealed the presence of an inter-grain region network created around the LAGP grains at the grain boundaries. The inter-grains region was found in a higher volume for the low sintering temperatures compared to high sintering temperatures. The sample that exhibited the highest total ionic conductivity (680 °C) also displayed the lowest amount of the inter-grain region. Based on 3D-FIB-BE-SEM,XRD, SEM-EDX and ^{31}P MAS NMR analysis we concluded that the inter-grain region presented like a network around the LAGP grains is actually a mixture of $Li_4P_2O_7$ and $Li_9Al_3(P_2O_7)_2(PO_4)_3$.

Keywords: Ionic conductivity; Inter-grain phase; FIB-SEM tomography; XRD; SEM-EDX; MAS NMR; Grain boundaries

.

Appendix A

LAGP synthesis using sol-gel method

Stoichiometric amount of $Al(OC_4H_9)_3$ (Sigma Aldrich) was dissolved in 100 mL THF solution for 2h. Using a syringe, $Ge(OC_2H_5)_4$ precursor (Sigma Aldrich) was added drop by drop in the THF solution and then mixed together at 50 °C. In 100 mL water solution at 60 °C CH_3COOLi and $NH_4H_2PO_4$ precursors were dissolved for 2 hours. After the dissolution of the precursors using a pipette the water solution is added drop by drop in the THF solution and let it overnight at 70 °C for the evaporation of the solvent. The powder obtained is grounded in an agate mortar and then placed for a heat treatment using a heat rate of 1 °C/min. at 850 °C for 2 hours for obtaining the LAGP phase.

Spark Plasma sintering on LAGP solid electrolyte

LAGP powder is packed in a 10 mm (inner diameter) graphite die which was previously inside covered it with graphite paper. A pressure of 100 MPa was applied on the pellets to compress the powder and a heating rate of 1 °C/s until the maximum temperature of heating, followed by a plateau of 5 minutes at the maximum temperature and then a controlled cooling within 5 minutes at the RT resulting in a total sintering time of 27 min (**Figure A1**).The obtained pellets were polished using SiC paper to remove the graphite that was covering SE surface.

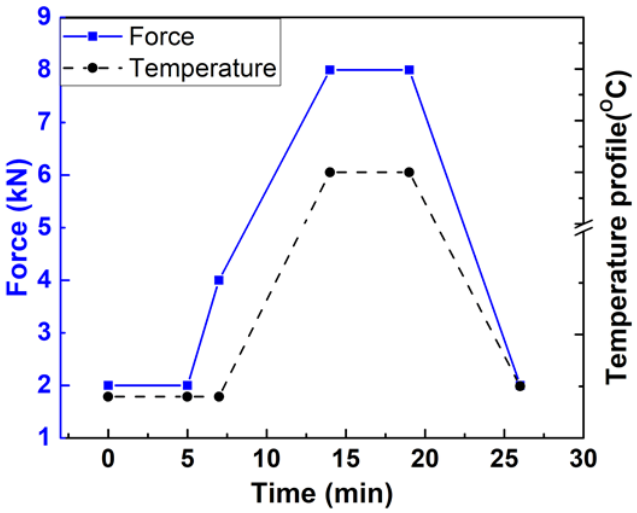


Figure A1. Spark plasma Sintering parameters used in order to obtain the compact pellets at 650 °C, 665 °C, 680 °C and 700 °C with a heating rate of 1 °C/s under a pressure of 100 MPa.

Electrochemical impedance spectroscopy

A gold layer of 100 nm was deposited on both sides of the pellets to ensure a better contact with the blocking electrodes. The AC impedance spectra was recorded using an MTZ-35 (BioLogic) frequency response analyzer from a frequency range of 1 Hz to 10 MHz with an excitation signal of 5 mV coupled with an Intermediate Temperature System furnaces (ITS, BioLogic) temperature controller. The impedance data were treated using Zview software and Brick Layer Model (BLM) as equivalent circuit.

Focused Ion Beam-Scanning Electron microscopy tomography

ZEISS Gemini 2 Crossbeam 540 was used for the FIB-SEM tomography. An interest area of 6 µm x 5.5 µm was designated for all the solid electrolytes pellets. The interest area was chosen based on the top view images to avoid the presence of large secondary phases such GeO_2 and $AlPO_4$ and mostly focus on LAGP grains morphology. A platinum layer of 500 nm was deposited with the electron beam using a current of 2000 pA and another platinum layer using the focused ion beam of 600 nm with a current of 100 pA for the protection of the sample against beam damage. To define the interest area, a double milling with 30 kV, 15 nA and 30 kV, 700 pA was realized to define the volume of interest to analyze. The automatic slice milling in the volume was realized using a current of 30 kV, 100 pA with a slice thickness of 21 nm and a depth of 8 µm. For the recording imaging conditions, we used 5 kV and 100 pA in order to avoid the damages in the solid electrolyte by a high current probe. Tilt compensator was set to 36 degrees to avoid the distortions which are induced in the image since the images are recorded when the sample is tilted to 54 degrees. Dynamic focus option was used to insure the focus from the top to the bottom of the recorded images.

Image segmentation for the SEM-EDX analysis

Image segmentation process was done using the FIJI package, Trainable Weka Segmentation. For the 650 °C pellet, on the segmentation image the colors are corresponding to the following phases. Green is attributed to LAGP grains, red to inter-grain phase, purple to pores and voids, blue to germanium oxide and yellow for the $AlPO_4$ phase. For the 665 °C pellet, on the segmentation image green is attributed to LAGP grains, red to inter-grain phase and purple to pores. For the 680 °C pellet, on the segmentation image green is attributed to LAGP grains, red to inter-grain phase and purple to germanium oxide. For the 700 °C pellet, on the segmentation image green is attributed to LAGP grains and red to pores and voids.

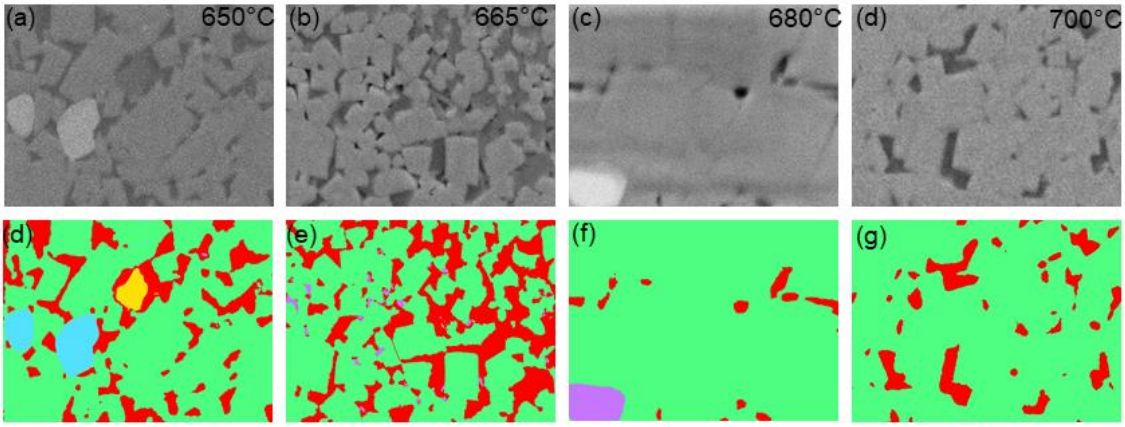
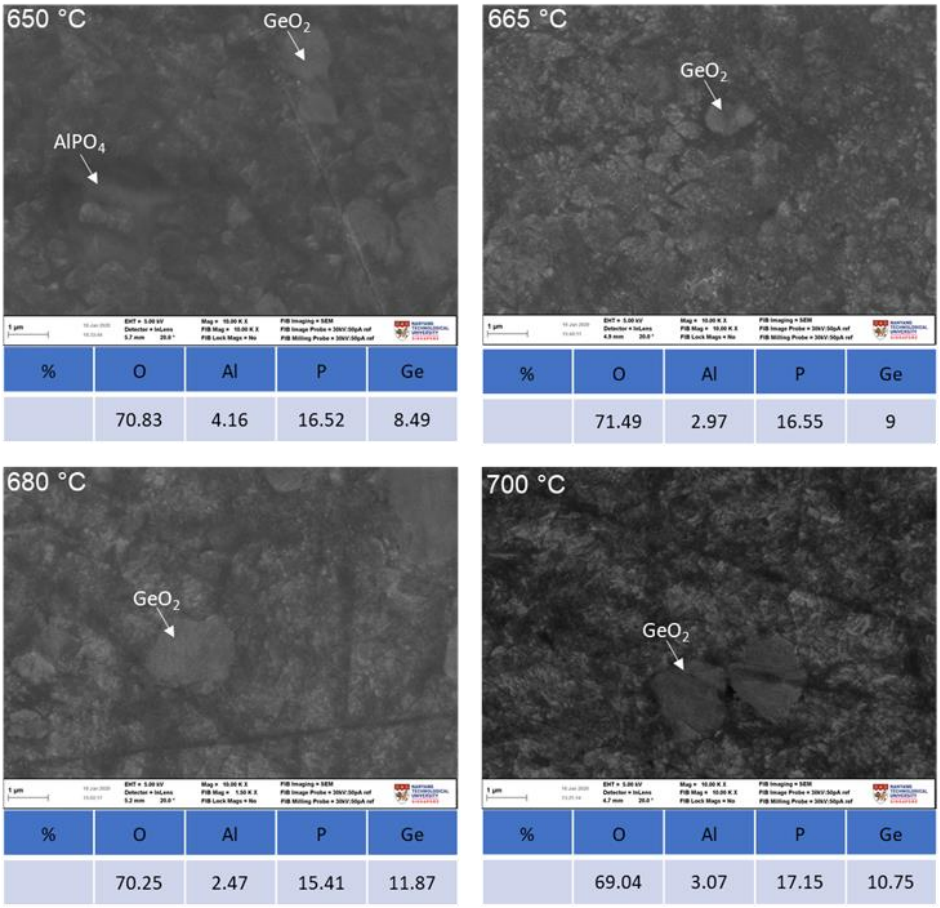


Figure A2. BE-SEM and segmented images used to obtain the concentration of each phase presented on our analyzed area.



%	O	Al	P	Ge
	70.83	4.16	16.52	8.49

%	O	Al	P	Ge
	71.49	2.97	16.55	9

%	O	Al	P	Ge
	70.25	2.47	15.41	11.87

%	O	Al	P	Ge
	69.04	3.07	17.15	10.75

Figure A3. Selected top surface secondary electron images of LAGP pellets sintered at various temperatures where it shows the presence of GeO_2 and $AlPO_4$ inside of the solid electrolyte.

Solid State Nuclear Magnetic Resonance

All ^{31}P MAS NMR measurements were performed at 11.7 T using a Bruker Avance III spectrometer operating at a ^{31}P Larmor frequency of 202.4 MHz. Rotational (MAS) frequencies of 30 kHz were achieved using a Bruker 2.5 mm HXY probe. Data were acquired at room temperature employing single pulse experiments which used π/8 pulses of 1 µs duration, and long recycle delay of 3600 s implemented to ensure the full relaxation of all ^{31}P nuclei and ^{31}P MAS NMR data. All ^{31}P MAS NMR data were referenced against the IUPAC recommended reference of phosphoric acid (H_3PO_4) (δ_{iso} = 0.0 ppm) via a secondary solid reference of ammonium dihydrogen phosphate (ADP) (δ_{iso} = 0.99 ppm).

The ^{27}Al MAS NMR measurements were acquired at using Bruker Avance III-500 (11.7 T), Bruker Avance III HD-400 (9.4 T) and Varian InfinityPlus-300 (7.05 T) spectrometers operating at a ^{27}Al Larmor frequencies of 130.3, 103.9 and 78.2 MHz, respectively. All measurements were performed at room temperature and at MAS frequencies of 20 kHz, using Bruker 3.2 mm HX probes at 11.7 and 9.4 T, and a Varian HX probe at 7.05 T. Non-selective (solution) π/2 pulse times of 18 µs were calibrated using 1.1 M $AlNO_3$ from which a selective (solid) π/2 pulses of 6 µs were associated. All 1D ^{27}Al MAS NMR data were acquired using single pulse experiments employing selective 1 µs π/12 pulses, and a recycle delay of 10 s. The corresponding 2D ^{27}Al MQMAS data were acquired at 11.7 and 9.4 T using a 3Q Z-filtered experiment consisting of a 4 µs multiple quantum excitation pulse, a 1.4 µs conversion pulse, a soft π/2 20 µs selective pulse, a 20 µs inter-pulse Z-filter delay, and a 5 s recycle delay. A total of 80 slices were acquired to generate the indirect dimension, and 192 transients were acquired per slice. All ^{27}Al MAS NMR data were referenced against the IUPAC recommended reference of 1.1 M aluminum nitrate ($AlNO_3$) solution (δ_{iso}= 0 ppm). The determination of the NMR parameters from featureless quadrupole dominated ^{27}Al resonances is achieved by graphical presentation of variable field ^{27}Al MAS NMR data. The ^{27}Al apparent center-of-gravity shifts δ_{cg} are the sum of the field independent isotropic chemical shift δ_{iso}, and the field-dependent second-order quadrupolar shift $\delta_{Q,iso}^{(2)}$ such that:

$$\delta_{cg} = \delta_{iso} + {\delta_{Q,iso}}^{(2)}(I,m) \qquad \text{where:}$$

$${\delta_{Q,iso}}^{(2)}(I,m) = \left(\frac{3{C_Q}^2}{40{v_0}^2 I^2(2I-1)^2}\right)[I(I+1) - 9m(m-1) - 3](1+\frac{\eta^2}{3})$$

By measuring the δ_{cg} variation over multiple magnetic fields (i.e. by changing v_0), a determination ot the δ_{iso} (from the y intercept) and P_Q (from the slope) parameters is achieved by linear regression of the above equation for δ_{cg}. The P_Q parameter:

$$P_Q = C_Q\sqrt{(1+\frac{\eta^2}{3})}$$

is closely related to the quadrupolar coupling constant C_Q by a factor of ~10 - 15%.

Table A1 Measured ^{31}P and ^{27}Al NMR parameters determined by lineshape simulation of the data displayed in Fig. 3. For comparison, the DFT-calculated δ_{iso} values for $Li_4P_2O_7$, $AlPO_4$ and OPLA phases are also shown.

Phase	650 °C		665 °C		680 °C		700 °C		Calculated δ_{iso} (ppm)
	δ_{iso} (ppm)	Relative Intensity (%)	δ_{iso} (ppm)	Relative Intensity (%)	δ_{iso} (ppm)	Relative Intensity (%)	δ_{iso} (ppm)	Relative Intensity (%)	
$Li_4P_2O_7$	-3.5 -5.7	5.1 5.0	-3.6 -5.8	6.1 5.9	-3.5 -5.7 -6.5	2.2 2.1 1.3	-3.6 -5.7 -6.5	4.0 4.0 2.2	-2.6 (Triclinic) -5.4 (Triclinic) -6.0 (Trigonal)
$Li_9Al_3(P_2O_7)_3(PO_4)_2$	-13.2 -14.7 -16.0 -17.7 -20.7	0.5 0.7 1.6 0.5 0.6	-13.5 -15.1 -16.1 -17.8 -20.6	0.7 0.4 1.8 0.6 0.8	-13.2 -14.8 -16.1 -17.9 -20.7	0.6 1.0 0.6 2.5 0.6	-16.1 -20.4	0.8 0.1	-16.2 (Pristine) -12.6 – -22.8 (Li2O removed) -12.1 – -35.3 (Li removed, Ge subs. Al)
$AlPO_4$[a]	-24.9 -27.2	0.5 3.5	-25.1 -27.1	1.4 2.2	-25.0 -26.6	1.1 2.6	-25.0 -26.5	2.0 2.3	-24.5 (Berlinite) -23.3 (Low-cristobalite)[b]
Other NASICON Phases [P(OGe)4], [P(OGe)3(OAl)], [P(OGe)2(OAl)2]	-31.6 -36.4 -41.1 -42.3	16.8 41.9 14.7 8.5	-31.5 -36.4 -41.4 -42.6	17.2 40.5 15.8 6.7	-31.4 -36.4 -41.3 -42.4	18.8 43.5 15.6 8.0	-31.4 -36.4 -41.4 -42.5	19.4 41.5 17.0 6.6	

[a] Possible overlap of low cristobalite $AlPO_4$ and LAGP phase.
[b] This shift was previously reported as δ_{iso} = –27.1 ppm

Overlap of the low cristobalite $AlPO_4$ and the LAGP resonances in the ~25 ppm region reduces the accuracy of the reported quantitative estimate of the low cristobalite $AlPO_4$ phase; however, the GIPAW DFT calculated ^{31}P chemical shifts of these $AlPO_4$ phases confirms their appearance in this spectral region.

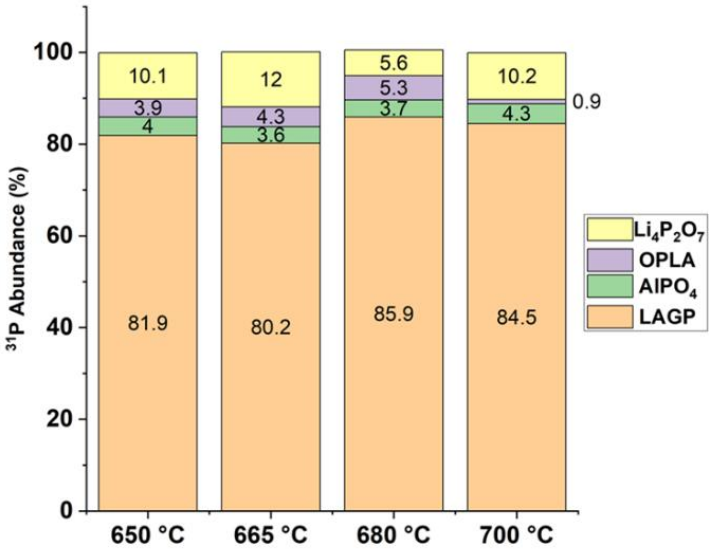


Figure A4. % of phases in the sintered pellets at various temperatures based on the relative intensities of ^{31}P abundance.

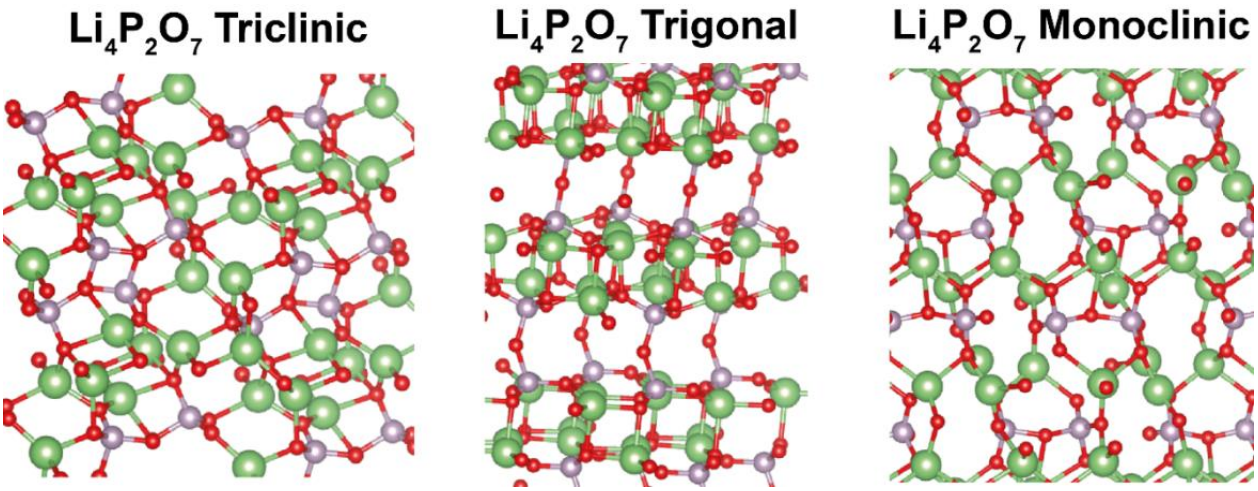


Figure A5. Crystal structure diagrams of the triclinic, trigonal, and monoclinic polymorphs of $Li_4P_2O_7$.

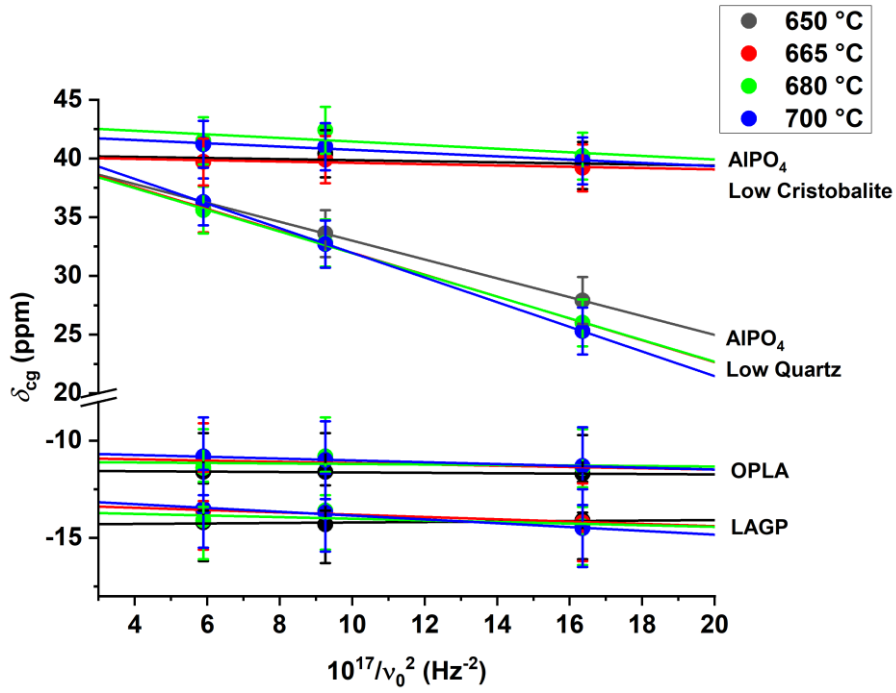


Figure A6. Plot of the measured ^{27}Al centre-of-gravity shifts (δ_{cg}) values for the four SPS synthesized LAGP materials as a function of the inverse squared Larmor frequency (magnetic field strength). Linear fitting of these data yields the isotropic chemical shifts (δ_{iso}) determined from the y-intercept, and the quadrupole product values $P_Q = C_Q\sqrt{(1 + \eta_Q^2/3)}$ determined from the slope. More accurate NMR parameters for the low quartz $AlPO_4$ polymorph are presented in Figure 4 from direct simulation.

Density Functional Theory (DFT) Calculations

CASTEP version 17.21[209], a plane-wave pseudopotential DFT package was used to perform geometry relaxation calculations, NMR calculations, and energy calculations for all systems. The PBE generalized gradient functional was used to model the exchange-correlation energy term[210]. CASTEP's built-in "on-the-fly" C17 pseudopotential library was used for these calculations. All unit cell parameters were fixed for geometry optimizations. Atomic positions were relaxed up to a tolerance of 0.05 eVÅ^{-1} in atomic forces for all systems. NMR parameters were computed using the GIPAW method[211,212]. For both geometry relaxation calculations and NMR parameter calculations, an electronic cut off energy of 600 eV for the plane-wave basis set was used. Structures for triclinic $Li_4P_2O_7$[213], trigonal $Li_4P_2O_7$[204], monoclinic $Li_4P_2O_7$[213], $Li_9Al_3(P_2O_7)_2(PO_4)_3$ (OPLA)[214], Li_2O[215], GeO_2[216], and $LiAlO_2$[217] were taken from associated references.

Github link for the python segmentation code data:

https://github.com/sorinacretu/EDX_map-segmentation

Chapter III 66
LAGP interface with Li metal 66
3.1 Introduction 66
3.2 Ionic transport in LAGP pellets 68
3.3 Chemical stability of LAGP versus Li metal 71
3.4 Electrochemical stability window of LAGP 74
3.5 Current density influence on LAGP 75
3.6 Protection layer of the solid electrolyte 83
3.7 Conclusions and perspectives 87
Appendix B 90

Chapter III

LAGP interface with Li metal

3.1 Introduction

The transaction to electric vehicles (EV) for a more sustainable environment comes with certain requirements for the battery technology as high safety and improvement of the actual battery performances in terms of energy density[9]. All-solid-state Li metal batteries (ASSLMBs) are a highly desired technology as they are safer and are the most promising system which can lead to enormous increase in the batteries performances due to their high volumetric energy density[66,110,172]. The high energy density of the ASSLMBs comes from the possibility to use lithium metal as anode which presents a negative electrochemical potential (-3.04 V vs. the standard hydrogen electrode) and an extremely high theoretical capacity (3860 $mA.g^{-1}$)[218]. The use of lithium metal as anode in the current conventional Li-ion battery technology it was impeded by the short-circuit formation due to lithium metal dendrites growth in the battery and flammable nature of the liquid electrolyte[219,220]. Although, the formation of dendrites is still possible in solid-state batteries, their formation won't induce any safety hazardous as the inexistence of liquid electrolyte in the solid-state batteries makes the system harmless regarding safety concerns[135,142,221].

In a conventional Li-ion batteries due to chemical and mechanical origins various degradation mechanisms are independent occurring resulting in capacity loss and power fade[222]. Similar, in the case of ASSB, the degradation mechanism is induced by the formation of an interfacial layer[126], dendrites[142,221] and cracks propagation[141,149,151]. The interface between solid electrolyte and lithium metal represents one of the most challenging points in solid-state batteries as its initial degradation could further trigger the formation of dendrites and cracks resulting in battery failure[223,224]. Most of the solid electrolytes are known for their instability versus lithium metal where a huge interfacial resistance due to side products and dendrites are observed at the interface with lithium metal[225] as shown in the **Figure 3.1**. Based on the literature, the interfaces between SE and Li metal, depending on their reactivity are classified as following:

i) thermodynamically stable with no decomposition.
ii) kinetically stable with low thermodynamic energy.
iii) thermodynamically unstable and high decomposition energy[226].

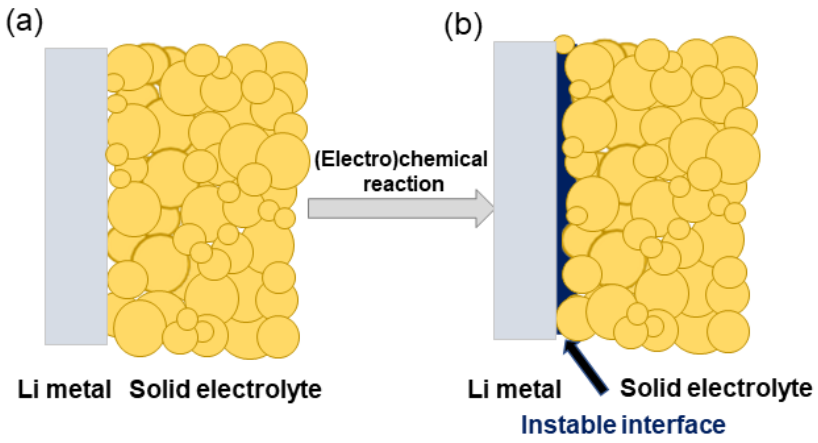


Figure 3.1 Schematic representation of the interface between the solid electrolyte and the Li metal before (a) (electro)chemical reaction and (b) after the (electro)chemical reaction showing the interphase formed between SE and Li metal.

Solid electrolytes as LLZO and Li_6PS_5X (X = Cl, Br, I) present an interface with Li metal that is electronically insulative and does not promote the reduction of the SE[129,131]. LAGP, similar to LATP and LGPS presents an interface that is highly ionic and electronic conductive stimulating a continuous degradation of the solid electrolyte. As a result, lithium metal when put in contact with LAGP triggers the reduction of the solid electrolyte by a spontaneous reaction where the Ge^{4+} ions are reduced to Ge^{2+} (in the form of GeO_2) and metallic Ge[121]. The new formed interphase with accumulated side products results in increased interfacial resistance that contributes to LAGP structure destruction, triggers the formation of lithium dendrites and in the end cause cell failure[225,227].

Recently, as a strategy to diminish the interface reactions between SE and Li metal, a protection buffer layer was inserted between the two battery components[228]. Various protection layers as amorphous Ge thin films, PEO-LiTFSI mixture, LIPON, Al_2O_3 and silicon were investigated as a solution for interfacial reaction reduction in LAGP[153,229,230]. The insertion of the amorphous Ge thin film showed a suppression of the side reactions and improvement of the contact, the Ge-coated cell presenting superior stability and cycle performances at 0.1 mA/cm^{-2} for 100 cycles compared to unprotected cell[229]. The use of PEO-LiTFSI mixture showed satisfactory interface contact and good mechanical properties, the inserted thin film preventing Li metal from reacting with the solid electrolyte and inhibiting the formation of lithium dendrites[153].

A comprehensive understanding of the kinetics and morphological changes occurring at the interface between Li metal and solid electrolyte is required to optimize and obtain performant ASSLMBs. During this study, we are investigating the chemical and electrochemical reactions occurring at the interface between Li metal and LAGP. Using a symmetrical cell composed of LAGP as solid electrolyte and Li metal as both electrodes,

platting and stripping process will be followed to understand better the phenomena occurring at the interface. SEM-EDX, STEM, SIMS and X-ray tomography analysis are used to characterize the morphological and compositional changes occurring at the interface. In the end, a strategy that involves the insertion of a protection layer of LIPON between lithium metal and SE that could improve the cycling conditions was considered.

3.2 Ionic transport in LAGP pellets

In the previous work, solid electrolyte was synthetized in the laboratory using sol-gel method, but different secondary phases such as GeO_2, and $AlPO_4$ were always presented. For further studies, $Li_{1.5}Al_{0.5}Ge_{1.5}(PO_4)_3$ (LAGP) with two different average grains size distributions of 300 nm and 500 nm were purchased from Ampcera (MSE Suppliers). The XRD Profile fitting of commercial LAGP (500 nm and 300nm) are displayed in the **Figure 3.2a** where only the diffraction peaks corresponding to $Li_{1.5}Al_{0.5}Ge_{1.5}(PO_4)_3$ (rhombohedral crystal structure with R3c space group) were detected.

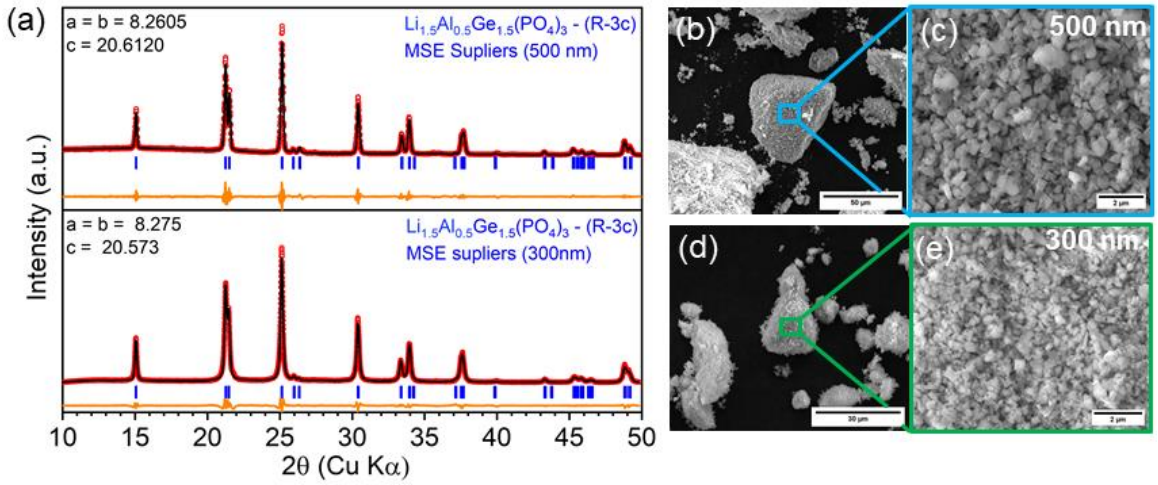


Figure 3.2 a) X-ray diffractograms of the LAGP solid electrolyte purchased from Ampcera (MSE Suppliers) with average grain size of a) 500 nm and 300 nm. Secondary electrons micrographs of LAGP particles of (b) 500 nm and (d) of 300 nm showing LAGP agglomerates. Backscattering electrons images showing the tetragonal morphology of (c) 500 nm and (e) 300 nm LAGP particles.

LAGP powder characterized using secondary electrons-SEM (SE-SEM) images shows that solid electrolyte particles are agglomerated in large clusters of tens of microns (**Figure 3.3b** and **Figure 3.3d**). Backscattering electrons SEM images (**Figure 3.3c** and **Figure 3.3e)** display a combined morphology between tetragonal and irregular shape of LAGP particles, like the synthesis of LAGP made in the lab and presented in the **Chapter II**.

Solid electrolyte pellets with high ionic conductivity represents an essential requirement for a sustainable solid-state battery performance. For oxide solid electrolytes, as shown in **Chapter II**, the compacity plays an important role in the total ionic conductivity values, as higher compacity generate less grain boundaries. As the commercial LAGP

powder presents different particle size distribution and different morphology compared to synthetized powder from **Chapter II**, the optimum value for sintering LAGP pellets and obtain the best performances in ionic conductivity may differ. Like previous study, spark plasma sintering method[95] was used to obtain densified pellets (see details in **Appendix B**) at various temperatures (600, 650, 680 and 700 °C) in order to determine the optimum sintering temperature for the highest ionic conductivity in LAGP.

The ionic conductivities of LAGP pellets were measured using electrochemical impedance spectroscopy (EIS) in a temperature range spanning 0 − 50 °C (Methods in **Appendix B**). The impedance data was fitted using Brick-Layer model. The obtained Nyquist plots of the four pellets at RT are displayed in the **Figure 3.3a**; like previous study the presence of two semicircles followed by a linear tail can be noticed. The first high frequency semicircle in the Nyquist plot was attributed to grain contribution and the second semi-circle was attributes to grain boundary contribution. Compared to previous study, a decrease in the grain boundaries volume on the Nyquist plots can be noticed, a possible hypothesis indicating a higher number of percolation paths[231]. The ionic conductivities (σ_g and σ_{gb}) were calculated from the obtained resistances values using ***Eq. 2*** and the total ionic conductivity represents the sum of grain and grain boundaries ionic conductivity. On the Arrhenius plot of grain boundaries ionic conductivity vs 1/T (**Figure 3.3b**) a clearly increase in the grain boundaries ionic conductivity with the sintering temperature can be observed. The Arrhenius plot of grains ionic conductivity vs 1/T (**Figure 3.3c**) shows quite constant bulk ionic conductivities values for the pellets sintered at higher temperature than 650 °C; with the 600 °C pellet displaying fluctuating values (higher than the rest of the pellets at lower sintering temperatures, but lower when the sintering temperature increased to 50 °C). The total ionic conductivity vs 1/T graph (**Figure 3.3d**) indicated that 680 °C and 700 °C pellets present the highest total ionic conductivities at 50 °C. The total ionic conductivity of the new LAGP powder sintered pellet at 680 °C exhibits similar values (2.77×10^{-3} S.cm^{-1}) compared to previous LAGP pellets sintered using synthetized powder in the laboratory (2.62×10^{-3} S.cm^{-1}). For the following studies, LAGP pellets were sintered at 680 °C as presented an optimal total ionic conductivity.

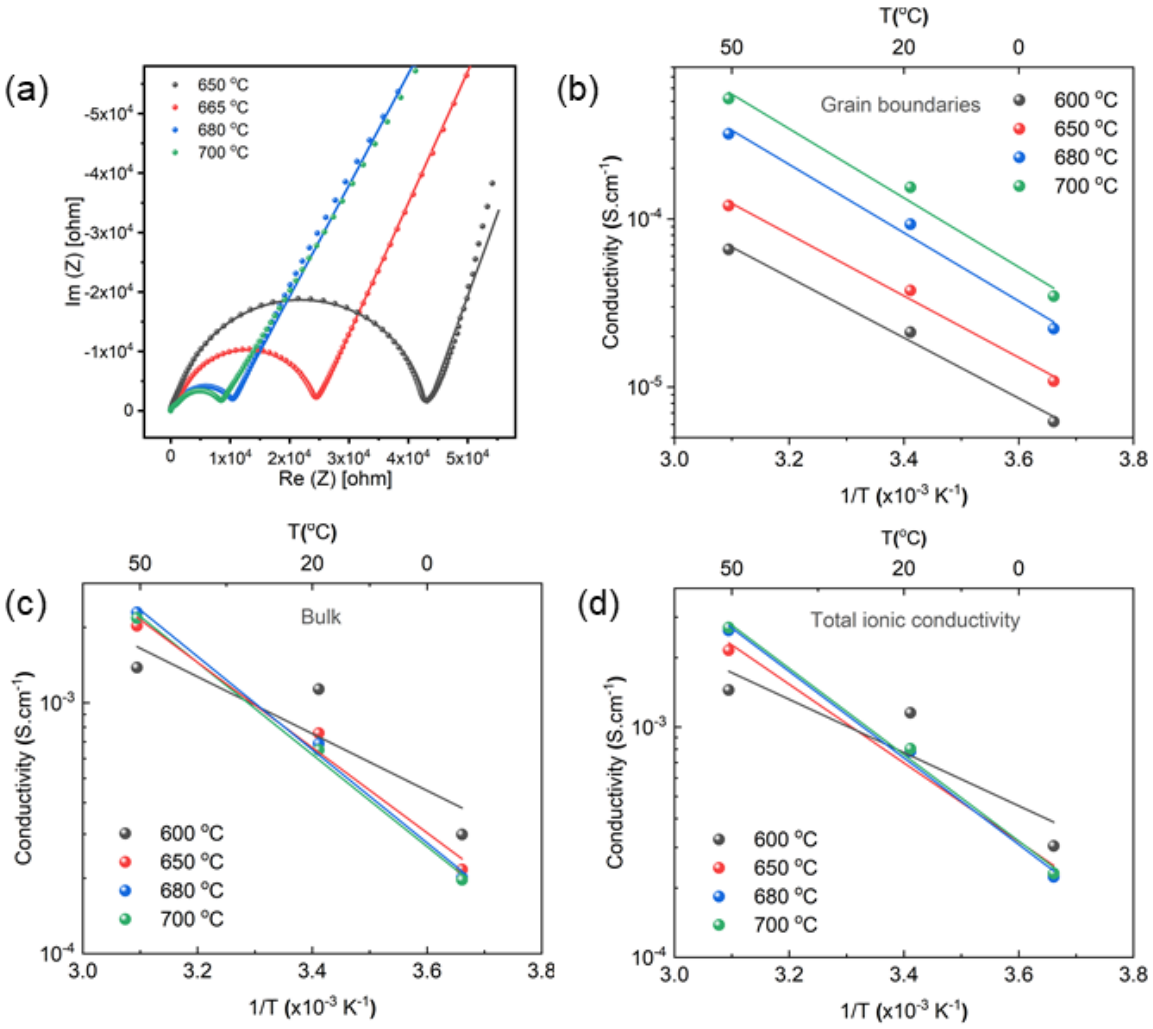


Figure 3.3 (a) Room temperature Nyquist plots of the pellets sintered at 600, 650, 680 and 700 °C; the fitted semi-circles of the grain and inter-grain regions are displayed. (b-d) Arrhenius plots of the (d) grain boundaries, (e) grain and (e) total ionic conductivity values.

The crystal structure of the sintered pellets was verified using X-ray diffraction to ensure that the high sintering temperature did not induce structural changes in the solid electrolyte. **Figure 3.4** displays the XRD profile fitting of the original powder and the sintered pellets at various temperatures where no structural changes or impurities are detected in the pellets sintered at temperatures higher than 650 °C. Various changes were observed in the XRD profile fitting of the 600°C pellet; (012) reflection observed in original powder disappeared, (110) and (113) reflections diminished, while (024), (211) (122) and (300) reflection increased in intensity indicating that SPS induced special orientations for the pellet sintered at 600 °C. Moreover, a small amount of secondary phase, $AlPO_4$ which was not present in the initial powder was detected in the pellet after the sintering process. Additionally, a change regarding the color of the pellets was noticed (for all sintered temperatures), LAGP powder turning from white in the initial state to light and dark grey in the sintered pellets. The color of the pellet was observed to vary from one sample to another

despite using the same sintering parameters conditions, a hypothesis for this change in color being that most likely was induced by the carbon from the SPS die (as it was the only parameter that changed from one sample to another).

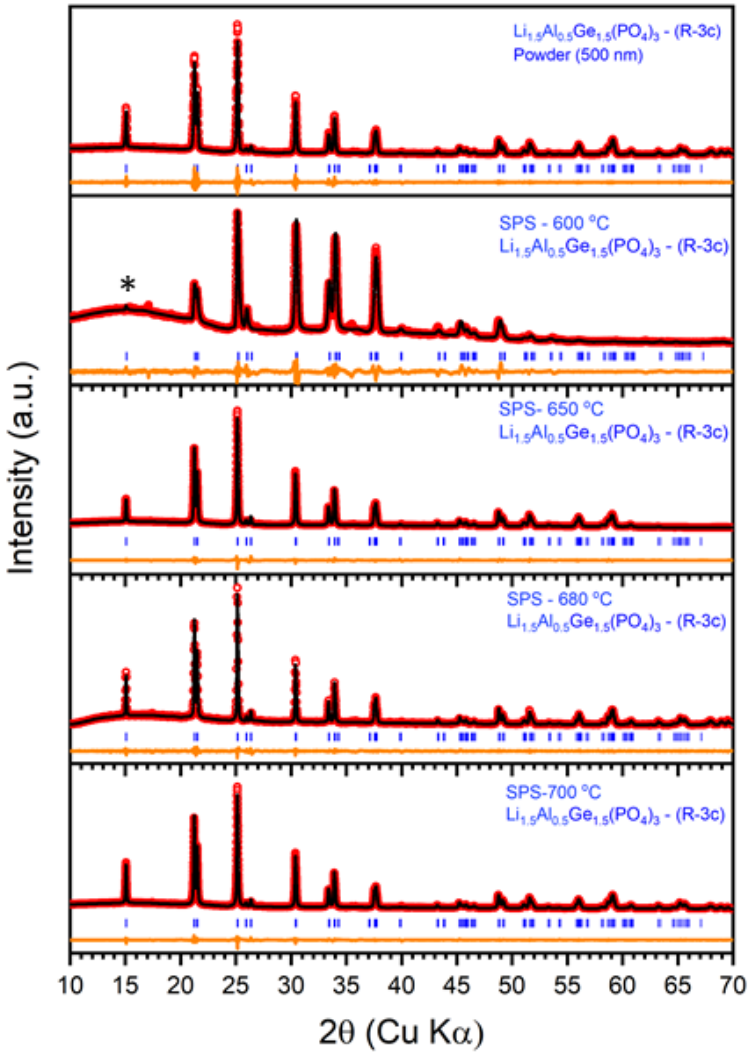


Figure 3.4 X-ray diffractograms of the initial powder and the pellets obtained using Spark Plasma Sintering at different temperatures.

3.3 Chemical stability of LAGP versus Li metal

A good chemical stability between solid electrolyte and Li metal is crucial as the specific contact area between the two layers will be maximized and an incompatibility between them will result in degradation products and an interphase layer formation. A series of degradation reactions were reported to occur at the physical contact of LAGP and Li metal interface resulting in a mixed conducting interphase (MCI), interphase that presents high electronic conductivity and poor ionic conductivity[124,232,233]. Density functional theory studies have predicted the formation of Li_9Al_4, $Li_{15}Ge_4$, Li_3P, AlGe and Li_2O as LAGP degradation products at the interface with Li metal[128,148]. During this study we investigated the chemical stability of LAGP versus Li metal based on Li/LAGP/Li symmetrical cells under a controlled

atmosphere environment over a period of 21 days using EIS, SEM and TEM. For this test, various cells were assembled in Swagelok devices and placed in a rest state where using EIS the cell resistance was measured every 24 hours within 21 days.

The Nyquist plot graph of the 21 days Li/LAGP/Li symmetrical cell is presented in the **Figure 3.5a** and it can be observed that in the initial state the cell displayed two semicircles, probably attributed to grain and grain boundaries resistances. After 24 hours of LAGP-Li metal contact, the EIS measurement showed an increase of 19% in the electrical resistance of the cell (**Figure 3.5b**) reaching up to 45% after 48h demonstrating that the formation of an interphase between LAGP and Li metal is occurring within the first hours of chemical contact. After this stage, for almost two weeks, the cell displayed a moderate electrical resistance increase over time. At day 19, a dramatic increase of the electrical resistance up to 168 % occurred, reaching 247% in day 20 and 278% in day 21. Moreover, if during the first two weeks of chemical contact the Nyquist plot displayed both grains and grain boundaries contribution, starting with day 19 the presence of a single semicircle on the Nyquist plot was noticed, most likely because the interfacial impedance dominated the internal resistance of the cell.

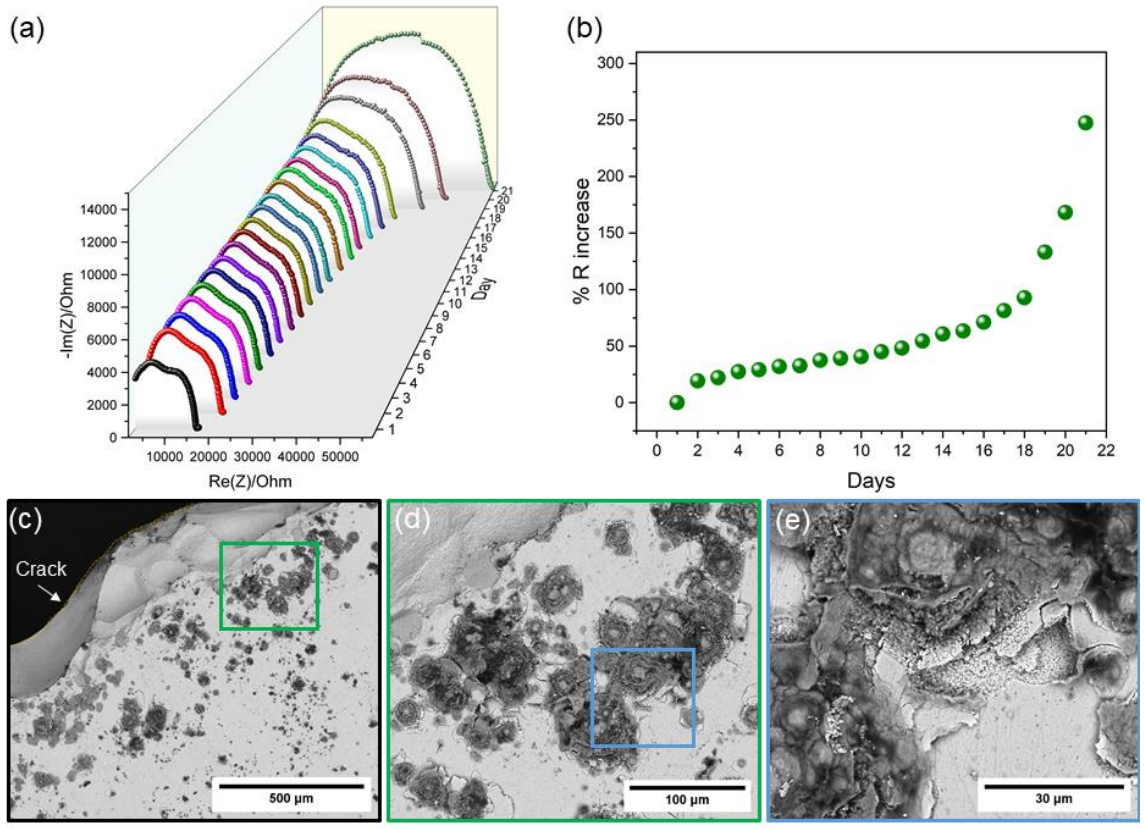


Figure 3.5 Chemical stability of the LAGP versus Li metal tested for a period of 21 days showing the (a) increase in resistance over time and (b) Resistance % over time graph of the chemical reaction between LAGP and Li metal over 21 days, (c-e) BSE-SEM images showing the evolution of the chemical reaction between LAGP and Li metal.

Morphological changes induced at the LAGP-Li metal interface during the chemical stability experiment investigated using SEM analysis are displayed in the **Figure 3.5c-e** (Li metal was removed from LAGP surface prior to SEM analysis). Even though no current was applied in the cell, the solid electrolyte showed the presence of large cracks (**Figure 3.5c**) that propagated in the solid electrolyte and the presence of degradation products clusters on the surface of the pellet containing lithium metal growth areas and delaminated parts of the solid electrolyte (**Figure 3.5d** and **Figure 3.5e**). No compositional changes compared to LAGP were identified on a micrometer scale in the according to SEM-EDX analysis (data not presented).

The degradation products resulted from the chemical reaction were investigated in nanometric scale using Scanning Transmission Electron microscopy (STEM) as it offers a more local analysis compared to SEM. For this investigation, a cold pressed LAGP pellet was placed in a contact with Li metal for a couple of days under a controlled atmosphere. Lithium metal was removed from LAGP surface pellet, and a copper grid was passed on the surface of the pellet to collect the solid electrolyte particles that were in contact with lithium metal and degradation products results. The copper grid was mounted on the TEM holder in the glovebox and sealed in a plastic bag under Argon atmosphere. Using an Argon flow placed next to the sealed bag to avoid air exposure as much as possible, the holder was transferred inside the TEM column in less than few seconds.

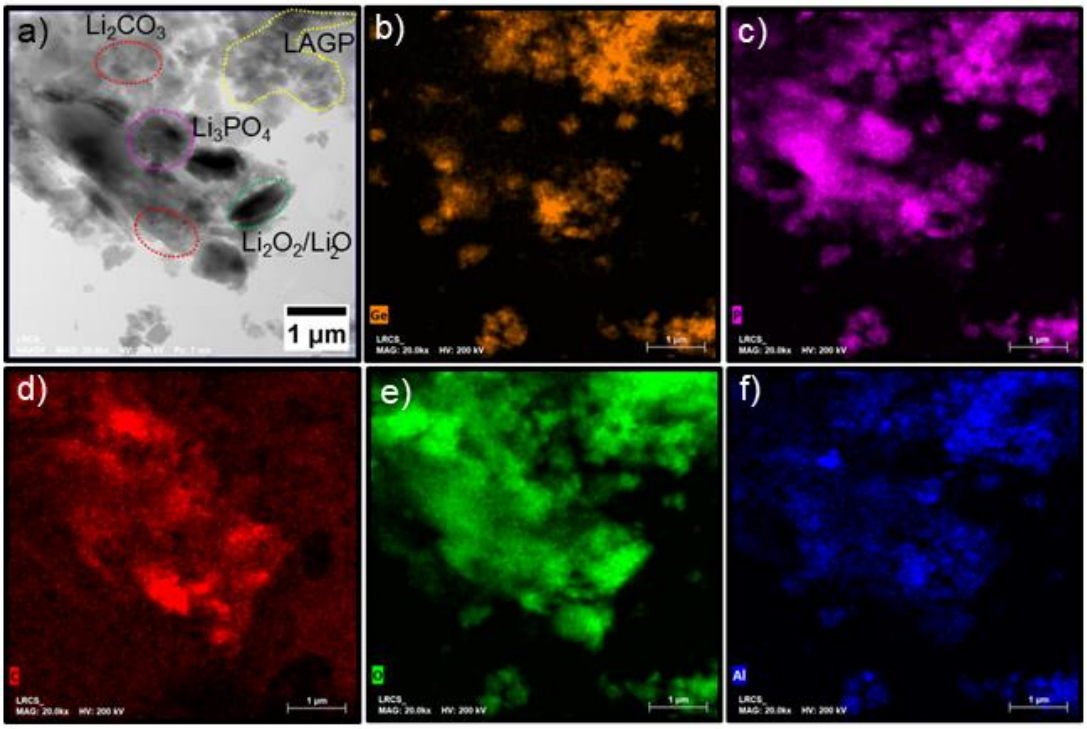


Figure 3.6 STEM image of (a) LAGP powder which was kept in contact with Li metal for one week and the maps of (b) Ge, (c) P, (d) C, (e) O, (f) Al generated after the EDX analysis.

STEM-EDX map analysis of solid electrolyte particles placed in contact with lithium metal for one week (**Figure 3.6)** shows the presence of LAGP particles (right corner up), but also the appearance of various side reactions products because of a chemical reaction. The pink marked area (**Figure 3.6a**) displays a strong P and O concentration compared to LAGP powder, meanwhile Al and Ge signals are absent which may indicate the presence of Li_3PO_4 as degradation products. Possible Li_2CO_3 as secondary phase (marked with red) was also spotted as areas containing high carbon concentrations were detected. A strong oxygen concentration was observed in the area displayed with green, where almost no other elements were identified, a possible assumption being that degradation products as Li_2O_2 or Li_2O were formed during the chemical reaction or due to the short air exposure during holder insertion in the TEM column

SEM and TEM analysis showed a low compatibility between LAGP and Li metal as an interphase containing degradation products was formed. Moreover, the formed interphase probably induced high volumes changes in the cell which induced stress as multiple cracks were observed in the solid electrolyte pellet.

3.4 Electrochemical stability window of LAGP

A chemical incompatibility between the solid electrolyte and the electrode results in interfacial decomposition and interphase formation. However, an interphase can be the result of an electrochemical reaction as well. A narrow electrochemical stability window of the solid electrolyte will trigger during solid electrolyte oxidation/reduction reaction the formation of an interphase or electrochemically decomposed electrolyte can contribute to interphase formation or growth[226]. The mechanical factors should not be neglected as well, as an improper contact between the solid electrolyte and the electrode will lead to inhomogeneous current density distributions across the battery interface and result in battery failure[128,232].

Oxide solid electrolyte are known for presenting a larger electrochemical window compared to sulfide SEs[226,234]. In the case of LAGP, in literature the electrochemical stability window varies according to the characterization technique used. Some studies using cyclic voltammetry (CV) reported a larger electrochemical stability window between 0.5 V and up to 7 V[179,228,235], while other studies using all density functional theory (DFT) calculations reported a much narrow electrochemical window between 2.8 and 4.3 V[234].

During this study, the electrochemical stability window of LAGP and possible interphase formation as a result of an electrochemical reaction between LAGP and Li metal were investigated. We used cyclic voltammetry as method to test the electrochemical

stability of LAGP; a mixture of 70 wt% LAGP and 30 wt% C45 (to ensure the required electronic conductivity) was cycled in a liquid electrolyte (LP30) vs. Li^+/Li.

Figure 3.7 displays the cyclic voltammetry plot of LAGP-C mixture vs. Li^+/Li between 0 and 5V at a speed scan of 0.05 mV/s where a stable electrochemical window of LAGP with no fluctuations between 1.5 and 4.5 V was observed. The presence of two oxidation reactions peaks, first located between 0 and 1.5 V and second one between 4.5 and 5V corresponding to O_2, $GeO(PO_4)_6$, $Li_4P_2O_7$ and $AlPO_4$ and the presence of a reduction reaction located between 1.5 and 0 V can be observed on the graph indicating the presence of decompositions reactions.

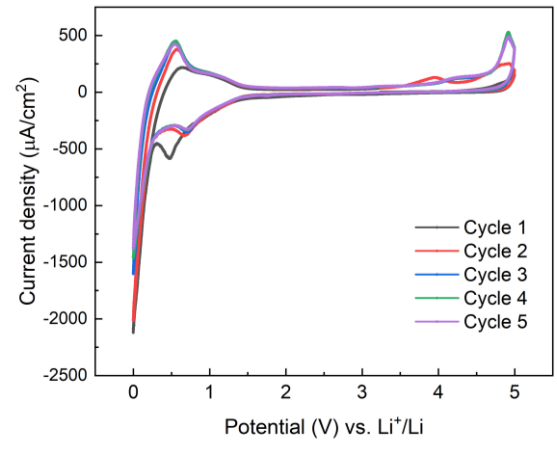


Figure 3.7 Electrochemical stability window of the $Li_{1.5}Al_{0.5}Ge_{1.5}(PO_4)_3$ (500 nm) tested using LAGP-C mixture in liquid electrolyte (LP30) vs. Li metal.

It should be noted that most of the inorganic solid electrolytes presents very narrow electrochemical stability window with values around 2-3 V for oxide solid electrolyte and around 0.5-1 V for sulfide based solid electrolytes[234]. The observed 3 V electrochemical stability window of LAGP and up to ~4.5 V is quite high allowing this solid electrolyte to be paired with high voltage cathode material without degradation in the solid electrolyte.

3.5 Current density influence on LAGP

Cracks formation and lithium dendrites penetration have been reported as the main causes that leads to a short-circuit in the ASSBs. Unfortunately, all-solid-state batteries cannot be operated at larger current densities than the critical current density (CCD), therefore is important to know the CCD limits and to find ways to improve their values for better cycling performances. CCD represents the highest current that can be applied on a cell before dendrites grow and induce cell failure. In the case of inorganic solid electrolyte, it was reported that the maximum CCD applied during lithium and stripping process was smaller than 0.5 $mA.cm^{-2}$ before inducing battery degradations[221,236,237].

In this study we tested the influence of different current densities values on LAGP during lithium plating and stripping process; symmetrical Li/LAGP/Li cells where different critical current densities as 80 µA.cm^{-2} (defined as low current density), 120 µA.cm^{-2} (defined as medium current density), and 160 µA.cm^{-2} (defined as high current density) were applied on the cells. No temperature or controlled pressure were applied on the cells.

The time dependent voltage profiles of Li/LAGP/Li cells during platting/stripping process are displayed in the **Figure 3.8** where one-hour intervals of positive/negative current densities were applied on the cells followed by two minutes resting time. All the cells were stopped when a maximum potential value of 10 V was reached. Any voltage change leading to polarization during the lithium plating stripping processes is a fingerprint of differences in active surface areas. The potential value and the shape of the voltage profile curve indicate any rearrangements occurring at the LAGP/Li metal surface[238]. A minimal polarization will indicate a stable interface and high efficiency cycling performances.

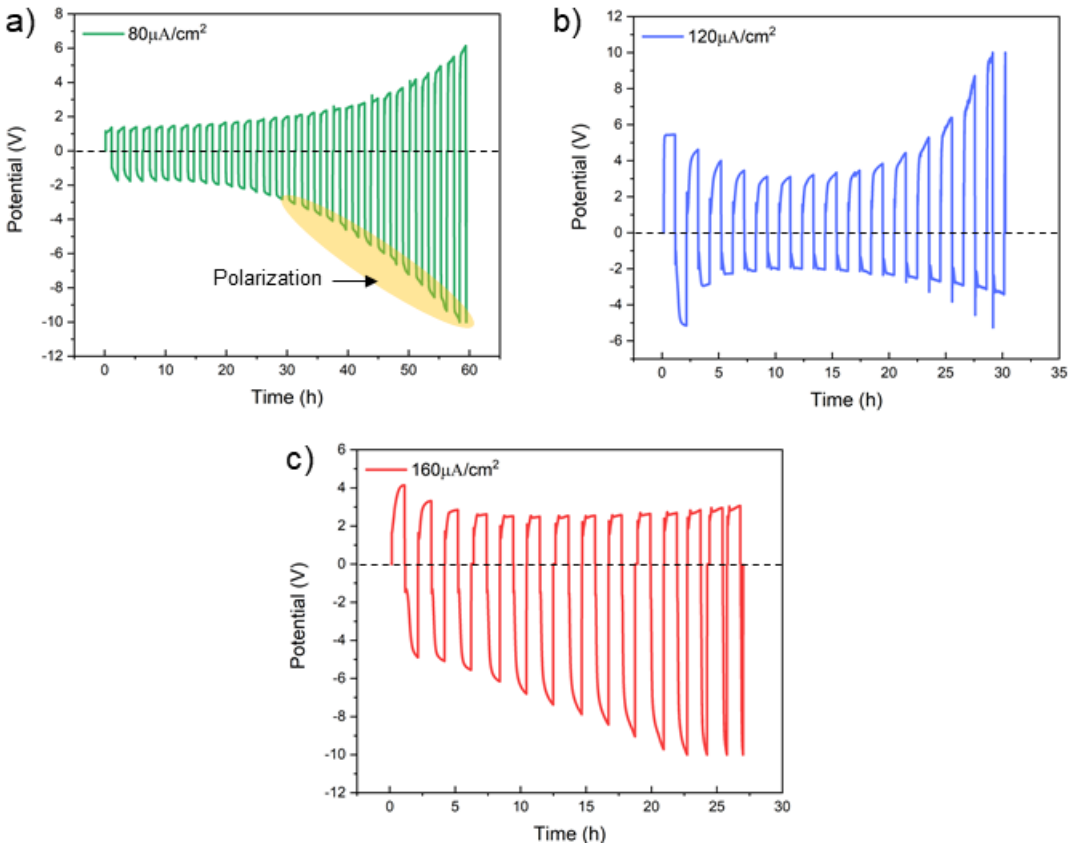


Figure 3.8 Galvanostatic cycling with potential limitation of a symmetrical Li/LAGP/Li where different current densities of (a) 80µA/cm^2, (b) 120µA/cm^2, (c) 160µA/cm^2 were applied.

We can observe that at the start of the cycling process all the cells displayed an increased potential value, one hypothesis being that a smooth interphase was probably formed post cell assembly. The lithium and platting process lasted longer for the lower

current density cell **(Figure 3.8a)**, reaching a potential value of 10 V after 60 hours of cycling compared to cells cycled at a medium current density **(Figure 3.8b)** and higher current density **(Figure 3.8c)** that reached 10 V shortly after 30 and respectively 27 hours. The cell cycled at lower current density shows a stable profile with slightly ohmic behavior and low polarization increase for the first 25 hours; according to literature, this stage corresponds to a stable morphology of Li metal, no pores formation and the applied current density does not exceed vacancy diffusion limit in Li metal[239].

After this stage, the cell displays a high increase in polarization, most likely due to pores formation and growth which leads to instable interface. The cell cycled at medium current density presents a non-ohmic behavior on the first cycle and ohmic behavior in the following cycles. It can be observed that after the second positive current applied, the cell potential started to decrease from a higher to a lower potential value, this type of behavior corresponding to generation hot spots in cells where the local current density presents very high local values and initiate Li filaments growth[239]. During the negative current application, starting with the third cycle the presence of small fluctuations was noticed, corresponding to difficulties on lithium stripping, most likely due to the interphase formation. The presence of fluctuation increased in the final stages of the cell and the presence of large spikes was also observed. When such spikes are presented at the end of platting/stripping it indicates the usage of previously unused fresh lithium[240], but in our case, one assumption for spikes presence could be explained by the lithium growth and cracks formation in the cell. The high current density cell, similar to the medium current cell showed a decrease in the cell potential after the second cycle indicating the initiation growth of Li filaments in the early stages of the cell. During the negative current application, the cell displays a high polarization indicating growth and pores formation, probably due to Li filaments growth[241].

Another important aspect that should be discussed is that the medium and high current cells showed high asymmetry of the electrodes during the cycling process. This asymmetry was most likely induced due to electrochemical reactions, but there are also other phenomena that could have contributed to this process. One phenomenon that could have contributes to the cell asymmetries could be related to a possible difference in compacity on the LAGP surface after the SPS process (polishing graphite from the top surface of the SE was always easier compared to bottom surface). Another aspect that should be considered is that the surface contact area between Li metal and solid electrolyte may differ from one electrode to another as no controlled pressure was applied on the cell. If the surface contact area was larger in one electrode compared to the other, different current densities were applied resulting in a faster degradation on a LAGP interface.

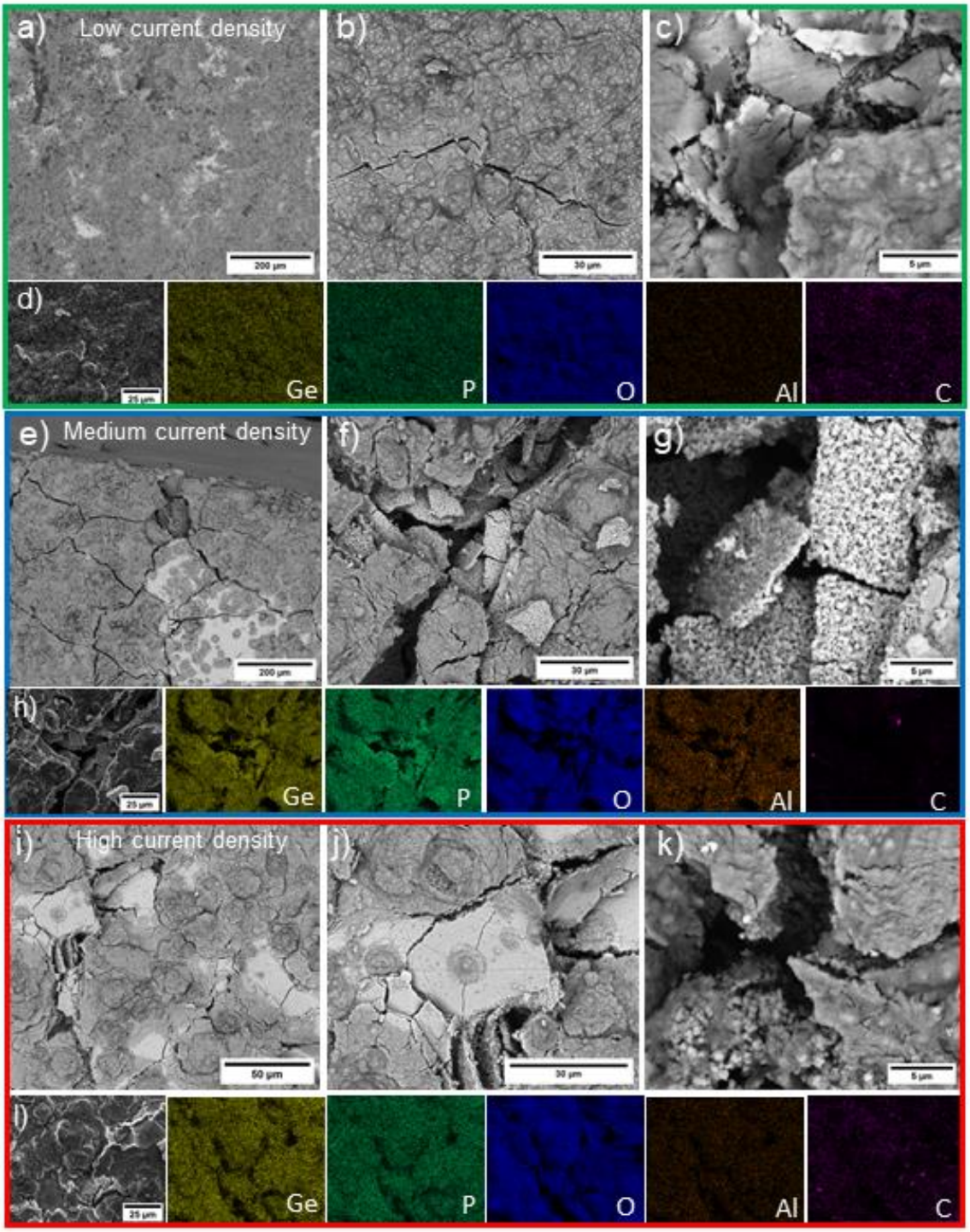


Figure 3.9 SEM images of galvanostatic cycling with potential limitation of a symmetrical Li/LAGP/Li where different current densities of (a-c) 80µA/cm^2, (e-g) 120µA/cm^2, (i-k) 160µA/cm^2 were applied. SEM-EDX analysis of (d) 80µA/cm^2, (h) 120µA/cm^2 and (l) 160µA/cm^2 cells.

For a better understanding of current density influence on electrochemical degradation mechanism of LAGP vs Li^+/Li, the cycled cells were exanimated using SEM. The samples were opened in a glovebox and transferred to SEM chamber using a controlled atmosphere holder to prevent further SE degradation from air exposure. **Figure 3.9** displays the post-mortem BSE-SEM and SEM-EDX analysis of LAGP surface after the electrochemical

reaction. On the BSE-SEM images, it can be observed that all the cycled cells developed an interphase layer (dark gray) between the SE (light gray) and Li metal; the interphase covering almost the entire surface of the SE. The generated interphase is presented on the LAGP surface in the form of clusters of various dimensions, increasing with the current density applied on the cell. SEM-EDX map analysis performed on top surface of LAGP pellets indicated a chemical composition like LAGP with the presence of locally carbon signal in small areas. A possible assumption based on the SEM-EDX analysis for the interphase containing clusters degradation products is that Li_2CO_3 or another lithium compound formed at the interface. The carbon, although not present in the initial composition of LAGP, most likely arrived small amount in the LAGP after the SPS process from SPS dies (LAGP powder changed the color from white to pellets in light and dark gray after the SPS process).

Another important phenomenon noticed on the cycled cell was the apparition of cracks after the cycling process. All the 3 cells presented large cracks which completely penetrated the solid electrolyte destroying it many different pieces. Based on SEM images it was noticed that higher the current density applied on the cell, the number, and the size of cracks on LAGP pellet increased. From the SEM images it was observed that around the larger cracks the formation of LAGP “sheets” (**Figures 3.9c,f,g,j**) corresponding to a lamination effect on LAGP was observed in all the cells. This phenomenon was probably induced due to Li movement during the cycling process.

For a 3D visualization of the crack’s propagation and dendrites growth inside the solid electrolyte, postmortem X-ray computed tomography (CT) analysis was performed. Compared to SEM which offers a visualization of top surface solid electrolyte, X-ray CT analysis offers 3D insights on the formed interphase, dendrites growth and cracks propagation. The reconstructed 3D volumes of the cycled solid electrolyte (a part of the SE as due to large cracks, the cell was fractured in many pieces) at different current densities are displayed in the **Figure 3.10**), where in purple is represented the LAGP layer and in green the combination between interphase dendritic layer and cracks.

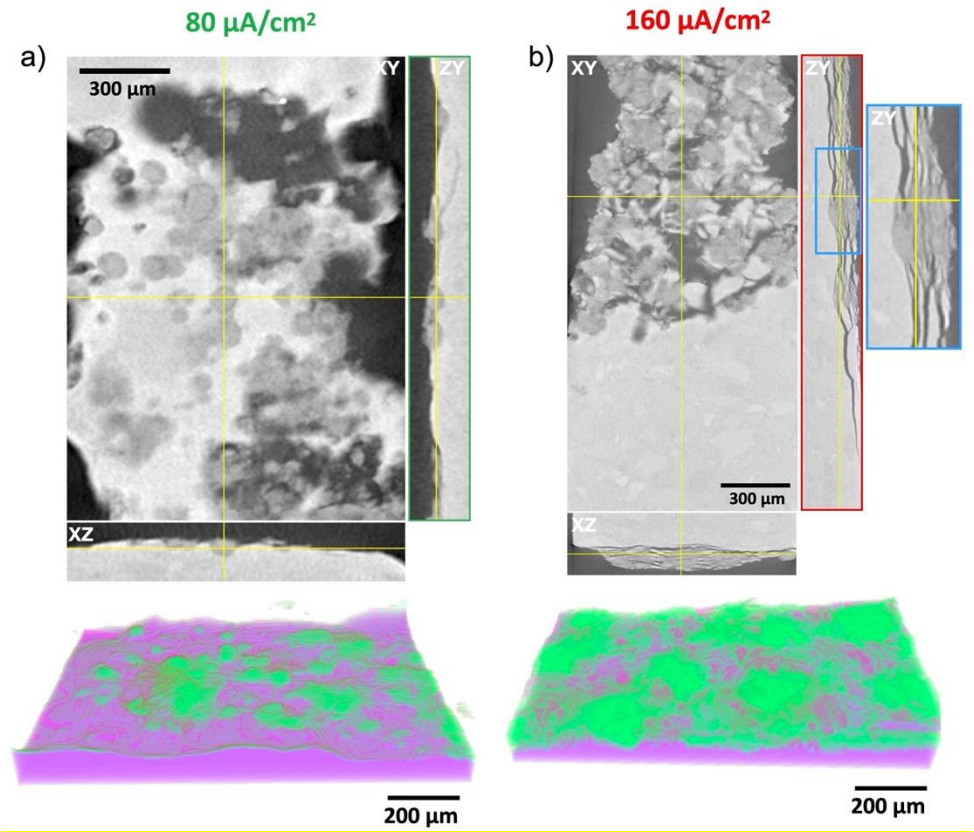


Figure 3.10 X-ray microtomography on the Li/LAGP/Li cells cycled at a) 80µA/cm^2, b) 160µA/cm^2 showing the dendrites formation and SE destruction after the cycling.

As it was already observed from the SEM images, all the cells present an interphase layer covering almost entirely the surface of the SE. Based on X-ray CT images, the cell cycled at 80µA.cm^{-2} (low current density) displayed a thinner interphase layer with few dendrites clusters slightly penetrating the LAGP layer (**Figure 3.10a**); lithium dendrites being mostly located around the areas with large cracks. The cells cycled at 160µA.cm^{-2} (high current density) showed a much thicker layer of interphase with dendrites uniformities and cracks deeply penetrating inside the solid electrolyte layer inducing lamellar degradation nearly the surface of the SE. In the case of low current density applied cell, it was observed that the entirely interphase was mainly formed from small dendrites clusters (**Figure 3.10a**) with the interphase layer penetrating inside the cracks where lamellar degradation on LAGP was observed. In the case of high current density cell, even larger dendrites, and interphase (**Figure 3.10b**) are noticed on the top surface of the LAGP. The interphase penetrated much deeper inside the LAGP layer creating larger cracks and a lamellar “sheets” effect on LAGP. If in the case of low current density applied on the cell, the interphase layer was located on the top surface of LAGP or near the top surface respectively, in the case of higher critical current density cell, the interphase layer completely penetrated and filled the cracks. Based on these observations we can hypothesize that cracks/mechanical damages are easily induced as they were extensively

observed in the solid electrolyte, but lithium dendrites growth are considerably influenced by the applied current density, higher current density values promoting a faster growth of the lithium dendrites leading to a quicker short-circuit in the cell.

As SEM-EDX did not provide deeper insights about the chemical composition of the new formed interphase, secondary ions mass spectroscopy (SIMS) analysis was performed on the cells cycled at different current densities values as part of a collaboration with Ametek Cameca (Paris). SIMS method allows to determine the surface composition by sputtering using a primary ion beam the surface of the sample, ions from the primary beam create a collisional cascade in the top layers which results in the ejection of secondary ions from the surface of sample that are further examined. Secondary ions are analyzed using a mass spectrometer that determines the elemental or molecular composition of the surface.

For this analysis, an IMS 7f-Auto device was used to determine the chemical composition of the interphase layer. A negative source with O_2^+ at 5 keV impact energy was used as primary ions source, therefore the positive secondary electrons will be collected. For high performances in terms of sensitivity, a double focusing mass spectrometer was used (depth resolution and mass resolution). An electron beam sputtering (Ip=30 nA) for charge neutralization was performed between each cycle of analysis. For each analyzed sample, a random area of 200*200 μm^2 was chosen. For low and medium current density 15 cycles of analysis were performed resulting in approximatively 2h20 minutes of analysis and for the high current density sample 124 cycles were performed (overnight analysis) resulting in 15h50 minutes of analysis. It should be kept in mind that using this method we are analyzing the first nanometers layer of the cell (~500 nm) for the low and medium current cells and ~4 µm in the case of high current cell.

The ions accumulated images of ^{6}Li, ^{12}C, ^{27}Al, ^{31}P and ^{74}Ge of a random selected area from the cells cycled at different current density values are displayed in the **Figure 3.11**. Due to a strong charging effect, ^{6}Li ions were detected and not ^{7}Li ions, but a test performed on the same cell indicated the same positions for both ions within the map with the only difference that ^{6}Li ions were less abundant (less counts) compared to ^{7}Li ions. Also, oxygens ions were not possible to detect as oxygen ions were used for the primary beam.

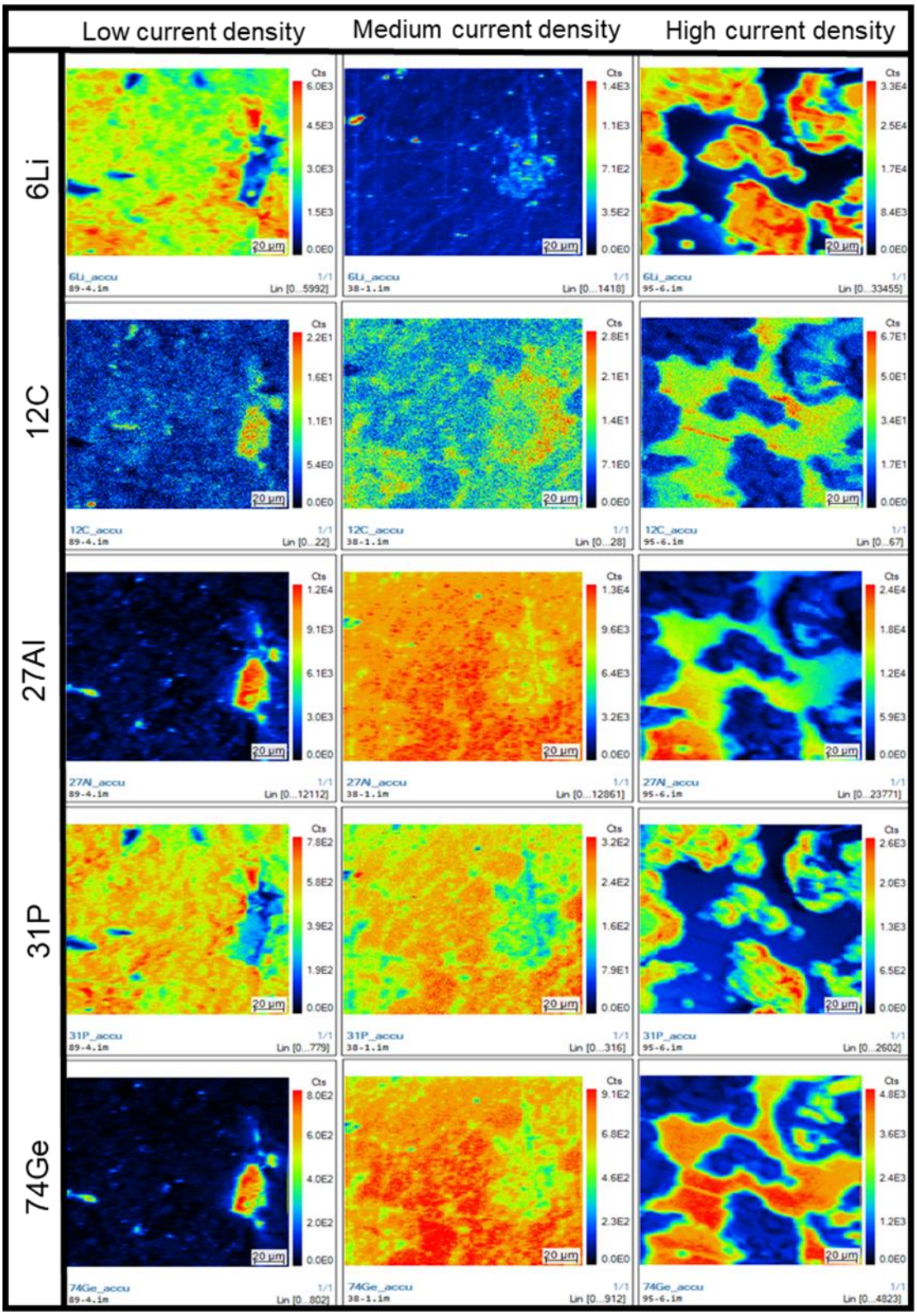


Figure 3.11 SIMS analysis (CAMECA IMS 7f-Auto) done on LAGP pellets which that were cycled in a symmetrical cell Li/LAGP/Li to follow lithium and plating at different current densities (analysis done after the electrodes (lithium) were removed).

The cell cycled at 80 µA.cm^{-2} (low current density value) displayed a strong lithium signal covering almost the entirely surface of the SE with small areas where lithium signal was less abundant. The same areas that displayed a stronger lithium signal, also exhibited a stronger phosphorus signal indicating a correlation between the two and that the formed interphase surface may contains degradation products rich in Li and P. A possible hypothesis for such a degradation product could be Li_3P which was already noticed to appear in the case of argyrodite SE[232,242]. Interesting enough, the areas where ^{6}Li and ^{31}P ions were less abundant, a stronger signal of ^{27}Al and ^{74}Ge ions was observed, a possible hypothesis being the formation of Al_xGe_y compounds as a reduction product from LAGP.

The medium current density cell, cycled at 120 µA.cm^{-2} displayed almost no strong ^{6}Li signal indicating no dendrite presence, possible because an area without stronger degradation was analyzed. The high current density cell, cycled at 160 µA.cm^{-2} shows the dendrites clusters abundant in ^{6}Li and ^{31}P ions, similar to low current density cell, conforming that the interphase layers contain Li_xP_y degradation products. Moreover, as a higher number of cycles analysis was performed on this cell, it allowed the observation up to 4 µm thickness on the sample surface. The analysis revealed that ^{31}P ions were found in a stronger concentration at the dendrite clusters tip/top compared to the base, meanwhile lithium ions signal was observed to be homogeneously distributed in the dendrites. The presence of carbon on the top surface of LAGP pellets was also detected, ^{12}C ions being observed mostly in the areas containing higher amounts of ^{27}Al and ^{74}Ge ions; with ^{12}C ions exhibiting by far less counts.

3.6 Protection layer of the solid electrolyte

A strategy to mitigate the interfacial reactions occurring between the solid electrolyte and lithium metal involves the insertion of a buffer layer between the electrode and solid electrolyte[124]. As revealed in the previous experiments, LAGP displayed chemical and electrochemical instability towards metallic lithium, therefore the insertion of a protection layer is necessary for better battery performances. The buffer layer selected as protection for LAGP should be thermodynamically stable or to passivate further reactions with Li metal and should present good mechanical and ionic conductivity properties[234,243–245].

Our strategy to minimize the degradation on solid electrolyte consists of inserting lithium phosphorous oxynitride (LIPON) as a protection layer which will be deposited on the top surface of LAGP pellets after the sintering process. For this experiment, LIPON was chose as protection layer as previous studies reported that LIPON layer passivated and limited the reactivity towards Li metal. In our study, different thickness of 100, 200 and 400 nm LIPON layer were deposited using atomic layer deposition (ALD) on one surface of

LAGP-680 °C sintered pellets. Like previous studies, no controlled pressure or temperature was applied on the cells.

The time dependent voltage profiles of symmetrical Li/LAGP/Li cells cycled with and without LIPON protection layer at a current density of 50 μA/cm^2 are shown in the **Figure3.12**. The cell without a protection layer (**Figure3.12a**) displayed high polarization and showed the presence of spikes after ~10 hours of cycling which indicated Li dendrites growth in the SE. The cell reached a potential value of 10 V after quite shortly, after ~15 hours, but the cell was still let to cycle for more than 40 hours as during the positive current application a low potential value was recorded (asymmetry in the cell).

Surprisingly, the time dependent voltage profiles of the cells with a protection layer of 100 nm (**Figure 3.12b**), 200 nm (**Figure 3.12c**) and 400 nm (**Figure 3.12d**) show that the cells reached a potential value of 10 V faster compared to the cell that did not presented a protection layer between LAGP and Li metal. It can be noticed that as the thickness of deposited LIPON layer increased, the cell was able to cycle (platting and stripping) for longer period, but still shorter compared to bare LAGP-Li cell. The cell with 100 nm protection layer displayed large overpotential under both positive and negative current application suggesting pores formation probably resulted from a morphological instable interface. The cells with 200 and 400 nm protection layer showed the presence of spikes from the first positive current application, followed by a slightly decrease in the recorded potential values indicating lithium dendrites growth from the first cycles.

It is known that LIPON presents an electrochemical stability window between 0.5 and 2.5 V vs. Li^+/Li[246], although is not a large electrochemical window, LIPON is one of the few solid electrolytes that present a good electrochemical stability at low potential values. On all the time dependent voltage profiles graphs we can see that the cells displayed high polarization, reaching a value above the stability window of LIPON from the first stages, the cells not fully taking the advantage of the protection layer. The ascendant trend towards a longer stability of LAGP vs. Li^+/Li when the protection layer increased indicates that LIPON could represent indeed a good protection for LAGP vs. Li^+/Li, but the thickness of LIPON needs to be increased to higher values.

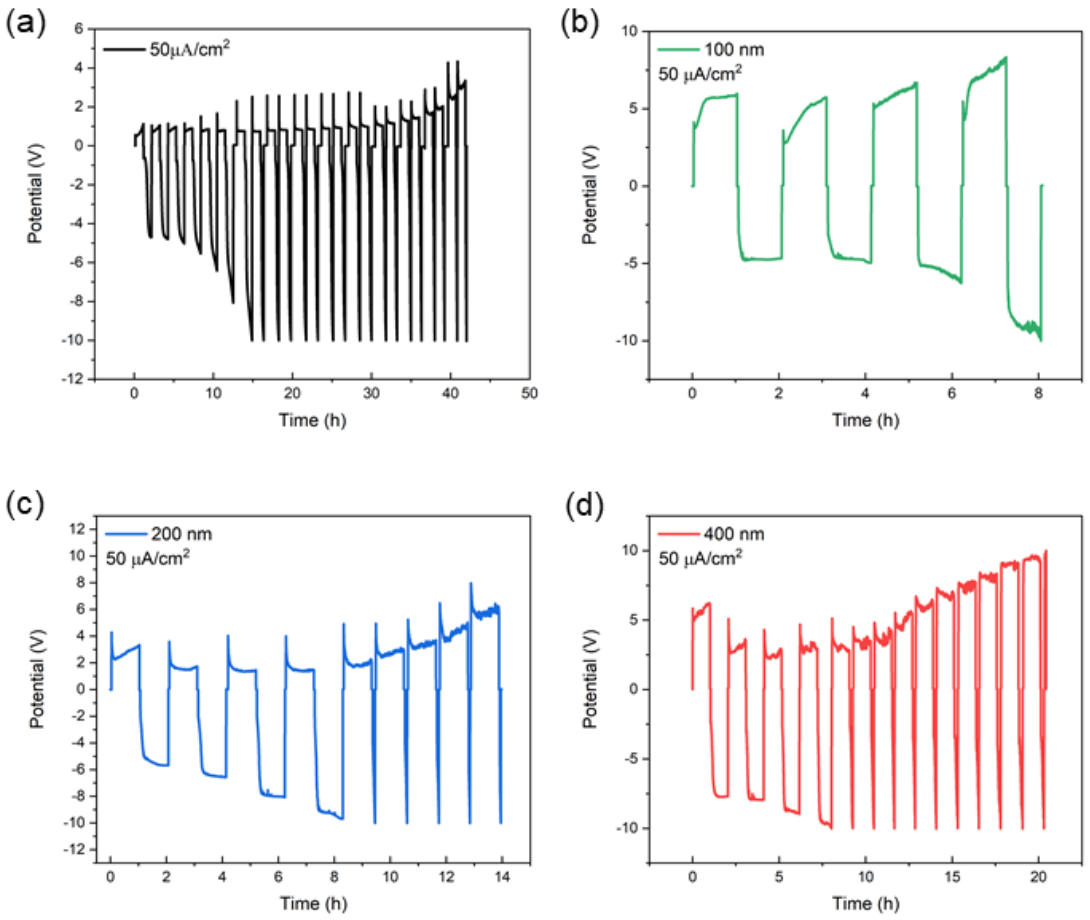


Figure 3.12 Galvanostatic cycling with potential limitation where a current densities of 50μA/cm^2 was applied on (a) a symmetrical Li/LAGP/Li with no protection and a symmetrical Li/LAGP/Li where LAGP surface was covered with a layer of LIPON of (b) 100 nm, (c) 200 nm, (d) 400 nm.

For a better understanding of the faster degradation induced in the samples with a protection layer, at the end of the cycling process, the cells were opened in a glovebox, lithium was detached from the solid electrolyte and top surface of the LAGP and Li metal side were analyzed using SEM. **Figure 3.13** displays the electrodes SEM images after lithium plating and stripping process where the presence of LIPON (gray) covering the surface of lithium metal (black) can be observed. The cell where a protection layer of 100 nm was applied (**Figure3.13a** and **Figure3.13d**) displays intermittent areas with and without a LIPON layer suggesting that a thicker layer was required. The presence of such areas creates an improper contact between the electrode and solid electrolyte resulting in locally larger current density applied on the cell. The SEM images revealed that the presence of areas with no protection layer was still present in the 200 nm LIPON layer, but their appearance was less abundant. Moreover, the presence of needle-like lithium dendrites was observed in the areas with no LIPON layer (**Figure3.13e**) indicting a preference for dendrites to grow in those areas. The cell where a protection layer of 400 nm was applied displayed a thicker layer of LIPON (**Figure3.13f**), but small area where no

particles were deposited were spotted (top corner left **Figure3.13c**) resulting in locally larger current densities which promoted lithium dendrites growth and a faster degradation of the cells.

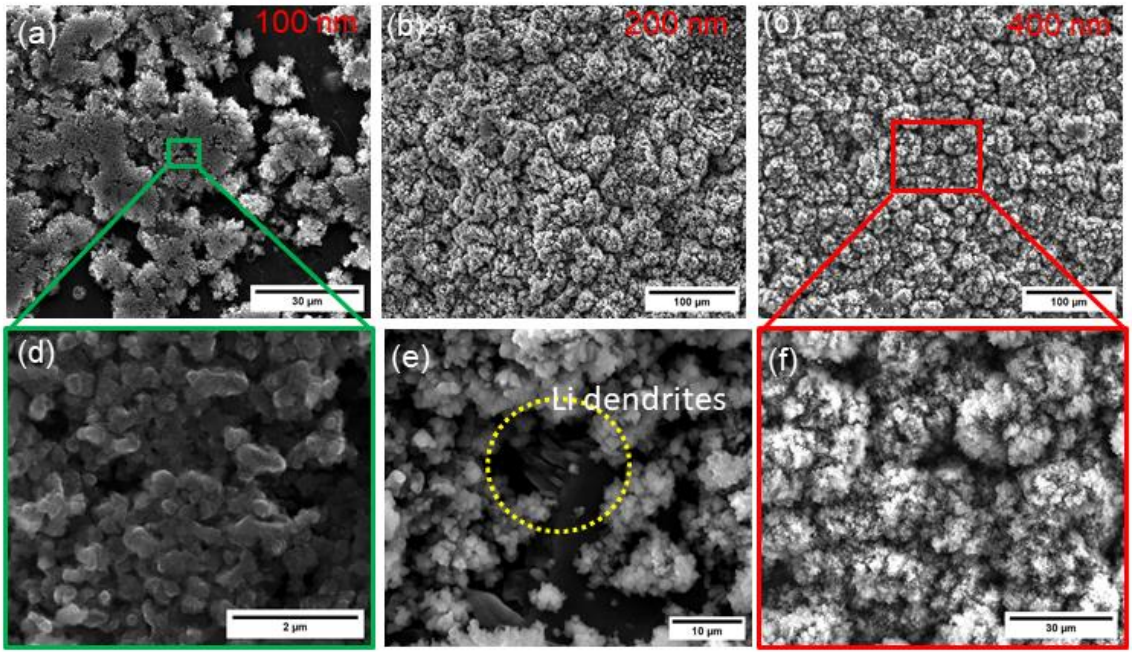


Figure 3.13 SEM analysis on lithium electrode from the GCPL cycling on the symmetrical cell with a protection of (a, d) 100nm, (b, e) 200nm and (c, f) 400 nm.

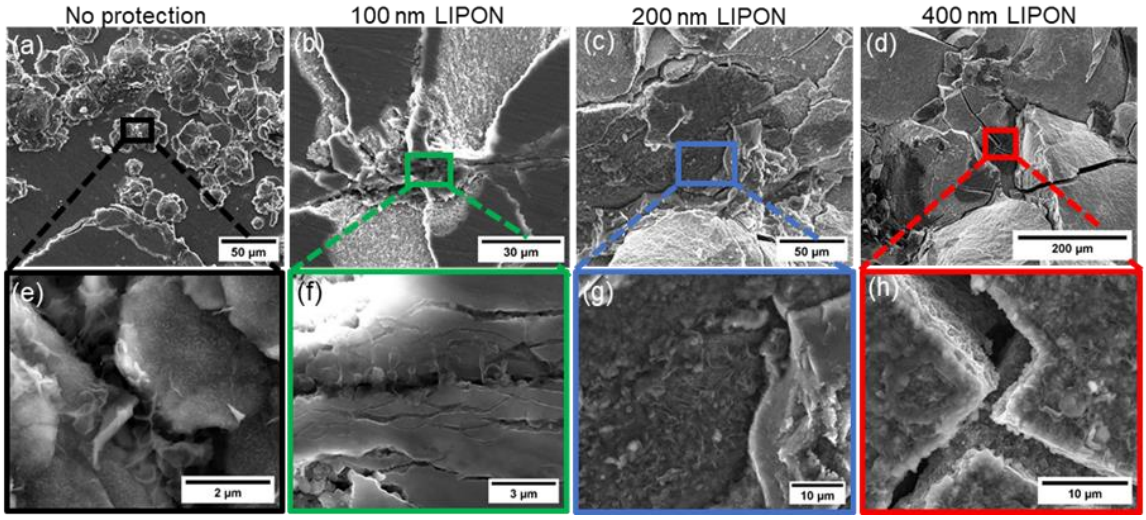


Figure 3.14 SEM analysis on LAGP from the GCPL cycling on the symmetrical cell (a, e) without protection and with a protection layer of LIPON of (b, f) 100nm, (c, g) 200nm and (d, h) 400 nm.

Post-mortem SEM analysis was performed also on the top surface of LAGP pellets after the cycling process (**Figure 3.14**). It can be observed that the cell with no protection layer showed the formation of an interphase layer **(Figure3.14a)** containing lithium dendrites **(Figure3.14e)** and large cracks that fractured the pellet (not shown here). In the case of the cells with the protection layer, the formation of an interphase between SE and

Li metal was still remarked, but less abundant suggesting that LIPON is a good solution as a protection layer for preventing (electro)chemical degradation between Li metal and LAGP. The presence of lithium dendrites and large cracks were noticed within all the cycled samples. In the case of the cell with no protection, lithium dendrites were mostly noticed on the top of the interphase layer, but in the case of the cells with protection, lithium dendrites penetrated directly inside the LAGP **(Figure3.14b,c,d)** producing larger dendrites and cracks resulting in a faster degradation of the cell.

LIPON buffer layer inserted between LAGP and Li metal helped ameliorating the formation of the interphase layer which slowly destroyed the solid electrolyte through (electro)chemical degradation. The presence of intermittent areas with no LIPON layer in the cell could not provide an entirely protection to LAGP creating small surfaces contact areas with larger current densities. This resulted in free paths for lithium metal that penetrated inside the solid electrolyte and produced cracks and larger dendrites resulting in a faster degradation of the cell.

3.7 Conclusions and perspectives

In summary, solid electrolyte pellets were sintered by SPS starting from LAGP commercial powder; an optimal total ionic conductivity was found for 680 °C pellet, similar previously LAGP sintered pellets obtained from sol-gel LAGP powder which was synthetized in the laboratory.

Chemical degradation occurring between LAGP and Li metal was tested by measuring every 24 hours for 21 days the electrochemical impedance spectroscopy of a Li/LAGP/Li symmetrical cell; the Nyquist plot graph indicating a 19% increase in the electrical resistance of the cell after 24 hours, 45% only after 48 hours, reaching an increase of 278 % after 21 days. Moreover, in the first two weeks, the Nyquist plot displayed the presence of two semicircles indicating the presence of grain and grain boundaries but starting with the third week the presence of a single large semicircle was detected indicating that the interface is dominating the internal resistance of the cell. The post-mortem SEM analysis indicating the presence of large cracks which fractured the entire LAGP pellet after 21 days contact with Li metal.

The electrochemical degradation between LAGP and Li metal was probed by performing galvanostatic cycling with potential limitation on three on Li/LAGP/Li cells cycled different current densities values. Our SEM experiments showed that presence of large cracks which penetrated the entirely LAGP pellet. In the case of a lower critical current density the failure of the cell was mostly induced by the pores and interphase formation which resulted in high cell polarization. In the case of medium and high current densities

cells, the failure was mainly caused by the generation of hot spots in the cell where the current density presented locally high values which initiated Li filaments growth. X-ray computed tomography experiments confirmed indeed a thinner interphase in the case of a lower current density cell and the presence of few dendrites located mostly around the large cracks in the SE. Medium current density cell displayed a much thicker interphase with lithium dendrites deeply penetrating inside the pellet inducing an easy lamellar surface degradation of the solid electrolyte. The high current density cell showed even a larger interphase which deeply penetrated inside the solid electrolyte, dendrites appearance being located all over the surface of LAGP inducing large cracks with lamellar "sheets" effect. Chemical composition of interphase and generated dendrites was verified using SIMS analysis performed on top surface of the pellets after the electrochemical reaction. SIMS analysis showed a strong correlation between ^{6}Li and ^{31}P signals indicating that lithium dendrites could contain Li_xP_y degradation products.

To minimize LAGP degradation vs. Li/Li^+, a buffer layer of lithium phosphorous oxynitride (LIPON) of various thickness (100, 200 and 400 nm) was deposited on solid electrolytes surface. The cell with 100 nm of LIPON as protection layer showed a larger overpotential indicating pores formation which leads to a morphological instable interface. The time dependent voltage profiles of the cells with 200 and 400 nm of LIPON layer showed the presence of spikes followed by a decrease in the recorded potential values indicating lithium initiation and growth from the first positive current application. Post-mortem SEM analysis showed the presence of intermittent LIPON areas on the LAGP surface which created an improper contact between the electrode and the solid electrolyte resulting in local areas with larger current densities that promoted a faster propagation of dendrites and cell failure.

As perspectives, for a better understanding of the current density influence on degradation mechanism of LAGP, experiments which allow to control the external pressure applied on the cells should be considered as an improper contact result in inhomogeneous current densities across the battery interface. Our finding showed that LIPON represents indeed a good candidate to protect LAGP/Li metal interface, but different strategy which allows a homogenous distribution of LIPON or a thicker layer will be required for a successful cycling battery.

Main takeaways:

We tested the chemical stability of LAGP towards Li metal using EIS, SEM and SIMS; our findings showed a high increase in the electrical resistance by 278 % after 21 days of contact with the presence of cracks which penetrated the solid electrolyte.

The electrochemical stability of LAGP vs. Li/Li^+ in function of the current density was analyzed using SEM, X-ray computed tomography and SIMS to investigate the degradation mechanism. We observed the formation of a thinner interphase with few cracks and dendrites in the cell that was cycled at lower current density while the cells cycled at a higher current density displayed a larger interphase full of lithium dendrites which deeply penetrated inside the solid electrolyte inducing an easy lamellar surface degradation of LAGP. SIMS analysis performed on top surface of LAGP pellets showed the formation of Li_xP_y as degradation products.

A protection layer of LIPON for the LAGP/Li metal interface was investigated and our findings showed that LIPON could indeed represent a good alternative for LAGP protection. Unfortunately, the presence of intermittent deposited areas which created larger current densities area promoting a faster degradation of the cell were observed, but a thicker layer of LIPON could induce more promising results.

Keywords: X-ray computed tomography; SEM; SIMS; LAGP degradation mechanism; Dendrites formation; Cracks; Interphase formation

Appendix B

Spark Plasma Sintering

Spark Plasma sintering under controlled atmosphere (Argon) was used to obtain dense pellets. To determine the optimum conditions for the pellet with the highest ionic conductivity, different pellets (similar to the previous study with the sintered powder in the lab) at different temperatures as: 600 °C, 650 °C, 680 °C and 700 °C were prepared. Identical sintering program as presented before where the solid electrolyte powder was packed in a 10 mm graphite die, sintered with a pressure of 8 kN and a heating rate of 1 °C/s until the maximum set temperature of sintering followed by a plateau of 5 minutes at the highest set temperature was employed.

Electrochemical impedance spectroscopy

A gold layer of 100 nm was deposited on both sides of the pellets to insure a better contact with the blocking electrodes. The AC impedance spectra was recorded using an MTZ-35 (BioLogic) frequency response analyzer from a frequency range of 1 Hz to 10 MHz with an excitation signal of 5 mV coupled with an Intermediate Temperature System furnaces (ITS, BioLogic) temperature controller. The impedance data were treated using Zview software and Brick Layer Model (BLM) as equivalent circuit.

Chapter IV 92
In-situ electrochemical X-ray µ Computed Tomography 92
4.1 Introduction 92
4.2 Cell design and experimental methods 94
4.3 Results and discussions 95
4.3a Initial state 95
4.3b Monitoring the lithium plating and stripping 97
4.4 3D analysis of LAGP lithium plating and stripping 102
4.5 LAGP/Li metal degradation mechanism 105
Conclusions and perspectives 106
Appendix C 109

Chapter IV

In-situ electrochemical X-ray µ Computed Tomography

4.1 Introduction

Ex-situ analysis methods describe the system in equilibrium state and allows obtaining information about the thermodynamics and relaxation processes occurring in the battery during electrochemical cycling. Using ex-situ analytical technics such as X-ray tomography and SEM we demonstrated and quantified the formation of interphases together with dendrites and cracks propagation during an electrochemical reaction in Li/LAGP/Li system leading to the failure of the battery. Unfortunately, we lack comprehensive information about the dynamical process (kinetics) occurring at the interface between the LAGP and Li metal during the electrochemical reaction. Thus *in-situ or operando* experiments are strongly required for a better understanding of the degradation mechanisms at different snapshot.

X-ray µ computed tomography (µ-CT) technique attracted great attention in the last years in the battery field as is a powerful observation method for studying interfaces which can penetrates even thick materials providing 3D information without destroying the analyzed sample[149,152]. In LRCS, within Imaging and Diffraction team (I&D), various *in-situ* X-ray CT cells were designed where the dynamics of LiO_2 batteries or electrode microstructure were studied. As massive data were acquired, to help with the time consumed on the segmentation, Zeliang Su *et al.*[247] worked on developing a deep learning approach. Although a powerful technique, the quality of obtained images are influenced by the voxel size, field of view, number of basics projections and image artefacts. For example, in samples where a larger field of view is analyzed, the obtained resolution will decrease as larger voxel will be obtained. Observing details as dendrites and small cracks within solid electrolytes is essential to understand the initial degradation reactions and images with high resolution are required. At the same time, visualizing the entire interface for a view on the overall reaction is required for statically confirmation of degradation reaction, therefore finding the right compromise between field of view and resolution represent an important parameter while performing *in-situ* experiments. X-ray µ-CT has been already

employed to study various degradation reactions between different solid electrolytes and lithium metal.

K. B. Hatzell *et al.* [248] used ex-situ synchrotron X-ray tomography to track structural transformation (grain boundaries, pores) on LLZO ($Li_7La_3Zr_2O_{12}$) pellets sintered at three different temperatures (1050 °C, 1100 °C, 1150 °C) after cycling. A faster short circuit was occurring in the sample sintered at lower temperature (higher density, but small pore size). This is due to a disconnected pore network contrary with the sample sintered at higher temperature (higher pore size and lower density), which provided a greater connectivity between the pores facilitating lithium transport and leading to a lower critical current density in the cell.

In-situ X-ray µ-CT was used by M. McDowell *et al.*[168] to monitor the evolution of mechanical damages induced within a symmetrical Li-metal/LAGP/Li-metal cell during electrochemical reaction. The evolution of the cracks network within the LAGP solid electrolyte was determined showing the appearance of the first two fractures in the SE extending radially towards the exterior of the pellet after 24h of galvanostatic cycling. As cycling progressed, the cracks grew and thickened leading further to circumferential cracks formation creating an interwoven web pattern[168]. In another experiment, using operando synchrotron X-ray µ-CT they observed the dynamical phenomena in $Li/Li_{10}SnP_2S_{12}/Li$ system modifying the 3D pellet morphology. They remarked that during lithium plating and stripping process, anodic lithium decrease in volume and while is transported to the other side an electrochemical interphase growth is rather noticed than lithium volume increases at the cathodic interface. Moreover, the lithium presented at the cathodic interface was also slightly consumed due to chemical reaction and contributed to interphase formation. The failure of the cell was induced due to loss of interfacial contact area by 52% at the bottom interface which created an increase in the cell voltage[152].

A. Hayashi *et al.* used also X-ray µ-CT observations to study the failure mechanism of Li/LPS/Li cells in which they proposed the following degradation mechanism: (a) LPS decompose into Li_2S and Li_3P and a reduction layer is formed; (b) reduction layer is growing leading to crack formation; (c) lithium is deposited in the cracks generating further reduction layer; (d) decomposition reaction occurs at lithium clusters in the cracks generating stress concentration and larger cracks in the SE; (e) lithium deposited along the large cracks causes the short-circuit of the cell[149].

P. Bruce *et al.* used X-ray µ-CT coupled with X-ray diffraction to track cracks and lithium dendrites propagation in the $Li/Li_6PS_5Cl/Li$ cell. In comparation with the other solid electrolytes, argyrodite formed a very thin interphase (a couple of nanometers and did not

propagate further). During the GCPL, the formation of spallations (vertical cracks near the surface) at the plated electrode were spotted meanwhile the stripping electrode remained clear. The formation of generated cracks, which grown wider and wider until they reached the electrode, but no short-circuit was recorded indicating that lithium did not fully cross the cracks. When lithium metal fills the cracks and arrives at the other electrode, a short-circuit take place[151].

More studies presented in the literature focus on others solid electrolytes interaction with lithium metal such as LGPS[249], LPS[150,250,251], thio-LISION[252] to understand better the degradation mechanism occurring at the interface. *In-situ* X-ray tomography experiments performed on Li/solid electrolyte/Li symmetrical cells offered excellent information regarding the kinetics of the failure mechanism. Thus, during this chapter we decided to follow the path to perform *in-situ* X-ray µ computed tomography coupled with electrochemical impedance spectroscopy on Li/LAGP/Li symmetrical cell to understand the kinetics leading to the degradation of LAGP during lithium plating and stripping process.

4.2 Cell design and experimental methods

The design of the X-ray tomography cell represents one important aspect which can influence our *in-situ* experiment as we will follow lithium plating and stripping process in the LAGP and lithium metal is known that when exposed to air will lead to the formation of lithium nitride[253], therefore we need a cell that will ensure the tightness of analyzed materials. Another critical aspect constitutes the overall thickness of cell cross-section as is impacting our final resolution and could make a big difference in spotting only large changes in solid electrolyte as cracks or help us to see details as dendrites and interphase formation.

A schematic representation of our *in-situ* X-ray tomography cell is displayed in the **Figure 4.1a**. The cell was adapted starting from a commercial polyethylene Swagelok where further modification as thinning cell cross section to reduce the thickness was implemented. The inside cross-section of the cell presents a dimeter of 3 mm, allowing us to obtain a good resolution where details as small cracks or lithium dendrites can be distinguished from the initial degradation process (previous studies where an 8 mm pellet of solid electrolyte was used allowed only the observation of large cracks, lithium dendrites were not observed).

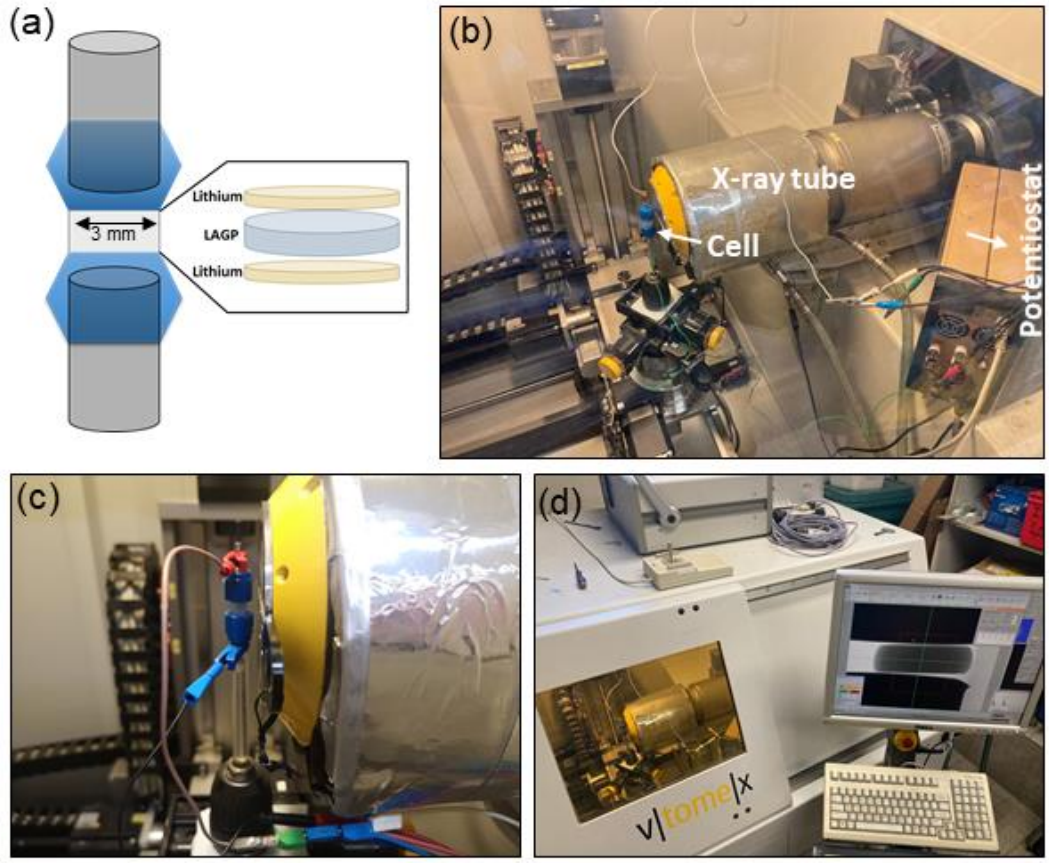


Figure 4.1 (a) Design of x-ray tomography cell used during the in-situ experiments, (b) images showing the in-situ cell connected to the potentiostat and (c) the cell during the acquisition of the x-ray tomography projections (d) overview of the cell during the in-situ x-ray µ-CT analysis.

To ensure contact during the electrochemical reaction, thin cables were connected from the potentiostat to the metallic pistons of the cell using alligator clips (**Figure 4.1b,c**). The cables were removed during the X-ray tomography acquisition to minimize the displacement and provide a more stable cell. During this in-situ experiment an SP-200 potentiostat from BioLogic and an GE Phoenix X-ray tomography device were used (See more details in **Appendix C**). For details regarding data processing and analysis see **Appendix C** and **Figure A4.1**.

4.3 Results and discussions

4.3a Initial state

LAGP pellets were sintered at 680 °C using spark plasma sintering following the procedure presented in **Chapter 2** and **Chapter 3**. The 10 mm diameter LAGP pellets were polished using SiC paper until a diameter bellow 3 mm and thickness of ~1 mm was obtained. Further LAGP pellets were dried overnight to remove any water traces presented in the solid electrolyte, sealed in aluminum bag and placed in a glovebox. The symmetrical cell, Li/LAGP/Li, was assembled in a glovebox one day prior to our *in-situ* experiments and kept overnight resulting in a slightly chemical reaction between the solid electrolyte and

lithium metal at the first scan analysis which in our case will be represented as the initial state.

Figure 4.2a displays cross section 2D projections of the bottom interface from various cell areas and show a perfect contact between the electrode and the solid electrolyte. Due to few hours cell preassembly, the formation of a slightly interphase because of a chemical reaction was spotted in an area in the bottom interface (**Figure 4.2a,** zone 3) and also in the top interface (**Figure 4.2c** zone 2). As LAGP is a highly ionic and electronic conductive, a spontaneous degradation between solid electrolyte and lithium metal is expected[121]. Moreover, the presence of voids is spotted in the top interface between LAGP and Li metal showing a slightly improper contact, which may result in higher current density applied on the cell. The improper contact at the top interface most likely resulted from (a) the hand assembling process as no controlled pressure is applied on the cell and (b) thinning down thickness of lithium metal by hand laminar process in order to avoid a contact between the electrodes during the assembly as solid electrolyte thickness was of ~1 mm.

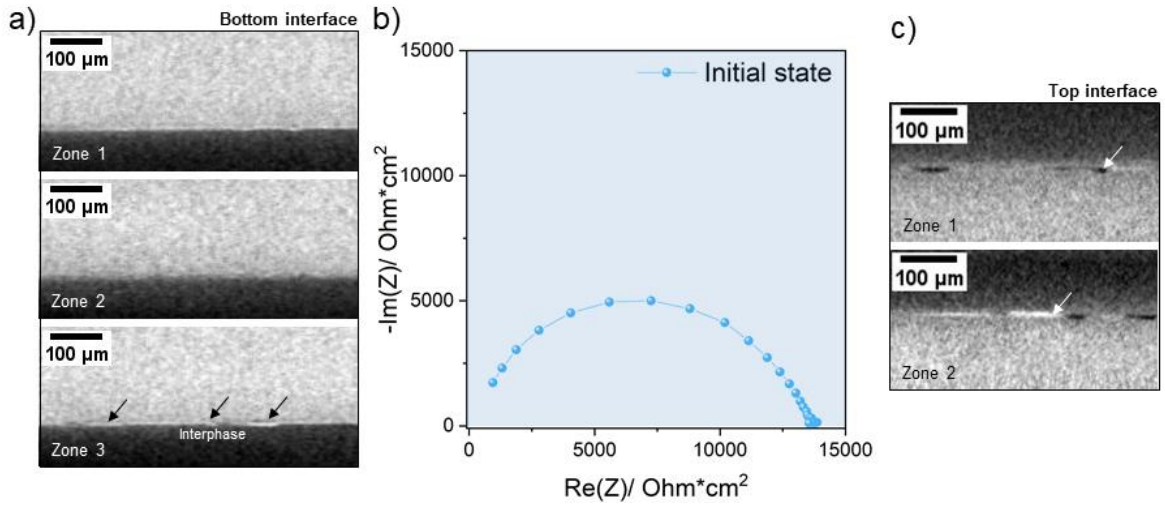


Figure 4.2 2D projections from different areas representing (a) bottom interface and (c) top interface between solid electrolyte and lithium and (b) Electrochemical impedance Spectroscopy (EIS) Nyquist plot of the Li/LAGP/Li recorded in the initial state.

During the *in-situ* experiment we will be analyzing a full cell behavior with lithium as both electrodes. In our case, analyzing the spectra is quite challenging as it will be a superposition of different contributions such as solid electrolyte, electrodes, and their interfaces[254]. Potentiostat electrochemical impedance spectroscopy (PEIS) (initial frequency: 200 MHz, final frequence:100 kHz, 6 points per decade) analysis were recorded after the “charge” or “discharge” was interrupted, the cell having sufficient time to relax before recording the data. Electrochemical impedance spectroscopy data of our system were recorded prior to every X-ray tomogram acquisition.

Figure 4.2b shows the Nyquist plot of our Li/LAGP/Li cell at the initial state where a single semi-circle is displayed. Based on the resistance value, we calculated the ionic conductivity of the overall cell and a value of $1.1*10^{-4}$ $S.cm^{-1}$ was obtained, value corresponding to the ionic conductivity of LAGP at RT, so we safely attributed the semi-circle as being the contribution of grains and grain boundaries in our cell.

4.3b Monitoring the lithium plating and stripping

During the two first cycles of lithium plating and stripping, galvanostatic pulses of ± 4.5 µA equivalent to a current density of 15.9 $µA/cm^2$ were imposed (**Figure 4.3a**). As there is one side always plating and the other side stripping, we are reporting the connotations "charge" as the stripping process and the "discharge" as the plating process taking as reference the bottom interface (the opposite process occurs at the top interface). The time-dependent voltage profile after the first current density application shows an ohmic behavior, only a negligible increase in potential was spotted towards the end of the first cycle of stripping (bottom interface).

The selected area 2D projection of bottom interface after the first stripping processes presented in the **Figure 4.3b2** shows quite stable interface with no voids generated or interface degradation compared to the initial state, but the presence of an electrochemical interphase layer was spotted on other areas displayed in the **FigureA4.2b** and **Figure A4.3b (Appendix C)**. After the first platting process, the LAGP/Li metal top interface (**Figure 4.3c2**) shows a minor filling of the voids which were previously generated due to an improper contact between the solid electrolyte and the electrode. Despite the slightly locally electrochemical interphase layer, the EIS Nyquist plot recorded after the first stripping (referred as to the bottom interface) displayed in the **Figure 4.3d** shows the presence of a semi-circle. No further increase in the resistance value compared to initial state was observed indicating that the presence of small "spots" of interphase between LAGP and Li metal doesn't induce limitation of lithium diffusion.

During the first plating process (bottom interface) a deviation from the ohmic behavior was observed inducing an increase in the potential and a slightly polarization in the cell. The recorded 2D X-ray image from the bottom interface (**Figure 4.3b3**) displays the formation of an interphase between LAGP and Li metal in the form of small spots, meanwhile the stripped interface (**Figure 4.3c3**) shows a small increase in the voids volume. At a carefully inspection of the bottom interface (**Figure A4.3c, Appendix C**) it was observed that the new formed interphase displays two type of contrast, a lighter contrast closer to the lithium metal layer and a darker contrast closer to the LAGP. As lighter elements displayed a darker contrast (X-ray absorption cross-section influence), our

assumption is that the dark contrast closer to the solid electrolyte layer are areas containing lithium dendrites (or lithium plated) and the lighter contrast closer to lithium metal represents a degradation layer formed from the reduction of the solid electrolyte where secondary phases resulted.

LAGP reported quite an instable interface (electrochemical stability window gap between LAGP and Li-metal) towards lithium metal where degradation products as GeAl, Li_3P, Li_2O, Li_9Al_4, $Li_{15}Ge_4$ were predicted using density functional theory studies to form at this interface[128,148]. The EIS Nyquist plot (**Figure 4.3e**) shows the presence of two semi-circles, the first semi-circle located at high frequencies corresponding to the diffusion of Li through the bulk and grain boundaries. The second semi-circle located at lower frequencies corresponds to the formation of the interphase as noticed in the X-ray images.

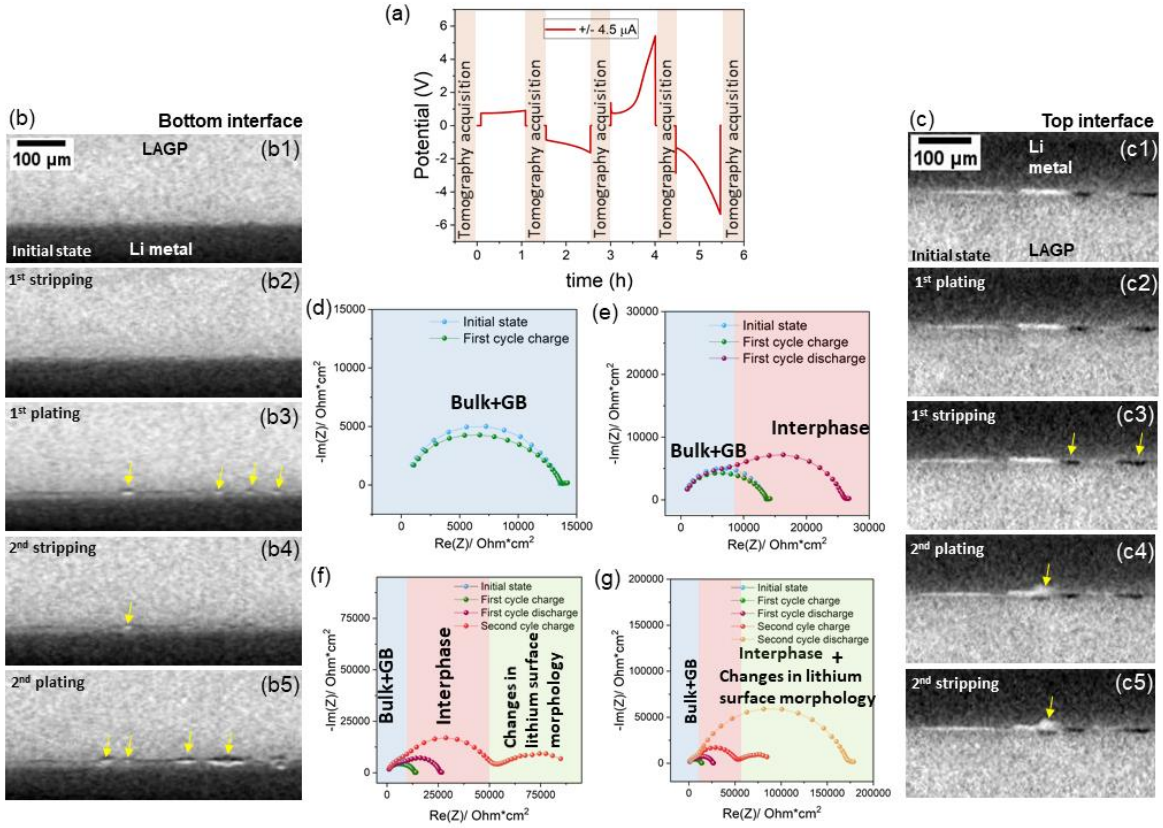


Figure 4.3 (a) Galvanostatic cyclic with potential limitation of Li/LAGP/Li cell in the first 2 cycles. 2D projections of the (b) bottom interface and (c) top interface at the initial state and during the first cycles of striping and plating (d-g) Electrochemical impedance Spectroscopy (EIS) Nyquist plot of the Li/LAGP/Li recorded after each cycle of stripping/plating.

At the second stripping process in the bottom interface, the time dependent voltage profile indicated the presence of a small spike at the begin of the stripping process followed by a large increase in the overpotential. According to literature, the presence of this spike followed by a decrease in potential indicates the formation of lithium dendrites and the consumption of the “fresh” deposited lithium at the interface[241]. As the amount of “fresh” deposited lithium is limited in the first cycles, the process will end up quite fast and pass to

the consumption of the "old" lithium resulting in an increase in overpotential. Based on the 2D X-ray tomography image from the bottom interface (**Figure 4.3b4**), a reduction in volume of the new formed interphase it was observed indicating that lithium is indeed removed from the deposited interphase and then passed on the bulk lithium metal. At the plated interface (**Figure 4.3c4**) we observed for the first time the formation of an electrochemically interphase layer in the form of spots.

Other zones in the cell (**Figure A4.3d, Appendix C**) indicating in the second stripping process (bottom interface) a combination of a dissolution of the "fresh" deposited lithium, with other areas in which an increase in the interphase layer were spotted. This observation shows the continuous degradation process that occurs with the LAGP-metallic lithium interface. At a stable interface, during the stripping process, only a dissolution of the lithium should occur, but in our case a combination of dissolution and interphase layer was observed (the interface grows on both platting and stripping process, although a grow only during the platting process was expected).

The EIS Nyquist plot (**Figure 4.3f**) displays the semi-circle corresponding to LAGP bulk and grain boundaries conductivity at high frequencies, followed by a semi-circle at medium frequencies corresponding to the interphase formation and a third semi-circle at low frequencies corresponding to changes in lithium surface morphology. We can observe that the resistance corresponding to the interphase layer doubled from the previous cycle indicating a fast degradation of the LAGP.

At the second plating process (bottom interface), the GCPL graph displayed a similar profile as in the second stripping where it showed the presence of a spike, followed by a decrease in potential and then high overpotential. The EIS Nyquist plot (**Figure 4.3g**) showed the semi-circles at high frequencies corresponding to bulk and grain boundaries Li diffusion followed by a large semi-circle corresponding to the interphase layer. The third semi-circle corresponding to changes in lithium surface morphology was not present.

X-ray images of plated interface displayed a volume increase in the overall interphase of both deposited lithium layer and degradation product layer. Moreover, the presence of a new slightly darker contrast (**Figure 4.3b5**, **Figure S4.2e**) was noticed, which could indicate the presence of another lithium compound or voids. Regarding the stripped interface (**Figure 4.3c5**) no visible changes were observed.

At the third LAGP plating and stripping we increased the applied current on the cell (from 4.5 to 9.0 μA as a faster degradation of cell was tried to be induced due to available time limitation at the device) and the cell reached a potential value of 10 V in a short period of time. We can observe that the new formed interphase containing the reduction layer and

dendrites started to cover almost entirely the LAGP/Li metal interface (**Figure 4.4a1**) resulting also in an increased interphase resistance value.

After this stage, due to a fast LAGP lithium plating and striping process and high associated polarization, the galvanostatic current was decreased back to 4.5 µA. Starting with the fourth stripping of the bottom interface the time-dependent voltage profile started to show the presence of small fluctuations (**Figure 4.4e**) and during the fourth plating, we can observe the presence of a larger fluctuation, which suddenly decreased in potential (**Figure 4.4f**) indicating a faster route for the lithium conduction.

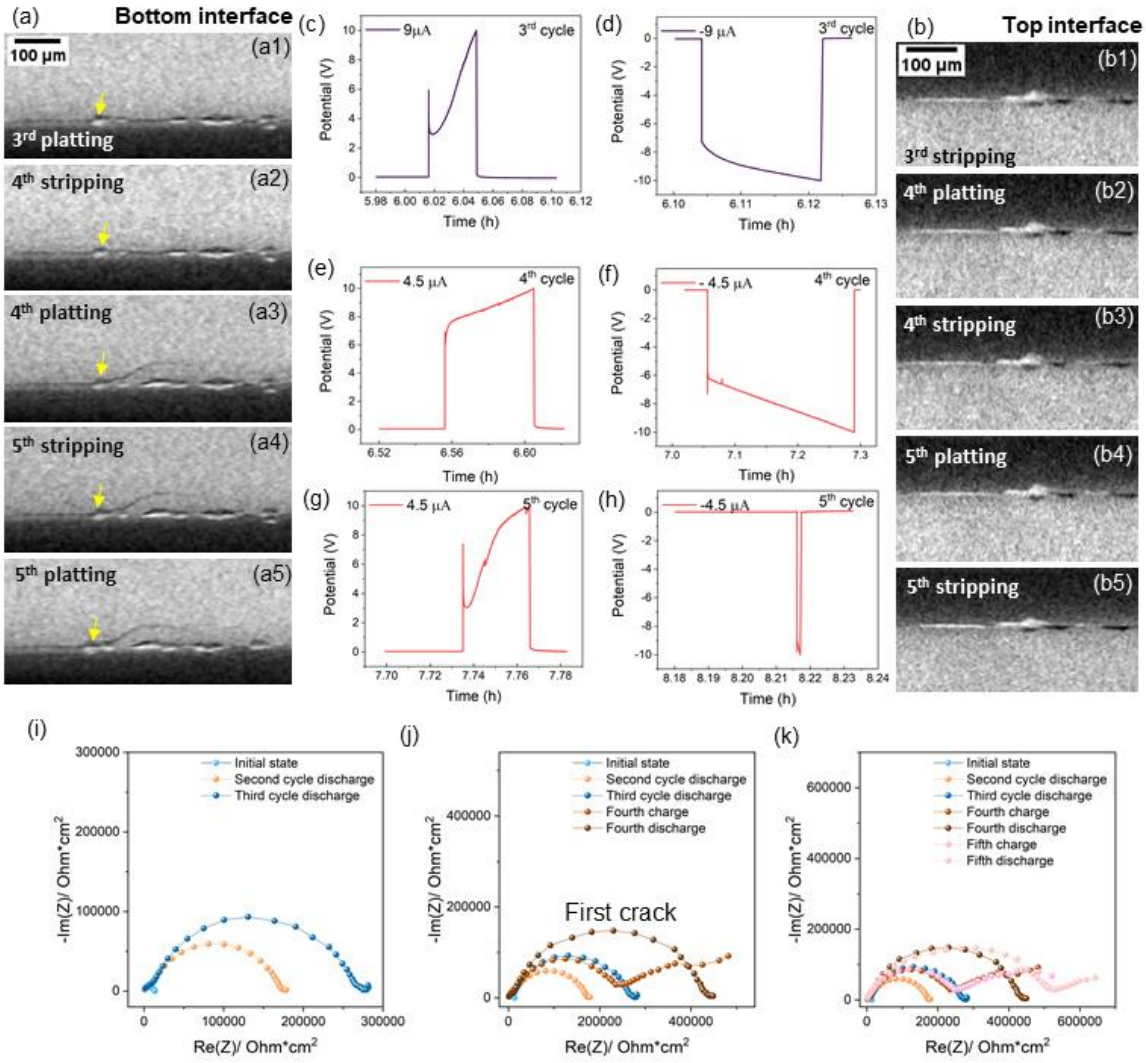


Figure 4.4 2D X-ray images of the (a) bottom interface and (b) top interface from the third to fifth cycle of plating and stripping (c-h) Galvanostatic cyclic with potential limitation of Li/LAGP/Li cell from the third, fourth and fifth. (i-k) Electrochemical impedance Spectroscopy (EIS) Nyquist plot of the Li/LAGP/Li cell recorded after GCPL.

The 2D images of the Li/LAGP/Li cell showed no noticeable changes at the bottom interface during the stripping process, but during the plating process the appearance of the first crack/dendrite in the cell was identified (**Figure 4.4a3**). The dendrite initiated from an

area, in which a pre-existent interphase and lithium deposition was already present and formed more like a spatulation morphology.

It was expected that the dendrite will propagate through the entirely pellet fracturing the solid electrolyte, but we noticed that the dendrite propagated very close to LAGP surface. This observation is in a good agreement with the GCPL data confirming that the droppage in potential is indeed related to initial cracks propagation and dendrites formation. When the dendrite propagated in the solid electrolyte, a faster route for lithium diffusion appeared exhibiting a lower potential value. Regarding the EIS data, during the stripping of the bottom interface, the appearance of a semi-circle indicating changes in lithium surface morphology was observed on the Nyquist plot. After the crack propagation, the Nyquist plot unveils only the presence of the two semi-circles attributed to LAGP ionic conductivity and interphase formation.

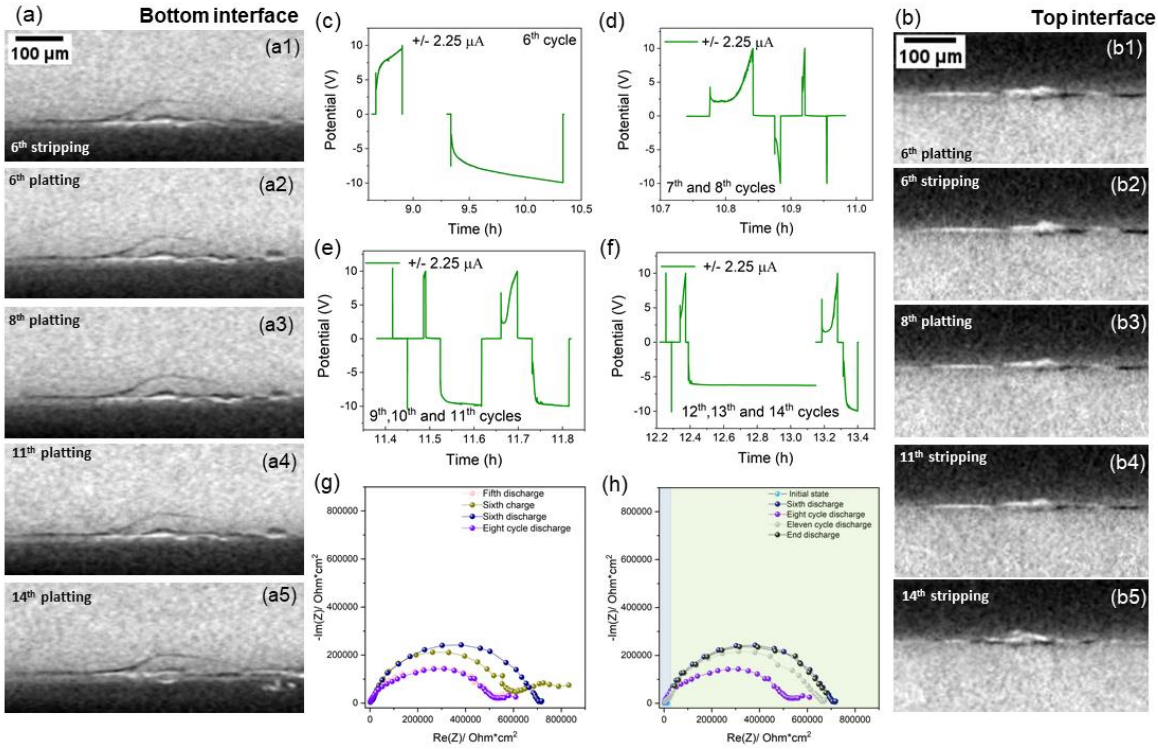


Figure 4.5 Selected 2D projections of the (a) bottom interface and (b) top interface from the sixth to fourteen cycles of plating and stripping (c-f) Galvanostatic cyclic with potential limitation of Li/LAGP/Li cell from the sixth to fourteen cycles. Electrochemical impedance Spectroscopy (EIS) Nyquist plot of the Li/LAGP/Li cell after the (g) 8 cycles and (h) 14 cycles of lithium plating and stripping process.

Starting with the fifth plating/stripping sequence a darker contrast appeared in the bottom interface at the base of dendrite (**Figure 4.3a4,5)** indicating the formation of possible voids that translated on the time-dependent voltage profile by the presence of the fluctuations (**Figure 4.4g**). Over cycling, the void that appeared at the base of the dendrite

was observed to start fill with lithium dendrites inducing possibly high stress in these areas, which can further promote the formation of large cracks in the solid electrolyte.

Between the sixth stripping (**Figure A4.2k**) and plating (**Figure A4.2l**) processes, strong degradations are induced at the bottom interface where a high-volume increase of the interphase was observed over one cycle indicating that once the interphase layer formed along the LAGP/Li metal interface a faster failure of the cell will be induced.

On the EIS Nyquist plots it was observed that the apparition of the third semicircle appeared after the stripping process at the bottom interface and plating at the top interface indicating changes in lithium surface morphology. A possible hypothesis for the apparition of this semi-circle could be indicated by the fact that the formed cracks were filled with lithium dendrites.

At the end of our cycling process, at the bottom interface the formation of hot spots containing degradations products are observed including inside the lithium metal layer and “dead” lithium is observed inside the reduction layer. As the reduction layer covered entirely the LAGP/Li metal interface, lithium diffusion between the two electrodes was impeded and resulted in the accumulation of dead lithium at the interface between solid electrolyte and reduction layer.

Regarding the top interface the generation of more hot spots along the interface are noticed. The generated dendrite got closed inducing a spallation shape which was most likely created LAGP surface lamination observed in Chapter 3. After 13 hours of electrochemical reaction, we were not able to observe large cracks penetrating the entirely the solid electrolyte. However, it is worth noticing that no continuous galvanostatic pulses were induced as the cell was in a relaxed state during the X-ray tomography acquisitions.

4.4 3D analysis of LAGP lithium plating and stripping

For a better understanding of the LAGP/Li metal interfaces evolution over cycling, a 3D volumes reconstruction on cell layers was performed. After tomographic reconstruction, each 3D tomographic volumes were processed (See more details in **Appendix C**) and 2D segmented with multiphase approach using Trainable Weka Segmentation plugin from FIJI (Random Forest algorithm). **Figure 4.6a,b** reveals the 3D reconstructed volumes of bottom interphases products where with red are represented the dendrites, with green is represented the reduction layer containing LAGP degradations products and with purple the voids (darker contrast).

On the initial state of the Li/LAGP/Li cell (**Figure 4.6b**) the presence of small stripes due to polishing are present on the LAGP surface which initially constituted a primary point

for the formation of the interphase layer. As mentioned earlier, on our initial state a small chemical reaction between the solid electrolyte and Li metal occurred as the cell was preassembled in a glovebox with few hours before the cycling process. At the first discharge, the apparition of hot spots containing dendrites was noticed on the LAGP surface. At the second discharge, dendrites reduced in volume indicating the use of fresh deposited lithium in the LAGP lithium plating and stripping process. The apparition of hot spots containing mostly degradation products appeared at the LAGP/Li interface. Starting with the third discharge the volume of dendrites and reduction layer started to increase forming larger hot stops at the interface. One of the most interesting aspects observed during this experiment was that lithium dendrites formed at the interface closer to LAGP and the decomposition products of LAGP formed at the interface closer to lithium metal, when the opposite result it was expected. **Figure 4.6c** shows the evolution of dendrites and reduction layer over the cycling.

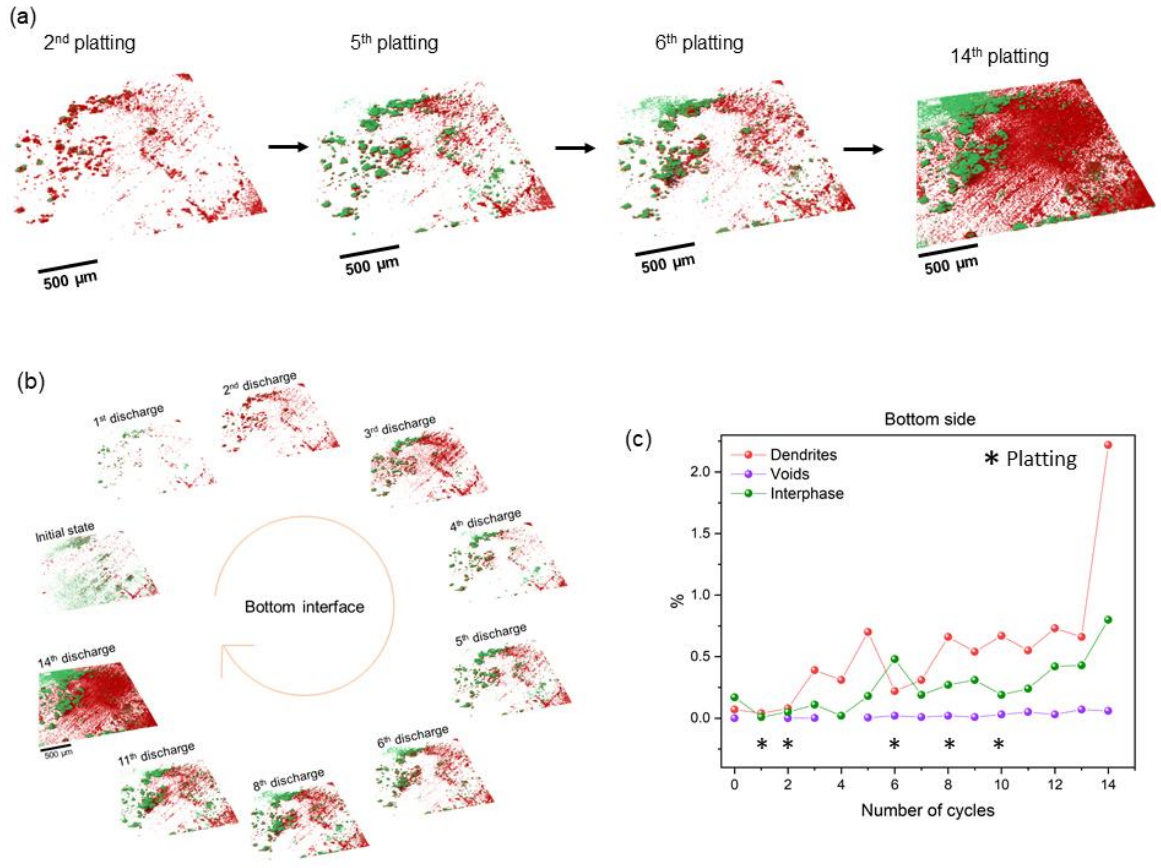


Figure 4.6 (a) Selected 3D reconstructed volumes of bottom interface from the X-ray tomography acquisition showing bottom interface increase in volume of the dendrites and interphase region over cycling (b) 3D evolution of the bottom interface LAGP/Li metal over cycling and (c) Bottom interface (dendrites, interphase region and voids) phases evolution over cycling.

We can observe almost a continuous increase in the volume of both reduction layer and lithium dendrites with the last one being present in a higher volume. By the end of our

cycling process, we can remark that at the 14th plating, the reduction layer covered almost entirely the LAGP surface. Hot spots of lithium dendrites and reduction layer grew in thickness getting more profound in the LAGP and lithium metal layer.

The 3D reconstructed volumes of top interphases products are displayed in the **Figure 4.7** where in red are represented the dendrites plus voids and with green the reduction layer containing degradation products. Unfortunately, the distinguish between dendrites and voids was not possible during the segmentation process, therefore the two phases are displayed together. The presence of stripes due to polishing process are stronger in the top interface as can be observed in the initial state of the cell interface (**Figure 4.7b**).

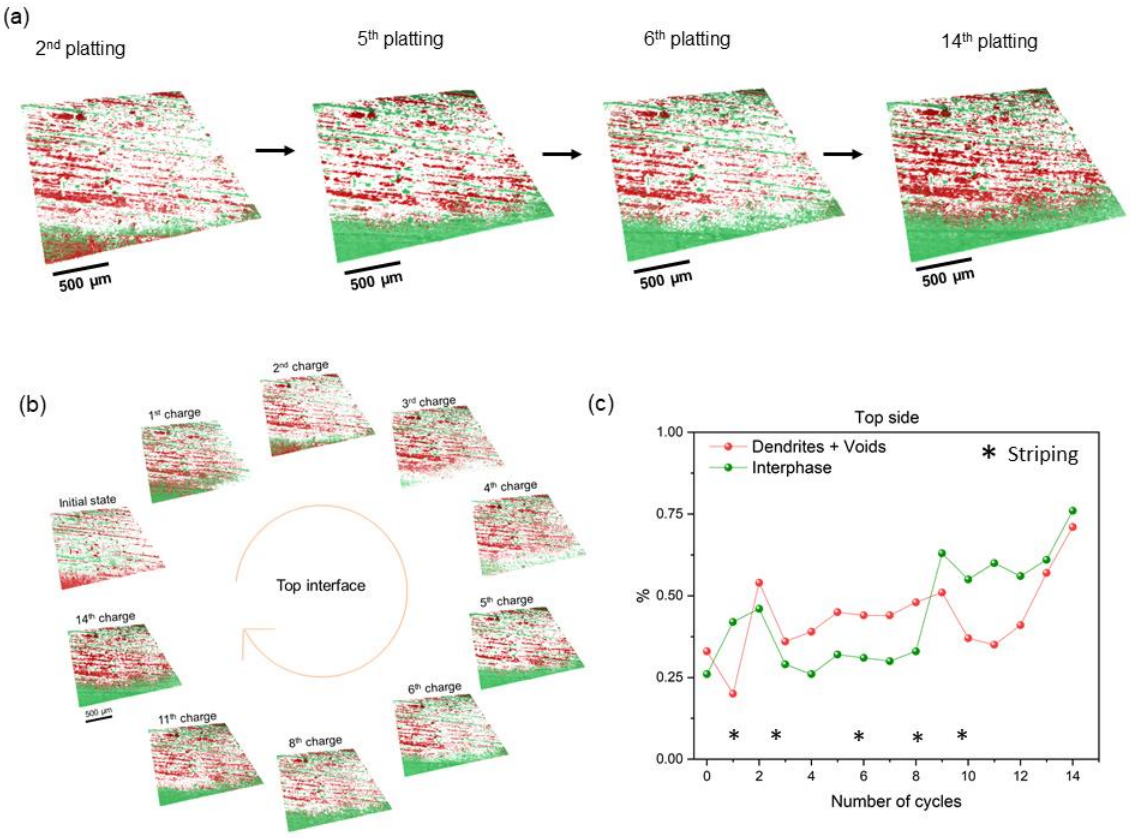


Figure 4.7 (a) Selected 3D reconstructed volumes of top interface from the X-ray tomography acquisition showing top interface increase in volume of the dendrites and interphase region over cycling (b) 3D evolution of the top interface LAGP/Li metal over cycling and (c) Top interface (dendrites+voids, interphase) phases evolution over cycling.

The 3D reconstructed volumes show a lower evolution of the top interface compared to bottom interface during the cycling process. The improper contact between the solid electrolyte and electrode was expected to generate larger critical current density in the cell and induce a larger degradation, but the opposite effect was noticed showing that the chemical degradation between LAGP and Li metal may enhance the electrochemical degradation. Interface phases evolution over the number of cycles graph (**Figure 4.7c**) of

the top interface shows a faster evolution of the lithium dendrites at the begin of the cycling process and faster growth of the reduction layer towards the end of the cycling process.

4.5 LAGP/Li metal degradation mechanism

The X-ray computed tomography and electrochemical impedance spectroscopy experiments were considered and based on them a degradation mechanism of LAGP lithium plating and stripping was proposed. The LAGP-metallic lithium interface is illustrated in the **Figure 4.8** where in yellow is represented the SE and with light gray metallic lithium.

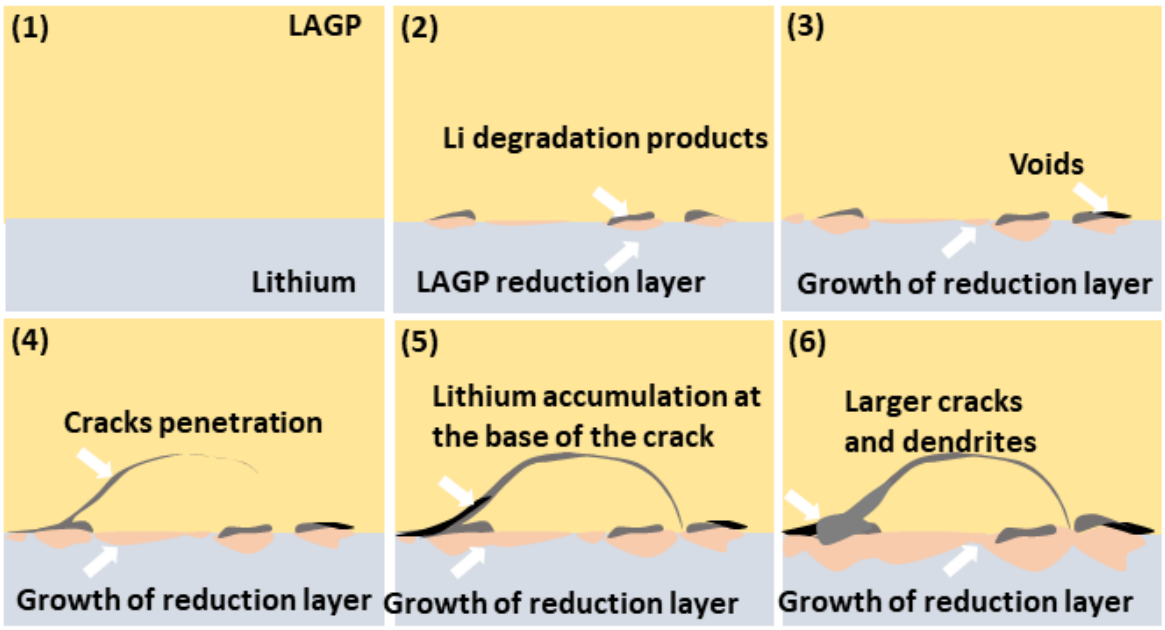


Figure 4.8 Schematic representation of the LAGP degradation mechanism versus lithium metal defined based on the x-ray tomography images.

From the initial state (1) under galvanostatic pulses LAGP interface decomposes and starts to form at the interface hot spots containing two products (2): lithium dendrites (dark gray) and a reduction layer containing LAGP degradation products (orange). It should be mentioned that our previous experiments showed that a similar degradation reaction will occur under a chemical reaction of LAGP and metallic lithium. As the electrochemical reaction progressed the reduction layer grew its thickness covering entirely LAGP/Li metal interface. Dendrites slowly started growing as well, and the formation of voids at the interface due to consecutive plating and stripping process started to appear (3). Once the new interphase layer (dendrites and reduction layer) started to cover the LAGP/Li interface, the penetration of cracks (possibly filled with lithium degradation products) inside the solid electrolyte was spotted (4). The crack forms more a spallation shape and doesn't propagate straight from one electrode to the other. The advance of the reaction showed further propagation of the cracks, the apparition of voids at the base of the new formed crack and further growth of the electrochemical layer (5). Lithium degradation products started to

accumulate at the base of the crack filling the formed voids (6) inducing extra stress in the cell and most likely contributing to the apparition and propagation of larger dendrites and cracks in the cell.

Conclusions and perspectives

In summary we designed a special cell and performed *in-situ* LAGP lithium plating and stripping reaction and followed the process using X-ray computed tomography and electrochemical impedance spectroscopy.

In-situ X-ray CT scanning of Li/LAGP/Li cell during operation showed the formation of hot spots at the interface resulting in an increase of cell resistance. With the growth of the formed hot spots, it was noticed the presence of two contrast in the interphase layer, lithium dendrites and degradation products resulted from the reduction of the LAGP. Contrary to expected, the degradation layer was formed at the interface closer to Li metal and lithium dendrites were formed at the interface close to LAGP. As the reaction progress, the hot spots start to grow and cover almost entirely the LAGP/Li metal interface. Although the volume of lithium dendrites detected was higher compared to the volume of the reduction layer, the apparition of voids and usage of fresh deposited lithium during the plating and stripping process was detected. The time-dependent voltage profile indicated the presence of small fluctuations over the cycling and X-ray computed tomography analysis confirmed the apparition of a crack which penetrated in the solid electrolyte. The crack was displayed as a spallation shape penetrating the near surface of LAGP and did not penetrate perpendicularly to LAGP/Li metal interface. The advancement of the cycling process showed the apparition of voids at the base of the new formed crack and with the reaction progression voids were filled with lithium degradation products making the crack to grow further in the solid electrolyte. The accumulation of lithium at the base of the crack will most likely induce stress in the battery and in the end lead to the presence of large cracks in the cell.

As perspectives, similar experiments could be designed where different critical current densities could be applied to visualize the dynamics of the LAGP degradation mechanism. For a complete understanding of the degradation mechanism, the cell should be cycled until a short-circuit in the cell is induced. Coupling X-ray computed tomography with an analytical method which could detect the degradation products formed at the interface between LAGP and Li metal will represent a useful experiment in understanding deeply the degradation mechanism of LAGP. Introducing a buffer layer as protection at LAGP/Li metal interface and following the experiment using *in-situ* X-ray CT will help the all-solid-state

battery community in understanding better the challenges facing this technology and design better solutions for suitable cycling all-solid-state batteries.

Main takeaways:

We performed *in-situ* LAGP lithium plating and stripping process, and we followed the reaction using X-ray computed tomography coupled with electrochemical impedance spectroscopy.

X-ray computed tomography showed the formation of an interphase layer in the form of hot spots containing lithium dendrites and a reduction layer resulted from the degradation of LAGP. The formation of the interphase layer showed on the Nyquist plot an increase in the resistance of the cell. As the reaction progressed, the reduction layer grew and covered the almost entirely the LAGP/Li metal interface and dendrites started to penetrate in the solid electrolyte forming a spallation. Fresh deposited lithium from dendrite was used during LAGP lithium plating and stripping reaction generating voids at the base of the dendrite, but ultimately, they filled with more lithium generating extra stress in the cell and potentially leading to larger cracks.

Keywords: LAGP lithium plating and stripping; X-ray computed tomography; Electrochemical impedance spectroscopy; Dendrite; Decomposition products; Degradation mechanism

Appendix C

X-ray tomography conditions

During this experiment a GE Phoenix v |tome| x s X-ray tomography device with a current of 100kV and 180 µA voltage was used where 1500 projections over 360° rotation for 33 minutes were collected per scan. A voxel size of 2.5 µm was used which allowed us to visualize the entire pellet and lithium interfaces in the cell (**Figure 4.1c)**. To ensure that no artefacts are induced during the data acquisition, each scan was verified at the end to ensure that no higher displacement than 2 pixels took place during the acquisition due to cables movement.

GCPL

Electrochemical measurements were done using a potentiostat SP-200 from Biologic. Galvanostatic pulses of ±4.5 µA equivalent to a current density of 15.9 µA/cm^2 were imposed for the first two cycles, then further increased to 9 µA in the third cycles for promoting a faster degradation due to time limitation of the x-ray tomography device. Due to a strong polarization, pulses were decreased to ±4.5 µA for the 4th and 5th cycles and then further decreased to ±2.25 µA. At the end of each series of electrochemical reaction, an electrochemical impedance spectroscopy was collected to track the resistance cell evolution.

Data processing and analysis

A region of interest from the top and bottom interfaces was selected and its evolution was followed during the cycling (region surrounding the LAGP pellet was eliminated). All the stacks were aligned (small rotation of the cell during manipulation) to ensure the same view on the XY, YZ and XZ planes using Fiji software.

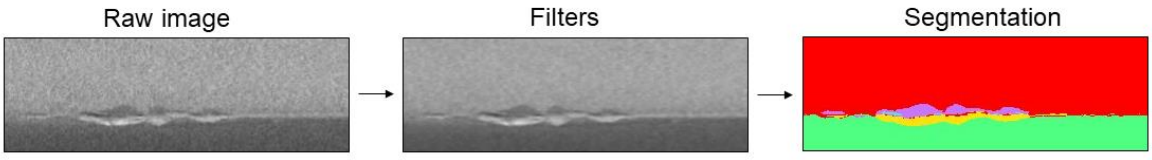


Figure A4.1 Data processing applied on the cross-section view of the a) raw images obtained from the tomography acquisition, b) after the filters were applied and c) after the segmentation process.

To facilitate the segmentation process, a series of filters Mean (2 pixels) and Unsharp Mask (1 pixels and 0.6) were applied on our images. For the segmentation process, Trainable Weka Segmentation tool was used where each pixel based in the images was classified in 5 different categories for the bottom side: solid electrolyte (red),

lithium (green), dendrites (purple), interphase (yellow) and a void (blue) and 4 categories for the top side: solid electrolyte (red), lithium (green), dendrites + voids (purple) and interphase (yellow). The process was repeated for each stack of 2D images inducing a slightly error in the percent of each phase as not all the stacks were treated at once. **Figure A4.1** displays an example of the raw images, images after the filter were applied and after the segmentation process for the side of the pellet.

2D projection from the X-ray tomography experiment

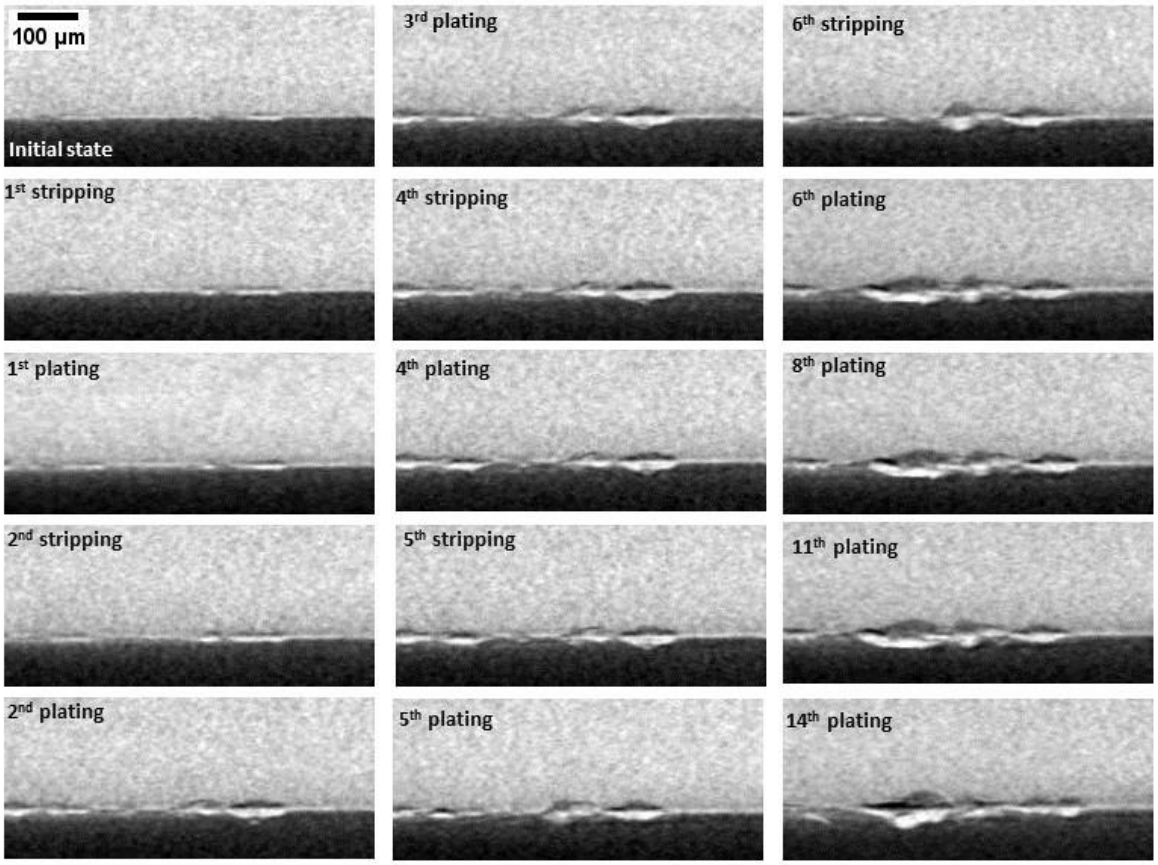


Figure A4.2 X-ray tomography 2D projections from a selected area showing the **bottom** LAGP/Li metal interface during the LAGP lithium plating and stripping process.

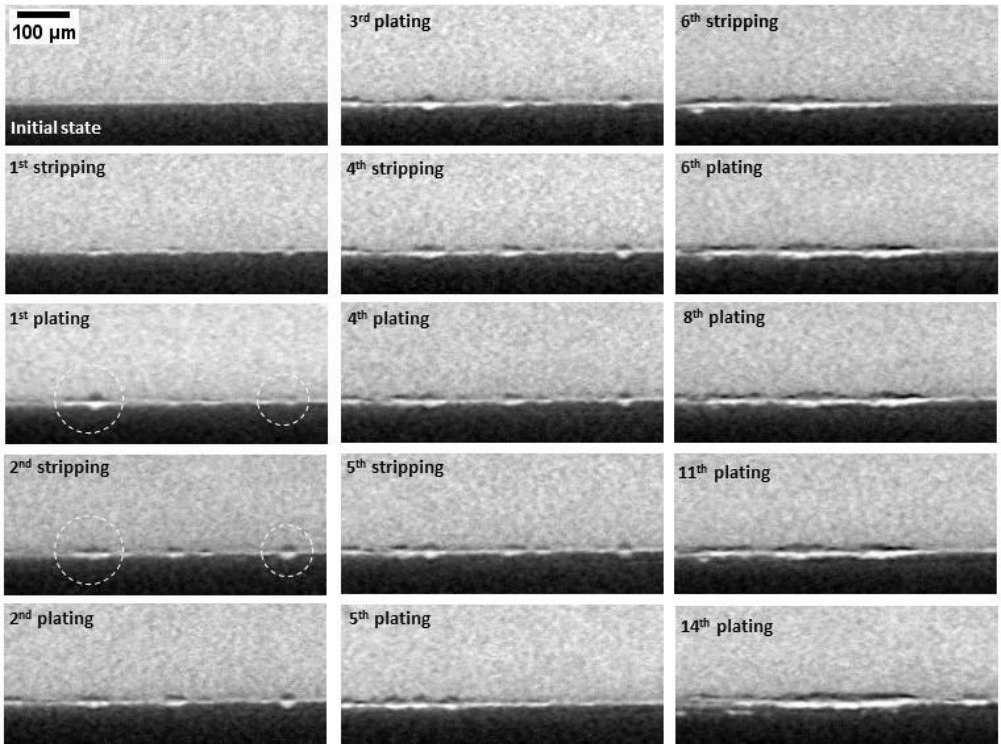


Figure A4.3 X-ray tomography 2D projections from a selected area showing the **bottom** LAGP/Li metal interface during the LAGP lithium plating and stripping process.

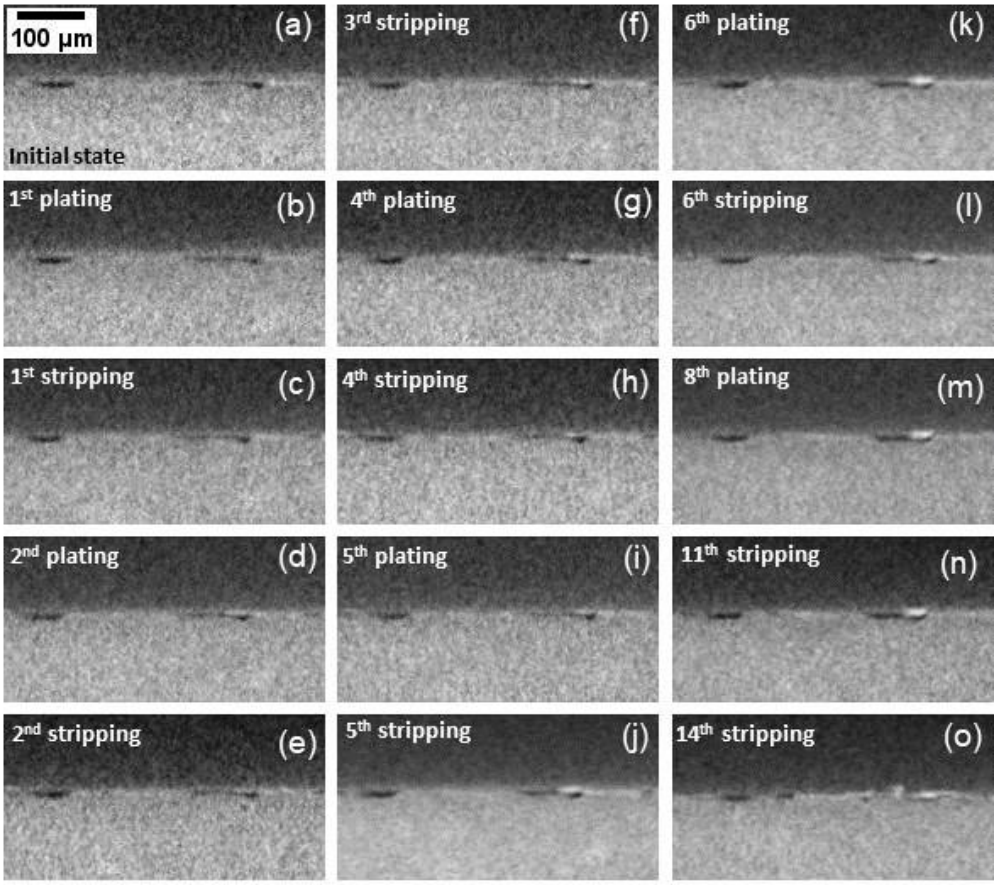


Figure A4.3 X-ray tomography 2D projections from a selected area showing the **top** LAGP/Li metal interface during the LAGP lithium plating and stripping process.

Chapter V 113
Oxide all-solid-state battery using Li metal as anode 113
5.1 Introduction 113
5.2 First cycling results of the solid-state battery 115
5.3 Parameters optimization of the solid-state battery 118
5.4 Electrochemical performances of improved SSBs 120
5.5 Degradation mechanism of the solid-state battery 122
Conclusions and perspectives 128
Appendix D 131

Chapter V

Oxide all-solid-state battery using Li metal as anode

5.1 Introduction

Currently rechargeable all-solid-state LiB attracted great attention due to high energy density, long cycle capabilities and high safety, performances which are desired to be implemented in large scale facilities as smart grids and electric vehicles[69,175,255].

So far, different types of SSB have been developed [81,93,255] by matching various cathode and anode materials to find out the perfect combination for the next generation rechargeable battery[122,153,175,256,257]. Various SEs as sulfides, halides, oxides, and solid-polymers electrolytes have been integrated in SSBs, but among them halides and sulfides are sensitive to moisture limiting their practical application and solid-polymers electrolytes present low ionic conductivity at RT[82,85]. Oxides SEs attracted great attention due to their improved moisture stability compared to sulfides and halides, good ionic conductivity, wide electrochemical window, and good chemical compatibility with cathode materials[258]. In terms of anode materials, metallic lithium remains one of the most attractive candidates due to its high theoretical specific capacity values (3860 $mAh.g^{-1}$), low gravimetric density (0.534 g cm^{-3}) and lowest redox potential (-3.040 V vs. the standard hydrogen electrode)[259]. Various cathode materials as LiFePO4 (LFP), $LiCoO_2$ (LCO) and $LiNixCoyMn_{1-x-y}O_2$ (NMC) have been successfully implemented with oxide SEs and showed comparable cycle stability and specific capacity with the conventional liquid electrolytes[258].

Despite potential advantages of solid-state batteries over conventional Li-ion technology[260], their practical applications are still impeded by new challenges as numerous interfaces presented between the electrode and solid electrolyte[123,124,131,261,262], dendrites[56,142] and cracks formation[141,149,151] which induces drawbacks in the battery. The interface between Li metal and solid electrolyte is quite unstable and prone to lead to an interphase layer causing high interfacial resistance and large polarization during battery operation[263]. An intimate contact between the cathode and the solid electrolyte represents one important challenge because the two materials present different mechanical properties resulting in improper interface contact[264,265]. Moreover, the contact between the two battery components can be lost during the cycling due to volume changes[266].

When comes to pick up the best cathode materials to be paired with the solid electrolyte, the choice of cathodes materials is made based on discharge capacity, security, power performances, cost, and environmental factor. LFP cathode, although it cannot achieve the same high energy density as Ni-rich cathode materials, attracted significant attention due to its high theoretical capacity (170 $mAh.g^{-1}$), high thermal stability, high safety, low toxicity, and high redox potential (flat potential of 3.45V vs. Li^+/Li) making in 2018 up to 34% of cathode material production in the Li-ion battery industry[267–269].

Up to now, various SSBs using diverse solid electrolytes, lithium metal and LFP as cathode material have been reported presenting a cycling life between 50 and 400 cycles. A Li/LAGP/LFP battery cycled for 30 cycles at an applied current density set between 0.068-0.085 $mA.cm^{-2}$ according to studies reported by C. Peng *et al.*[270] meanwhile Y. Meesala *et al.*[269] reported 50 cycles at an applied current density set between 0.017 and 0.255 $mA.cm^{-2}$ and A. Paolella *et al.*[258] reported 50 cycles for 0.272 $mA.cm^{-2}$ current density. Improved results have been obtained when LAGP solid electrolyte was replaced with the solid electrolyte LLZTO[258,270,271] resulting in cycling life of 100 cycles for F. Du *et al.*[272] and 400 cycles for Y. Zhong *et al.*[273] at a current density of 0.05 $mA.cm^{-2}$. However, it is worth mentioning that the positive electrode was more of a slurry composite based on the active material mixed with Li salt and binder which created more a polymer electrolyte.

Although compared to conventional Li-ion battery technology, in the previous mentioned studies the liquid electrolyte is well replaced by a solid electrolyte, but unfortunately the liquid electrolyte is still present in the electrode composite of the SSBs to ensure the mobility of ions. If in the case of conventional Li-ion batteries cells, the liquid electrolyte penetrates inside the electrodes ensuring the required ionic conductivity, in the case of solid-state batteries, the solid electrolyte creates a physical barrier between the electrodes and electrolyte and to ensure ions/electrons mobility, additional electrolyte should be added in the electrode composite. Ideally, the electrolyte added inside the electrode composite should be also a solid electrolyte to make the next generation of Li-ion batteries entirely safer. Very few studies where a full-solid state battery is prepared entirely from inorganic materials without any liquid electrolyte have been performed, mostly showing the key concept of such technology[264,274]. E. Kobayashi *et al.* realized an all-solid-state phosphate symmetrical cell using ($Li_3V_2(PO_4)_3$) (LVP) as both positive and negative electrode and LAGP as solid electrolyte obtaining a discharge capacity of 104 $mAh.g^{-1}$ at 80 °C and 42 $mAh.g^{-1}$ at 25 °C[274]. A. Aboulaich et al. realized also a $LiFePO_4$/LAGP/ $Li_3V_2(PO_4)_3$ all-solid-state battery which was able to cycle up to 30 cycles obtaining a capacity of 80 $mAh.g^{-1}$ at 120 °C[264].

During this study we will present our approach to realize an all-solid-state battery using Li metal as anode, LAGP as solid electrolyte and $LiFePO_4$ as cathode material; without using liquid electrolyte, binder, or additives in any of the battery components. The challenges faced in cycling such a key concept of an all-solid-state battery and our improvements brought in the system will be discussed. Finally, we will deeply investigate the degradation mechanism of the ASSB using multiscale characterization methods.

5.2 First cycling results of the solid-state battery

As mentioned before, our all-solid-state battery will be made of Li metal as anode, LAGP as solid electrolyte and LFP as cathode. The difficulty of this study consists in cycling an SSB completely free of liquid electrolyte, binder, or additives. Therefore, the electrode formulation considered for this work will be composed of a mixture containing active material, solid electrolyte, and carbon. The electrode formulation must present a good compromise between the active material ($LiFePO_4$) and the electronic/ionic conductive additives (solid electrolyte and carbon). A higher content of active material will ensure higher energy density in our battery, while a higher content of solid electrolyte and carbon will establish a homogeneous and efficient transfer of ions/electrons in the electrode. $LiFePO_4$ exhibits quite a low electronic conductivity, so more carbon in the electrode formulation will be required. Our electrode formulation consists of 30 % active material, 60 % solid electrolyte and 10 % carbon, adapted from previous studies[265,274].

An intimate interface between the electrode and solid electrolyte represents the greatest challenge in battery preparation. The solid electrolyte and electrode layers usually exhibit different mechanical properties and require different optimal sintering temperatures. Additionally, the different coefficient of thermal expansion of the two layers can lead cracking or delamination at the interface[275]. To overcome such challenges, we will prepare a half battery (solid electrolyte and positive electrode) in a single shot using spark plasma sintering as it promotes good interfacial contacts between the two layers. The sintering temperature of the half battery was chosen based on the optimal sintering temperature of the solid electrolyte to ensure the required ionic conductivity. **Figure A5.1a** shows a half battery with good mechanical contact between the two layers of the battery sintered in SPS at 680 °C.

Metallic lithium was added as anode by hand pressing on top of the sintered half battery and the assembled cell was inserted in the high temperature Swagelok device. A papiex layer (graphite) was inserted between Swagelok cell and positive electrode (LFP) to allow a better contact between the electrode and the piston of the cell. Also, a thin copper foil was inserted between Li metal and the other piston of the cell for an easier disassembly and proper further analysis.

To operate a solid-state battery, a minimum ionic conductivity of the solid electrolyte around 10^{-3} S.cm^{-1} is required. To reach the required minimum ionic conductivity of LAGP during cycling an external stimulus such as temperature should be applied on the cell to increase the ionic conductivity value. In LRCS, a Swagelok cell for high temperature cycling of solid-state batteries was designed by Jean-Bernard Leriche in 2013 (**Figure A5.1b**). The high temperature Swagelok cell consists of a quartz tube and two Swagelok connections. Two pistons and a spring are used to create a connection between the sample and Swagelok parts. In the end, the cell will be inserted in a tubular furnace that will control the temperature of the cell.

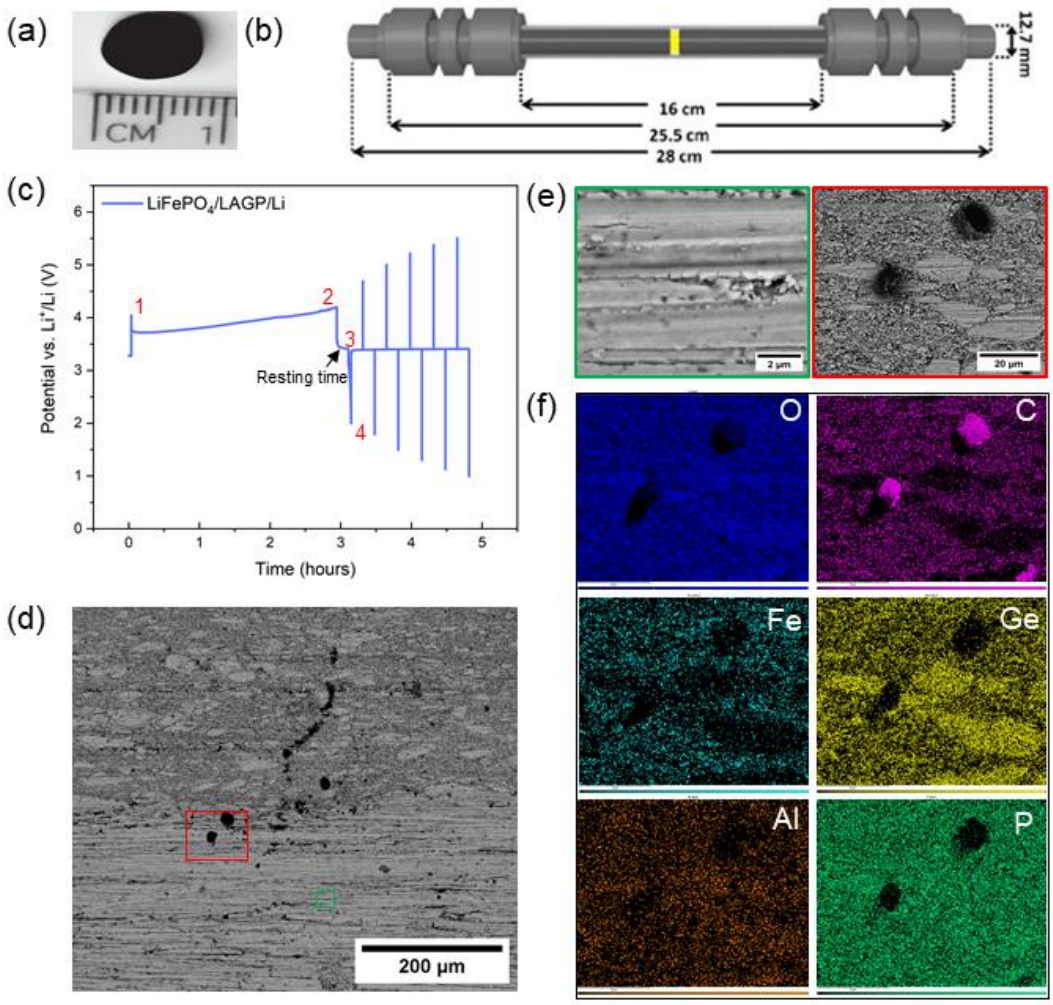


Figure 5.1 (a) Half battery (LAGP-LFP) prepared by spark plasma sintering, (b) Swagelok cell used to cycle solid-state batteries at high temperature; (c) galvanostatic cycling with potential limit of a $LiFePO_4$/LAGP/Li metal solid-state battery, (b) Postmortem SEM analysis of the cycled battery where it shows the apparition of (e) cracks and dendrites in the battery after the cycling process (f) SEM-EDX map analysis of the dendrites area indicating strong carbon signal at the LAGP-LFP interface.

Figure 5.1c displays the galvanostatic cycling with potential limit graph of the $LiFePO_4$/LAGP/Li metal battery cycled at 80 °C at a regime of C/20 in the high temperature

Swagelok cell. The battery starts with the delithiation process from LFP active materials (charge). It can be observed that the battery displays a slightly activation overpotential (zone 1) at the beginning of the delithiation process, followed by small ohmic polarization region (zone 2). A resting time of ~2 min is inserted between the (de)lithiations processes (zone 3). The lithiation process is almost inexistent as instead of the plateau only a spike is registered (zone 4). The activation overpotential (zone 1) is most likely registered due to an interface resistance between the electrode and the solid electrolyte and cathode components. The slightly ohmic polarization region (zone 2) is usually caused by the current flowing through the internal resistance of the battery cell [276].

Despite the recorded overpotential, the graph indicates that the delithiation process occurs, Li being removed from LFP structure as a reaction plateau close to the corresponding plateau of LFP vs Li^+/Li is observed (theoretical value at 3.45 V). It should be noted that a density current corresponding to C/20 was set considering both positive and negative charge. However, the reaction process was completed faster than expected, indicating that a higher density current was indeed applied which showed a large deviation from the recorded current. The high surge recorded during the lithiation process (zone 4) suggests that the lithiation process is not occurring. An even higher current density than applied one was recorded during the lithiation process as the reaction occurred in about few minutes (a current density corresponding to 20 h discharge process was defined). This indicates improper interface contact between the metallic lithium and the solid electrolyte which resulted in a locally higher current density and the presence of leakage currents [140].

Post-mortem SEM analysis of the cycled SSB displayed in the **Figure 5.1d** shows the BSE image of the $LiFePO_4$/LAGP interface. The presence of small cracks was spotted on the solid electrolyte (**Figure 5.1e, green**) indicating that mechanical stresses were induced in the battery during operation. Moreover, the presence of secondary phases was observed both on the solid electrolyte and the electrode (**Figure 5.1e, red**). According to SEM-EDX analysis performed on the secondary phases (**Figure 5.1f**), a high carbon signal was detected. A possible assumption for the detected carbon in the battery is that it diffused from the graphite layer used to line the inside of the SPS die.

Early studies on the $LiFePO_4$/LAGP/Li system showed the challenges encountered when cycling a solid-state battery without any liquid electrolyte, binder, or additives. Although the number of batteries we tried to run was high, all batteries showed a similar graph during the cycling process, indicating that further system improvements need to be made to make an SSB durable.

5.3 Parameters optimization of the solid-state battery

To obtain better cycling performances, improvements in the battery preparation and cycling conditions need to be considered. Parameters such as ionic transport limitations, interface contacts, solid electrolyte thickness, ionic percolation network inhomogeneous electrode mixture were identified as possible limitations in restricting the cycling performances.

- *Ionic transport limitations*

The limitations regrading ionic transport in the battery are dependent on the ionic conductivity of the solid electrolyte and the morphology of the composite electrode. Solid electrolyte ionic conductivity can be influenced by various parameters as temperature and pressure. An elevated temperature will induce higher ionic conductivity due to a faster move of the ions[277], while highly fabrication pressure was reported to increase considerably the ionic conductivity due to higher compacity of the pellet[278,279]. To increase the ionic conductivity of the solid electrolyte during battery operation, the temperature of cycling was increased from 80 °C to 120 °C. Moreover, a pressure of 5 t was applied on each layer of the battery before the sintering process as shown in the **Figure 5.2** to promote a higher compacity which induces a higher ionic conductivity in the solid electrolyte as less grain boundaries are present[278].

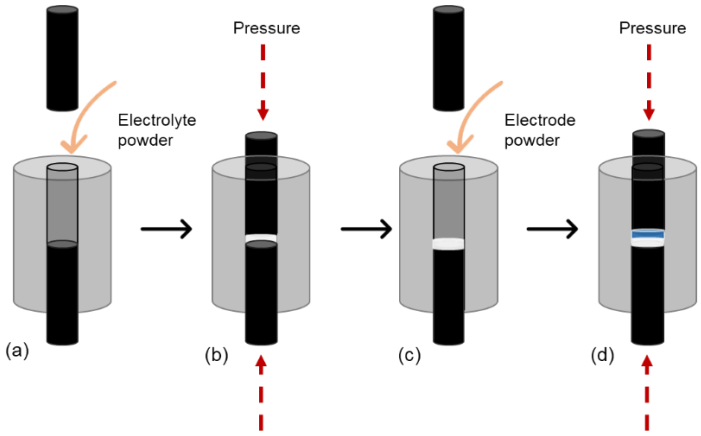


Figure 5.2 Schema showing the assembling steps of an all-solid-state battery using cold pressure in a graphite die before the SPS process.

- *Inhomogeneous electrode mixture*

The BSE-SEM images of the previous cells (**Figure 5.3a**) showed clearly that our electrode contains clusters of LAGPs which are isolated from other components. Our formulation is based on mixing the electrode components in a mortar and pestle and does not appear to be effective in terms of mixing homogeneity. Such outcome resulted from the initial (synthesis) LAGP powder being formed into agglomerates. Such effect leads to less effectiveness of the ion transport in the electrode volume as the ions migrate across longer

pathways within the volume[280]. To overcome this issue, a new method of preparing the electrode formulation where a straighter pathway for the ion migration was required.

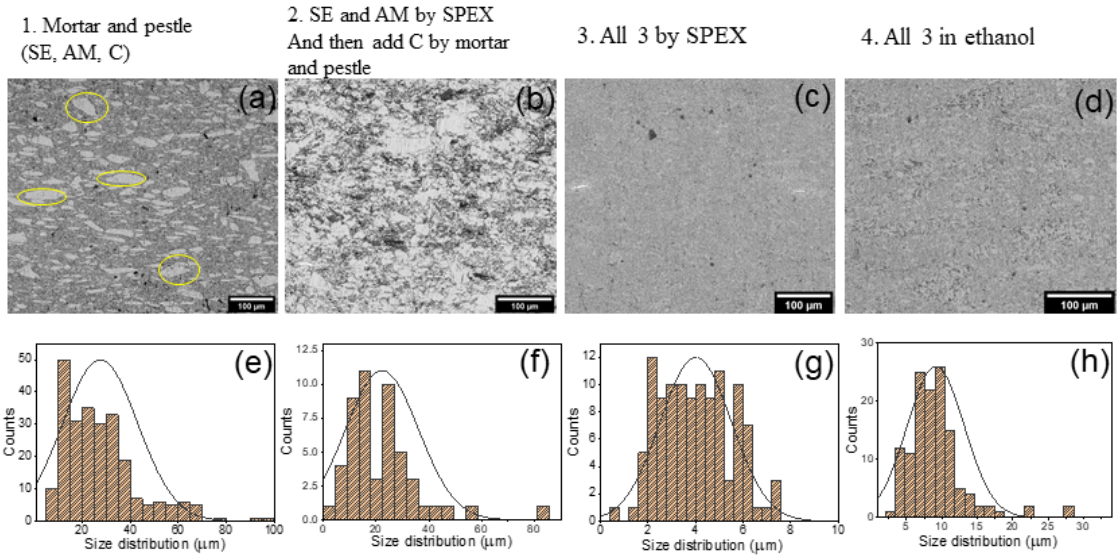


Figure 5.3 Backscattering electrons images of electrode mixture (LAGP, LFP and carbon) done by (a) mortar and pestle (b) SE and active materials by SPEX and then carbon added and mixed by carbon and pestle (c) all 3 electrode components by SPEX and (d) all mixed in ethanol; (e-h) Size distribution of LAGP clusters presented in the electrode formulation.

Three new methods for preparing the electrode formulation were investigated. In the first, the solid electrolyte and the active material were mixed using a high energy ball mill mixer (SPEX) for 30 minutes, then carbon was incorporated with the rest of components using of a mortar and pestle. In the second method, all the electrode components were mixed using SPEX for 30 minutes and in the last one all the electrode parts were mixed overnight in ethanol using a stirring magnet. **Figure 5.3 (b-d)** present cross-section BSE-SEM images of SPS pellets sintered at 680 °C where the electrode formulation mixture was prepared using the previously presented methods. In the case of the first method (**Figure 5.3b**) we can still observe the presence of large agglomerates areas with an evolution of the particle size distribution from few micrometers up to ~80 µm (**Figure 5.3f**), displaying almost negligible changes compared to our first study. In the case of electrode components mixed altogether by SPEX, the BSE-SEM image (**Figure 5.3c**) displays a homogeneous mixture with a particle size distribution of the agglomerates up to maximum ~10 µm (**Figure 5.3g)** showing significant improvements compared to our first method. **Figure 5.3d** shows the BSE-SEM image of electrode parts in ethanol in which the presence of smaller agglomerates areas is observed, but still larger compared to mixture using SPEX reaching a particle size distribution up to ~30 µm (**Figure 5.3h)**. For further studies, we decided to mix the electrode components altogether using SPEX for 30 minutes as this method showed the most homogeneous distribution of LAGP where straighter pathways for the ion migration could be created.

- *Interface contacts, solid electrolyte thickness and current density limitations*

As all the battery components are solid there are also many interfaces created due to solid-solid contact. There are interfaces generated inside the electrode, cathode-solid electrolyte interface and anode-solid electrolyte interface. The new method of preparing the electrode formulation (SPEX formulation) together with the extra pressure added during electrode preparation should also induce fewer interfaces inside the cathode due to higher compacity. The pressure applied during the assembling step will promote an intimate interface between the cathode and LAGP. Additionally, Li metal has been exfoliated to promote a cleaner interface and has been laminated prior assembly step to promote an intimate contact between anode and LAGP layer.

According to simulation, oxide solid-state batteries where the solid electrolyte thickness is thicker than 0.5 mm will result in low practical gravimetric energy density as solid electrolyte will account for most of the weight cell. Also, to minimize the resistance of the cell, the SE thickness was reduced considerably from ~1 mm to a value of ~ 200-400 µm.

The cycled cells in the first studies displayed large overpotential. This phenomenon occurred most likely due to inhomogeneities presented at the interfaces which lead to higher current density values in the cell compared to the applied values. To minimize this phenomenon, further batteries were cycled at a c-rate of C/40 compared to C/20 in the initial study.

5.4 Electrochemical performances of improved SSBs

All the previously mentioned improvements regarding battery preparation and cycling conditions have been considered for subsequent cycling batteries. **Figure 5.4a,b** displays the SEM images of the half battery (LFP/LAGP) prepared by SPS at 680 °C before the cycling process. It can be observed that the electrode layer presents a homogeneous mixture and a good mechanical interface with the solid electrolyte. Small carbon impurities are present (left, upper part) most likely coming from the graphite paper covering the SPS die during the sintering process.

Electrochemical impedance spectroscopy analysis was performed before and after the cycling process. **Figure 5.4c** displays the Nyquist diagram of the LFP/LAGP/Li metal battery (red) measured at 100 °C before the cycling process, where a semicircle followed by a linear tail can be observed. The half semicircle corresponds to ionic conductivity of the solid electrolyte and to any interfaces generated inside the battery.

The galvanostatic cycling plot with potential limit of the enhanced LiFePO4/LAGP/Li metal battery cycled (at 100 °C at C/40 regime) is shown in **Figure 5.4d**. It can be observed

that the electrochemical reaction starts with a flat plateau corresponding to the delithiation process of $LiFePO_4$, but towards high potential values, the cell displays a slightly overpotential. During the first discharge cycle, it can be observed that the discharge capacity only reaches ~60 % of the charge capacity because not all the metallic lithium is reincorporated into the $LiFePO_4$ structure (normally the extra lithium in the anode is not necessary as during the cycling process, the lithium removed from the $LiFePO_4$ structure will be reincorporated).

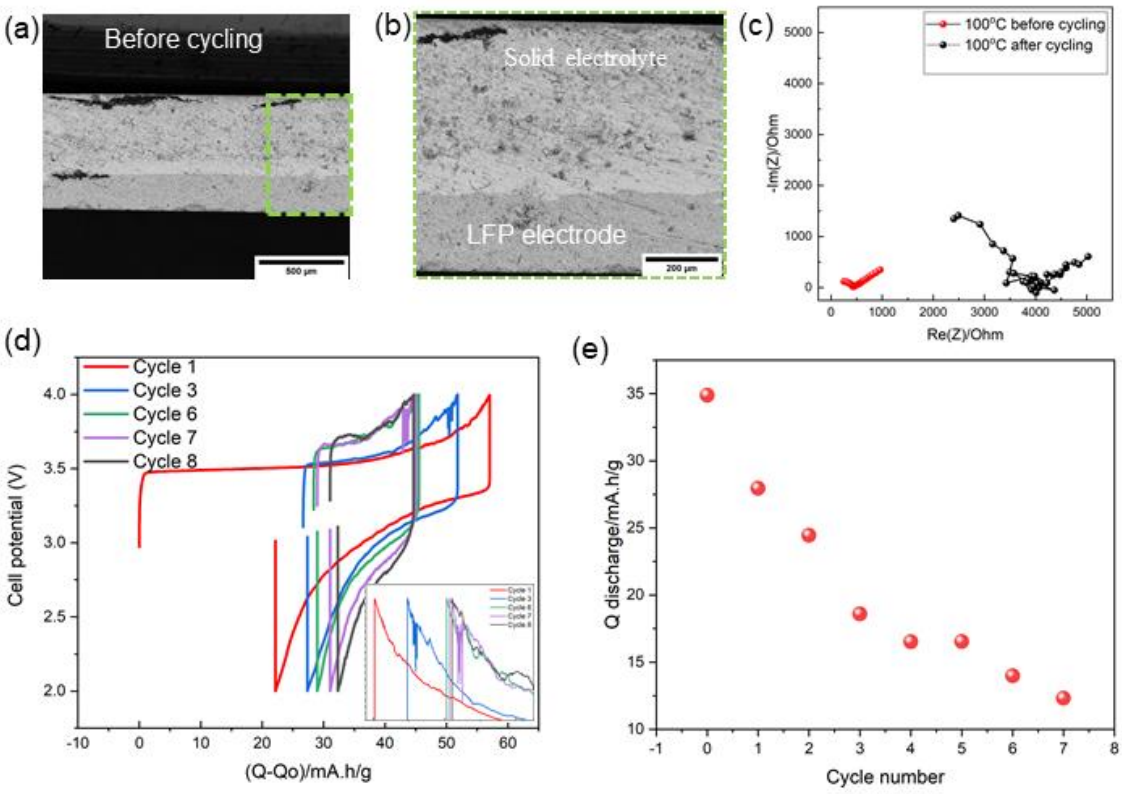


Figure 5.4 (a, b) Backscattering electron SEM images of half battery prepared by SPS at 680 °C before cycling (c) electrochemical impedance spectroscopy of the system LFP/LAGP/Li metal before and after the cycling process (d) galvanostatic cycling with potential limit of a $LiFePO_4$/LAGP/Li metal battery prepared with optimized conditions and (e) Capacity discharge graph in function of the number of cycles of the LFP/LAGP/Li metal battery.

In the third cycle, the presence of high voltage fluctuations began to appear and became more pronounced as the number of cycles increased. The cell started to show a slightly surge, which induced stronger variations to appear as the reaction progressed. The appearance of fluctuations usually indicated the formation of voids inside the cell, which in our case we could indicate the apparition of dendrites and cracks inside the battery[141].

The variations were still present only during the charging process, while discharging only an overvoltage was noticed. In terms of battery performances, as the cycling reaction progresses over time, the capacity of the cell (charging and discharging) constantly decreases (**Figure 5.4e**). It should be mentioned that the performances of this all-solid-

state battery (charge capacity of 56 mAh.g^{-1} in the first cycle) is a far cry from similar cells where the electrode formulation was prepared using binder and liquid electrolyte, with the cells being able to cycle for over 50 cycles at larger capacities values[269].

5.5 Degradation mechanism of the solid-state battery

To understand the degradation mechanism of the oxide solid-state battery, we decided to conclude a complex post-mortem analysis of the cell using various characterization methods such as SEM, STEM-EDX and 4D-STEM ACOM. To obtain information about the morphology evolution of the battery components after the cycling process, post-mortem SEM analysis was performed. To prevent any degradation of the cell from air exposure, the cycled cell was opened in a glovebox and carried to SEM antechamber using a transfer holder.

During the cell opening, the presence of large cracks which penetrated entirely the solid electrolyte and the positive electrode were spotted. **Figures 5.5a,e** display secondary electron and backscattering electrons images of the Li metal-LAGP interface after the cycling process. The presence of Li metal dendrites can be observed in the **Figures 5.5b,f**, which grew from the anode towards the solid electrolyte layer leading to crack formation**.** Due to the high rigid properties of LAGP, the dendrites growth resulted in enormous number of cracks. **Figures 5.5c,d,g,h** presents a part of the solid electrolyte which was fractured due to a large cracks formation in which the presence of small microcracks can be observed. It was interesting to discover that the microcracks are distributed in horizontal and vertical way, the last ones being larger compared to the first ones.

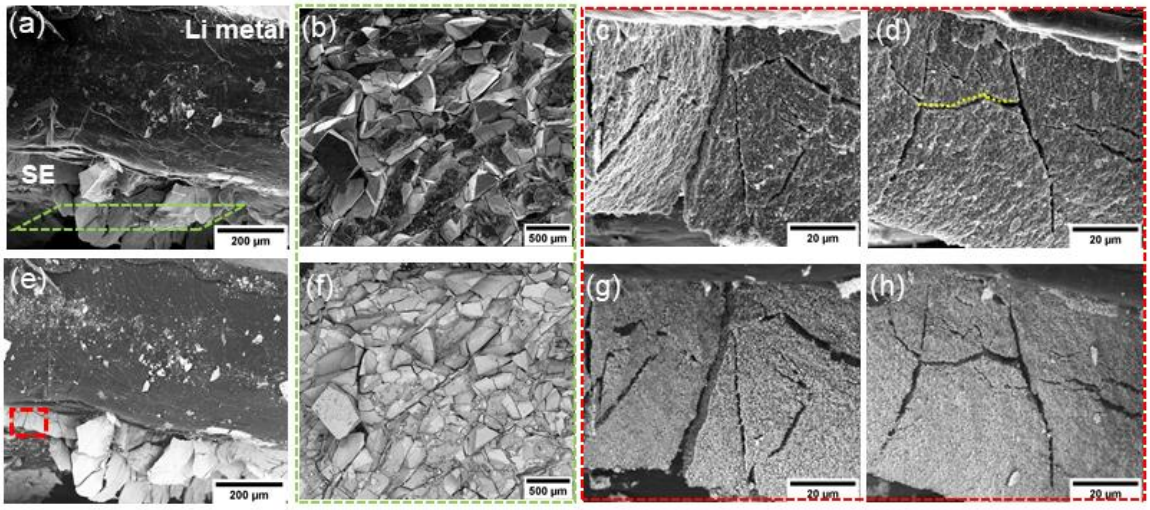


Figure 5.5 Post-mortem SEM (a-d) Secondary electron images and (e-h) Backscattering electrons images of LFP/LAGP/Li cycled battery with the focus on the solid electrolyte/Li metal interface.

To investigate deeper the mechanism of Li metal dendrites formation and growth inside the solid electrolyte, various places with the presence of dendrites were analyzed. **Figures**

5.6a displays the BSE-SEM image of the solid electrolyte after cycling where two types of contrast can be observed, *i.e*. a lighter one corresponding to LAGP and the darker one corresponding mainly to LAGP strongly impacted by the lithium metal dendrites.

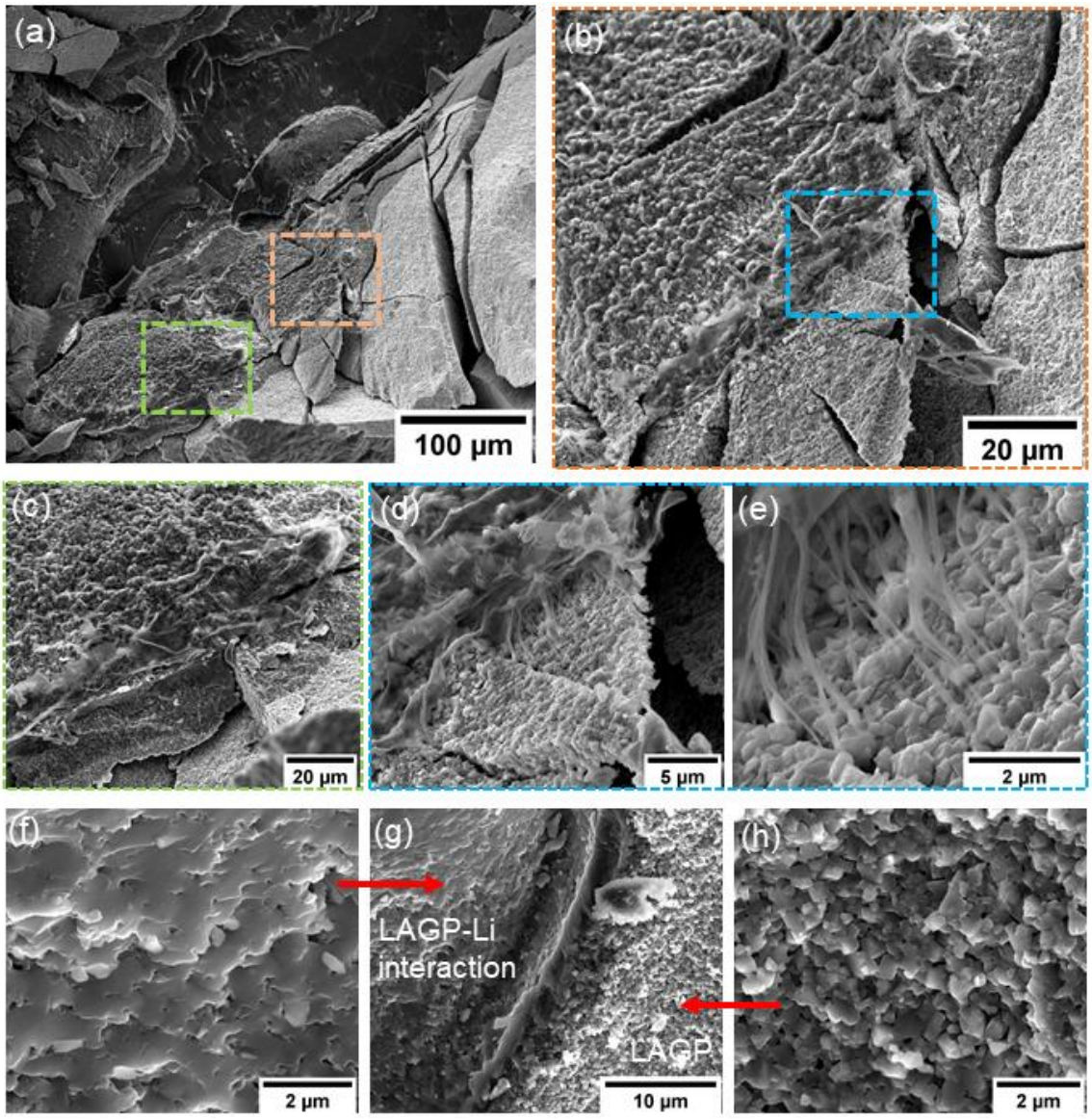


Figure 5.6 Post-mortem SEM secondary electron images of the solid electrolyte from a cycled LFP/LAGP/Li battery showing (a) cracks and dendrites after cycling process (b-c) dendrites morphology in LAGP (d-e) ”medusa-arms” attaching of dendrites inside the solid electrolyte and (f-h) LAGP morphology after and before interaction with Li dendrites.

The presence of the tips of two lithium dendrites can be as well visualized (highlighted with the green and orange square). Following the tip of the dendrite (**Figure 5.5b-e**) it can be noticed that the lithium metal spreads and covers like a sheet the areas where an interaction with LAGP occurred. The infiltration of the lithium metal dendrites inside the solid electrolyte layer occurs via “medusa-arms” of the lithium dendrites (**Figure 5.5e**). Once infiltrated inside the LAGP layer, the morphology of the solid electrolyte is impacted (**Figure 5.5g**), LAGP particles changing from their tetragonal shape in the initial

state (**Figure 5.5h**) to agglomerates with irregular shape that present also a slightly lamellar effect (**Figure 5.5f**).

The interface between the solid electrolyte and positive electrode is displayed in the **Figure5.7**. Although the entirely cell was fractured due to the presence of large cracks, it can be observed that no microcracks are spotted inside the positive electrode or close to the interface with the solid electrolyte. Such an observation indicates that the cracks propagate from the anode towards to cathode and are the result of lithium metal dendrites formation and no volume changes occurring in the positive electrode.

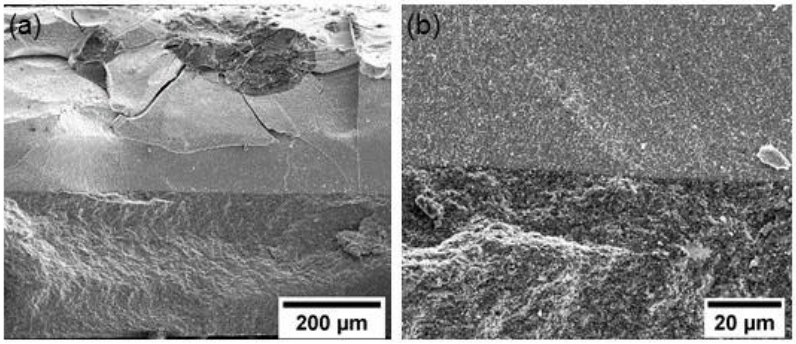


Figure 5.7 Post-mortem SEM backscattering electron images of the solid electrolyte-positive electrode interface after the cycling process.

For a deeper understanding of the degradation mechanism at local scale, two FIB lamellas were extracted from the LAFP-LFP interface (**Figure 5.8a**) (See details in **Appendix D**). The analysis focused mostly on the interface between the solid electrolyte and positive electrode as no degradations at the micrometer scale were spotted during the SEM analysis. The first FIB lamella was extracted with the LAGP/LFP interface placed horizontally (**Figure 5.8b**) allowing us a larger area of investigation at the interface. The second FIB lamella was extracted with the interface placed vertically (**Figure 5.8c)** providing a wider area of analysis from the LAGP/LFP interface to electrode composite and solid electrolyte.

Both FIB lamellas were analyzed by Scanning Transmission Electron Microscopy (STEM). **Figure 5.9** displays the post-mortem STEM-EDX map analysis of the LFP/LAGP interface and the positive electrode after the cycling process. STEM-EDX analysis focused on the near-neighbor positive electrode with the LAGP interface (**Figures 5.9a,c**) displays a well-mixed composite electrode where the solid electrolyte connects to the active material providing the required ionic conductivity. The overall analysis suggests that the ratio between active ingredient to carbon is slightly unbalanced as a higher volume of carbon is observed compared to LFP. Ideally, the balance during the electrode formulation should be

inclined towards a higher amount of active material in the electrode to deliver a higher energy density.

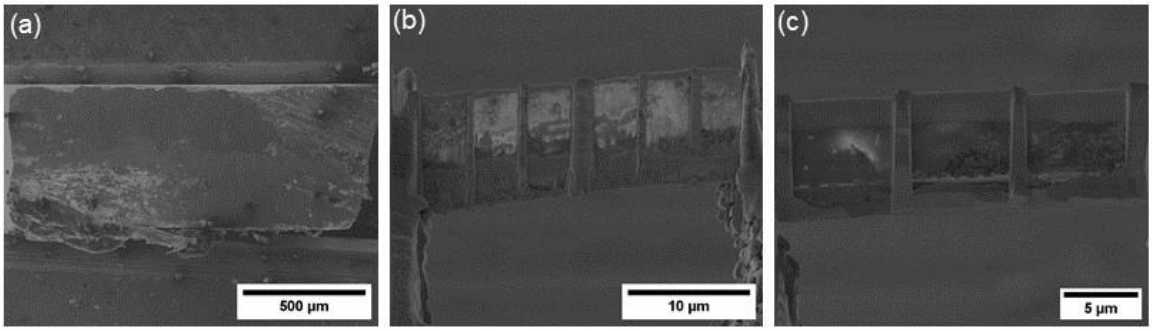


Figure 5.8 (a) Post-mortem SEM secondary electron image of LAGP/LFP interface after cycling process from where (b-c) FIB lamellas with focus on the LAGP/LFP interface were extracted.

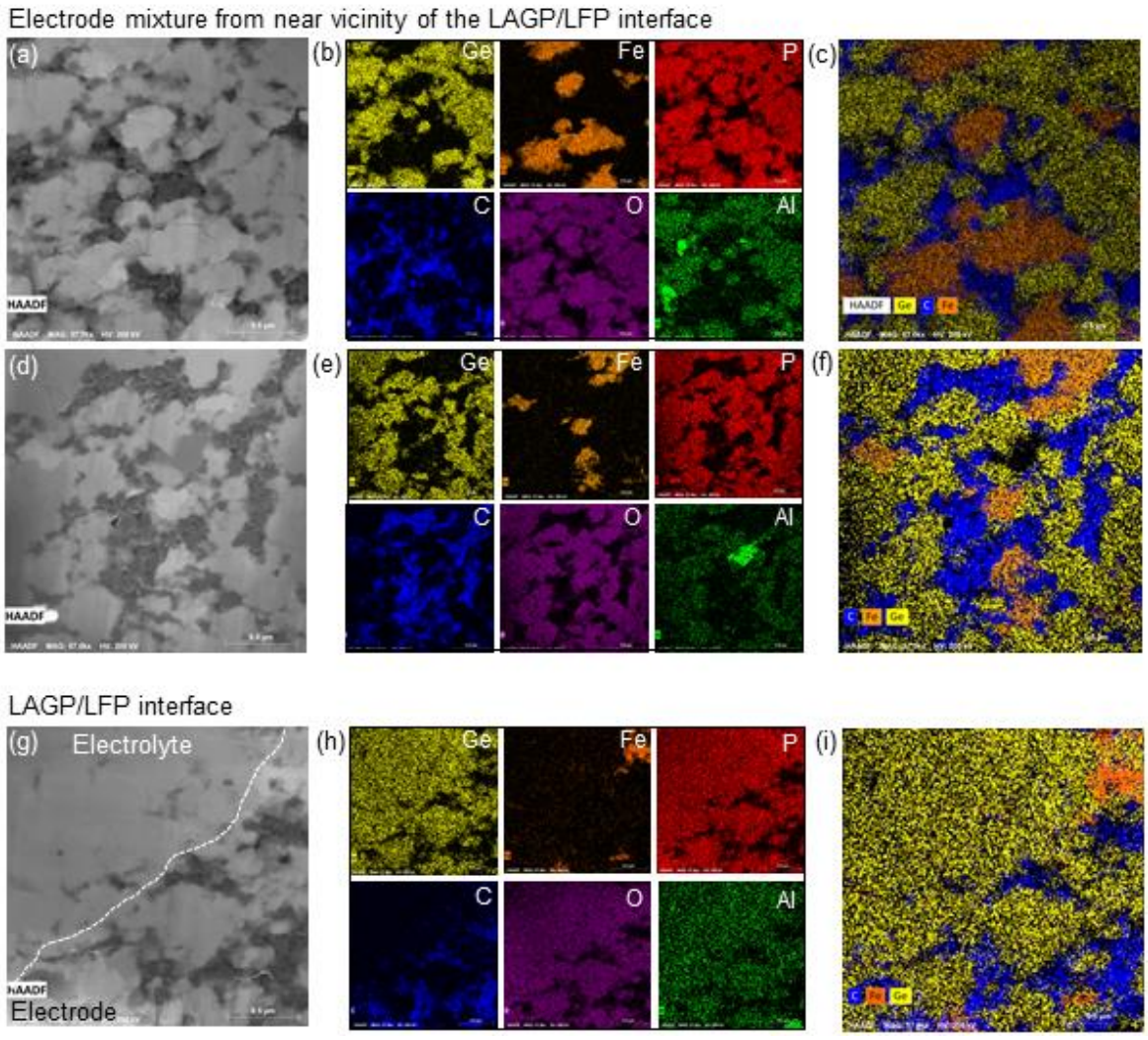


Figure 5.9 Post-mortem STEM analysis of a FIB lamella extracted from (a,d) the near vicinity of the positive electrode/solid electrolyte interface, (g) LAGP/LFP interface after the cycling process and (b,e,h) their associated STEM-EDX map analysis. (c,f,i) STEM-EDX map analysis showing the contribution of the solid electrolyte (yellow), electrode (orange) and carbon (bleu).

STEM-EDX analysis indicated the presence of Al-rich areas that were spotted in various locations of the electrode composite. An assumption for the Al-rich areas is that were formed during the sintering process as a partially decomposition process of LAGP due to the high temperature and pressure conditions.

Figures 5.9e displays the STEM-EDX map analysis of the solid electrolyte (left)-composite electrode (right) interface. The analysis revealed the presence of small amounts of carbon and iron from the electrode composite layer to LAGP layer. The diffusion of various elements between the electrode and solid electrolyte layer was already reported to occur because of an electrochemical reaction. A. Brazier *et al.*[281] reported the migration of Si and V into the SnO electrode from the LVSO electrolyte during the cycling and M. Fawey *et al*.[282] reported the migration of fluoride into the cathode composite forming copper (II) fluoride (fluoride battery).

Most likely, the diffusion of iron and carbon from the positive electrode to solid electrolyte occurred also because of the cycling process, but for a better clarification the analysis of a pristine FIB lamella would have been required (to eliminate the diffusion as a result of spark plasma sintering process). **Figure5.10** displays the STEM-EDX map analysis of a FIB lamella containing the solid electrolyte extracted from the near vicinity interface with the composite electrode. Like the interface map analysis, the presence of iron was detected inside the LAGP layer. Iron migrated from the composite electrode and gathered at the grain boundaries inside the LAGP layer which may have impacted the battery cycling performances as they can induce SE fracture[283,284].

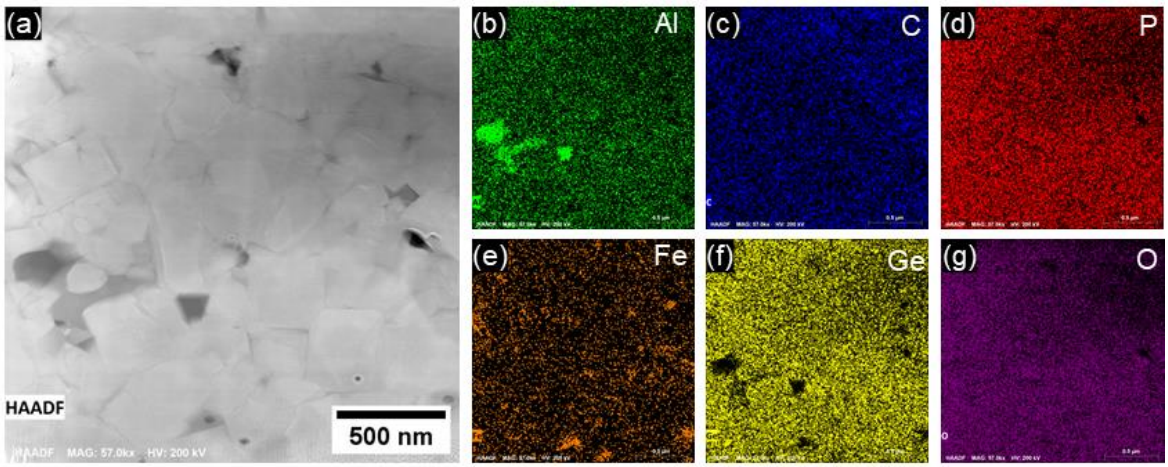


Figure 5.10 (a) Post-mortem STEM-EDX map analysis of a solid electrolyte FIB lamella after the cycling process extracted from the near vicinity with the LFP electrode mixture showing (b) Al (c) carbon (d) phosphorus (e) iron (f) germanium and (g) oxygen map analysis.

Post-mortem 4D-STEM ACOM analysis was carried out on the cycled lamellas to investigate the crystal structure changes induced at the LAGP-LFP interface after the

electrochemical reaction (**Figure 5.11**). 4D-STEM method uses nano-probe scanning approach to acquire electron diffraction patterns over an analyzed area. The electron beam is usually focused to a small spot of ~2 nm diameter and used to scan and record using an external camera the electron diffraction pattern on each pixel position (the size of the pixels is predefined before scan). The collection of acquired electron diffraction patterns are further indexed automatically using a template matching which are banks of simulated diffraction pattern for the possible phases containing all crystals orientations. 4D-STEM ACOM analysis is usually used along with precession electron beam technique for dynamic effects reduction.

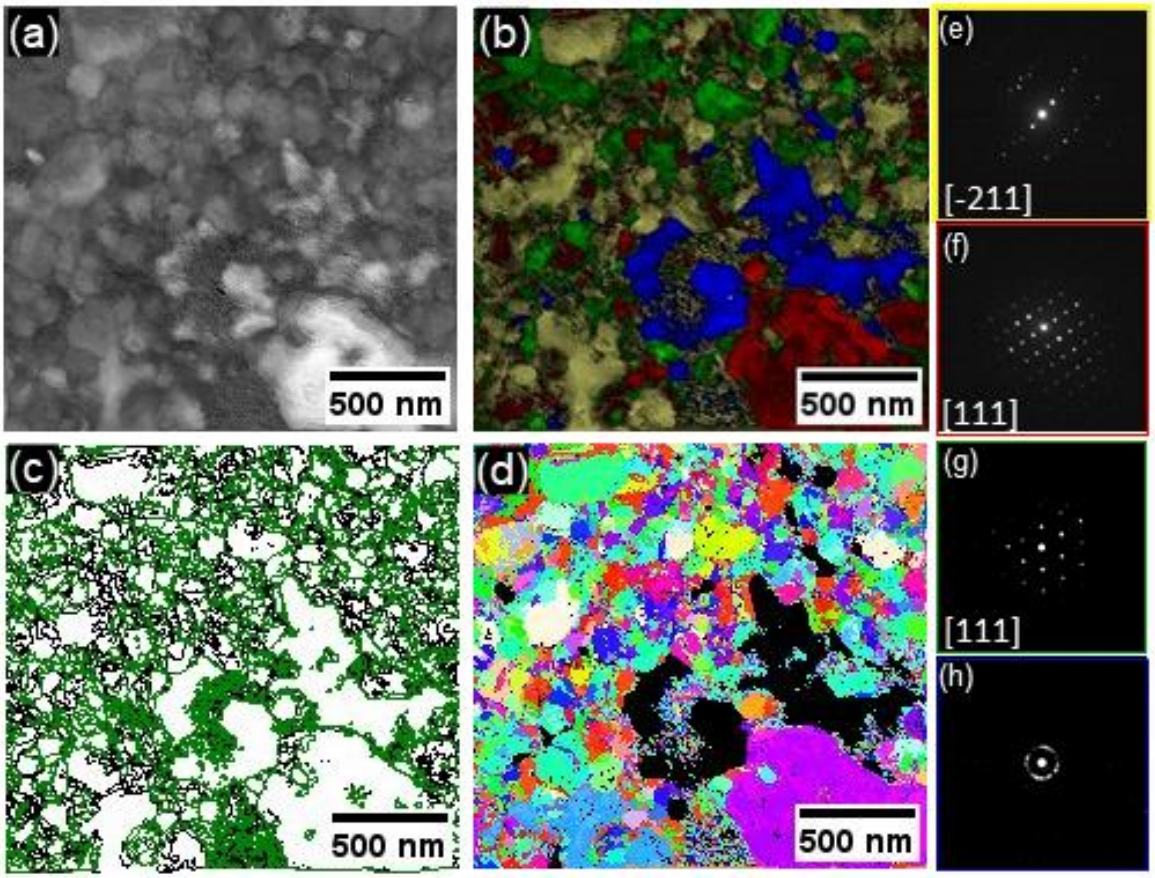


Figure 5.11 (a) Post-mortem ASTAR analysis on LAGP/LFP interphase analyzed on a FIB lamella after cycling where it shows: a) index map used for the analysis b) combination map between phase and phase reliability maps; c) grain boundaries map, d) orientation on the Z axis and representative electron diffraction patterns of e) LAGP, f) FP, i) LFP.

Figure 5.11a displays the index map of solid electrolyte (LAGP) and electrode composite (LAGP, LFP-FP and carbon) after the electrochemical reaction. The index quality map is related to reliability. The presence of black areas indicated an unsafe indexing, while white area indicates a unique solution. A value of 15 (out of 100) for the orientation reliability will be enough to assert a good matching between the acquired electron diffraction pattern and generated orientations[285]. It is worth mentioning that the

template matching ACOM software will always end up with a solution. To eliminate the unsafe matching, a minimum value of 18 was selected for our index map (21 points disabled) to eliminate the points with low reliability.

Figure 5.11b displays a combination map between phase reliability map and the reconstructed map phase. In the reconstructed phase map the LAGP is displayed in yellow (45.2%), $LiFePO_4$ is shown in red (21.8%), $FePO_4$ is presented with green (20.6%) and carbon is displayed in blue (12.3%). The inactive point due to a minimum value of 18 in the index map, are displayed with black and represent 0.1% of the reconstructed phase map. The phase map is reconstructed based on the best matching solution (highest reliability) between acquired electron diffraction pattern and all possible generated orientations from all the phases inputted in the matching template software. An example of an electron diffraction of LAGP is displayed in the **Figure 5.11e**, of $LiFePO_4$ in the **Figure 5.11f**, of $FePO_4$ in the **Figure 5.11g** and of amorphous carbon in the **Figure5.11h**. The reconstructed phase map displays many $LiFePO_4$ and $FePO_4$ particles which are fully liathiated or deliathiated. This observation confirms that at the nanoscale level, the lithium deintercalation/intercalation mechanism follows the domino-cascade model.

The grain boundary map phase (**Figure 5.11c**) displays in black grain boundaries between particles with the same crystal structure and with green grain boundaries between different crystal structures particles. It can be observed that the grain boundary map is predominant green indicating that lithium may require a higher energy for migration from grain to grain. The crystal orientation map along Z direction is presented in the **Figure 5.11d** (color code in the **Appendix D**). It can be observed the presence of a $LiFePO_4$ cluster particles (right down corner) where all the particles display the same orientation, among [111] direction. LAGP and $FePO_4$ particles were not observed to display a preferred orientation within the analyzed area.

Conclusions and perspectives

A solid-state battery using LAGP as solid electrolyte and an all-solid electrode formulation containing 30% of $LiFePO_4$ as active material, 60% of LAGP and 10% of black carbon was prepared by spark plasma sintering. No liquid electrolyte, binder or additives were added during the battery preparation making the cycling conditions quite challenging. Additional metallic lithium was added on the LAGP surface of the half-sintered battery as anode. A laboratory-developed high-temperature cycling device was used to cycle at high-temperature the solid-state batteries. The cycled batteries exhibited a high overvoltage most likely due to various interface resistances between the solid electrolyte and the electrode composite (or within it).

Various improvements in the solid-state battery preparation and cycling conditions have been considered to get better cycling performances. Improving ionic conductivity by cycling the battery at a higher temperature, promoting better interface contacts by applying additional pressure during assembly steps, generating a more even electrode composition distributions, and cycling the battery at a lower C rate gave better cycling results. Unfortunately, despite of the improvements, the $LiFePO_4$/LAGP/Li metal battery delivered a low charge capacity of 56 $mAh.g^{-1}$ in the first cycle and the battery performance decreased even more after 7 cycles. The GCPL graph showed the presence of large fluctuations during the delithiation process of $LiFePO_4$ indicating the formation of voids which in our case could indicate the appearance of dendrites and cracks inside the battery.

Post-mortem analysis indicated the presence of large cracks that fully penetrated the battery. Although, the completely battery was mechanical damaged by the presence of cracks, the cell did not present a short-circuit. SEM analysis indicated the presence of lithium dendrites that infiltrate inside the solid electrolyte layer growing "jellyfish arms". Once infiltrated inside the LAGP, the morphology of the solid electrolyte particles changes completely from a tetragonal shape to LAGP stratified clusters entirely covered with metallic lithium. Although large cracks penetrated the cell producing mechanical damage, the presence of microcracks (vertically and horizontally) were observed only near the interface between the metallic lithium and solid electrolyte. No cracks were observed positive electrode-solid electrolyte interface suggesting their formation is due to lithium dendrites growth and not changes in the volumes of the positive electrode.

STEM-EDX map analysis performed on FIB lamellas extracted from the LAGP-composite electrode interface revealed the diffusion of iron and carbon from the positive layer inside the solid electrolyte after the electrochemical reaction. 4D-STEM ACOM analysis allowed us to obtain a phase map by comparing the acquired electron diffraction patterns with the generated orientation models of the expected phases. The reconstructed phase map revealed $LiFePO_4$ and $FePO_4$ particles which are fully bound or deliathiated, confirming that at the nanoscale level the lithium deintercalation/intercalation mechanism follows the domino-cascade model.

As other perspectives, designing a cell that allows controlling the pressure during cycling will be ideal, as pressure is one of the detrimental parameters for a successful operating solid-state battery. Controlling the amount of lithium at the anode could be another important aspect because lithium is highly reactive, and a continuous interphase is generated between LAGP and Li metal.

Main takeaways:

We realized, tested and improved the performances of an oxide solid-state battery with the following configuration: LFP/LAGP/Li metal.

The degradation mechanism of the s solid-state battery investigated using SEM analysis revealed the presence of dendrites that grew using “medusa-arms” tips with the presence of large cracks on the entirely battery and microcracks within the solid electrolyte. Lithium meal dendrites were observed to induce LAGP morphological changes creating rather larger clusters with a slightly laminated effect covered with lithium metal. STEM-EDX analysis revealed the diffusion of iron and carbon inside the solid electrolyte which could further induce fractures in the battery. 4D-STEM ACOM analysis displayed $LiFePO_4$ and $FePO_4$ particles that were fully liathiated or deliathiated confirming the domino-cascade model for the lithium intercalation/deintercalation mechanism.

Keywords: All-solid-state battery; Lithium dendrites; Cracks; Domino-cascade model; Metal migration; Carbon migration

Appendix D

FIB lamella preparation

Fib lamellas were prepared using a Focused Ion Beam (FIB) FEI STRATA DB 235 microscope. A local platinum deposition assisted by the ion beam was performed to protect the Fib lamella. The initial milling to obtain a cross sectional FIB lamella was done using a current of 7 nA. A final thinning down to 100 nm in the FIB lamella for the electron beam transparency was realized with a current of 100 pA.

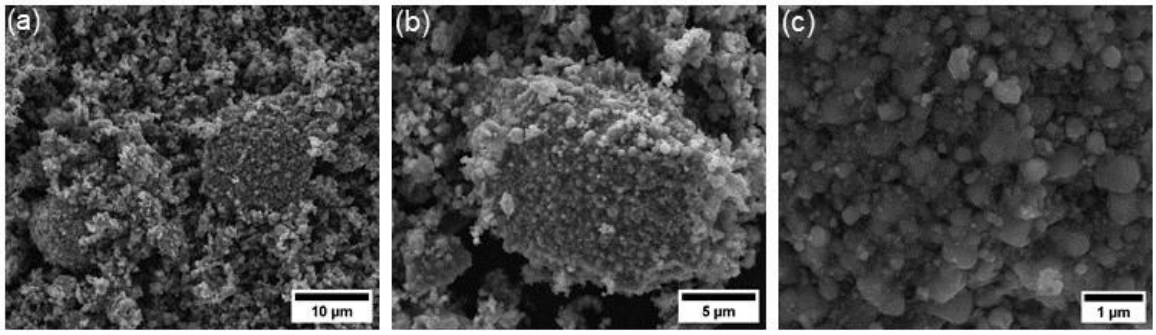


Figure A5.1 SEM analysis of the $LiFePO_4$ particles before the sintering process.

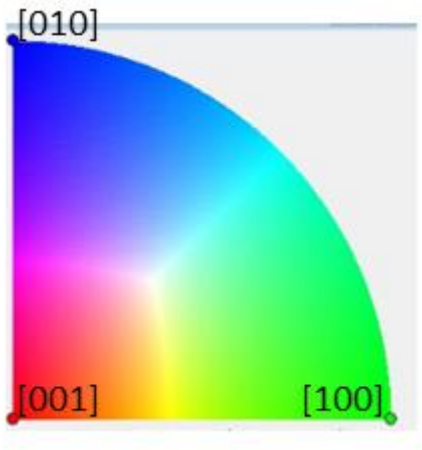


Figure A5.2 colour code indicating the crystal orientation of the analyzed area presented in the Figure 5.1.

Chapter VI 133
In-situ electrochemical TEM experiments 133
6.1 Introduction 133
6.2 All solid-state Li-ion battery system 135
6.3 Ex-situ cycling of all solid-state battery 137
6.4 Solid-state battery preparation for in-situ electrochemical TEM 140
6.5 Study of the pristine FIB lamellas 143
6.6 In-situ electrochemical TEM cycling 146
6.7 Post-mortem studies of the FIB lamellas 149
Conclusions and perspectives 153

Chapter VI

In-situ electrochemical TEM experiments

6.1 Introduction

ASSBs could represent the future promising battery technology as they provide enhanced safety and higher energy density[286–288]. Great progress has been reached until now in this technology by the synthesis of highly conductor solid electrolytes[111,289,290] and very promising cycling solid-state batteries with more than 500 cycles and 80% capacity retention[113].

Despite the advances, there are still challenges in many aspects, as SE/electrode interface[123,124,291], morphological transformations during the cycling process [56,148,292], dendrite growth and crack propagation[135,221,293], which triggers the failure mechanism of the cells. Such challenging issues need to be fully understood and resolved to make SSBs a reliable technology for practical applications.

Different ex-situ studies have been used to understand various steps in the failure mechanism of the solid-state batteries as changes in morphology (cracks, voids, dendrites) or changes in crystal structure[149]. Unfortunately, in the ex-situ studies the battery is settled outside of the electrochemical system in a relaxation state (usually the cell needs to be disassembled) and for a deeper comprehension of the degradation mechanism, a real-time monitoring of the dynamic process during cycling is required (*in-situ*/operando measurements)[292,294,295]. The various limitations of SSBs are present in different parts of the battery at different scales and to follow and understand the dynamic evolutions at the solid electrolyte/electrode interface, it is crucial to find the right observation tool, which offers the possibility of analyzing the structural changes occurring during cycling in the cell at the nanoscale. *In-situ* TEM (Transmission Electron Microscopy) represents the perfect tool for understanding the failure mechanism in ASSB as it allows us to visualize the interfaces with high spatial resolution. It will enable us to follow the structural changes using complementary techniques such as electron diffraction (SAED, 4DSTEM) and EELS spectroscopy as well as EDX mapping for the chemical changes[296–298].

In recent years, only a few in-situ TEM studies have been performed to study ASSB, mainly due to technical difficulties in obtaining a battery capable of providing good cycling conditions and meeting the requirements of TEM observation as the sample must be less than a few hundred nanometers to ensure beam transparency. Two different approaches were used for performing *in-situ* TEM experiments on SSBs having different technical looks. A first experiment involves the use of Li-metal deposited on an adjustable metal tip, which induces polarization when put in contact with the solid electrolyte and then monitoring of the (electro)chemical evolution is made using different TEM techniques. M. McDowell *et al.*[148] investigated the nanoscale reaction process of LAGP particles and Li metal during bias using *in-situ* TEM and observed in real time a clear decrease in lithium particle volume and the expansion of LAGP particles indicating lithium diffusion into the LAGP. Moreover, a change of contrast in the reacted LAGP particles was remarked, SAED analysis performed before and after bias application indicated an amorphization of the LAGP particles. X. Liu *et al*. [299] combined *in-situ* TEM and EELS and observed that, for LLZO solid electrolyte, Li diffusion initiate at the grain boundaries (GB) during cycling and not at the interface, resulting in the segregation of isolated intergranular lithium. Li nucleation at the GB was explained by the fact that when current leakage occurs some Li ions will receive electrons at the grain boundaries instead from the cathode (GB will act as an electron source as they present higher electron conductivity, about 1-3 eV reduced bandgap at the GB compared to grains) and will result in isolated Li segregation at the GB.

The second configuration involves the use of a thin FIB lamella connected on an e-chip, which presents a transparent window to the electron beam and allows bias application. This approach is much difficult compared to the previous one. The challenge of this method consists of realizing a micro-battery presenting a length that meet the requirements of contact dimensions of the micro-chip (several micrometers) and concurrently a thickness of 200 nm to ensure beam transparency. First cross section observation of all-solid state nanobattery was done by A. Brazier *et al.* [281] in 2008 at LRCS laboratory where by comparing a pristine and a cycle nanobattery obtained from micro-batteries they observed Si and V chemical migration from the LVSO electrolyte into the SnO electrode. In 2011 Y. S. Meng research group [300] prepared a FIB nanoscale solid-state battery on the same configuration as the previous one (LVSO as solid electrolyte, LCO as cathode and SnO as anode) for *in-situ* TEM experiments. A current of 100 nA was applied on the FIB lamella (10 µm × 30 µm × 100 nm) and during the bias application the battery exploded inside the TEM column due to the high local current, the electrolyte and electrode being damaged. Recently, C. Kubel research group [282] succeed to realize the first *in-situ* TEM study on a fluoride all-solid-state battery using Cu/C composite as cathode,

$La_{0.9}Ba_{0.1}F_{2.9}$ as solid electrolyte and a nanocomposite of MgF_2, Mg, $La_{0.9}Ba_{0.1}F_{2.9}$ and C as anode. After cycling, fluoride migration from the solid electrolyte into the cathode and copper diffusion into the electrolyte was observed. Moreover, voids and cracks were detected in both thick and thin part of the battery after the cycling process.

In this chapter, we carry out an *in-situ* electrochemical STEM experiment on all solid-state Li-ion battery FIB lamella containing $Li_3V_2(PO_4)_3$ as anode, LAGP as solid electrolyte and $LiFePO_4$ as positive electrode. To successfully implement the experiment, various challenges need to be fulfilled. One of the difficult parts of this study consisted in designing a micro-battery with a thin solid electrolyte layer. Extracting a FIB lamella from the micro-battery, thinning it down without inducing any degradation and realizing proper contacts on the chip represented another provocation. Applying the right imaging conditions to not induce e-beam degradation and cycling such a difficult battery system represented another challenge. The dynamic evolution of the solid-state Li-ion battery was observed at the nanoscale using *in-situ* STEM analysis combined with several advanced electron microscopy techniques. Energy dispersive X-ray (EDX) spectroscopy and electron energy loss spectroscopy (EELS) were used for a chemical analysis at nanometric scale, while 4D-STEM analysis was used for a crystal structure analysis of the micro-battery.

6.2 All solid-state Li-ion battery system

To design a successful all-solid-state battery for *in-situ* electrochemical STEM, several criteria regarding the choice of materials, their formulation and cell preparation need to be satisfied. The selection of materials with similar mechanical properties and with resistance at high sintering temperatures are required for this study to obtain a successful solid-state battery. The electrochemical properties of the selected materials should also not be neglected if building a battery with high performances is desired.

The choice of the solid electrolyte integrated in the all-solid-state battery needs to fulfill few requirements as high ionic conductivity ($>10^{-3}$ $S.cm^{-1}$ at RT to conduct Li-ion), large electrochemical window to ensure that the occurring reactions are due only to electrochemical bias and the chemical reaction and high stability in the air as the FIB lamella will be exposed to air during the transfer from the FIB device to the mounting on the holder and TEM insertion. For this study, we used LAGP as solid electrolyte as presents high stability in the air, large electrochemical window, higher e-beam stability compared to sulfide solid electrolytes and we intensively studied it in our previous studies One challenging parameter in using LAGP as SE could be represented by its low ionic conductivity at RT, high temperatures being required for triggering the electrochemical

reaction. An LAGP pellet sintered at 680 °C in similar conditions as the full all-solid-state battery, presents at RT an ionic conductivity of $4.7*10^{-4}$ $S.cm^{-1}$.

$LiFePO_4$ (LFP) was used as active material for the positive electrode due to its advantages as long cycle life, low cost due to iron abundant material supply, flat voltage profile and good environmental compatibility. Another advantage of using LFP as positive electrode for the *in-situ* STEM study is represented by the fact that is a biphasic material. Analysis methods as EELS and 4D-STEM will indicate the presence of LFP in a lithiated or delithiated state, as a proof of the electrochemical reaction. However, its main drawbacks are represented by poor electronic conductivity, low ionic diffusivity and relatively low theoretical capacity (170 $mAhg^{-1}$ at a potential of 3.45 V versus Li^+/Li) compared to other positive electrode materials as LCO that presents a higher theoretical capacity (274 $mAhg^{-1}$). To enhance the electronic conductivity, LFP particles were coated with a thin layer of carbon.

Monoclinic $Li_3V_2(PO_4)_3$ (LVP) with a reversible capacity of 80 $mAhg^{-1}$ between 1.8 and 3 V vs Li^+/Li was used as active material for the negative electrode allowing us to build a full solid-state battery based on phosphates materials. The synthesis of $Li_3V_2(PO_4)_3$ as anode material was done in the laboratory (See **Appendix E** for more details). It should be noted that LVP can also be used as positive electrode between 3 and 4.65 V vs. Li^+/Li with a reversible capacity of 140 $mAh.g^{-1}$, but during this study we used LVP only as negative electrode. The system of using LFP as positive electrode and LVP as negative electrode using an oxide solid electrolyte was already tested with a certain success. A. Aboulaich *et al*. [264] formulated an LFP/LAGP/LVP battery system sintered by SPS that delivered a reversible capacity of ~ 80 $mAh.g^{-1}$ for approximately 30 cycles.

Both positive and negative electrodes are a composite of active materials, solid electrolyte, and carbon. In the electrode formulation, C45 black carbon was added as electronic additive to increase the poor electronic conductivity of our active materials. The electrode formulation was adapted from a study done few years ago in LRCS laboratory by G. Delaizir *et al*. [265] in which they showed a successful solid-state battery containing $Li_3V_2(PO_4)_3$ electrode with an optimal formulation of 25LVP/60LAGP/15C (wt%). The electrodes used in this study presents the following composition: 60% solid electrolyte to ensure enough ionic conductivity in the electrodes, 10% of C45 to ensure enough electronic conductivity and 30% of active material. According to a study performed by G. Delaizir *et al.*[265] a carbon content of at least 10 % by mass is required in the electrode formulation to obtain an electron conductivity of 1 S/cm. During their study, 15 % weight of carbon was added in the electrode formulation to enhance the electronic conductivity and to absorb the

macroscopic part of volume changes during cycling as carbon is ductile and known for its ”lubricant” properties. In our work, the amount was reduced to 10 % weight of carbon to obtain highly dense pellet with optimal ionic conductivity at the determined sintering temperature as a higher amount of carbon would have required a higher sintering temperature. High compacity pellets with good mechanical properties represents an essential step for successful delivering a standing micro-battery FIB lamella.

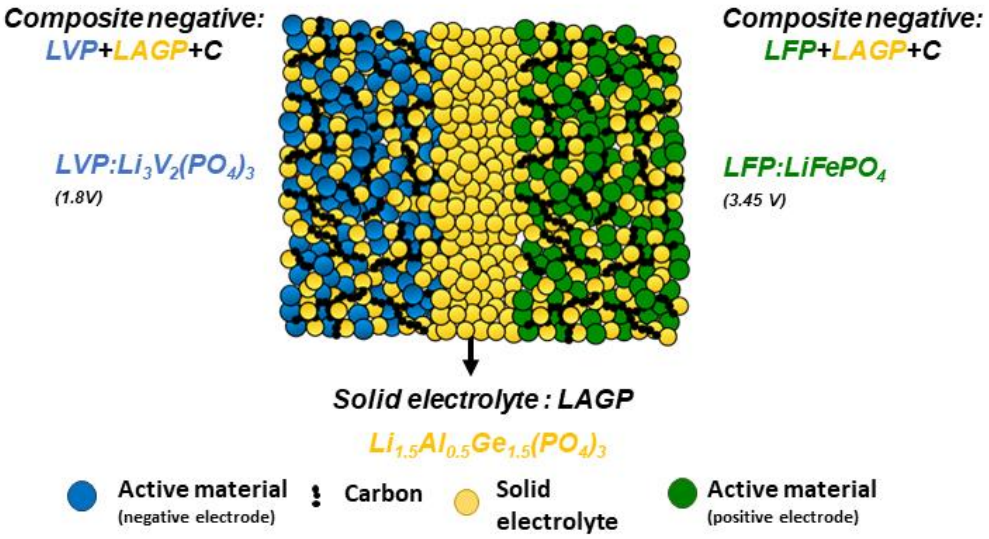


Figure 6.1. Schematic illustration of the all-solid-state battery prepared by Spark Plasma Sintering.

A schematic representation of the all-solid-state battery used in this study is represented in the **Figure 6.1** in which in yellow is represented the solid electrolyte found as a separator between the electrodes, LFP and LVP are marked in green, respectively blue and the additive carbon used for electronic conductivity enhancement is represented in black. During the electrochemical charge process electrons and lithium ions are removed from the $LiFePO_4$ structure resulting $FePO_4$ structure via biphasic transformation and inserted in the $Li_3V_2(PO_4)_3$ anode via 2 step reaction initially to $Li_{3.5}V_2(PO_4)_3$ structure and then $Li_4V_2(PO_4)_3$. During the discharge process, the opposite process occurs, lithium ions and electrons are removed from the anode, also in the two step reactions and then inserted in the cathode material. (See reactions details in **Appendix E**)

6.3 Ex-situ cycling of all solid-state battery

Obtaining a full solid-state battery with intimate interface contact represents a crucial step. The battery components usually have different mechanical properties and assembling them together may be challenging as they exhibit different thermal expansion coefficients[79]. Spark plasma sintering (SPS) is an efficient technique to prepare stacks of different materials with well-connected interfaces for battery applications[264,265]. SSBs with the

$LiFePO_4$/LAGP/ $Li_3V_2(PO_4)_3$ configuration have been sintered at 680 °C in one single shot in a controlled atmosphere using spark plasma sintering. The temperature of 680 °C was chosen as the solid electrolyte presents an optimized ionic conductivity at this temperature (see **Chapter II**), the compacity of the battery is high enough to ensure a good mechanical stability and at the same time allows enough space for ionic/electronic percolation without causing high mechanical strains.

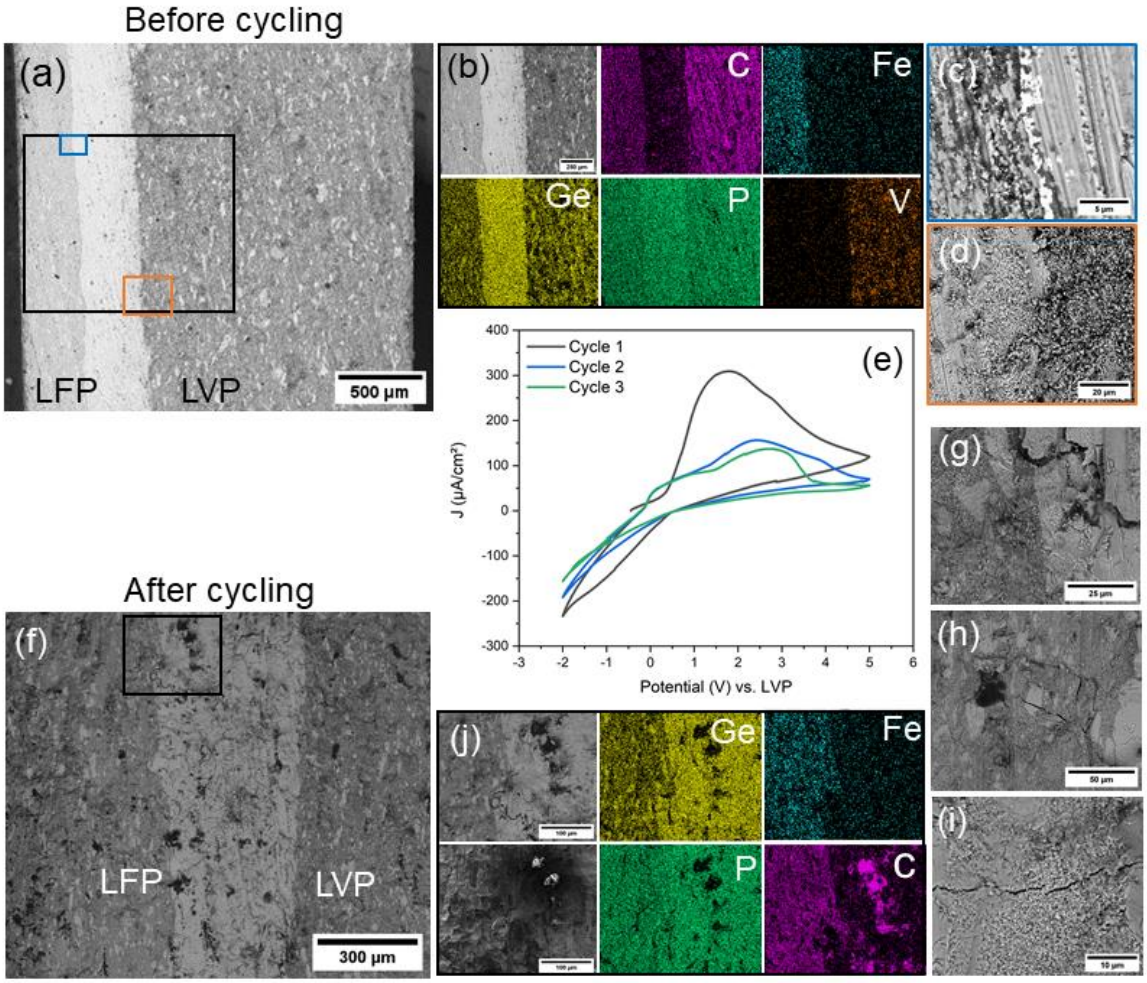


Figure 6.2 $LiFePO_4$/LAGP/$Li_3V_2(PO_4)_3$ ASSB configuration prepared by SPS showing (a-c) SEM micrographs and (d) SEM-EDX analysis before (e) galvanostatic cycling with potential limitation at 100 °C, C/20 and (f) SEM micrographs and (j) SEM-EDX analysis of the battery after the cycling showing cracks and rich-carbon formation.

The backscattering SEM image of the $LiFePO_4$/LAGP/ $Li_3V_2(PO_4)_3$ battery prepared by SPS is displayed in the **Figure 6.2a**. It can be observed that the thickness of the positive electrode (LFP) is smaller compared to negative electrode (LVP) as the positive electrode presents a much higher theoretical capacity vs Li^+/Li (170 $mAh.g^{-1}$) compared to LVP (80 $mAh.g^{-1}$), so the weights balances were equilibrated to maximize battery performances and avoid lithium plating formation.

SEM-EDX analysis performed on the SSBs revealed the presence of an interphase layer located at the LAGP-LVP interface (white contrast in the **Figure 6.2c**). From the numerous batteries sintered, it was noticed that the interphase layer formed only in some of the batteries, despite the same sintering conditions used constantly (only the SPS die differed from one sample to another). Also, the interphase layer was detected only in one interface of the battery, regardless of the electrode material used (see **Figure A6.2**, **Appendix E**) with the other interface displaying good contact with no degradation products. In this study, the interphase with degradation products is present between the LAGP and LFP layers. Moreover, it was noticed that the upper electrode layer presented a higher compacity compared to the bottom electrode layer (in the presented case LFP presents higher compacity than LVP). The SEM-EDX analysis performed on the generated interphase showed a mixture of rich Ge and Al phases (See **Appendix E, Figure A6.2** for more details). A possible assumption for the interphase resulted could be explained by a reduction of Ge^{4+} to probably metallic germanium or a lower oxidation state in the solid electrolyte layer due to the high current during the sintering process. A recent study also reported the formation of an interphase between LAGP and LFP[301]. They showed the formation of an interphase between the electrode and the solid electrolyte on top and bottom layer of an LFP/LAFP/LFP system. In the closest interface to sintering current direction a poor Li, rich Fe layer plus a rich Li, poor Al layer were formed. In the further interface to sintering current a poor Li, rich Al layer plus a rich Li layer were formed. They speculated that the interphases form based on Li migration, *i.e.* lithium ions shifts and migrate from LFP to LAGP layer resulting to a poor lithium layer in LFP and rich lithium layer on LAGP. As a result of lithium migration, $LiFePO_4$ transforms into $Fe_2P_2O_7$ phase which is a delithiation products of LFP[301].

Figure 6.2e displays the cyclic voltammetry (CV) of one the all-solid-state battery cycled at 100 °C (to ensure a higher ionic conductivity) where a scan rate of 0.25 mV/s was applied on the sample. The positive electrode potential (LFP) is located at 3.45 V vs Li^+/Li and the negative electrode potential (LVP) is located at 1.8 V vs Li^+/Li which is also our reference electrode; resulting that the peak corresponding to LFP delithiation located at 3.45 V vs Li^+/Li will be placed around 1.65 V vs LVP. We cycled our battery between -2 and 5 V as some overpotential is usually expected in the SSBs. On the CV graph during the first cycle, it can be observed the presence of a large peak with the highest current density located close to ~1.7 V indicating the delithiation process of $LiFePO_4$ towards $FePO_4$ structure. Unfortunately, during the discharge process, the peak corresponding to $Li_3V_2PO_4$ delithiation is absent indicating that lithium was not further inserted into $FePO_4$ structure. Moreover, during the discharge process towards negative potential values the apparition

of a new peak is observed, most likely corresponding to the formation of degradation products. Although $Li_3V_2PO_4$ presented the right crystal structure after the synthesis process (**Figure A6.1a, Appendix E**) and the potentials corresponding to LVP delithiation were located at right position (**Figure A6.1b, Appendix E**) after the sintering process, changes were detected in the crystal structure of the electrodes. XRD profile fitting analysis presented in the **Figure A6.3** (**Appendix E**) shows the crystal structure of the electrodes powder before and after the sintering process. Both electrodes (LFP and LVP) displayed an intensity peak reduction alongside with the apparition of new peaks confirming the formation of degradation products after the sintering process (already observed using SEM analysis). Starting with the second and the third cycle alongside with the peak corresponding to $LiFePO_4$ delithiation (which displayed higher polarization), the apparition of a new peak between 0 and 1 V was observed. The new peak most likely corresponds to the activity of a degradation products formed during the first discharge cycle.

After the cycling process, the all-solid-state battery was investigated using SEM analysis (**Figure 6.2f**). Although during the optical analysis, the battery did not show the presence of large cracks, the SEM analysis detected the apparition of small cracks in the solid electrolyte and nearer the interfaces with the electrodes (**Figure 6.2g-i**). The cracks presented rather a smaller length (~50 µm) and a thickness bellow ~2 µm with no lithium dendrites or degradation products spotted inside of them. Alongside the cracks, SEM analysis revealed the apparition of a degradation products in the form of bullets of irregular shape (dark contrast region in **Figure 6.2h**). The SEM-EDX analysis (**Figure 6.2j**) revealed that the chemical compositions of the dark regions were high in carbon. As no other elements were detected in the chemical composition of these degradation products, one possible hypothesis about their composition could be that they also contain Li (non-detectable with SEM-EDX) and they may be $LiCO_3$, a degradation product encountered quite often after the cycling process.

6.4 Solid-state battery preparation for *in-situ* electrochemical TEM

Preparing a micro-battery for *in-situ* electrochemical TEM cycling was quite challenging and represented one of the most difficult parts of this project. The micro-battery for *in-situ* TEM experiment needed to be in the micron size order to successfully connect it on the special e-chip which allowed bias application (dimensions of e-chip electrodes are fixed). Another challenging point was the thickness of the micro-battery which needed to be thin enough (around 100 nm) to ensure electron beam transparency.

As methods to obtain the micro-battery, ALD method offers a better control of the solid electrolyte thickness compared to SPS. This method was successfully used in our group

for obtaining a LMNO thin-film cathode for *in-situ* TEM cycling in a liquid electrolyte. After the cycling process, the thin film revealed the formation of voids and cracks, loss of contact with the current collector and the presence of decomposition products[298]. Obtaining a battery by SPS from which the micro-battery is extracted by FIB/SEM technique, as it was done in this work, was quite challenging and many trials were necessary until getting a very thin layer. The total length of the full all-solid-state battery that needed to be connected on the e-chip must present a maximum length of 50 µm and must contain the 3 layers of the battery (positive electrode, solid electrolyte and negative electrode), limitation imposed by the fixed electrodes of the e-chip that allows bias applications. **Figure 6.3a** shows one of the successful trials in which we can observe a battery prepared by SPS with a non-uniform layer of solid electrolyte varying from few to hundreds of micrometers. The presence of area with a layer of solid electrolyte below 20 µm as shown in the **Figures 6.3b,c,** allowed us to extract a FIB lamella and obtain a micro-battery within 50 µm length. It should be observed that the presence of the interphase due to SPS between the solid electrolyte and the bottom electrode was absent in the battery used for micro-battery extraction as confirmed also by the SEM-EDX analysis of the battery interface presented in the **Figure 6.3d,e,f,g**. Our assumption for the non-existence interface previously reported can be explained by the thin LAGP layer which most likely limited the lithium concentration and further lithium migration into LFP or LVP layers.

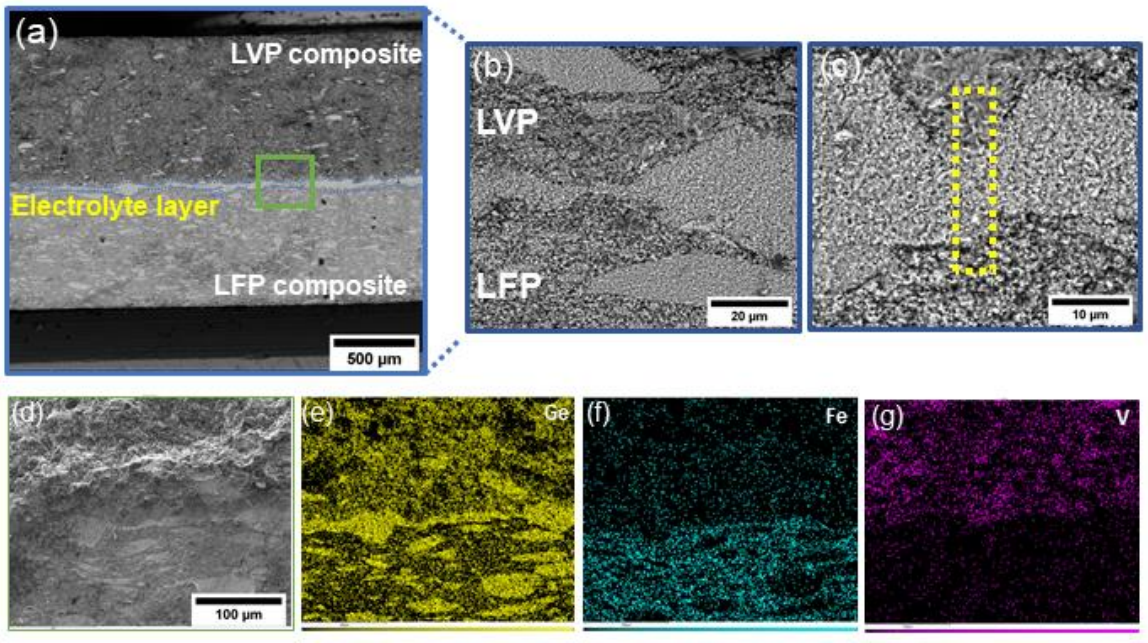


Figure 6.3. (a) All-solid-state battery prepared by Spark Plasma Sintering at 680 °C (b), (c), (d) zoom on the interfaces of the solid electrolyte displaying the thin layer of solid electrolyte intentionally prepared for extracting the FIB lamella for in-situ STEM cycling.

The all-solid-state micro-battery was prepared using a Focused Ion Beam (FIB) FEI STRATA DB 235 microscope via a collaboration with IEMN laboratory in Lille with the help of Dr. David Troadec. Local platinum deposition using Gas Injection System (GIS) assisted by the Ga-ion beam was used to protect the micro-battery surface and improve the quality of the etching process. The initial milling to obtain a cross sectional FIB lamella containing all 3 layers (**Figure 6.4a**) of the battery was performed using a current of 7 nA. The FIB lamella of 1.5 µm thickness was transferred to Protochips e-chip (**Figure 6.2b**) by using a Kleindiek micromanipulator. Due to small space between electrodes and the thickness of the solid electrolyte, only one interface of the micro-battery was visible for TEM observation. Various FIB lamellas were prepared with a focus on cathode/solid electrolyte and anode/solid electrolyte interface. FIB lamella cross section was connected to Protochips e-chip using a platinum deposition (GIS) on both extreme sides of the micro-battery electrodes (**Figure 6.4c**). To optimize the quality of Pt bridge in terms of electronic conductivity, Ga-ion beam was used to form the connection with a long exposition (5 min.). To get good conductivity between sample and e-chip this step has been optimized in a previous work performed in the laboratory[298]. The initially platinum layer used for protection of the micro-battery was slowly milled to avoid a short-circuit in the micro-battery as the two electrodes are connected between them by a platinum layer (**Figure 6.4d**). A final thinning down to 100 nm in the FIB lamella for the electron beam transparency was realized with a current of 100 pA. Various FIB lamellas focusing on the solid electrolyte/cathode and solid electrolyte/anode interface were prepared for this experiment as only one interface of the FIB lamella was visible and the second was on top of the e-chip due to full all-solid-state FIB lamella micro-battery length.

Obtaining a successfully FIB lamella micro-battery was quite challenging as various difficulties are encountered during this process. Any FIB damage or Ga contamination on the micro-battery should be completely avoided, therefore choosing the right parameters for the FIB extraction, and thinning down was crucial. As the FIB lamella was designed for *in-situ* electrochemical TEM experiments, having a proper contact between the micro-battery and the e-chip electrodes is existential for a successfully analysis. In the end, thinning it down and removing a part of the top platinum layer to avoid the short-circuit in battery represented one challenging point as the micro-battery needed to present good and sustainable mechanical properties while was thin enough to ensure e-beam transparency.

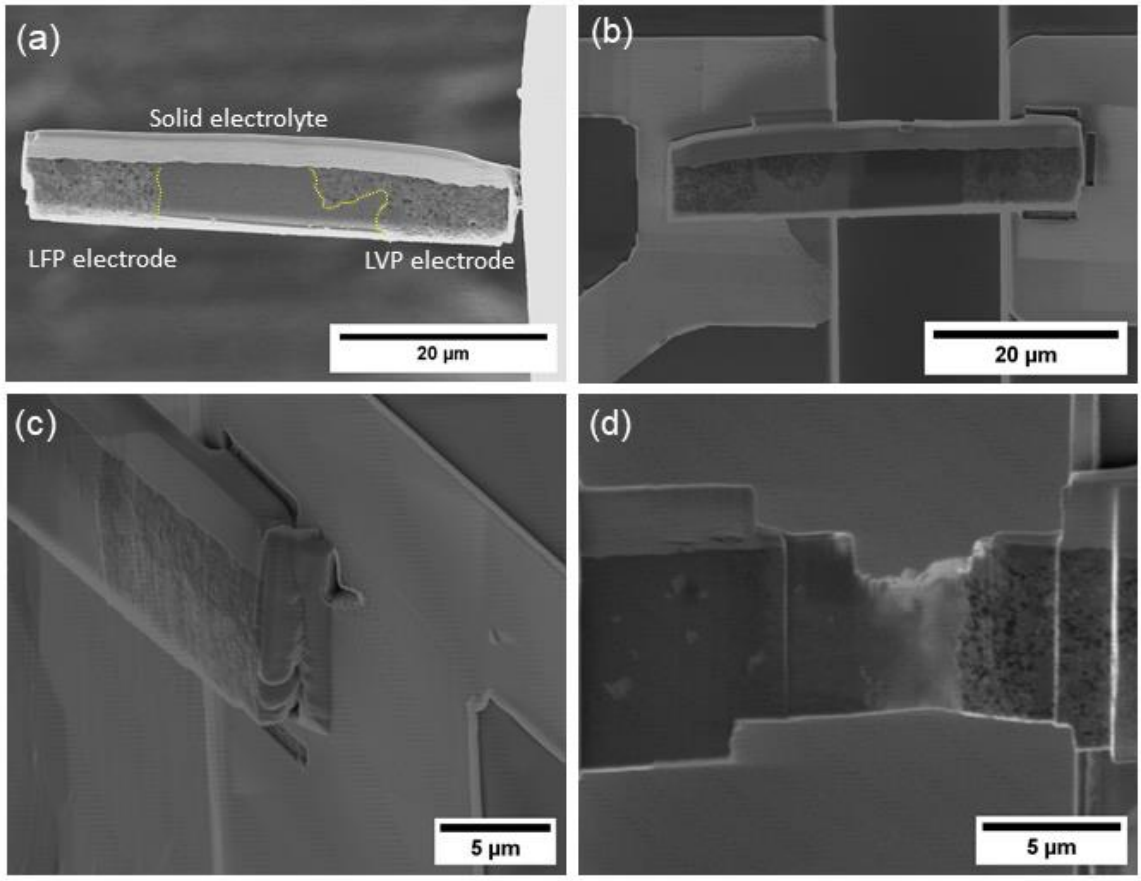


Figure 6.4: (a) FIB lamella extracted from a full battery containing all the 3 layers (from left to right) : negative electrode (LVP: 30 %, LAGP 60 %, Carbon 10 %), solid electrolyte (LAGP) and positive electrode (LFP: 30 %, LAGP 60 %, Carbon 10 %) (b) FIB lamella mounted on the Protochips chips (c) platinum contacts realized between the electrodes of the FIB lamella and the electrodes of the chips and (d) lamella tinned down below 300 nm at the interphase between positive electrode and solid electrolyte and cut of the platinum contact in order to avoid the short-circuit.

6.5 Study of the pristine FIB lamellas

After successful FIB lamellas extraction and connection on the e-chip, pristine FIB lamellas are investigated using 4D-STEM ACOM analysis method. As mentioned in **Chapter V**, 4D-STEM method uses nano-probe scanning approach to acquire electron diffraction patterns that are further indexed automatically using a template matching software which contains the simulated diffraction pattern with all the possible orientations for all the inputted phases. We used 4D-STEM ACOM to obtain structural and morphological information about the solid electrolyte and electrode components. **Figure 6.5** presents structural images of solid electrolyte/cathode interfaces before *in-situ* electrochemical TEM. For this study, to avoid electron beam damage on the lamella during the acquisition, the time used for scanning an electron diffraction is limited to 20 ms per pixel. At this dwell time, based on diffraction spot intensity evolution, no beam damage has been observed in the micro-battery sample, regardless of the irradiated components. The acquired dataset of electron diffraction patterns was automatically compared using pattern

matching approach with generated pattern dataset from the structural CIF files of the different expected structural phases, (*i.e.* LAGP, LFP). The amorphous carbon phase was added manually based on the specific carbon ring observed on the electron diffraction patterns.

Based on the ACOM pattern matching treatment, we generated the orientation maps along X, Y and Z axes (only Z axis presented here), phase map and grain boundaries map as well as associated reliability map to evaluate the identification confidence in each pixel of the map. The orientation map along Z axis presented in the **Figure 6.5.a** shows LFP and LAGP grains with various orientation even among the same particle LAGP and LFP interface presents no special orientation induced from one battery component to another and the solid electrolyte layer displays various orientation, the most encountered being [100] orientation.

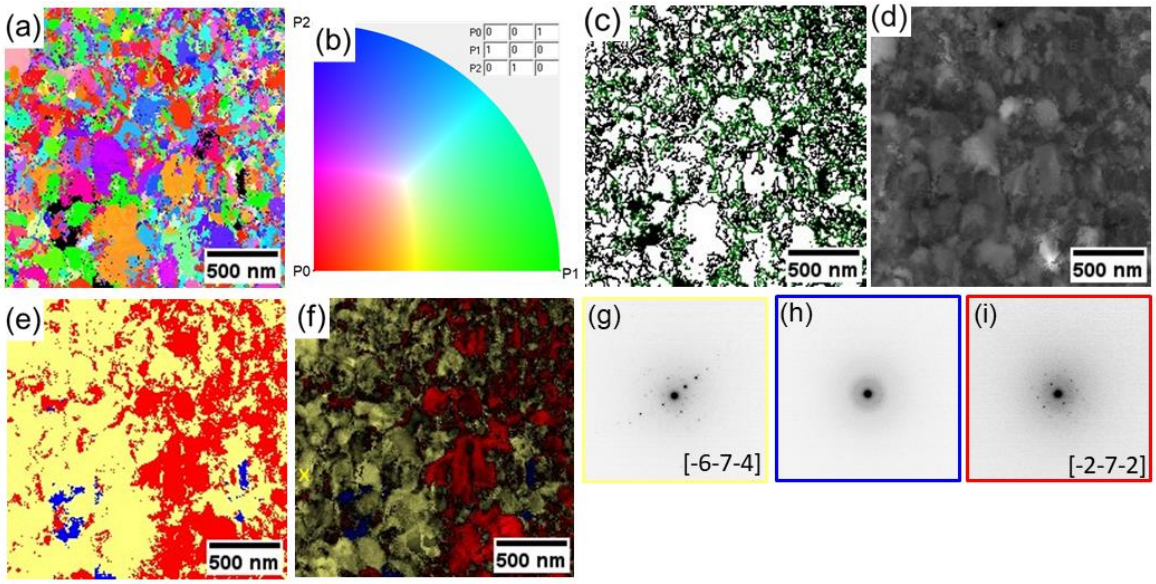


Figure 6.5: LAGP/LFP interphase analyzed on a pristine FIB lamella before cycling where it shows: (a) orientation on the Z axis and (b) their color code corresponding to the orientation planes (c) grain boundaries map (d) index map used for the analysis, (e) phase map where LAGP (62.6 %) it is represented in yellow, LFP (35.9 %) in red and C (1.6 %) in blue (f) combination map between phase and phase reliability and electron diffraction patterns of (g) LAGP, (h) carbon and (i) LFP.

Figure 6.5.c reveals the grain boundary map in the micro-battery (only grains higher than 20 nm were selected) showing a high number of boundaries located between the grains of the same phase (black) and different phases (green), which impacts the ionic conduction and enhance the probability of interface reactions. Reconstructed phase map (**Figure 6.5e**) and the combination between phase map and phase reliability (**Figure 6.5f**) displays the solid electrolyte/cathode interface where the solid electrolyte is represented in yellow (62.6 %), the active material is displayed in red (35.9 %) and in blue is represented the carbon additive (1.6 %). The phase map is reconstructed from the acquired electron

diffractions patterns. A representation of the solid electrolyte diffraction pattern is presented in the **Figure 6.5g,** of the LFP in **Figure 6.5i** and of the carbon additive in the **Figure 6.5h** for which the scattered ring, corresponding to amorphous carbon contribution can be observed. Based on the reconstructed map we can see that the solid electrolyte is well incorporated between the LFP grains ensuring a good ionic conductivity of the electrode. However, the amount of carbon additive in the electrode area probed with 4D-STEM (very local analysis) is too low, 1.6 % even if an amount of 10 % was added inside the electrode. This lower amount of carbon potentially generates issues in terms of the percolation network of electronic conductivity, at least in the region of interest, and questions the impact of electrode heterogeneity on electrochemical performance. LFP migration from the electrode to the solid electrolyte was also detected (red regions presented in the solid electrolyte), LFP migration possible occurring during sample preparation or sintering process.

Solid electrolyte/anode interface analysis was performed on another FIB lamella extracted from the same battery as this interface was not visible in the first FIB lamella. The orientation map along Z axis in the LAGP/LVP interfaces (**Figure 6.6a**) shows no preferential orientation for LVP grains. Regarding the LAGP particles, there were various orientation observed, but [100] orientation was the most encountered one. Grain boundary map (**Figure 6.6c**) reveals the presence of less grain boundaries at the solid electrolyte/anode interface compared to cathode interface. Reconstructed phase map (**Figure 6.6d**) and the combination (**Figure 6.6f**) between the reconstructed phase map and reliability map (**Figure 6.6e**) reveals in pink the active material for the negative electrode in a percent of 7.9 %, solid electrolyte similar to the previously analyzed interface is represented in yellow with 68.6 % and the additive carbon represented in blue with 23.5 %. Phase reliability map (**Figure 6.6e**) reveals with light gray high reliability matching pattern between the acquired and simulated electron diffraction patterns and in black/dark grey a low reliability for the matching patterns. It can be observed that our reliability map is predominant light gray indicating a good indexation between the acquired electron diffraction patterns and the simulated ones. An example of the acquired electron diffraction pattern for the LAGP, LVP and additive carbon are displayed in the **Figures 6.6g,h,i**. Contrary to the positive electrode/solid electrolyte interface, at the anode/solid electrolyte interface the amount of carbon increased, even higher than the amount of active material, indicating an heterogeneous distribution of the carbon in the electrodes formulation. The amount of active material detected in the electrode seems lower, this impacting the capacity of the battery. Migration of carbon and active material from the electrode mixture at the

solid electrolyte grain boundaries is also detected in the pristine FIB lamellas most likely as a result of the sample preparation.

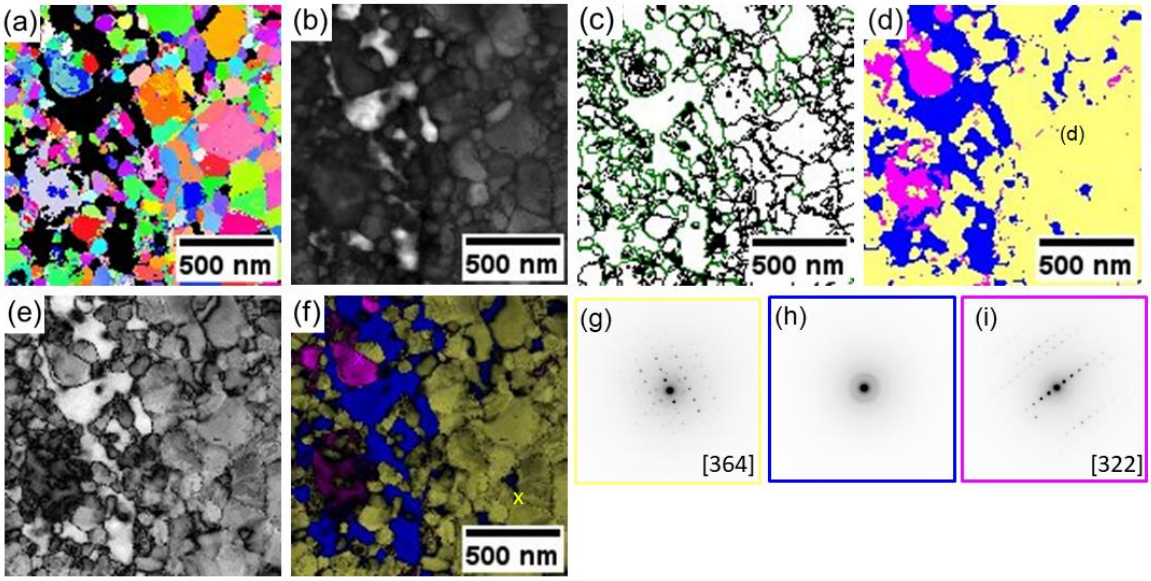


Figure 6.6: LAGP/LVP interface analyzed on a pristine FIB lamella before cycling where it shows: (a) orientation on the Z axis and (b) index quality map used for the analysis (c)grain boundaries map (d) phase map where LAGP(68.6 %) it is represented in yellow, LVP (7.9%) in pink and C (23.5 %) in blue (e) phase reliability (f) combination map between phase and phase reliability and electron diffraction patterns of (g) LAGP, (h) carbon and (i) LVP.

6.6 *In-situ* electrochemical TEM cycling

Fusion Select holder from Protochips (**Figure 6.7.a**) as part of a demo collaboration was used for this experiment. Fusion Select holder consists of a metallic support that allows the placement of the e-chip meme devices where the FIB lamella is placed. The metallic pins ensure reliable electrical contact between the holder and the e-chip and allows the application of electrical biasing. Although the Fusion Select holder may allow the application of heat and electrical bias at the same time, during this experiment the holder allowed only the application of electrical bias.

Thinned FIB lamella connected on the Protochips e-chip was mounted on the Fusion Select holder from Protochips and further inserted in the TEM column. A Keithley system was used to drive the electrochemical measurements controlling the current/potential applied to our FIB lamella. Bias application within our FIB lamella from the Keithley system is realized by the gold electrodes presented on the e-chip (**Figure 6.7b**) connecting the lamella by deposited platinum using FIB. **Figure 6.7c** displays our lamella mounted on the e-chip designed for *in-situ* electrochemical TEM experiment in which with light contrast we can distinguish the gold electrodes and with dark contrast the electrons beam transparent area. The electron beam transparent area is approximately 20 µm and only one interface of our battery (approximately 35 µm) will be visible during the *in-situ* experiment. The

interface that we selected to put on the e-chip on the e-beam transparent side is the cathode $LiFePO_4$/LAGP interface, meanwhile the $Li_3V_2(PO_4)_3$/LAGP interface is presented on the e-chip (not the e-beam transparent area).

It is known that $Li_{1.5}Al_{0.5}Ge_{1.5}(PO_4)_3$ presents a relatively low ionic conductivity at RT (around 1.01 * 10^{-3} $S.cm^{-1}$), the used LAGP for this study exhibited an ionic conductivity around 4.9 10^{-3} $S.cm^{-1}$ at 60°C as shown previously in **Chapter II**. As the Fusion holder does not allow us to apply heat during the electrochemical cycles, the *in-situ* experiment has been carried out with no extra heating, except heating induces by electron beam. Low dimensions of the micro-battery provide small diffusion pathway especially due to the low thickness of lamella and favor the lithium diffusion compensating for the low ionic conductivity at RT which could represent an impediment for a successful cycling process[258].

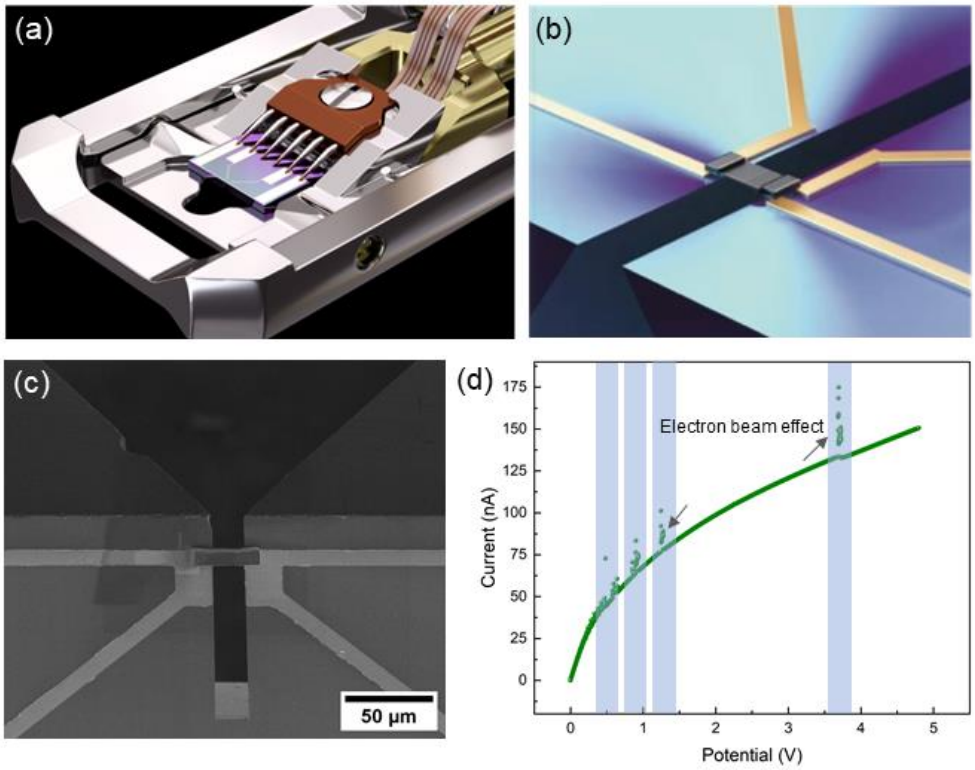


Figure 6.7: Electrochemical study of solid-state battery FIB lamella using (a) Fusion holder (Protochips) for operando experiments which allows to apply bias for electrochemical measurements on (b) a chip adapted for FIB lamella and (c) ASSB FIB lamella connected on the Protochips chip (d) Cyclic voltammetry curve of the LVP/LAGP/LFP system during the cycling and electron beam effect on the FIB lamella.

The cycling voltammetry curve of the LVP/LAGP/LFP all-solid-state battery where a scan rate of 10 mV/s was applied up to 5 V on FIB lamella, resulting in a time scan of ~17 minutes for the charge process is presented in the **Figure 6.7d**. It can be noticed that the graph displays more a resistance plot, most likely due to high overpotential presented on the battery impacting its electrochemical properties. Possible causes for the overpotential arise from poor interfacial contact area between the electrode components and internal

resistances of the all-solid-state battery[302]. A difference between the potential of the thermodynamically reactions occurring in battery and the potential values read on the graph (almost no present) was probably induced by the overpotential. Moreover, the electron beam was noticed to also introduce an effect on the electrochemical curve. An increase in the current was noticed all the time when the projection screen was removed, the e-beam was placed on the battery and an image was acquired. The current values recorded due to e-beam (200 kV) effect are around 20 nA and are highlighted on the **Figure6.7d** on blue. This observation clearly show that electron beam can affect the electrochemical properties of the micro-battery and for further investigation, electron beam effect should be minimized.

Figure6.8a presents a STEM-HAADF image (Scanning Transmission Electron Microscopy – High Angle Annular Dark Field) of the all-solid-state micro-battery FIB lamella before bias application where the LFP cathode can be observed on the right side of the lamella and the solid electrolyte on the left side. The presence of darker contrast areas can be observed within the solid electrolyte layer (left, bottom side) and according to the STEM-EDX analysis recorded before the electrochemical measurements, those area contains more Al in the composition and lack Ge, similar to the grain boundary phase detected between LAGP grains discussed in **Chapter 2**.

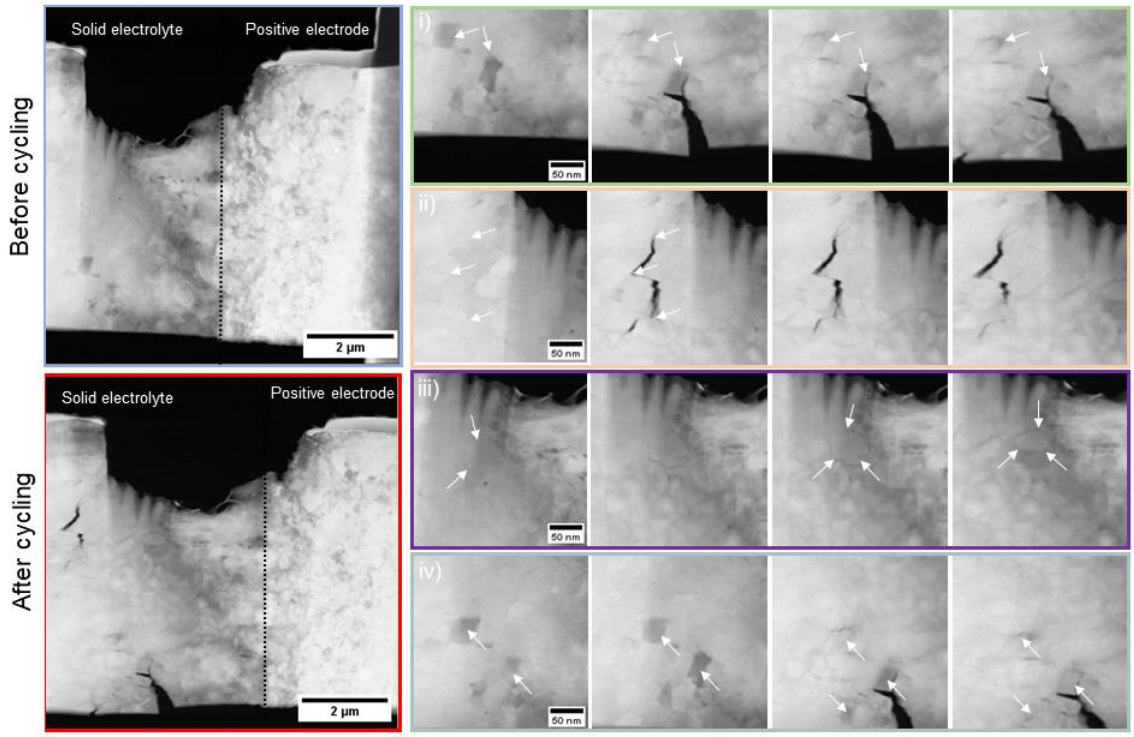


Figure 6.8 (a) ASSB FIB lamella before cycling and (b) after in-situ STEM cycling showing (i), (ii) presence of cracks induces by the bias in the solid electrolyte, (iii) particles shrinkage and grain boundaries increasing and (iv) contrast change after cycling.

During the cyclic voltammetry measurement, STEM images were recorded at relatively low magnification (low dose condition) to minimize the electron dose provided to the sample and avoiding beam damage on the micro-battery. While applying the bias on the battery various degradations as large cracks apparition in the LAGP solid electrolyte, changes in contrast and particles shrinkage with grains boundaries expansion were noticed. Most visible degradation produced on the battery was the appearance of cracks in the solid electrolyte, both in thin and thick part of micro-battery. **Figures 6.8i** reveals the formation of one of the cracks that appeared in the LAGP layer of the micro-battery; with the crack initiating from the region that contains secondary phases in the solid electrolyte. Moreover, a change in the contrast before and during crack evolution for the secondary phase is observed. together with a higher visibility for the grain boundaries. A second large crack in the thicker part of the solid electrolyte appeared during bias application**, Figures 6.8ii** revealing the crack propagation where in the initial image no visible cracks were spotted, in the second image a large crack appears between SE grains and towards the final stages of the reaction a slightly filling inside the cracks was noticed. Also, the morphology of the LAGP grains around the crack presented in the **Figure 6.8ii** changes over time during bias application showing a reduction in the LAGP grains and an increase in the grain boundaries areas. A change in the grain morphology was spotted on other places in the SE as shown in the **Figure 6.8iii** where the arrows marked in purple point towards one of the particles which displays a significant shrinkage during the electrochemistry reaction, a reduction 11.65 % of the surface area particle was noticed. In fact, most of the SE particles displays a significant shrinkage together with an important increase in the grain boundaries areas. The increase in the grain boundaries area may create higher internal resistance in the battery. **Figure 6.8iv** focus on the changes of contrast over time of the secondary phases observed during electrochemical reaction. In the first STEM-HAADF image a large rectangular grain with small irregular areas is spotted evolving towards 2 larger rectangular grains. Towards the end, the darker contrast presented in the larger rectangular area slowly disappears completely, and the presence of cracks are noticed. This observation shows the high dynamics of the secondary phases in the SE during bias application and their influence on the crack appearance.

6.7 Post-mortem studies of the FIB lamellas

STEM-EDX analysis on the micro-battery was performed before (**Figure 6.9a-b**) and after the *in-situ* electrochemical TEM experiment(**Figure 6.9e-i**). STEM-EDX map analysis performed before the electrochemical reaction displays in yellow Ge signal from LAGP found in both SE and in electrode, in orange Fe signal from the active material and in blue is presented the signal of carbon which normally it was supposed to be located only in the

electrode, but surprisingly it was found also in the SE. It can be observed that the electrode components are well mixed between them, ensuring good interfaces contact between the solid electrolyte, active material, and carbon, but the amount of solid electrolyte presented in the electrode mixture on this lamella it too low which could have impacted the ionic conductivity properties of the micro-battery. The unexpectable presence of the carbon in the SE probably increased the electronic conductivity of the solid electrolyte and further contributed to the propagation of cracks.

STEM-EDX map analysis after *in-situ* cycling (**Figure 6.9c-d** and **Figure 6.9j-n**) shows no change of Ge signal in the solid electrolyte, but the presence of carbon that was initially spotted in the SE layer was no longer detected indicating that the carbon from the SE was consumed during the electrochemical reaction. Also, the signal of oxygen (**Figure 6.9m**) from the near vicinity of the solid electrolyte interface with the cathode (thin part of the solid electrolyte in the lamella) was diminished after the *in-situ* reaction. A possible assumption for the reduced amount of oxygen could be explained by the possible formation of Li_2CO_3 (as C signal was also reduced) in some parts of the FIB lamella that are not visible during analysis. The presence of Al-rich phase with slightly modified morphology is still detected in the same area after the electrochemical reaction (**Figure 6.9n**) although no darker contrast corresponding to the secondary phase was spotted on the STEM-HAADF image at the end of cycling process.

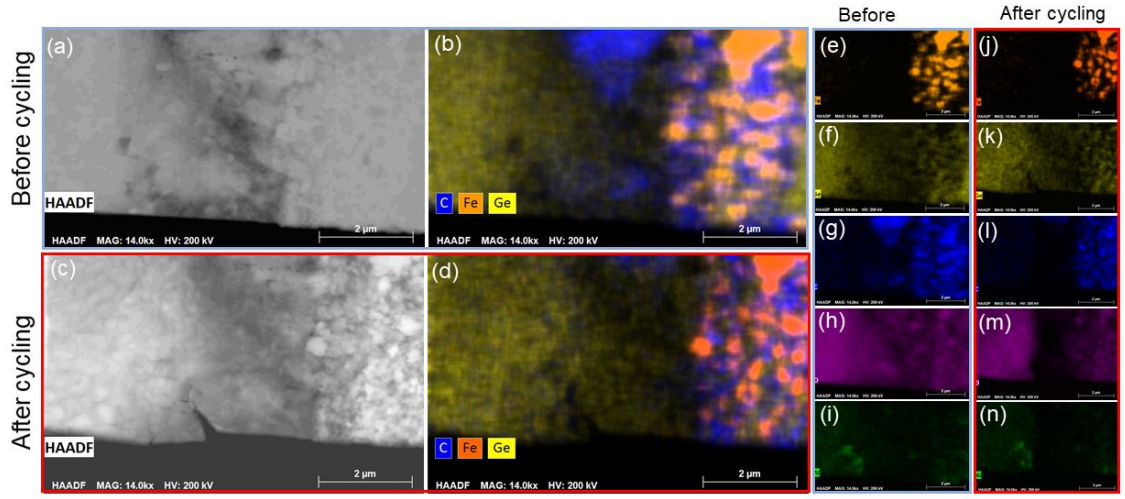


Figure 6.9 ASSB FIB lamella (a) before and (c) after the cycling process and their corresponding STEM-EDX map analysis (b) before and (d) after the cycling process showing the map signal of (e, j) Fe, (f, k) Ge, (g, l) O, (h, m) P and (i,n) Al.

Post-mortem 4D-ASTAR analysis was carried out on the cycled lamella in order to investigate the changes induced in the crystal structure after the electrochemical reaction, this analysis focuses only on the positive electrode area. **Figure 6.10b** displays the orientation map on the Z axis where most of the grains, with a few exception present

arbitrary orientations. The grain boundaries map (**Figure 6.10c**) indicates a small number of boundaries for amorphous area and one single orientation crystals and a larger number of boundaries for the active material in the electrode.

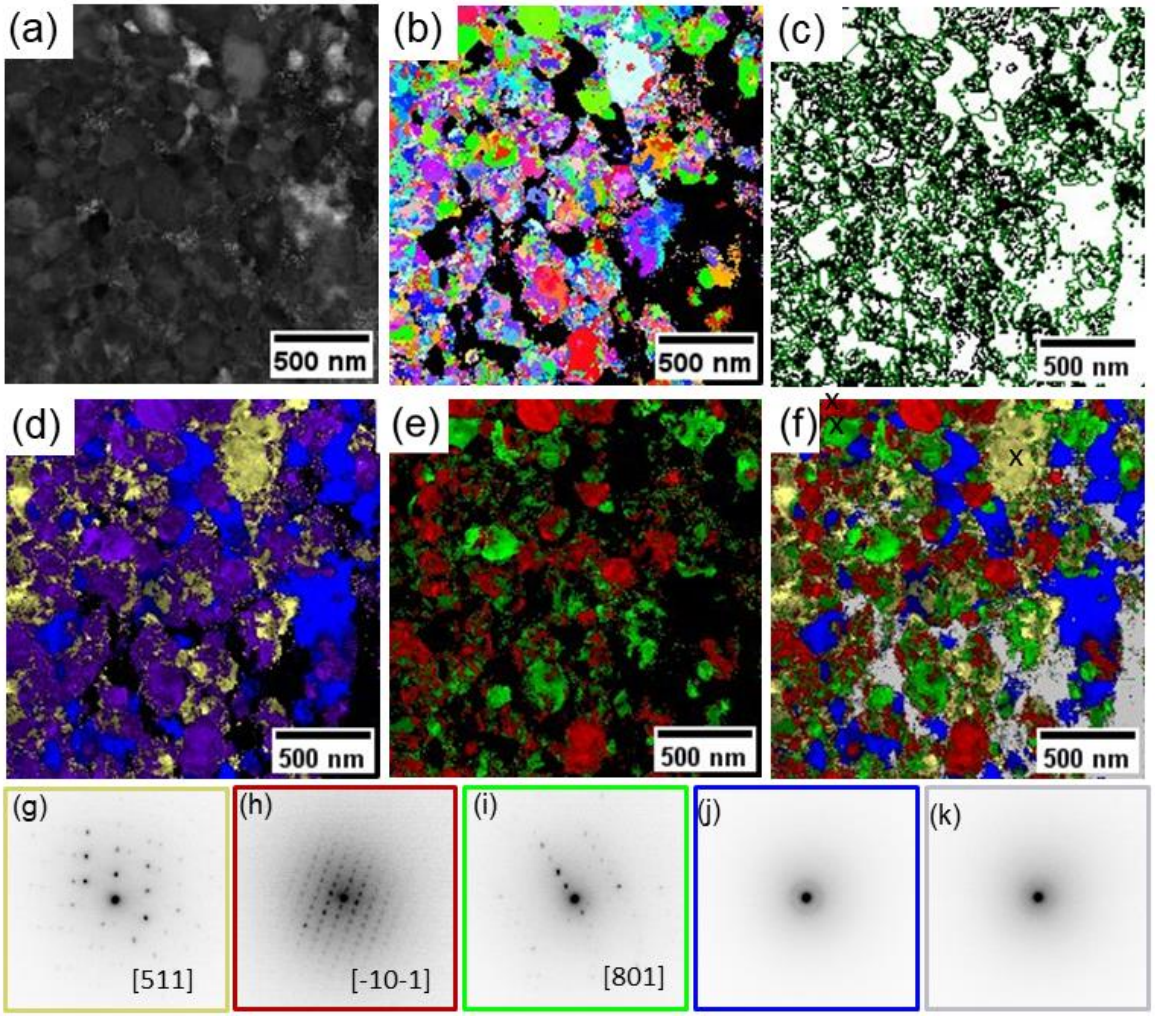


Figure 6.10 LAGP/LFP interphase analyzed on a pristine FIB lamella after cycling where it shows: (a) Index map used for the analysis (b) Orientation on the Z axis, (c) Grain boundary map analysis, (d) Phase map where active materials is represented in purple, solid electrolyte with yellow, carbon with bleu and amorphous areas with black (e) Phase map that focus on the active materials particles (LFP and FP) where in red are represented the LFP particles and in green the FP particles (f) Overall phase map where LAGP (20.5 %) is represented in yellow, LFP (24.5 %) in red, carbon (18.5%) in blue, FP (21 %) represented in green and (15.4 %) amorphous points represented with grey and (g-k) electron diffraction patterns of g) LAGP, h) LFP, i) FP, j) carbon and k) amorphous.

Phase and phase reliability maps of the analyzed area (**Figure 6.10d**) show in purple the active material in a proportion of 45.5 %, the solid electrolyte in a proportion of 20.5 % and the carbon in a proportion of 18.5 %. In additional to the pristine FIB lamella, after the cycling process another type of pattern was detected where only the presence of the direct e-beam was observed indicating the presence of amorphous regions or pores in the electrode. The difference between the electron diffraction patterns of additive carbon (**Figure 6.10j**) and pores (**Figure 6.10k**) can be easy spotted as the specific ring of

amorphous carbon is absent in the pores/voids electrons diffraction patterns. The presence of amorphous regions found in the electrode in a proportion of 15.4 % of the total analyzed area reveals the irreversible damages produced on the battery, impacting the further performances of the solid-state batteries.

As the same area was not analyzed before and after the cycling process is hard to put a pin on which specific phase from the electrode formulation induced the amorphization after the cycling process, but similar phenomena were detected during K-ion intercalation into $FePO_4$ after first cycle using XRD analysis and TEM measurements[303].

To confirm $LiFePO_4$ delithiation after the electrochemical reaction, $FePO_4$ cif file was added for the matching pattern process. **Figure 6.10e** reveals the phase map of the active materials where the presence of $FePO_4$ (FP) and $LiFePO_4$ phase structures were detected using 4D-STEM mapping, the presence of $FePO_4$ being consistent with the delithiation process occurring over the electrochemical cycling. The phase mapping also revealed the presence of the domino-cascade lithiation process with a clear phase separated between LFP and FP grains as sharp interface between the two phases was observed (top left), but also the presence of broad diffuse interfaces (center of the analyzed area). **Figures 6.10g-k** presents the electrons diffraction patterns of LAGP, LFP, FP, amorphous carbon and pores recorded during the scan acquisitions and used for the pattern matching to build the reconstructed the overall phase map presented in the **Figure 6.10f** where it can be observed the presence of broadly diffuse interfaces between LFP and FP particles are located mostly around the amorphous areas.

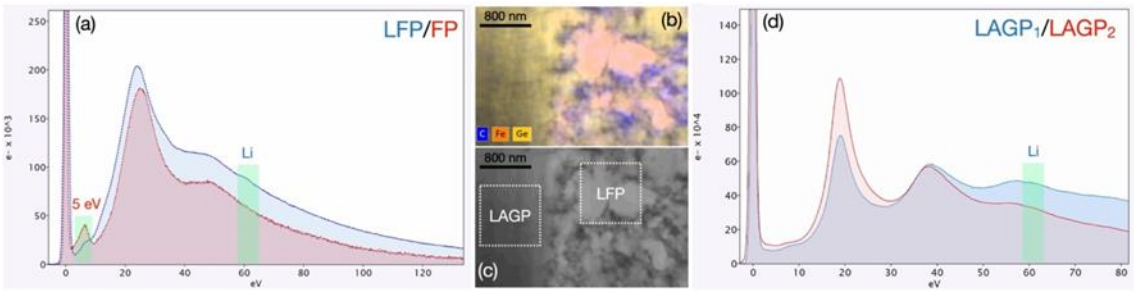


Figure 6.11. (a) EELS spectra of LFP particles inside positive electrode before and after delithiation with bond a 5 eV corresponding to the presence of FePO4 and a modification of Li K-edge peak at 60 eV after lithiation. (b,c) EDX map and STEM-HAADF images of LAGP/cathode interface with probed zone area. (d) EELS spectra in low loss energy of LAGP solid electrolyte before and after delithiation exhibiting slight modifications with presence of Li K-edge peak at 60 eV.

EELS spectroscopy analysis was carried out to estimate the chemical evolution after delithiation process. As shown in **Figure 6.11a**, the presence of a peak at 5 eV is consistence with the delithiation of LFP and the presence of FP structure. The lithium K-edge peak at 60 eV clearly decrease after the electrochemical process indicating a

modification in the lithiation composition inside the iron phosphate crystals. The **Figure 6.11d** shows EELS spectra of LAGP solid electrolyte before and after delithiation exhibiting almost no modifications except slight changes in -Li K-edge peak at 60 eV.

Conclusions and perspectives

$LiFePO_4$/LAGP/$Li_3V_2(PO_4)_3$ all-solid-state battery with high compacity and well-connected interfaces was successfully prepared by Spark Plasma Sintering. The ex-situ cycling results showed the difficulty in cycling such solid-state battery system and revealed the presence of cracks within the solid electrolyte layer and the apparition of rich carbon areas (most likely Li_2CO_3) after the cycling process. Our approach to prepare a FIB lamella micro-battery for *in-situ* electrochemical TEM study from a SPS battery was challenging as the solid electrolyte required a maximum thickness of few tens of micrometers and the full solid-state micro-battery a maximum length of 50 micrometers to fit on the e-chip which allowed bias application. Starting from SPS sintering process and FIB lamella extraction, 5 all-solid-state micro-batteries were successfully obtained.

During the *in-situ* electrochemical TEM experiments, a scan rate of 10 mV/s was applied on the $LiFePO_4$/LAGP/ $Li_3V_2(PO_4)_3$ micro-battery between 0 and 5 V. The CV curve displayed more a resistance graph due to high polarization. After the cycling process, the apparition of two large cracks in the solid electrolyte were noticed. The first crack was located around the secondary phases presented in the micro-battery showing the possible influence of such phases presence within the micro-battery and their electrochemical impact. A second crack was spotted in a thicker area of the solid electrolyte confirming its presence dur to electrochemical reaction. After the cycling process, 2D STEM images showed a reduction in the LAGP particles surface area by ~11.5 % and increase in the grain boundaries regions creating an inter-grain region after the cycling process. Moreover, it was observed that during the cycling process, the secondary particles presented in the solid electrolyte slowly diffused towards to grain boundaries creating large areas.

STEM-EDX map showed the presence of unexpected carbon in the pristine FIB lamella which was no longer detected after the cycling process. Oxygen signal from the solid electrolyte / cathode interface was also reduced, a possible assumption being the formation of Li_2CO_3. 4D-STEM ACOM analysis showed the presence of sharp interfaces between $LiFePO_4$ and $FePO_4$ indicating a domino-cascade lithiation process, but also the presence of broad diffuse interfaces specially located around the amorphous areas induced by cycling. The delithiation process and the confirmation of the electrochemical reaction were

validated by 4D-STEM ACOM and STEM-EELS analysis that confirmed the presence of $FePO_4$ phase.

Main takeaways:

We performed *in-situ* electrochemical STEM study on a LFP/LAGP/LVP FIB lamella micro-battery to understand the nanoscale degradation mechanism of solid-state batteries.

In-situ STEM analysis revealed the apparition of large cracks within solid electrolyte during the cycling process. The presence of secondary phases in the solid electrolyte may influence cracks apparition as their apparition was observed to start around those areas. A reduction by ~11.5 % of the solid electrolyte particles together with the apparition of larger grain boundary phases areas was observed to appear during the battery operation. STEM-EDX map performed before and after the battery cycling indicated a reduction of the oxygen and carbon signals in the solid electrolyte, a possible assumption being the formation of $LiCO_3$. 4D-STEM ACOM analysis revealed sharp interphases between $LiFePO_4$ and $FePO_4$ particles indicating again a domino-cascade lithiation process.

Keywords: *In-situ* electrochemical STEM analysis; Dendrites; Particles shrinkage; Grain boundary phase; Domino-cascade model; Degradation mechanism

Appendix E

$Li_3V_2(PO_4)_3$ synthesis

$Li_3V_2(PO_4)_3$ as anode material was synthetized using solid-state reaction where the precursors VPO_4 and Li_3PO_4 (2:1 molar ratio) were mixed using a mortar and pestle. The obtained composition was placed in a furnace oven under argon atmosphere at a temperature of 800 °C for 2h. **Figure S6.**1a displays the XRD profile fitting analysis of $Li_3V_2(PO_4)_3$ (P21/n space group) without any impurities. The cyclic voltammetry curve of $Li_3V_2(PO_4)_3$ vs. Li^+/Li as anode material is presented in the **Figure S6.**1b and displays between 2 and 1.5 V the peaks corresponding to lithium deinsertion (marked with black arrows).

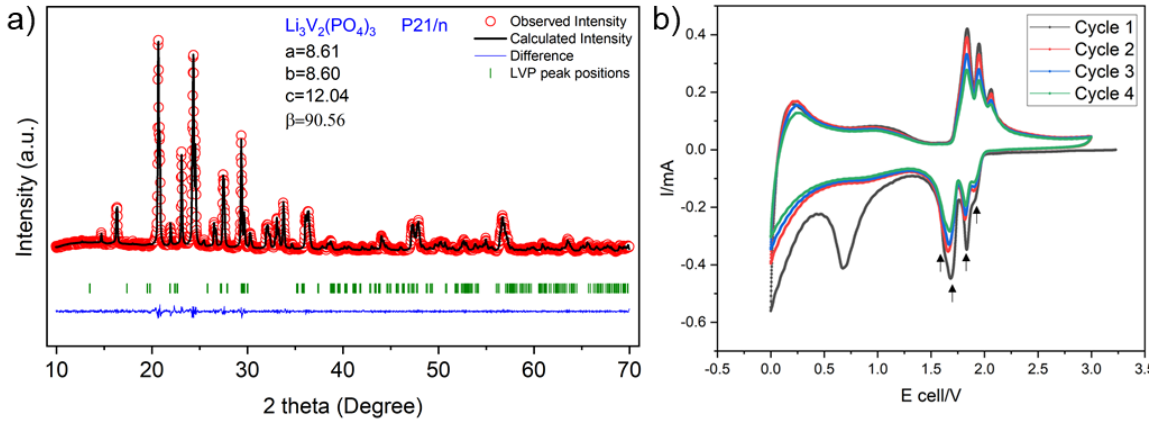


Figure A6.1 a) XRD profile fitting analysis on the $Li_3V_2(PO_4)_3$ using P 21/n space group and b) cyclic voltammetry of $Li_3V_2(PO_4)_3$ vs. Li^+/Li as anode

Electrochemical reaction occurring within the $LiFePO_4$/LAGP/ $Li_3V_2(PO_4)_3$ solid-state battery

Charge Cathode : $LiFePO_4 - 1e^- - 1Li^- \rightarrow FePO_4$

Anode : $Li_3V_2(PO_4)_3 + 0.5e^- + 0.5Li^- \rightarrow Li_{3.5}V_2(PO_4)_3$

$Li_{3.5}V_2(PO_4)_3 + 0.5e^- + 0.5Li^- \rightarrow Li_4V_2(PO_4)_3$

Discharge Cathode : $FePO_4 + 1e^- + 1Li^- \rightarrow LiFePO_4$

Anode : $Li_4V_2(PO_4)_3 - 0.5e^- - 0.5Li^- \rightarrow Li_{3.5}V_2(PO_4)_3$

$Li_{3.5}V_2(PO_4)_3 - 0.5e^- - 0.5Li^- \rightarrow Li_3V_2(PO_4)_3$

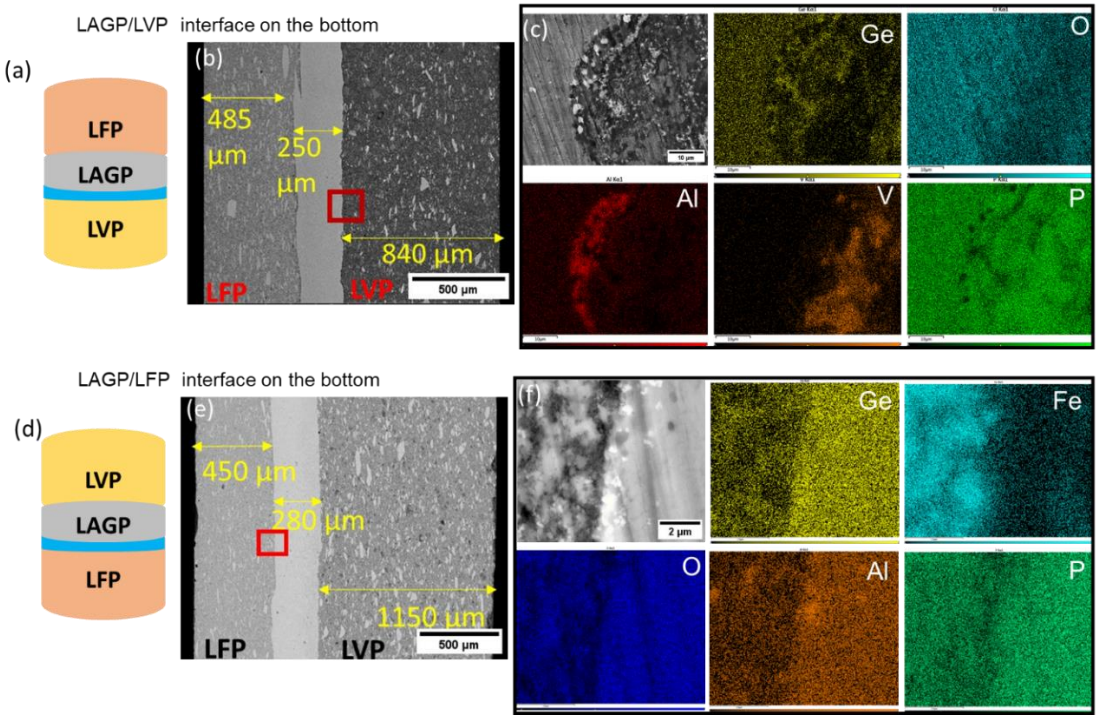


Figure A6.2 (a,d) Schematic representation of a $LiFePO_4$/LAGP/ $Li_3V_2(PO_4)_3$ battery and their (b,e) SEM micrograph after the SPS process showing the (c,f) the SEM-EDX analysis of the interphase formed at the bottom side.

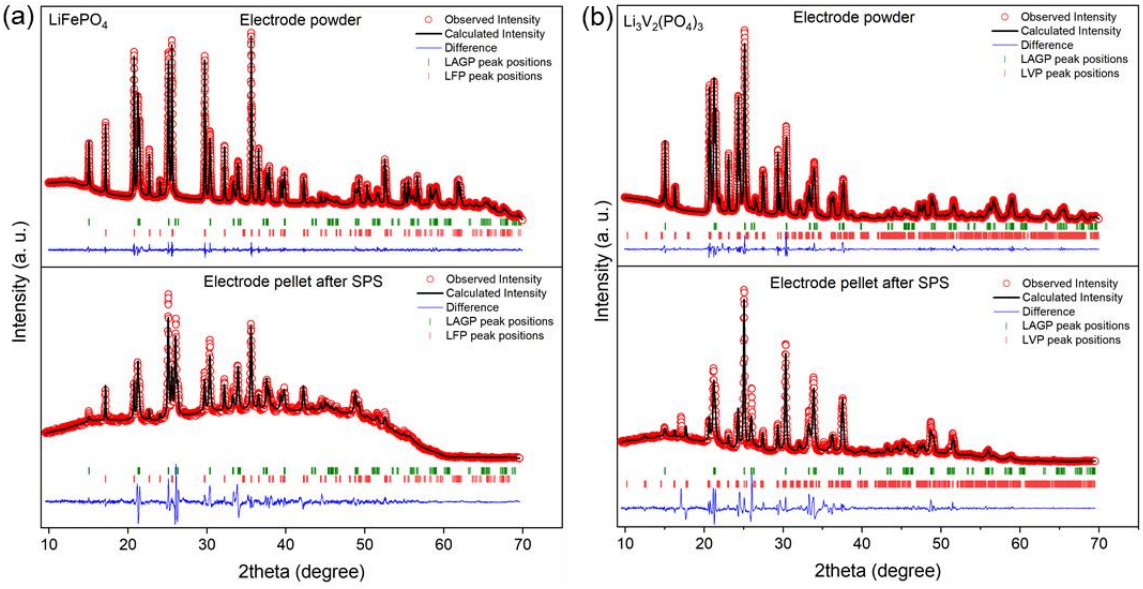


Figure A6.3 XRD profile fitting of (a) $LiFePO_4$ and (b) $Li_3V_2(PO_4)_3$ electrode mixture before and after the SPS process.

Chapter VII

Conclusions and perspectives

The work presented in this manuscript was performed in ~3.5 years as a collaboration between Université de Picardie Jules Verne & CNRS, Amiens, France and Nanyang Technological University, Singapore. During the doctoral studies, the author was hosted by Laboratoire de Reactivite et Chimie des Solides (LRCS) for 2.5 years and for one year by Facility for Analysis, Characterisation, Testing and Simulation (FACTS) at MSE, Nanyang Technological University, Singapore.

The work presented during this thesis involved the synthesis of battery components (solid electrolyte, active material), assembling, cycling, improving all-solid-state batteries performances and the main goal, understanding the overall degradation mechanism governing the failure of solid-state batteries in order to design better future batteries. To achieve this objective, various ex-situ (XRD, SEM, TEM, FIB-SEM tomography, X-ray CT, NMR, SIMS) and *in-situ* characterization methods (X-ray CT and electrochemical STEM) were carried out focusing on different parts of the battery. In the initial outline, the author was planned to focus for 1.7 years in LRCS on tasks as battery materials synthesis, battery preparation and cycling and for 1.7 years at NTU for battery investigations using FIB-SEM tomography, FIB lamella preparation and *in-situ* electrochemical (S)TEM experiments on all-solid-state batteries. Unfortunately, due to pandemic reasons the period hosted at NTU was drastically reduced. Several experiments which were initially planned to be performed at NTU (*in-situ* STEM experiments) were performed in LRCS and others characterization techniques were added to offer a broader view on the degradation mechanism of solid-state batteries.

The criteria for choosing the materials for our solid-state batteries was done based on battery performance, compatibility between solid electrolyte and electrodes and restricting parameters during the battery analysis. We choose $Li_{1.5}Al_{0.5}Ge_{1.5}(PO_4)_3$ as solid electrolyte due to its high stability in the air (*i.e.* FIB lamellas required air exposure during the transfer from FIB to TEM), wide electrochemical window compared to other solid electrolytes and acceptable ionic conductivity. As positive electrode, $LiFePO_4$ was chosen

due to its high theoretical capacity, high thermal stability, and safety. A high compatibility between battery components and no degradation during spark plasma sintering assembly constituted another important parameter. As anode, we based our studies on metallic lithium to obtain high energy density batteries and $Li_3V_2PO_4$ to make a monolithic all-solid-state battery.

As starting point, we synthetized the solid electrolyte using sol-gel method and obtained densified pellets with high ionic conductivity using spark plasma sintering. As the grain boundaries region restricts the ionic conductivity in oxide solid-state batteries, we focused on understanding the impact of the morphology of the grain boundary region and their structure on the total ionic conductivity of LAGP. FIB-SEM tomography analysis revealed the presence of an inter-grain region presented like a network around the LAGP grains, the inter-grain region being found in a lower volume for the high sintering temperatures, compared to low sintering temperatures. Our combined approach using SEM-EDX, XRD, MAS-NMR and DFT calculations revealed that the inter-grain region was comprised of $Li_4P_2O_7$ and disordered $Li_9Al_3(P_2O_7)_3(PO_4)_2$ phases. An optimum ionic conductivity value was achieved when LAGP pellet was sintered at 680 °C and $Li_9Al_3(P_2O_7)_3(PO_4)_2$ phase dominating the grain boundary region with reduced contributions from the highly ordered $Li_4P_2O_7$ phases. As perspectives, designing synthesis method where the grain boundaries region is constituted of highly conductive materials could represent an interesting approach to increase the ionic conductivity of oxide based solid electrolytes.

Understanding the (electro)chemical-mechanical reactions occurring at the interface between LAGP and metallic lithium represented one of our main objectives. SEM and TEM analysis revealed a high chemical instability of LAGP towards metallic lithium, the presence of dendrites and degradation products being spotted on the surface of LAGP within the first hours of contact. During the electrochemical reaction, ex-situ X-ray tomography experiments showed the presence of dendrites, cracks, and a surface lamination effect on the solid electrolyte; their number increasing when a higher current density was applied.

Our *in-situ* X-ray µ computed tomography experiments revealed the dynamics of the electrochemical reactions occurring at the interface of LAGP and metallic lithium. The presence of hot spots containing a layer with lithium degradation products and a layer with degradation products resulted from the reduction reaction of LAGP were spotted. We observed the apparition of cracks in the form of spallations in the solid electrolyte and its growth over the cycling process. Based on our observation, we proposed a degradation

mechanism of LAGP when cycled vs. Li^+/Li. As perspectives, designing a cell that allows the control of the pressure during cycling and experiments where combining X-ray µ-computed tomography with analytic methods as XPS could provide a better comprehension of the reactions occurring at the interface between solid electrolyte and metallic lithium.

Our ambition in preparing and cycling an all-solid-state battery without liquid electrolyte in any part of the battery turned out to be more challenging than expected. We identified various limitations parameters in the battery as: ionic transport limitations, interfacial resistance, inhomogeneous electrode compositions and cycling conditions for which we tried to bring solutions to improve the cycling performances. Compared to first trials, the electrochemical performances of the all-solid-state battery were improved but unfortunately, they are still far from the reported literature where the electrode composite is prepared based on a mixture containing additives and also liquid electrolyte. Our all-solid state $LiFePO_4$/LAGP/Li metal battery delivered a low charge capacity of 56 $mAh.g^{-1}$ in the first cycle and battery performances decreased even more after only 7 cycles. As degradation mechanism, post-mortem SEM analysis indicated the presence of large cracks and lithium dendrites that infiltrate inside the solid electrolyte layer growing "jellyfish arms". STEM-EDX map analysis performed on a FIB lamella exacted from the interface indicated the diffusion of iron and carbon from the cathode into the solid electrolyte layer. 4D-STEM ACOM analysis showed the presence of $LiFePO_4$ and $FePO_4$ particles which are fully deliathiated and bound proving the domino-cascade model at nanoscale level. As perspectives, playing with parameters as the thickness of the solid electrolyte, cathode and anode, controlling the pressure of the cell and inserting a protection layer between the solid electrolyte and metallic lithium could further improve the cycling performances of an oxide solid-state battery.

In the end, we tried to understand the degradation mechanism of all-solid-state batteries at the nanoscale by performing *in-situ* electrochemical TEM experiments. This experiment came out with more challenges that expected: FIB lamella restrictions, ionic conductivity limitations at room temperature and avoiding e-beam damage on the FIB lamella. To carry out such challenging experiment, a micro-battery was extracted from thin layer solid electrolyte spark plasma sintered battery and installed on an e-chip from Protochips. Our *in-situ* electrochemical TEM experiment revealed after the cycling process the formation of cracks within the solid electrolyte and the apparition of a grain boundary area between the shrinked LAGP particles. The diffusion of iron from the positive electrode into the solid electrolyte layer after the cycling process was detected using STEM-EDX map analysis. The appearance of amorphous areas in the solid electrolyte after the electrochemical reaction was detected using 4D-STEM ACOM analysis method. The

presence of $LiFePO_4$ and $FePO_4$ particles which proves that the electrochemical reaction took well place was confirmed with 4D-STEM ACOM and STEM-EELS analysis methods.

It should be noted that performing such experiment is quite challenging giving the number of limiting parameters encountered during this experiment and this study remains one of the few performed in the battery field. As perspectives, cycling the micro-battery at a higher temperature to increase the ionic conductivity will help removing the ionic transport limitations. Also, designing a new configuration of the micro-battery that offers more support/strength and will induce fewer mechanical damages during the cycling process will be required.

As general conclusion, the work in this thesis tried to focus on understanding of the degradation mechanisms of all-solid-state batteries by combining various characterization methods and tried to offer a multiscale view on the processes occurring in the different parts of the LAGP-based battery. To understand the failure mechanism from a microscale point of view we used FIB-SEM tomography, SEM and X-ray µ-computed tomography techniques and for a nanoscale point of view we used a combined approach between STEM and 4D-STEM ACOM analysis methods. Our experiments showed that at microscale the failure mechanism consist of dendrites and cracks formation, together with a delamination surface effect of LAGP. At a nanoscale, the degradation mechanism consisted of LAGP particles shrinkage, formation of an inter-grain phase, apparition of amorphous areas in the solid electrolyte and iron diffusion the electrodes to solid electrolyte layer.

As further perspectives regarding the battery field, probably the successful solid-state battery will be based on a hybrid technology (sulfide solid electrolyte and solid polymer electrolyte or oxide and solid polymer electrolyte) where different types of solid electrolytes are combined to obtain better cycling performances. Investigating such a hybrid solid-state battery using in-situ/operando experiments (*i.e* X-ray nano/µ computed tomography) could provide valuable insights about the limiting factors of the next generation of solid-state batteries.

Résume de la thèse en français

Les travaux présentés dans ce manuscrit ont été réalisés en ~3,5 ans dans le cadre d'une collaboration entre l'Université de Picardie Jules Verne & CNRS, Amiens, France et la Nanyang Technological University, Singapour. Pendant les études doctorales, l'auteur a été accueilli pour 2,5 ans par le Laboratoire de Réactivité et Chimie des Solides (LRCS) et un an par Ecole de science des matériaux et ingénierie à Nanyang Technological University, Singapour.

Les travaux présentés au cours de cette thèse ont impliqué la synthèse des composants de la batterie (électrolyte solide, matériau actif), l'assemblage, le cyclage, l'amélioration des performances des batteries tout-solides et l'objectif principal : la compréhension du mécanisme de dégradation des batteries tout-solides afin de concevoir de meilleures batteries dans l'avenir. Pour atteindre ces objectifs, différentes méthodes de caractérisation ex-situ (*i.e.* XRD, MEB, TEM, tomographie FIB-SEM, X-ray CT, NMR, SIMS) et *in-situ* (*i.e.* X-ray CT et STEM) ont été employés en se concentrant sur différentes parties de la batterie ou sur toute la batterie tout-solide. Dans le planning initial du projet, il était prévu que l'auteur passera 1,7 an au LRCS sur des tâches telles que la synthèse de matériaux des batteries, la préparation, assemblage et le cyclage des batteries tout-solide. Un autre demi de la thèse (1,7 an) était prévu à NTU pour la caractérisation des batteries en utilisant la tomographie FIB-SEM, la préparation de lamelles FIB pour réalise des expériences électrochimiques *in-situ* (S)TEM sur des batteries tout-solides. Malheureusement, pour des raisons de pandémie, la période passée à NTU a été considérablement réduite. Plusieurs expériences initialement prévues à NTU (expériences *in-situ* STEM) ont été réalisées au LRCS et des autres techniques de caractérisation ont été ajoutées afin d'offrir une vision plus large sur le mécanisme de dégradation des batteries tout-solide.

Les critères de sélection des matériaux pour nos batteries solides ont été basés sur les performances des batteries, la compatibilité entre l'électrolyte solide et les électrodes et aussi les paramètres restrictifs pendant l'analyse des batteries (sensibilité a l'air). Nous

avons choisi $Li_{1.5}Al_{0.5}Ge_{1.5}(PO_4)_3$ comme électrolyte solide suite à sa bonne stabilité dans l'air (les lamelles FIB ont dû être exposées à l'air pendant le transfert du FIB au TEM), sa large stabilité électrochimique par rapport aux autres électrolytes solides et de sa conductivité ionique acceptable. Comme électrode positive, nous avons choisi $LiFePO_4$ suite à sa capacité théorique élevée, grande stabilité thermique et bonne conditionne des sécurités. En tant qu'anode, nous avons basé nos études sur le lithium métallique pour obtenir des batteries à haute densité d'énergie et sur le $Li_3V_2PO_4$ pour réaliser une batterie monolithique à l'état solide. Une compatibilité élevée entre les composants de la batterie et l'absence de dégradation pendant l'assemblage par frittage au plasma constituaient un autre paramètre important.

Comme point de départ, nous avons commencé par la synthèse de l'électrolyte solide en utilisant la méthode sol-gel et obtenir des pastilles très densifiées par frittage au plasma afin d'obtenir des pellets avec une haute conductivité ionique. Comme les joints de grains sont connu pour limite la conductivité ionique dans les électrolytes solides à base d'oxyde nous avons cherché à comprendre l'impact de la morphologie et de la structure des joints de grains sur la conductivité ionique totale du LAGP. L'analyse par tomographie FIB-MEB a révélé la présence d'une région aux joints des grains présentée comme un réseau autour des grains de LAGP. Nous avons constaté que la région détecte aux joints des grains a été trouvé dans un volume plus faible pour les hautes températures de frittage, par rapport aux échantillons prépare à basses températures de frittage. Notre approche combinée utilisant MEB-EDX, XRD, MAS-NMR et des calculs DFT a révélé que la région situe aux joints des grains était composée de $Li_4P_2O_7$ et $Li_9Al_3(P_2O_7)_3(PO_4)_2$ désordonnées. Une valeur optimale de conductivité ionique a été obtenue lorsque la pastille de LAGP a été frittée à 680 °C et que la phase $Li_9Al_3(P_2O_7)_3(PO_4)_2$ a dominé la région des joints des grains avec des contributions réduites du $Li_4P_2O_7$ hautement ordonnées. Comme perspectives, la conception d'une méthode de synthèse où la région des joints des grains est constituée de matériaux hautement conducteurs pourrait représenter une approche intéressante pour augmenter la conductivité ionique des électrolytes solides à base d'oxydes.

La compréhension des réactions (électro)chimiques-mécaniques qui se produisant à l'interface entre le LAGP et le lithium métallique représentait l'un de nos principaux objectifs. Les analyses MEB et TEM ont révélé une grande instabilité chimique du LAGP vis-à-vis du lithium métallique, où la présence des dendrites et de produits de dégradation étant repérée à la surface du LAGP lors des premières heures de contact entre les deux. Pendant la réaction électrochimique, les expériences ex-situ de tomographie aux rayons X ont montré la présence des dendrites, des fissures et d'un effet de laminage de surface sur

l'électrolyte solide ; leur présence augmentant lorsqu'une densité de courant plus élevée a été appliquée.

Nos expériences *in-situ* de tomographie aux rayons X ont révélé la dynamique des réactions électrochimiques qui se produisant à l'interface du LAGP et du lithium métallique. Nous avons repéré la présence des zones contenant une couche avec des produits de dégradation du lithium et une couche avec des produits de dégradation résultant de la réaction de réduction du LAGP. Nous avons observé l'apparition de fissures sous forme de spallations dans l'électrolyte solide et leur croissance au cours du processus de cyclage. En nous basent sur ces observations, nous avons proposé un mécanisme de dégradation du LAGP lors du cyclage vs. Li^+/Li. Comme perspectives, la conception d'une cellule qui permet le contrôle de la pression pendant le cyclage et des expériences où combiner la tomographie aux rayons X avec des méthodes analytiques comme le XPS pourrait fournir une meilleure compréhension des réactions qui se produisant à l'interface entre l'électrolyte solide et le lithium métallique.

Notre ambition de préparer et de cycler une batterie entièrement solide, sans ajoute d'électrolyte liquide dans aucune partie de la batterie, a été plus difficile que prévu. Nous avons identifié plusieurs paramètres limitants les performances des batteries tout-solides tels que : les limitations suite au transport ionique, la résistance interfaciale, les compositions d'électrodes inhomogènes et les conditions de cyclage. Pour tout ça nous avons essayé d'apporter des solutions pour améliorer les performances de cyclage des batteries tout-solides. Par rapport aux premiers essais, les performances électrochimiques des batteries tout-solides ont été améliorées mais malheureusement, elles sont encore loin de celles rapportées dans la littérature où le composite d'électrode est préparé à partir d'un mélange contenant des additifs et électrolyte liquide. Notre batterie $LiFePO_4$/LAGP/Li métal a présente une faible capacité de charge de 56 mAh.g-1 dans le premier cycle et les performances de la batterie ont diminué encore plus après seulement 7 cycles. Comme mécanisme de dégradation, l'analyse MEB post-mortem a indiqué la présence de grandes fissures et des dendrites de lithium qui s'infiltrent à l'intérieur de la couche d'électrolyte solide en formant des " bras de méduse ". L'analyse cartographique STEM-EDX effectuée sur une lamelle FIB prélevée à l'interface (l'electrolyte solide avec $LiFePO_4$) a indiqué une diffusion de fer et de carbone du la couche de cathode dans la couche d'électrolyte solide. L'analyse ACOM 4D-STEM a montré la présence de particules de $LiFePO_4$ et de $FePO_4$ qui sont entièrement déliées et liées, ce qui prouve qu'à l'échelle nanométrique on a le modèle domino-cascade comme modelé de delithiation. Comme perspectives, jouer avec des paramètres tels que l'épaisseur de l'électrolyte solide, de la cathode et de l'anode, contrôler la pression de la cellule et insérer une couche de protection entre l'électrolyte

solide et le lithium métallique pourrait encore améliorer les performances de cyclage d'une batterie tout-solide à base des oxydes.

Nous avons essayé de comprendre le mécanisme de dégradation des batteries tout-solides à l'échelle nanométrique en réalisant des expériences *in-situ* électrochimiques TEM. Cette expérience a été plus difficile que prévu suite aux : restrictions de la lamelle FIB et longueur totale de la batterie tout solide (mois du 50 µm pour une batterie qui doit contenir l'électrode positive, l'electrolyte solide et l'électrode négatif), les limitations en conductivité ionique à température ambiante et la nécessité d'éviter les dommages causés par le faisceau d'électrons sur la lamelle du FIB. Pour réaliser cette expérience difficile, une microbatterie a été extraite d'une batterie plus large frittée par plasma, batterie qui présentait une couche d'electrolyte solide très fine. Ultérieurement, la microbatterie a été installée sur un chip désigne spécialement par Protochips pour réalise des manip *in-situ* (application du curent électrique).

Notre expérience *in-situ* TEM a révélé après le processus de cyclage la formation de fissures dans l'électrolyte solide, la croissance de la zone aux joins de grains et la réduction des particules du LAGP. En utilisant l'analyse cartographique STEM-EDX, la diffusion du fer de l'électrode positive dans la couche d'électrolyte solide après le processus de cyclage a été détectée. L'apparition de zones amorphes dans l'électrolyte solide après la réaction électrochimique a été également observe. La présence de particules de $LiFePO_4$ et de $FePO_4$, qui prouve que la réaction électrochimique a bien eu lieu, a été confirmée par les méthodes d'analyse 4D-STEM ACOM et STEM-EELS.

Il faut noter que la réalisation d'une telle expérience est assez difficile étant donné le nombre de paramètres limitatifs rencontrés au cours de cette expérience et cette étude reste l'une des rares expériences réalisées dans le domaine des batteries. Comme perspectives, le cyclage de la microbatterie à une température plus élevée pour augmenter la conductivité ionique aidera à éliminer les limitations du transport ionique. Il faudra également concevoir une nouvelle configuration de la microbatterie qui offre plus de support/résistance et qui induira moins de dommages mécaniques pendant le processus de cyclage.

En conclusion générale, le travail de cette thèse a essayé de se concentrer sur la compréhension des mécanismes de dégradation des batteries tout-solides en combinant diverses méthodes de caractérisation et a essayé d'offrir une vue multi-échelle sur les processus qui se produisant dans les différentes parties de la batterie. Pour comprendre le mécanisme de degradation d'un point de vue microscopique, nous avons utilisé des techniques de tomographie FIB-SEM, MEB et la tomographie aux rayons X. D'un point de

vue nanométrique, nous avons utilisé une approche combinée entre les méthodes d'analyse STEM et 4D-STEM ACOM. Nos expériences ont montré qu'à l'échelle microscopique, le mécanisme de degradation consiste en la formation des dendrites et de fissures, ainsi qu'en un effet de surface de délamination du LAGP. A l'échelle nanométrique, le mécanisme de dégradation consiste en la réduction de taille des particules de LAGP, la croissance de la région aux joints des grains, l'apparition de zones amorphes dans l'électrolyte solide et la diffusion du fer présent dans l'électrodes vers la couche d'électrolyte solide.

En ce qui concerne les perspectives dans le domaine des batteries, il est probable que la batterie tout-solide la plus performante sera basée sur une technologie hybride (*i.e.* électrolyte solide à base de sulfure et électrolyte solide à base de polymère) où différents types d'électrolytes solides sont combinés pour obtenir les meilleures performances de cyclage et stabilité chimique. L'étude d'une telle batterie hybride en utilisant des méthodes d'analyse *in-situ/operando* (tomographie aux rayons X, MEB, TEM) pourrait fournir des informations précieuses sur les facteurs limitants de la prochaine génération de batteries solides.

References

(1) *Total greenhouse gas emission trends and projections in Europe*. https://www.eea.europa.eu/ims/total-greenhouse-gas-emission-trends (accessed 2021-12-16).

(2) *Global CO2 emissions have been flat for a decade, new data reveals*. https://www.carbonbrief.org/global-co2-emissions-have-been-flat-for-a-decade-new-data-reveals/.

(3) Chu, S.; Majumdar, A. Opportunities and Challenges for a Sustainable Energy Future. *Nature* **2012**, *488* (7411), 294–303. https://doi.org/10.1038/nature11475.

(4) Chu, S.; Cui, Y.; Liu, N. The Path towards Sustainable Energy. *Nat Mater* **2016**, *16* (1), 16–22. https://doi.org/10.1038/nmat4834.

(5) Ritchie, H.; Roser, M. CO_2 and Greenhouse Gas Emissions. *Our World in Data* **2020**.

(6) Yang, Z.; Zhang, J.; Kintner-Meyer, M. C. W.; Lu, X.; Choi, D.; Lemmon, J. P.; Liu, J. Electrochemical Energy Storage for Green Grid. *Chem Rev* **2011**, *111* (5), 3577–3613. https://doi.org/10.1021/cr100290v.

(7) Yang, Y.; Bremner, S.; Menictas, C.; Kay, M. Battery Energy Storage System Size Determination in Renewable Energy Systems: A Review. *Renewable and Sustainable Energy Reviews* **2018**, *91* (March), 109–125. https://doi.org/10.1016/j.rser.2018.03.047.

(8) Chen, H.; Cong, T. N.; Yang, W.; Tan, C.; Li, Y.; Ding, Y. Progress in Electrical Energy Storage System: A Critical Review. *Progress in Natural Science* **2009**, *19* (3), 291–312. https://doi.org/10.1016/j.pnsc.2008.07.014.

(9) Deng, J.; Bae, C.; Denlinger, A.; Miller, T. Electric Vehicles Batteries: Requirements and Challenges. *Joule* **2020**, *4* (3), 511–515. https://doi.org/10.1016/j.joule.2020.01.013.

(10) Mahlia, T. M. I.; Saktisahdan, T. J.; Jannifar, A.; Hasan, M. H.; Matseelar, H. S. C. A Review of Available Methods and Development on Energy Storage; Technology Update. *Renewable and Sustainable Energy Reviews* **2014**, *33*, 532–545. https://doi.org/10.1016/j.rser.2014.01.068.

(11) Goodenough, J. B.; Park, K. S. The Li-Ion Rechargeable Battery: A Perspective. *J Am Chem Soc* **2013**, *135* (4), 1167–1176. https://doi.org/10.1021/ja3091438.

(12) Ruyet, R. le. Identification of New Mg2+ Solid Ionic Conductors through the Exploration of the Mg(BH4)2-Mg(NH2)2 Phases Diagram-PhD Thesis. **2020**, No. Université de Picardie Jules Verne.

(13) Palacín, M. R.; de Guibert, A. Batteries: Why Do Batteries Fail? *Science (1979)* **2016**, *351* (6273). https://doi.org/10.1126/science.1253292.

(14) Yoshino, A. The Birth of the Lithium-Ion Battery. *Angewandte Chemie - International Edition* **2012**, *51* (24), 5798–5800. https://doi.org/10.1002/anie.201105006.

(15) Lopes, B. P. P.; Stamenkovic, V. R. Past, Present, and Future of Lead–Acid Batteries. 923–925.

(16) Zhang, J.; Chen, C.; Zhang, X.; Liu, S. Study on the Environmental Risk Assessment of Lead-Acid Batteries. *Procedia Environ Sci* **2016**, *31*, 873–879. https://doi.org/10.1016/j.proenv.2016.02.103.

(17) J.M. Tarascon and M. Armand. Issues and Challenges Facing Rechargeable Lithium Batteries. *Nature* **2001**, *414*, 359–367.

(18) Nitta, N.; Wu, F.; Lee, J. T.; Yushin, G. Li-Ion Battery Materials : Present and Future. *Materials Today* **2015**, *18* (5), 252–264. https://doi.org/10.1016/j.mattod.2014.10.040.

(19) Blomgren, G. E. The Development and Future of Lithium Ion Batteries. *J Electrochem Soc* **2017**, *164* (1), A5019–A5025. https://doi.org/10.1149/2.0251701jes.

(20) Scrosati, B.; Garche, J. Lithium Batteries: Status, Prospects and Future. *J Power Sources* **2010**, *195* (9), 2419–2430. https://doi.org/10.1016/j.jpowsour.2009.11.048.

(21) Ding, Y.; Cano, Z. P.; Yu, A.; Lu, J.; Chen, Z. Automotive Li-Ion Batteries: Current Status and Future Perspectives. *Electrochemical Energy Reviews* **2019**, *2* (1). https://doi.org/10.1007/s41918-018-0022-z.

(22) Deng, D. Li-Ion Batteries: Basics, Progress, and Challenges. *Energy Sci Eng* **2015**, *3* (5), 385–418. https://doi.org/10.1002/ese3.95.

(23) Hajndl, O. Batterie Tout Solide Pour Application Automobile : Processus de Mise En Forme et Étude Des Interfaces. *Http://Www.Theses.Fr* **2019**.

(24) Li, M.; Lu, J.; Chen, Z.; Amine, K. 30 Years of Lithium-Ion Batteries. **2018**, *1800561*, 1–24. https://doi.org/10.1002/adma.201800561.

(25) Dunn, B.; Kamath, H.; Tarascon, J. M. Electrical Energy Storage for the Grid: A Battery of Choices. *Science (1979)* **2011**, *334* (6058), 928–935. https://doi.org/10.1126/science.1212741.

(26) Mishra, A.; Mehta, A.; Basu, S.; Malode, S. J.; Shetti, N. P.; Shukla, S. S.; Nadagouda, M. N.; Aminabhavi, T. M. Electrode Materials for Lithium-Ion Batteries. *Mater Sci Energy Technol* **2018**, *1* (2), 182–187. https://doi.org/10.1016/j.mset.2018.08.001.

(27) Lung-Hao Hu, B.; Wu, F. Y.; Lin, C. te; Khlobystov, A. N.; Li, L. J. Graphene-Modified LiFePO4 Cathode for Lithium Ion Battery beyond Theoretical Capacity. *Nat Commun* **2013**, *4*, 1–7. https://doi.org/10.1038/ncomms2705.

(28) Shu, J.; Shui, M.; Huang, F.; Ren, Y.; Wang, Q.; Xu, D.; Hou, L. A New Look at Lithium Cobalt Oxide in a Broad Voltage Range for Lithium-Ion Batteries. *Journal of Physical Chemistry C* **2010**, *114* (7), 3323–3328. https://doi.org/10.1021/jp911994b.

(29) Yang, Y.; Shu, D.; Yu, H.; Xia, X.; Lin, Z. G. Investigations of Lithium Manganese Oxide Materials for Lithium-Ion Batteries. *J Power Sources* **1997**, *65* (1–2), 227–230. https://doi.org/10.1016/S0378-7753(97)02476-2.

(30) Liu, C.; Neale, Z. G.; Cao, G. Understanding Electrochemical Potentials of Cathode Materials in Rechargeable Batteries. *Materials Today* **2016**, *19* (2), 109–123. https://doi.org/10.1016/j.mattod.2015.10.009.

(31) Mohamed, N.; Allam, N. K. Recent Advances in the Design of Cathode Materials for Li-Ion Batteries. *RSC Adv* **2020**, *10* (37), 21662–21685. https://doi.org/10.1039/d0ra03314f.

(32) Wang, L.; Wu, Z.; Zou, J.; Gao, P.; Niu, X.; Li, H.; Chen, L. Li-Free Cathode Materials for High Energy Density Lithium Batteries. *Joule* **2019**, *3* (9), 2086–2102. https://doi.org/10.1016/j.joule.2019.07.011.

(33) Manthiram, A. A Reflection on Lithium-Ion Battery Cathode Chemistry. *Nat Commun* **2020**, *11* (1), 1–9. https://doi.org/10.1038/s41467-020-15355-0.

(34) Kim, S.; Yin, L.; Lee, M. H.; Parajuli, P.; Blanc, L.; Fister, T. T.; Park, H.; Kwon, B. J.; Ingram, B. J.; Zapol, P.; Klie, R. F.; Kang, K.; Nazar, L. F.; Lapidus, S. H.; Vaughey, J. T. High-Voltage Phosphate Cathodes for Rechargeable Ca-Ion Batteries. *ACS Energy Lett* **2020**, *5* (10), 3203–3211. https://doi.org/10.1021/acsenergylett.0c01663.

(35) Université, D.; Jules, D. P. Thèse de Doctorat Tuan-Tu Nguyen. **2021**, No. Ed 585.

(36) Wang, K.; Jin, Y.; Sun, S.; Huang, Y.; Peng, J.; Luo, J.; Zhang, Q.; Qiu, Y.; Fang, C.; Han, J. Low-Cost and High-Performance Hard Carbon Anode Materials for Sodium-Ion Batteries. **2017**. https://doi.org/10.1021/acsomega.7b00259.

(37) Zheng, H.; Qu, Q.; Zhang, L.; Battaglia, V. S. RSC Advances Hard Carbon : A Promising Lithium-Ion Battery Anode for High Temperature Applications with Ionic Electrolyte. **2012**, 4904–4912. https://doi.org/10.1039/c2ra20536j.

(38) Ma, C.; Zhao, Y.; Guo, Q.; Liu, L.; Shi, J. Synthesis and Electrochemical Properties of Artificial Graphite as an Anode for High-Performance Lithium-Ion Batteries. *Carbon N Y* **2013**, *64*, 553–556. https://doi.org/10.1016/j.carbon.2013.07.089.

(39) Xu, W.; Wang, J.; Ding, F.; Chen, X.; Nasybulin, E.; Zhang, Y.; Zhang, J. G. Lithium Metal Anodes for Rechargeable Batteries. *Energy Environ Sci* **2014**, *7* (2), 513–537. https://doi.org/10.1039/c3ee40795k.

(40) Yi, T. F.; Yang, S. Y.; Xie, Y. Recent Advances of Li4Ti5O12 as a Promising next Generation Anode Material for High Power Lithium-Ion Batteries. *J Mater Chem A Mater* **2015**, *3* (11), 5750–5777. https://doi.org/10.1039/c4ta06882c.

(41) Casimir, A.; Zhang, H.; Ogoke, O.; Amine, J. C.; Lu, J.; Wu, G. Nano Energy Silicon-Based Anodes for Lithium-Ion Batteries : Effectiveness of Materials Synthesis and Electrode Preparation. *Nano Energy* **2016**, *27*, 359–376. https://doi.org/10.1016/j.nanoen.2016.07.023.

(42) Loaiza, L. C.; Monconduit, L.; Seznec, V. Si and Ge-Based Anode Materials for Li-, Na-, and K-Ion Batteries: A Perspective from Structure to Electrochemical Mechanism. *Small* **2020**, *16* (5), 1–29. https://doi.org/10.1002/smll.201905260.

(43) Yin, L.; Chai, S.; Wang, F.; Huang, J.; Li, J.; Liu, C.; Kong, X. Ultrafine SnO2 Nanoparticles as a High Performance Anode Material for Lithium Ion Battery. *Ceram Int* **2016**, *42* (8), 9433–9437. https://doi.org/10.1016/j.ceramint.2016.02.173.

(44) Wang, P.; Gou, X. X.; Xin, S.; Cao, F. F. Facile Synthesis of CuO Nanochains as High-Rate Anode Materials for Lithium-Ion Batteries. *New Journal of Chemistry* **2019**, *43* (17), 6535–6539. https://doi.org/10.1039/c9nj01015g.

(45) Kim, M. C.; Kim, S. J.; Han, S. B.; Kwak, D. H.; Hwang, E. T.; Kim, D. M.; Lee, G. H.; Choe, H. S.; Park, K. W. Cubic and Octahedral Cu2O Nanostructures as Anodes for Lithium-Ion Batteries. *J Mater Chem A Mater* **2015**, *3* (45), 23003–23010. https://doi.org/10.1039/c5ta05455a.

(46) Yang, Y.; Yuan, W.; Zhang, X.; Wang, C.; Yuan, Y.; Huang, Y.; Ye, Y.; Qiu, Z.; Tang, Y. A Review on FexOy-Based Materials for Advanced Lithium-Ion Batteries. *Renewable and Sustainable Energy Reviews* **2020**, *127* (July 2019), 109884. https://doi.org/10.1016/j.rser.2020.109884.

(47) Liu, H.; Wang, G.; Liu, J.; Qiao, S.; Ahn, H. Highly Ordered Mesoporous NiO Anode Material for Lithium Ion Batteries with an Excellent Electrochemical Performance. *J Mater Chem* **2011**, *21* (9), 3046–3052. https://doi.org/10.1039/c0jm03132a.

(48) Zhong, K.; Xia, X.; Zhang, B.; Li, H.; Wang, Z.; Chen, L. MnO Powder as Anode Active Materials for Lithium Ion Batteries. *J Power Sources* **2010**, *195* (10), 3300–3308. https://doi.org/10.1016/j.jpowsour.2009.11.133.

(49) Zhang, H.; Yang, Y.; Ren, D.; Wang, L.; He, X. Graphite as Anode Materials: Fundamental Mechanism, Recent Progress and Advances. *Energy Storage Mater* **2021**, *36* (October 2020), 147–170. https://doi.org/10.1016/j.ensm.2020.12.027.

(50) Asenbauer, J.; Eisenmann, T.; Kuenzel, M.; Kazzazi, A.; Chen, Z.; Bresser, D. The Success Story of Graphite as a Lithium-Ion Anode Material-Fundamentals, Remaining Challenges, and Recent Developments Including Silicon (Oxide) Composites. *Sustain Energy Fuels* **2020**, *4* (11), 5387–5416. https://doi.org/10.1039/d0se00175a.

(51) Université, D.; Jules, D. P. Studies on Inorganic Solid Electrolytes for Batteries : Focus on Na3PS4 Theodosios Famprikis To Cite This Version : HAL Id : Tel-03626202 Thèse de Doctorat Theodosios Famprikis Pour Obtenir Le Grade de Docteur de l ' Université de Picardie Jules Verne Stu. **2022**.

(52) Ashuri, M.; He, Q.; Shaw, L. L. Silicon as a Potential Anode Material for Li-Ion Batteries: Where Size, Geometry and Structure Matter. *Nanoscale* **2016**, *8* (1), 74–103. https://doi.org/10.1039/c5nr05116a.

(53) Zekoll, S. Tuning the Properties of Ceramic Solid Electrolytes for Lithium Batteries. **2018**.

(54) Pinson, M. B.; Bazant, M. Z. Theory of SEI Formation in Rechargeable Batteries: Capacity Fade, Accelerated Aging and Lifetime Prediction. *J Electrochem Soc* **2013**, *160* (2), A243–A250. https://doi.org/10.1149/2.044302jes.

(55) Kong, F.; Kostecki, R.; Nadeau, G.; Song, X.; Zaghib, K.; Kinoshita, K.; McLarnon, F. In Situ Studies of SEI Formation. *J Power Sources* **2001**, *97–98*, 58–66. https://doi.org/10.1016/S0378-7753(01)00588-2.

(56) Frenck, L.; Sethi, G. K.; Maslyn, J. A.; Balsara, N. P. Factors That Control the Formation of Dendrites and Other Morphologies on Lithium Metal Anodes. *Front Energy Res* **2019**, *7* (November). https://doi.org/10.3389/fenrg.2019.00115.

(57) Ramasubramanian, B.; Reddy, M. v.; Zaghib, K.; Armand, M.; Ramakrishna, S. Growth Mechanism of Micro/Nano Metal Dendrites and Cumulative Strategies for Countering Its Impacts in Metal Ion Batteries: A Review†. *Nanomaterials* **2021**, *11* (10). https://doi.org/10.3390/nano11102476.

(58) Wood, K. N.; Kazyak, E.; Chadwick, A. F.; Chen, K. H.; Zhang, J. G.; Thornton, K.; Dasgupta, N. P. Dendrites and Pits: Untangling the Complex Behavior of Lithium Metal Anodes through Operando Video Microscopy. *ACS Cent Sci* **2016**, *2* (11), 790–801. https://doi.org/10.1021/acscentsci.6b00260.

(59) Kohlmeyer, R. R.; Horrocks, G. A.; Blake, A. J.; Yu, Z.; Maruyama, B.; Huang, H.; Durstock, M. F. Pushing the Thermal Limits of Li-Ion Batteries. *Nano Energy* **2019**, *64* (June), 103927. https://doi.org/10.1016/j.nanoen.2019.103927.

(60) Rahardian, S.; Budiman, B. A.; Lebdo Sambegoro, P.; Nurprasetio, I. P. Review of Solid-State Battery Technology Progress. **2020**, No. 1, 310–315. https://doi.org/10.1109/icevt48285.2019.8993863.

(61) Manthiram, A.; Yu, X.; Wang, S. Lithium Battery Chemistries Enabled by Solid-State Electrolytes. *Nat Rev Mater* **2017**, *2* (4), 1–16. https://doi.org/10.1038/natrevmats.2016.103.

(62) Bachman, J. C.; Muy, S.; Grimaud, A.; Chang, H. H.; Pour, N.; Lux, S. F.; Paschos, O.; Maglia, F.; Lupart, S.; Lamp, P.; Giordano, L.; Shao-Horn, Y. Inorganic Solid-State Electrolytes for Lithium Batteries: Mechanisms and Properties Governing Ion Conduction. *Chem Rev* **2016**, *116* (1), 140–162. https://doi.org/10.1021/acs.chemrev.5b00563.

(63) Famprikis, T.; Canepa, P.; Dawson, J. A.; Islam, M. S.; Masquelier, C. Fundamentals of Inorganic Solid-State Electrolytes for Batteries. *Nat Mater* **2019**, *18* (12), 1278–1291. https://doi.org/10.1038/s41563-019-0431-3.

(64) Zhao, W.; Yi, J.; He, P.; Zhou, H. Solid-State Electrolytes for Lithium-Ion Batteries: Fundamentals, Challenges and Perspectives. *Electrochemical Energy Reviews* **2019**, *2* (4), 574–605. https://doi.org/10.1007/s41918-019-00048-0.

(65) Hu, Y.-S. Batteries: Getting Solid. *Nat Energy* **2016**, *1* (4). https://doi.org/10.1038/nenergy.2016.42.

(66) Huang, Y.; Shao, B.; Han, F. Solid - State Batteries : An Introduction. *Solid State Batteries Volume 1: Emerging Materials and Applications, Part 1 - Solid-State Batteries: An Introduction* **2022**, *1*, 1–20. https://doi.org/10.1021/bk-2022-1413.ch001.

(67) Gong, Y. X.; Wang, J. J. Solid-State Batteries: From Fundamental Interface Characterization to Realize Sustainable Promise. *Rare Metals* **2020**, *39* (7), 743–744. https://doi.org/10.1007/s12598-020-01429-x.

(68) Ye, L.; Li, X. A Dynamic Stability Design Strategy for Lithium Metal Solid State Batteries. *Nature* **2021**, *593* (7858), 218–222. https://doi.org/10.1038/s41586-021-03486-3.

(69) Randau, S.; Weber, D. A.; Kötz, O.; Koerver, R.; Braun, P.; Weber, A.; Ivers-Tiffée, E.; Adermann, T.; Kulisch, J.; Zeier, W. G.; Richter, F. H.; Janek, J. Benchmarking the

Performance of All-Solid-State Lithium Batteries. *Nat Energy* **2020**, *5* (3), 259–270. https://doi.org/10.1038/s41560-020-0565-1.

(70) Zheng, F.; Kotobuki, M.; Song, S.; Lai, M. O.; Lu, L. Review on Solid Electrolytes for All-Solid-State Lithium-Ion Batteries. **2018**, *389* (April), 198–213. https://doi.org/10.1016/j.jpowsour.2018.04.022.

(71) Zhang, X.; Yang, Y.; Zhou, Z. Towards Practical Lithium-Metal Anodes. *Chem Soc Rev* **2020**, *49* (10), 3040–3071. https://doi.org/10.1039/c9cs00838a.

(72) DeWees, R.; Wang, H. Synthesis and Properties of NaSICON-Type LATP and LAGP Solid Electrolytes. *ChemSusChem* **2019**, *12* (16), 3713–3725. https://doi.org/10.1002/cssc.201900725.

(73) Kravchyk, K. v.; Karabay, D. T.; Kovalenko, M. v. On the Feasibility of All-Solid-State Batteries with LLZO as a Single Electrolyte. *Sci Rep* **2022**, *12* (1), 1–10. https://doi.org/10.1038/s41598-022-05141-x.

(74) Lu, J.; Li, Y. Perovskite-type Li-ion Solid Electrolytes: A Review. *Journal of Materials Science: Materials in Electronics* **2021**, *32* (8), 9736–9754. https://doi.org/10.1007/s10854-021-05699-8.

(75) Dawson, J. A.; Attari, T. S.; Chen, H.; Emge, S. P.; Johnston, K. E.; Islam, M. S. Elucidating Lithium-Ion and Proton Dynamics in Anti-Perovskite Solid Electrolytes. *Energy Environ Sci* **2018**, *11* (10), 2993–3002. https://doi.org/10.1039/c8ee00779a.

(76) Deng, Y.; Eames, C.; Fleutot, B.; David, R.; Chotard, J. N.; Suard, E.; Masquelier, C.; Islam, M. S. Enhancing the Lithium Ion Conductivity in Lithium Superionic Conductor (LISICON) Solid Electrolytes through a Mixed Polyanion Effect. *ACS Appl Mater Interfaces* **2017**, *9* (8), 7050–7058. https://doi.org/10.1021/acsami.6b14402.

(77) Kozen, A. C.; Pearse, A. J.; Lin, C. F.; Noked, M.; Rubloff, G. W. Atomic Layer Deposition of the Solid Electrolyte LiPON. *Chemistry of Materials* **2015**, *27* (15), 5324–5331. https://doi.org/10.1021/acs.chemmater.5b01654.

(78) Ling, S. G.; Peng, J. Y.; Yang, Q.; Qiu, J. L.; Lu, J. Z.; Li, H. Enhanced Ionic Conductivity in LAGP/LATP Composite Electrolyte. *Chinese Physics B* **2018**, *27* (3), 0–8. https://doi.org/10.1088/1674-1056/27/3/038201.

(79) Wei, R.; Chen, S.; Gao, T.; Liu, W. Challenges, Fabrications and Horizons of Oxide Solid Electrolytes for Solid-state Lithium Batteries. *Nano Select* **2021**, *2* (12), 2256–2274. https://doi.org/10.1002/nano.202100110.

(80) Kamaya, N.; Homma, K.; Yamakawa, Y.; Hirayama, M.; Kanno, R.; Yonemura, M.; Kamiyama, T.; Kato, Y.; Hama, S.; Kawamoto, K.; Mitsui, A. A Lithium Superionic Conductor. *Nat Mater* **2011**, *10* (9), 682–686. https://doi.org/10.1038/nmat3066.

(81) Zhou, L.; Park, K. H.; Sun, X.; Lalère, F.; Adermann, T.; Hartmann, P.; Nazar, L. F. Solvent-Engineered Design of Argyrodite Li 6 PS 5 X (X = Cl, Br, I) Solid Electrolytes with High Ionic Conductivity. *ACS Energy Lett* **2019**, *4* (1), 265–270. https://doi.org/10.1021/acsenergylett.8b01997.

(82) Zhang, Z.; Shao, Y.; Lotsch, B.; Hu, Y. S.; Li, H.; Janek, J.; Nazar, L. F.; Nan, C. W.; Maier, J.; Armand, M.; Chen, L. New Horizons for Inorganic Solid State Ion Conductors. *Energy Environ Sci* **2018**, *11* (8), 1945–1976. https://doi.org/10.1039/c8ee01053f.

(83) Léa Rose Mangani, C. V. Mechanical vs. Chemical Stability of Sulphide-Based Solid-State-Batteries. Which One Is the Biggest Challenge to Tackle? Overview of Solid-State Batteries and Hybrid Solid State Batteries. *Journal of Materials Chemistry A, Royal Society of Chemistry* **2020**, *8 (20)*. https://doi.org/10.1039/x0xx00000x.

(84) Byeon, Y.-W.; Kim, H. Review on Interface and Interphase Issues in Sulfide Solid-State Electrolytes for All-Solid-State Li-Metal Batteries. *Electrochem* **2021**, *2* (3), 452–471. https://doi.org/10.3390/electrochem2030030.

(85) Kim, K.; Park, D.; Jung, H. G.; Chung, K. Y.; Shim, J. H.; Wood, B. C.; Yu, S. Material Design Strategy for Halide Solid Electrolytes Li3MX6(X = Cl, Br, and I) for All-Solid-State High-Voltage Li-Ion Batteries. *Chemistry of Materials* **2021**, *33* (10), 3669–3677. https://doi.org/10.1021/acs.chemmater.1c00555.

(86) Yu, T.; Liang, J.; Luo, L.; Wang, L.; Zhao, F.; Xu, G.; Bai, X.; Yang, R.; Zhao, S.; Wang, J.; Yu, J.; Sun, X. Superionic Fluorinated Halide Solid Electrolytes for Highly Stable Li-Metal in All-Solid-State Li Batteries. *Adv Energy Mater* **2021**, *11* (36), 1–9. https://doi.org/10.1002/aenm.202101915.

(87) Varzi, A.; Raccichini, R.; Passerini, S.; Scrosati, B. Challenges and Prospects of the Role of Solid Electrolytes in the Revitalization of Lithium Metal Batteries. *J Mater Chem A Mater* **2016**, *4* (44), 17251–17259. https://doi.org/10.1039/c6ta07384k.

(88) Yao, P.; Yu, H.; Ding, Z.; Liu, Y.; Lu, J.; Lavorgna, M.; Wu, J.; Liu, X. Review on Polymer-Based Composite Electrolytes for Lithium Batteries. *Front Chem* **2019**, *7* (August), 1–17. https://doi.org/10.3389/fchem.2019.00522.

(89) Teo, L. P.; Buraidah, M. H.; Arof, A. K. Development on Solid Polymer Electrolytes for Electrochemical Devices. *Molecules* **2021**, *26* (21). https://doi.org/10.3390/molecules26216499.

(90) Hajndl, O. Batterie Tout Solide Pour Application Automobile : Processus de Mise En Forme et Étude Des Interfaces. *Http://Www.Theses.Fr* **2019**.

(91) Zhang, Q.; Liu, K.; Ding, F.; Liu, X. Recent Advances in Solid Polymer Electrolytes for Lithium Batteries. *Nano Res* **2017**, *10* (12), 4139–4174. https://doi.org/10.1007/s12274-017-1763-4.

(92) Cheng, J.; Hou, G.; Sun, Q.; Liang, Z.; Xu, X.; Guo, J.; Dai, L.; Li, D.; Nie, X.; Zeng, Z.; Si, P.; Ci, L. Cold-Pressing PEO/LAGP Composite Electrolyte for Integrated All-Solid-State Lithium Metal Battery. *Solid State Ion* **2020**, *345* (November 2019), 115156. https://doi.org/10.1016/j.ssi.2019.115156.

(93) Wang, Y.; Hoang, B.; Hoerauf, J.; Lee, C.; Lin, C.-F.; Rubloff, G. W.; Lee, S. B.; Kozen, A. C. Hot and Cold Pressed LGPS Solid Electrolytes. *J Electrochem Soc* **2021**, *168* (1), 010533. https://doi.org/10.1149/1945-7111/abdb44.

(94) Doux, J. M.; Yang, Y.; Tan, D. H. S.; Nguyen, H.; Wu, E. A.; Wang, X.; Banerjee, A.; Meng, Y. S. Pressure Effects on Sulfide Electrolytes for All Solid-State Batteries. *J Mater Chem A Mater* **2020**, *8* (10), 5049–5055. https://doi.org/10.1039/c9ta12889a.

(95) Zhu, H.; Prasad, A.; Doja, S.; Bichler, L.; Liu, J. Spark Plasma Sintering of Lithium Aluminum Germanium Phosphate Solid Electrolyte and Its Electrochemical Properties. *Nanomaterials* **2019**, *9* (8), 1086. https://doi.org/10.3390/nano9081086.

(96) Pérez-Estébanez, M.; Isasi-Marín, J.; Rivera-Calzada, A.; León, C.; Nygren, M. Spark Plasma versus Conventional Sintering in the Electrical Properties of Nasicon-Type Materials. *J Alloys Compd* **2015**, *651*, 636–642. https://doi.org/10.1016/j.jallcom.2015.08.126.

(97) Nadeina, A.; Rozier, P.; Seznec, V. Facile Synthesis of a Common Na-Ion Battery Cathode Material Na3V2(PO4)2F3 by Spark Plasma Sintering. *Energy Technology* **2020**, *2*, 3–7. https://doi.org/10.1002/ente.201901304.

(98) Wei, X.; Rechtin, J.; Olevsky, E. A. The Fabrication of All-Solid-State Lithium-Ion Batteries via Spark Plasma Sintering. *Metals (Basel)* **2017**, *7* (9), 1–9. https://doi.org/10.3390/met7090372.

(99) Zhu, H.; Liu, J. Emerging Applications of Spark Plasma Sintering in All Solid-State Lithium-Ion Batteries and Beyond. *J Power Sources* **2018**, *391* (March), 10–25. https://doi.org/10.1016/j.jpowsour.2018.04.054.

(100) Liu, J.; Zhu, H.; Shiraz, M. H. A. Toward 3D Solid-State Batteries via Atomic Layer Deposition Approach. *Front Energy Res* **2018**, *6* (MAR), 1–5. https://doi.org/10.3389/fenrg.2018.00010.

(101) Kozen, A. C.; Pearse, A. J.; Lin, C. F.; Noked, M.; Rubloff, G. W. Atomic Layer Deposition of the Solid Electrolyte LiPON. *Chemistry of Materials* **2015**, *27* (15), 5324–5331. https://doi.org/10.1021/acs.chemmater.5b01654.

(102) Meng, X. Atomic Layer Deposition of Solid-State Electrolytes for next-Generation Lithium-Ion Batteries and beyond: Opportunities and Challenges. *Energy Storage Mater* **2020**, *30*, 296–328. https://doi.org/10.1016/j.ensm.2020.05.001.

(103) Lobe, S.; Bauer, A.; Uhlenbruck, S.; Fattakhova-Rohlfing, D. Physical Vapor Deposition in Solid-State Battery Development: From Materials to Devices. *Advanced Science* **2021**, *8* (11), 1–33. https://doi.org/10.1002/advs.202002044.

(104) McOwen, D. W.; Xu, S.; Gong, Y.; Wen, Y.; Godbey, G. L.; Gritton, J. E.; Hamann, T. R.; Dai, J.; Hitz, G. T.; Hu, L.; Wachsman, E. D. 3D-Printing Electrolytes for Solid-State Batteries. *Advanced Materials* **2018**, *30* (18), 1–7. https://doi.org/10.1002/adma.201707132.

(105) Pasta, M.; Deshpande, V.; Doerrer, C.; Dyer, M. S.; El-shinawi, H.; Fleck, N.; Irvine, J. T. S.; Lee, H. J.; Li, G.; Liberti, E.; Mcclelland, I.; Thomas, C. I.; Turrell, S. J.; Vestli, M.; Williams, C. K. Journal of Physics : 2020 Roadmap on Solid-State Batteries. *Journal of Physics: Energy* **2020**, *2* (3), 32008.

(106) *https://blue-storage.com/en/our-technology/*.

(107) *https://solidpowerbattery.com/electrolytes/*.

(108) *From Technologies to Markets Battery 2021*; 2021.

(109) *https://www.quantumscape.com/technology*.

(110) Mauger; Julien; Paolella; Armand; Zaghib. Building Better Batteries in the Solid State: A Review. *Materials* **2019**, *12* (23), 3892. https://doi.org/10.3390/ma12233892.

(111) Zhou, L.; Minafra, N.; Zeier, W. G.; Nazar, L. F. Innovative Approaches to Li-Argyrodite Solid Electrolytes for All-Solid-State Lithium Batteries. *Acc Chem Res* **2021**, *54* (12), 2717–2728. https://doi.org/10.1021/acs.accounts.0c00874.

(112) Sijie Liu, Le Zhou, Jian Han, Kaihua Wen, Shundong Guan, Chuanjiao Xue, Zheng Zhang, Ben Xu, Yuanhua Lin, Yang Shen, Liangliang Li, C.-W. N. Super Long-Cycling All-Solid-State Battery with Thin Li6PS5Cl-Based Electrolyte. *Adv Energy Mater* **2022**, *12* (25). https://doi.org/10.1002/aenm.202200660.

(113) Tan, D. H. S.; Chen, Y. T.; Yang, H.; Bao, W.; Sreenarayanan, B.; Doux, J. M.; Li, W.; Lu, B.; Ham, S. Y.; Sayahpour, B.; Scharf, J.; Wu, E. A.; Deysher, G.; Han, H. E.; Hah, H. J.; Jeong, H.; Lee, J. B.; Chen, Z.; Meng, Y. S. Carbon-Free High-Loading Silicon Anodes Enabled by Sulfide Solid Electrolytes. *Science (1979)* **2021**, *373* (6562), 1494–1499. https://doi.org/10.1126/science.abg7217.

(114) Ren, Y.; Chen, K.; Chen, R.; Liu, T.; Zhang, Y.; Nan, C. W. Oxide Electrolytes for Lithium Batteries. *Journal of the American Ceramic Society* **2015**, *98* (12), 3603–3623. https://doi.org/10.1111/jace.13844.

(115) Shoji, M.; Cheng, E. J.; Kimura, T.; Kanamura, K. Recent Progress for All Solid State Battery Using Sulfide and Oxide Solid Electrolytes. *J Phys D Appl Phys* **2019**, *52* (10). https://doi.org/10.1088/1361-6463/aaf7e2.

(116) Dawson, J. A.; Canepa, P.; Clarke, M. J.; Famprikis, T.; Ghosh, D.; Islam, M. S. Towards Understanding the Different Influences of Grain Boundaries on Ion Transport in Sulfide and Oxide Solid Electrolytes. *Chemistry of Materials* **2019**. https://doi.org/10.1021/acs.chemmater.9b01794.

(117) Yan, X.; Li, Z.; Wen, Z.; Han, W. Li/Li7La3Zr2O12/LiFePO4 All-Solid-State Battery with Ultrathin Nanoscale Solid Electrolyte. *Journal of Physical Chemistry C* **2017**, *121* (3), 1431–1435. https://doi.org/10.1021/acs.jpcc.6b10268.

(118) Wang, C.; Yang, Y.; Liu, X.; Zhong, H.; Xu, H.; Xu, Z.; Shao, H.; Ding, F. Suppression of Lithium Dendrite Formation by Using LAGP-PEO (LiTFSI) Composite Solid Electrolyte and Lithium Metal Anode Modified by PEO (LiTFSI) in All-Solid-State Lithium Batteries. *ACS Appl Mater Interfaces* **2017**, *9* (15), 13694–13702. https://doi.org/10.1021/acsami.7b00336.

(119) Yu, Q.; Han, D.; Lu, Q.; He, Y. B.; Li, S.; Liu, Q.; Han, C.; Kang, F.; Li, B. Constructing Effective Interfaces for Li 1.5 Al 0.5 Ge 1.5 (PO 4) 3 Pellets to Achieve Roomerature Hybrid Solid-State Lithium Metal Batteries. *ACS Appl Mater Interfaces* **2019**, *11* (10), 9911–9918. https://doi.org/10.1021/acsami.8b20413.

(120) Paolella, A.; Zhu, W.; Xu, G.; Monaca, A. la; Savoie, S.; Girard, G.; Vijh, A.; Demers, H.; Perea, A.; Delaporte, N.; Guerfi, A.; Liu, X.; Ren, Y.; Sun, C.; Lu, J.; Amine, K.; Zaghib, K. Solid-State Electrolyte toward Metallic Lithium Anode. **2020**, *5* (110), 1–7.

(121) Liu, Q.; Zhou, D.; Shanmukaraj, D.; Li, P.; Kang, F.; Li, B.; Armand, M.; Wang, G. Self-Healing Janus Interfaces for High-Performance LAGP-Based Lithium Metal Batteries. *ACS Energy Lett* **2020**, *5* (5), 1456–1464. https://doi.org/10.1021/acsenergylett.0c00542.

(122) Hou, G.; Ma, X.; Sun, Q.; Ai, Q.; Xu, X.; Chen, L.; Li, D.; Chen, J.; Zhong, H.; Li, Y.; Xu, Z.; Si, P.; Feng, J.; Zhang, L.; Ding, F.; Ci, L. Lithium Dendrite Suppression and Enhanced Interfacial Compatibility Enabled by an Ex Situ SEI on Li Anode for LAGP-Based All-Solid-State Batteries. *ACS Appl Mater Interfaces* **2018**, *10* (22), 18610–18618. https://doi.org/10.1021/acsami.8b01003.

(123) Richards, W. D.; Miara, L. J.; Wang, Y.; Kim, J. C.; Ceder, G. Interface Stability in Solid-State Batteries. *Chemistry of Materials* **2016**, *28* (1), 266–273. https://doi.org/10.1021/acs.chemmater.5b04082.

(124) Xiao, Y.; Wang, Y.; Bo, S. H.; Kim, J. C.; Miara, L. J.; Ceder, G. Understanding Interface Stability in Solid-State Batteries. *Nat Rev Mater* **2020**, *5* (2), 105–126. https://doi.org/10.1038/s41578-019-0157-5.

(125) Nolan, A. M.; Zhu, Y.; He, X.; Bai, Q.; Mo, Y. Computation-Accelerated Design of Materials and Interfaces for All-Solid-State Lithium-Ion Batteries. *Joule* **2018**, *2* (10), 2016–2046. https://doi.org/10.1016/j.joule.2018.08.017.

(126) Tong, Z.; Wang, S.; Liao, Y.; Hu, S.; Liu, R. Interface Between Solid-State Electrolytes and Li-Metal Anodes : Issues , Materials , and Processing Routes. **2020**. https://doi.org/10.1021/acsami.0c13591.

(127) Tong, Z.; Wang, S.; Jena, A.; Liu, C. Energy , Environmental , and Catalysis Applications Matchmaker of Marriage Between Li Metal Anode and NASICON-Structured Solid-State Electrolyte : Plastic Crystal Electrolyte and Three-Dimensional Host Structure Matchmaker of Marriage Between Li Metal Ano. **2020**. https://doi.org/10.1021/acsami.0c12962.

(128) Zhu, Y.; He, X.; Mo, Y. First Principles Study on Electrochemical and Chemical Stability of Solid Electrolyte-Electrode Interfaces in All-Solid-State Li-Ion Batteries. *J Mater Chem A Mater* **2016**, *4* (9), 3253–3266. https://doi.org/10.1039/c5ta08574h.

(129) Han, F.; Zhu, Y.; He, X.; Mo, Y.; Wang, C. Electrochemical Stability of Li10GeP2S12 and Li7La3Zr2O12 Solid Electrolytes. *Adv Energy Mater* **2016**, *6* (8), 1–9. https://doi.org/10.1002/aenm.201501590.

(130) Wenzel, S.; Leichtweiss, T.; Krüger, D.; Sann, J.; Janek, J. Interphase Formation on Lithium Solid Electrolytes — An in Situ Approach to Study Interfacial Reactions by Photoelectron Spectroscopy. *Solid State Ion* **2015**, *278*, 98–105. https://doi.org/10.1016/j.ssi.2015.06.001.

(131) Wenzel, S.; Sedlmaier, S. J.; Dietrich, C.; Zeier, W. G.; Janek, J. Interfacial Reactivity and Interphase Growth of Argyrodite Solid Electrolytes at Lithium Metal Electrodes. *Solid State Ion* **2018**, *318* (July), 102–112. https://doi.org/10.1016/j.ssi.2017.07.005.

(132) Nie, K.; Hong, Y.; Qiu, J.; Li, Q.; Yu, X.; Li, H.; Chen, L. Interfaces between Cathode and Electrolyte in Solid State Lithium Batteries: Challenges and Perspectives. *Front Chem* **2018**, *6* (DEC), 1–19. https://doi.org/10.3389/fchem.2018.00616.

(133) Banerjee, A.; Wang, X.; Fang, C.; Wu, E. A.; Meng, Y. S. Interfaces and Interphases in All-Solid-State Batteries with Inorganic Solid Electrolytes. *Chem Rev* **2020**, *120* (14), 6878–6933. https://doi.org/10.1021/acs.chemrev.0c00101.

(134) Cao, D.; Sun, X.; Li, Q.; Natan, A.; Xiang, P.; Zhu, H. Lithium Dendrite in All-Solid-State Batteries: Growth Mechanisms, Suppression Strategies, and Characterizations. *Matter* **2020**, *3* (1), 57–94. https://doi.org/10.1016/j.matt.2020.03.015.

(135) Luo, S.; Wang, Z.; Li, X.; Liu, X.; Wang, H.; Ma, W.; Zhang, L.; Zhu, L.; Zhang, X. Growth of Lithium-Indium Dendrites in All-Solid-State Lithium-Based Batteries with Sulfide Electrolytes. *Nat Commun* **2021**, *12* (1). https://doi.org/10.1038/s41467-021-27311-7.

(136) Cheng, E. J.; Sharafi, A.; Sakamoto, J. Intergranular Li Metal Propagation through Polycrystalline Li6.25Al0.25La3Zr2O12 Ceramic Electrolyte. *Electrochim Acta* **2017**, *223*, 85–91. https://doi.org/10.1016/j.electacta.2016.12.018.

(137) Wu, B.; Wang, S.; Lochala, J.; Desrochers, D.; Liu, B.; Zhang, W.; Yang, J.; Xiao, J. The Role of the Solid Electrolyte Interphase Layer in Preventing Li Dendrite Growth in Solid-State Batteries. *Energy Environ Sci* **2018**, *11* (7), 1803–1810. https://doi.org/10.1039/c8ee00540k.

(138) Monroe, C.; Newman, J. Dendrite Growth in Lithium/Polymer Systems. *J Electrochem Soc* **2003**, *150* (10), A1377. https://doi.org/10.1149/1.1606686.

(139) Frenck, L.; Maslyn, J. A.; Loo, W. S.; Parkinson, D. Y.; Balsara, N. P. Impact of Salt Concentration on Nonuniform Lithium Electrodeposition through Rigid Block Copolymer Electrolytes. *ACS Appl Mater Interfaces* **2019**, *11* (51), 47878–47885. https://doi.org/10.1021/acsami.9b15606.

(140) Sano, H.; Sakaebe, H.; Senoh, H.; Matsumoto, H. Effect of Current Density on Morphology of Lithium Electrodeposited in Ionic Liquid-Based Electrolytes. *J Electrochem Soc* **2014**, *161* (9), A1236–A1240. https://doi.org/10.1149/2.0331409jes.

(141) Yuan, C.; Gao, X.; Jia, Y.; Zhang, W.; Wu, Q.; Xu, J. Coupled Crack Propagation and Dendrite Growth in Solid Electrolyte of All-Solid-State Battery. *Nano Energy* **2021**, *86* (January), 106057. https://doi.org/10.1016/j.nanoen.2021.106057.

(142) Golozar, M.; Paolella, A.; Demers, H.; Savoie, S.; Girard, G.; Delaporte, N.; Gauvin, R.; Guerfi, A.; Lorrmann, H.; Zaghib, K. Direct Observation of Lithium Metal Dendrites with Ceramic Solid Electrolyte. *Sci Rep* **2020**, *10* (1), 1–11. https://doi.org/10.1038/s41598-020-75456-0.

(143) Li, Q.; Yi, T.; Wang, X.; Pan, H.; Quan, B.; Liang, T.; Guo, X.; Yu, X.; Wang, H.; Huang, X.; Chen, L.; Li, H. In-Situ Visualization of Lithium Plating in All-Solid-State Lithium-Metal Battery. *Nano Energy* **2019**, *63* (May), 103895. https://doi.org/10.1016/j.nanoen.2019.103895.

(144) Han, F.; Westover, A. S.; Yue, J.; Fan, X.; Wang, F.; Chi, M.; Leonard, D. N.; Dudney, N. J.; Wang, H.; Wang, C. High Electronic Conductivity as the Origin of Lithium Dendrite Formation within Solid Electrolytes. *Nat Energy* **2019**, *4* (3), 187–196. https://doi.org/10.1038/s41560-018-0312-z.

(145) Lv, Q.; Jiang, Y.; Wang, B.; Chen, Y.; Jin, F.; Wu, B.; Ren, H.; Zhang, N.; Xu, R.; Li, Y.; Zhang, T.; Zhou, Y.; Wang, D.; Liu, H.; Dou, S. Suppressing Lithium Dendrites within Inorganic Solid-State Electrolytes. *Cell Rep Phys Sci* **2022**, *3* (1), 100706. https://doi.org/10.1016/j.xcrp.2021.100706.

(146) Cao, D.; Sun, X.; Li, Q.; Natan, A.; Xiang, P.; Zhu, H. Lithium Dendrite in All-Solid-State Batteries: Growth Mechanisms, Suppression Strategies, and Characterizations. *Matter* **2020**, *3* (1), 57–94. https://doi.org/10.1016/j.matt.2020.03.015.

(147) Zhang, F.; Huang, Q. A.; Tang, Z.; Li, A.; Shao, Q.; Zhang, L.; Li, X.; Zhang, J. A Review of Mechanics-Related Material Damages in All-Solid-State Batteries: Mechanisms, Performance Impacts and Mitigation Strategies. *Nano Energy* **2020**, *70* (November 2019), 104545. https://doi.org/10.1016/j.nanoen.2020.104545.

(148) Lewis, J. A.; Cortes, F. J. Q.; Boebinger, M. G.; Tippens, J.; Marchese, T. S.; Kondekar, N.; Liu, X.; Chi, M.; McDowell, M. T. Interphase Morphology between a Solid-State Electrolyte and Lithium Controls Cell Failure. *ACS Energy Lett* **2019**, *4* (2), 591–599. https://doi.org/10.1021/acsenergylett.9b00093.

(149) Otoyama, M.; Suyama, M.; Hotehama, C.; Kowada, H.; Takeda, Y.; Ito, K.; Sakuda, A.; Tatsumisago, M.; Hayashi, A. Visualization and Control of Chemically Induced Crack Formation in All-Solid-State Lithium-Metal Batteries with Sulfide Electrolyte. *ACS Appl Mater Interfaces* **2021**, *13* (4), 5000–5007. https://doi.org/10.1021/acsami.0c18314.

(150) Hao, S.; Daemi, S. R.; Heenan, T. M. M.; Du, W.; Tan, C.; Storm, M.; Rau, C.; Brett, D. J. L.; Shearing, P. R. Tracking Lithium Penetration in Solid Electrolytes in 3D by In-Situ Synchrotron X-Ray Computed Tomography. *Nano Energy* **2021**, *82* (October 2020), 105744. https://doi.org/10.1016/j.nanoen.2021.105744.

(151) Ning, Z.; Jolly, D. S.; Li, G.; Meyere, R. de; Pu, S. D.; Chen, Y.; Kasemchainan, J.; Ihli, J.; Gong, C.; Liu, B.; Melvin, D. L. R.; Bonnin, A.; Magdysyuk, O.; Adamson, P.; Hartley, G. O.; Monroe, C. W.; Marrow, T. J.; Bruce, P. G. Visualizing Plating-Induced Cracking in Lithium-Anode Solid-Electrolyte Cells. *Nat Mater*. https://doi.org/10.1038/s41563-021-00967-8.

(152) Lewis, J. A.; Cortes, F. J. Q.; Liu, Y.; Miers, J. C.; Verma, A.; Vishnugopi, B. S.; Tippens, J.; Prakash, D.; Marchese, T. S.; Han, S. Y.; Lee, C.; Shetty, P. P.; Lee, H. W.; Shevchenko, P.; de Carlo, F.; Saldana, C.; Mukherjee, P. P.; McDowell, M. T. Linking Void and Interphase Evolution to Electrochemistry in Solid-State Batteries Using Operando X-Ray Tomography. *Nat Mater* **2021**, *20* (4), 503–510. https://doi.org/10.1038/s41563-020-00903-2.

(153) Wang, C.; Yang, Y.; Liu, X.; Zhong, H.; Xu, H.; Xu, Z.; Shao, H.; Ding, F. Suppression of Lithium Dendrite Formation by Using LAGP-PEO (LiTFSI) Composite Solid Electrolyte and Lithium Metal Anode Modified by PEO (LiTFSI) in All-Solid-State Lithium Batteries. *ACS Appl Mater Interfaces* **2017**, *9* (15), 13694–13702. https://doi.org/10.1021/acsami.7b00336.

(154) Lee, J. J. Fabrication and Characterizations of LAGP / PEO Composite Electrolytes for All Solid-State Lithium-Ion Batteries. **2018**.

(155) Reddy, M. v.; Julien, C. M.; Mauger, A.; Zaghib, K. Sulfide and Oxide Inorganic Solid Electrolytes for All-Solid-State Li Batteries: A Review. *Nanomaterials* **2020**, *10* (8), 1–80. https://doi.org/10.3390/nano10081606.

(156) Popovic, J.; Brandell, D.; Ohno, S.; Hatzell, K. B.; Zheng, J.; Hu, Y. Y. Polymer-Based Hybrid Battery Electrolytes: Theoretical Insights, Recent Advances and Challenges. *J Mater Chem A Mater* **2021**, *9* (10), 6050–6069. https://doi.org/10.1039/d0ta11679c.

(157) Bocharova, V.; Sokolov, A. P. Perspectives for Polymer Electrolytes: A View from Fundamentals of Ionic Conductivity. *Macromolecules* **2020**, *53* (11), 4141–4157. https://doi.org/10.1021/acs.macromol.9b02742.

(158) Zhang, Z.; Shao, Y.; Lotsch, B.; Hu, Y.; Nazar, L. F.; Nan, C.; Maier, J.; Armand, M.; Chen, L. New Horizons for Inorganic Solid State Ion Conductors. *Energy Environ Sci* **2018**, *11*, 1945–1976. https://doi.org/10.1039/c8ee01053f.

(159) Lau, J.; DeBlock, R. H.; Butts, D. M.; Ashby, D. S.; Choi, C. S.; Dunn, B. S. Sulfide Solid Electrolytes for Lithium Battery Applications. *Adv Energy Mater* **2018**, *8* (27), 1–24. https://doi.org/10.1002/aenm.201800933.

(160) Zahiri, B.; Patra, A.; Kiggins, C.; Yong, A. X. bin; Ertekin, E.; Cook, J. B.; Braun, P. v. Revealing the Role of the Cathode–Electrolyte Interface on Solid-State Batteries. *Nat Mater* **2021**, *20* (10), 1392–1400. https://doi.org/10.1038/s41563-021-01016-0.

(161) Tian, H.-K.; Qi, Y. Simulation of the Effect of Contact Area Loss in All-Solid-State Li-Ion Batteries. *J Electrochem Soc* **2017**, *164* (11), E3512–E3521. https://doi.org/10.1149/2.0481711jes.

(162) Parejiya, A.; Amin, R.; Dixit, M. B.; Essehli, R.; Jafta, C. J.; Wood, D. L.; Belharouak, I. Improving Contact Impedance via Electrochemical Pulses Applied to Lithium-Solid

Electrolyte Interface in Solid-State Batteries. *ACS Energy Lett* **2021**, *6* (10), 3669–3675. https://doi.org/10.1021/acsenergylett.1c01573.

(163) Tu, Q.; Barroso-Luque, L.; Shi, T.; Ceder, G. Electrodeposition and Mechanical Stability at Lithium-Solid Electrolyte Interface during Plating in Solid-State Batteries. *Cell Rep Phys Sci* **2020**, *1* (7), 100106. https://doi.org/10.1016/j.xcrp.2020.100106.

(164) Chang, W.; May, R.; Wang, M.; Thorsteinsson, G.; Sakamoto, J.; Marbella, L.; Steingart, D. Evolving Contact Mechanics and Microstructure Formation Dynamics of the Lithium Metal-Li7La3Zr2O12 Interface. *Nat Commun* **2021**, *12* (1), 1–12. https://doi.org/10.1038/s41467-021-26632-x.

(165) Su, S.; Ma, J.; Zhao, L.; Lin, K.; Li, Q.; Lv, S.; Kang, F.; He, Y. B. Progress and Perspective of the Cathode/Electrolyte Interface Construction in All-Solid-State Lithium Batteries. *Carbon Energy* **2021**, *3* (6), 866–894. https://doi.org/10.1002/cey2.129.

(166) Koç, T.; Marchini, F.; Rousse, G.; Dugas, R.; Tarascon, J. M. In Search of the Best Solid Electrolyte-Layered Oxide Pairing for Assembling Practical All-Solid-State Batteries. *ACS Appl Energy Mater* **2021**, *4* (12), 13575–13585. https://doi.org/10.1021/acsaem.1c02187.

(167) Dollé, M.; Lett, E. S. Live Scanning Electron Microscope Observations of Dendritic Growth in Lithium / Polymer Cells Live Scanning Electron Microscope Observations of Dendritic Growth in Lithium Õ Polymer Cells. **2002**, 0–4. https://doi.org/10.1149/1.1519970.

(168) Tippens, J.; Miers, J. C.; Afshar, A.; Lewis, J. A.; Cortes, F. J. Q.; Qiao, H.; Marchese, T. S.; di Leo, C. v.; Saldana, C.; McDowell, M. T. Visualizing Chemomechanical Degradation of a Solid-State Battery Electrolyte. *ACS Energy Lett* **2019**, *4* (6), 1475–1483. https://doi.org/10.1021/acsenergylett.9b00816.

(169) Lewis, J. A.; Tippens, J.; Cortes, F. J. Q.; McDowell, M. T. Chemo-Mechanical Challenges in Solid-State Batteries. *Trends Chem* **2019**, *1* (9), 845–857. https://doi.org/10.1016/j.trechm.2019.06.013.

(170) Marbella, L. E.; Zekoll, S.; Kasemchainan, J.; Emge, P.; Bruce, P. G.; Grey, C. P. Li NMR Chemical Shift Imaging To Detect Microstructural Growth of Lithium in All-Solid-State Batteries. **2019**. https://doi.org/10.1021/acs.chemmater.8b04875.

(171) Nanda, J.; Wang, C.; Liu, P. Frontiers of Solid-State Batteries. *MRS Bull* **2018**, *43* (10), 752–758. https://doi.org/10.1557/mrs.2018.234.

(172) Takada, K. Solid Electrolytes and Solid-State Batteries. *AIP Conf Proc* **2016**, *1765* (August). https://doi.org/10.1063/1.4961900.

(173) Albertus, P.; Anandan, V.; Ban, C.; Balsara, N.; Belharouak, I.; Buettner-Garrett, J.; Chen, Z.; Daniel, C.; Doeff, M.; Dudney, N. J.; Dunn, B.; Harris, S. J.; Herle, S.; Herbert, E.; Kalnaus, S.; Libera, J. A.; Lu, D.; Martin, S.; McCloskey, B. D.; McDowell, M. T.; Meng, Y. S.; Nanda, J.; Sakamoto, J.; Self, E. C.; Tepavcevic, S.; Wachsman, E.; Wang, C.; Westover, A. S.; Xiao, J.; Yersak, T. Challenges for and Pathways toward Li-Metal-Based All-Solid-State Batteries. *ACS Energy Lett* **2021**, *6* (4), 1399–1404. https://doi.org/10.1021/acsenergylett.1c00445.

(174) Manthiram, A.; Chemelewski, K.; Lee, E. S. A Perspective on the High-Voltage LiMn1.5Ni0.5O 4 Spinel Cathode for Lithium-Ion Batteries. In *Energy and Environmental Science*; Royal Society of Chemistry, 2014; Vol. 7, pp 1339–1350. https://doi.org/10.1039/c3ee42981d.

(175) Doerrer, C.; Capone, I.; Narayanan, S.; Liu, J.; Grovenor, C. R. M.; Pasta, M.; Grant, P. S. High Energy Density Single-Crystal NMC/Li6PS5Cl Cathodes for All-Solid-State Lithium-Metal Batteries. *ACS Appl Mater Interfaces* **2021**, *13* (31), 37809–37815. https://doi.org/10.1021/acsami.1c07952.

(176) Goodenough JB, Hong HP, K. J. Fast Na+-Ion Transport in Skeleton Structures. *Mater Res Bull.* **1976**, *11* (2), 203–220.

(177) Oh, J. A. S.; He, L.; Plewa, A.; Morita, M.; Zhao, Y.; Sakamoto, T.; Song, X.; Zhai, W.; Zeng, K.; Lu, L. Composite NASICON (Na3Zr2Si2PO12) Solid-State Electrolyte with Enhanced Na+ Ionic Conductivity: Effect of Liquid Phase Sintering. *ACS Appl Mater Interfaces* **2019**, *11* (43), 40125–40133. https://doi.org/10.1021/acsami.9b14986.

(178) Pogosova, M.; Krasnikova, I.; Artem, S.; Zhugayevych, A.; Stevenson, K. Correlating Structure and Transport Properties in Pristine and Environmentally-Aged Superionic Conductors Based on Li1.3Al0.3Ti1.7(PO4)3 Ceramics. *Article Submitted* **2019**, No. July, 227367. https://doi.org/10.1016/j.jpowsour.2019.227367.

(179) Feng, J. K.; Lu, L.; Lai, M. O. Lithium Storage Capability of Lithium Ion Conductor Li1.5Al 0.5Ge1.5(PO4)3. *J Alloys Compd* **2010**, *501* (2), 255–258. https://doi.org/10.1016/j.jallcom.2010.04.084.

(180) Kubanska, A.; Castro, L.; Tortet, L.; Schäf, O.; Dollé, M.; Bouchet, R. Elaboration of Controlled Size Li1.5Al0.5Ge1.5(PO4)3 Crystallites from Glass-Ceramics. *Solid State Ion* **2014**, *266*, 44–50. https://doi.org/10.1016/j.ssi.2014.07.013.

(181) Symington, A. R.; Molinari, M.; Dawson, J. A.; Statham, J. M.; Purton, J.; Canepa, P.; Parker, S. C. Elucidating the Nature of Grain Boundary Resistance in Lithium Lanthanum Titanate. *J Mater Chem A Mater* **2021**, *9* (10), 6487–6498. https://doi.org/10.1039/d0ta11539h.

(182) He, X.; Sun, H.; Ding, X.; Zhao, K. Grain Boundaries and Their Impact on Li Kinetics in Layered-Oxide Cathodes for Li-Ion Batteries. *Journal of Physical Chemistry C* **2021**, *125* (19), 10284–10294. https://doi.org/10.1021/acs.jpcc.1c02400.

(183) Kim, Y.; Jung, K.; Lee, J.; Park, M. Improving the Ionic Conductivity of Li 1 + x Al x Ge 2- x (PO 4) 3 Solid Electrolyte for All-Solid-State Batteries Using Microstructural Modi Fi Ers. *Ceram Int* **2020**, *46* (14), 23200–23207. https://doi.org/10.1016/j.ceramint.2020.06.101.

(184) Kartini, E.; Yapriadi, V.; Jodi, H.; Manawan, M.; Panghegar, C.; Wahyudianingsih. Solid Electrolyte Composite Li4P2O7–Li3PO4 for Lithium Ion Battery. *Progress in Natural Science: Materials International* **2020**, *30* (2), 168–173. https://doi.org/10.1016/j.pnsc.2020.01.020.

(185) Il'ina, E.; Pershina, S.; Antonov, B.; Pankratov, A. Impact of Li3 BO3 Addition on Solid Electrode-Solid Electrolyte Interface in All-Solid-State Batteries. *Materials* **2021**, *14* (22). https://doi.org/10.3390/ma14227099.

(186) Zhu, J.; Xiang, Y.; Zhao, J.; Wang, H.; Li, Y.; Zheng, B.; He, H.; Zhang, Z.; Huang, J.; Yang, Y. Insights into the Local Structure, Microstructure and Ionic Conductivity of Silicon Doped NASICON-Type Solid Electrolyte Li1.3Al0.3Ti1.7P3O12. *Energy Storage Mater* **2021**. https://doi.org/10.1016/j.ensm.2021.10.003.

(187) Xu, Q.; Tsai, C. L.; Song, D.; Basak, S.; Kungl, H.; Tempel, H.; Hausen, F.; Yu, S.; Eichel, R. A. Insights into the Reactive Sintering and Separated Specific Grain/Grain Boundary Conductivities of Li1.3Al0.3Ti1.7(PO4)3. *J Power Sources* **2021**, *492* (February). https://doi.org/10.1016/j.jpowsour.2021.229631.

(188) Yu, S.; Mertens, A.; Gao, X.; Gunduz, D. C.; Schierholz, R.; Benning, S.; Hausen, F.; Mertens, J.; Kungl, H.; Tempel, H.; Eichel, R. A. Influence of Microstructure and AlPO4 Secondary-Phase on the Ionic Conductivity of Li1.3Al0.3Ti1.7 (PO4)3 Solid-State Electrolyte. *Functional Materials Letters* **2016**, *9* (5), 1–6. https://doi.org/10.1142/S1793604716500661.

(189) Chung, H.; Kang, B. Increase in Grain Boundary Ionic Conductivity of Li1.5Al0.5Ge1.5(PO4)3by Adding Excess Lithium. *Solid State Ion* **2014**, *263*, 125–130. https://doi.org/10.1016/j.ssi.2014.05.016.

(190) Zhu, Y.; Wu, T.; Sun, J.; Kotobuki, M. Highly Conductive Lithium Aluminum Germanium Phosphate Solid Electrolyte Prepared by Sol-Gel Method and Hot-Pressing. *Solid State Ion* **2020**, *350* (December 2019), 115320. https://doi.org/10.1016/j.ssi.2020.115320.

(191) Sun, Z.; Liu, L.; Lu, Y.; Shi, G.; Li, J.; Ma, L.; Zhao, J.; An, H. Preparation and Ionic Conduction of Li 1.5 Al 0.5 Ge 1.5 (PO 4) 3 Solid Electrolyte Using Inorganic Germanium as

Precursor. *J Eur Ceram Soc* **2019**, *39* (2–3), 402–408. https://doi.org/10.1016/j.jeurceramsoc.2018.09.025.

(192) Liu, Y.; Chen, J.; Gao, J. Preparation and Chemical Compatibility of Lithium Aluminum Germanium Phosphate Solid Electrolyte. *Solid State Ion* **2018**, *318* (November 2017), 27–34. https://doi.org/10.1016/j.ssi.2017.10.016.

(193) Kichambare, P. D.; Howell, T.; Rodrigues, S. Sol-Gel-Derived Lithium Superionic Conductor Li1.5Al0.5Ge1.5(PO4)3 Electrolyte for Solid-State Lithium-Oxygen Batteries. *Energy Technology* **2014**, *2* (4), 391–396. https://doi.org/10.1002/ente.201300139.

(194) He, K.; Wang, Y.; Zu, C.; Liu, Y.; Zhao, H.; Chen, J.; Han, B.; Ma, J. High-Temperature X-Ray Analysis of Phase Evolution in Lithium Ion Conductor Li1.5Al0.5Ge1.5(PO4)3. *Mater Charact* **2013**, *80*, 86–91. https://doi.org/10.1016/j.matchar.2013.03.012.

(195) Tong, H.; Liu, J.; Liu, J.; Liu, Y.; Wang, D.; Sun, X.; Song, X. Microstructure and Ionic Conductivity of Li1.5Al0.5Ge1.5(PO4)3 Solid Electrolyte Prepared by Spark Plasma Sintering. *Ceram Int* **2020**, *46* (6), 7634–7641. https://doi.org/10.1016/j.ceramint.2019.11.264.

(196) Martínez-Chaparro, S.; Kobylianska, S.; Sobrados, I.; Jiménez, R.; Sanz, J. Enhanced “Overall” Ionic Conductivity in Li1+xAlxTi2−x(PO4)3 (0.3 ≤ x ≤ 0.7) Ceramics Prepared from Sol-Gel Powders by Spark Plasma Sintering. *J Eur Ceram Soc* **2022**, *42* (10), 4248–4258. https://doi.org/10.1016/j.jeurceramsoc.2022.04.009.

(197) Fleig, J.; Maier, J. The Impedance of Ceramics with Highly Resistive Grain Boundaries: Validity and Limits of the Brick Layer Model. *J Eur Ceram Soc* **1999**, *19* (6–7), 693–696. https://doi.org/10.1016/s0955-2219(98)00298-2.

(198) Kidner, N. J.; Perry, N. H.; Mason, T. O.; Garboczi, E. J. The Brick Layer Model Revisited: Introducing the Nano-Grain Composite Model. *Journal of the American Ceramic Society* **2008**, *91* (6), 1733–1746. https://doi.org/10.1111/j.1551-2916.2008.02445.x.

(199) Song, B.; Sui, T.; Ying, S.; Li, L.; Lu, L.; Korsunsky, A. M. Nano-Structural Changes in Li-Ion Battery Cathodes during Cycling Revealed by FIB-SEM Serial Sectioning Tomography. *J Mater Chem A Mater* **2015**, *3* (35), 18171–18179. https://doi.org/10.1039/c5ta04151a.

(200) Liu, Z.; Chen-Wiegart, Y. C. K.; Wang, J.; Barnett, S. A.; Faber, K. T. Three-Phase 3D Reconstruction of a LiCoO2 Cathode via FIB-SEM Tomography. *Microscopy and Microanalysis* **2016**, *22* (1), 140–148. https://doi.org/10.1017/S1431927615015640.

(201) Arganda-Carreras, I.; Kaynig, V.; Rueden, C.; Eliceiri, K. W.; Schindelin, J.; Cardona, A.; Seung, H. S. Trainable Weka Segmentation: A Machine Learning Tool for Microscopy Pixel Classification. *Bioinformatics* **2017**, *33* (15), 2424–2426. https://doi.org/10.1093/bioinformatics/btx180.

(202) Nguyen, T. T.; Demortière, A.; Fleutot, B.; Delobel, B.; Delacourt, C.; Cooper, S. J. The Electrode Tortuosity Factor: Why the Conventional Tortuosity Factor Is Not Well Suited for Quantifying Transport in Porous Li-Ion Battery Electrodes and What to Use Instead. *NPJ Comput Mater* **2020**, *6* (1). https://doi.org/10.1038/s41524-020-00386-4.

(203) Chowdari, B. V. R.; Subba Rao, G. v.; Lee, G. Y. H. XPS and Ionic Conductivity Studies on Li2O-Al2O3-(TiO2 or GeO2)-P2O5 Glass-Ceramics. *Solid State Ion* **2000**, *136–137*, 1067–1075. https://doi.org/10.1016/S0167-2738(00)00500-2.

(204) Raguž, B.; Wittich, K.; Glaum, R. Two New, Metastable Polymorphs of Lithium Pyrophosphate Li 4 P 2 O 7. *Eur J Inorg Chem* **2019**, *2019* (11), 1688–1696. https://doi.org/10.1002/ejic.201801100.

(205) Müller, D.; Jahn, E.; Ladwig, G.; Haubenreisser, U. High-Resolution Solid-State 27Al and 31P NMR: Correlation between Chemical Shift and Mean Al-O-P Angle in AlPO4 Polymorphs. *Chem Phys Lett* **1984**, *109* (4), 332–336. https://doi.org/10.1016/0009-2614(84)85596-7.

(206) Yang, G.; Safanama, D.; Phuah, K. C.; Adams, S. Enhanced Li1+ XAlxGe2-x(PO4)3Anode-Protecting Membranes for Hybrid Lithium-Air Batteries by Spark Plasma Sintering. *ACS Omega* **2020**, *5* (29), 18205–18212. https://doi.org/10.1021/acsomega.0c01826.

(207) Hayamizu, K.; Seki, S. Long-Range Li Ion Diffusion in NASICON-Type Li1.5Al0.5Ge1.5(PO4)3 (LAGP) Studied by 7Li Pulsed-Gradient Spin-Echo NMR. *Physical Chemistry Chemical Physics* **2017**, *19* (34), 23483–23491. https://doi.org/10.1039/c7cp03647g.

(208) Liu, Z.; Venkatachalam, S.; Kirchhain, H.; van Wüllen, L. Study of the Glass-to-Crystal Transformation of the NASICON-Type Solid Electrolyte Li 1 + x Al x Ge 2 − x (PO 4) 3. *Solid State Ion* **2016**, *295*, 32–40. https://doi.org/10.1016/j.ssi.2016.07.006.

(209) Clark, S. J.; Segall, M. D.; Pickard, C. J.; Hasnip, P. J.; Probert, M. I. J.; Refson, K.; Payne, M. C. First Principles Methods Using CASTEP. *Zeitschrift fur Kristallographie* **2005**, *220* (5–6), 567–570. https://doi.org/10.1524/zkri.220.5.567.65075.

(210) Perdew, J. P.; Burke, K.; Ernzerhof, M. Generalized Gradient Approximation Made Simple. *Phys Rev Lett* **1996**, *77* (18), 3865–3868. https://doi.org/10.1103/PhysRevLett.77.3865.

(211) Yates, J. R.; Pickard, C. J.; Mauri, F. Calculation of NMR Chemical Shifts for Extended Systems Using Ultrasoft Pseudopotentials. *Phys Rev B Condens Matter Mater Phys* **2007**, *76* (2), 1–11. https://doi.org/10.1103/PhysRevB.76.024401.

(212) Pickard, C. J.; Mauri, F. All-Electron Magnetic Response with Pseudopotentials: NMR Chemical Shifts. *Phys Rev B Condens Matter Mater Phys* **2001**, *63* (24), 2451011–2451013. https://doi.org/10.1103/physrevb.63.245101.

(213) Voronin, V. I.; Sherstobitova, E. A.; Blatov, V. A.; Shekhtman, G. S. Lithium-Cation Conductivity and Crystal Structure of Lithium Diphosphate. *J Solid State Chem* **2014**, *211*, 170–175. https://doi.org/10.1016/j.jssc.2013.12.015.

(214) S. Poisson, F. d'Yvoire, NGuyen-Huy-Dung,- E. Bretey, and P. B. Crystal Structure and Cation Transport Properties of the Layered Monodiphosphates: Li9M3(P2 O7(PO4)3)2 (M=Al, Ga, Cr, Fe). *J Solid State Chem* **1998**, *138*, 32–40. https://doi.org/10.1016/S0022-4596(03)00108-7.

(215) Taylor, D. Thermal Expansion Data. II: Binary Oxides with the Fluorite and Rutile Structures, MO2, and the Antifluorite Structure, M2O. *Transactions and journal of the British Ceramic Society* **1984**, *83* (2), 32–37.

(216) Jorgensen, J. D. Compression Mechanisms in α-Quartz Structures - SiO2 and GeO2. *J Appl Phys* **1978**, *49* (11), 5473–5478. https://doi.org/10.1063/1.324517.

(217) Marezio, M.; Remeika, J. P. High-Pressure Synthesis and Crystal Structure of α-LiAlO2. *J Chem Phys* **1966**, *44* (8), 3143–3144. https://doi.org/10.1063/1.1727203.

(218) Hatzell, K. B.; Chen, X. C.; Cobb, C. L.; Dasgupta, N. P.; Dixit, M. B.; Marbella, L. E.; McDowell, M. T.; Mukherjee, P. P.; Verma, A.; Viswanathan, V.; Westover, A. S.; Zeier, W. G. Challenges in Lithium Metal Anodes for Solid-State Batteries. *ACS Energy Lett* **2020**, *5* (3), 922–934. https://doi.org/10.1021/acsenergylett.9b02668.

(219) Jana, A.; García, R. E. Lithium Dendrite Growth Mechanisms in Liquid Electrolytes. *Nano Energy* **2017**, *41* (August), 552–565. https://doi.org/10.1016/j.nanoen.2017.08.056.

(220) Arbizzani, C.; Gabrielli, G.; Mastragostino, M. Thermal Stability and Flammability of Electrolytes for Lithium-Ion Batteries. *J Power Sources* **2011**, *196* (10), 4801–4805. https://doi.org/10.1016/j.jpowsour.2011.01.068.

(221) Ke, X.; Wang, Y.; Dai, L.; Yuan, C. *Cell Failures of All-Solid-State Lithium Metal Batteries with Inorganic Solid Electrolytes: Lithium Dendrites*; 2020; Vol. 33. https://doi.org/10.1016/j.ensm.2020.07.024.

(222) M. M. Kabir, D. E. D. Degradation Mechanisms in Li-Ion Batteries: A State-Ofthe- Art Review. *Int. J. Energy Res.* **2017**, *41*, 1963–1986.

(223) Rettenwander, D.; Wagner, R.; Reyer, A.; Bonta, M.; Cheng, L.; Doeff, M. M.; Limbeck, A.; Wilkening, M.; Amthauer, G. Interface Instability of Fe-Stabilized Li7La3Zr2O12 versus Li Metal. *Journal of Physical Chemistry C* **2018**, *122* (7), 3780–3785. https://doi.org/10.1021/acs.jpcc.7b12387.

(224) Chen, C.; Jiang, M.; Zhou, T.; Raijmakers, L.; Vezhlev, E.; Wu, B.; Schülli, T. U.; Danilov, D. L.; Wei, Y.; Eichel, R. A.; Notten, P. H. L. Interface Aspects in All-Solid-State Li-Based Batteries Reviewed. *Adv Energy Mater* **2021**, *11* (13). https://doi.org/10.1002/aenm.202003939.

(225) Yu, J.; Liu, Q.; Hu, X.; Wang, S.; Wu, J.; Liang, B.; Han, C.; Kang, F.; Li, B. Smart Construction of Multifunctional Li1.5Al0.5Ge1.5(PO4)3|Li Intermediate Interfaces for Solid-State Batteries. *Energy Storage Mater* **2022**, *46* (November 2021), 68–75. https://doi.org/10.1016/j.ensm.2021.12.043.

(226) Banerjee, A.; Wang, X.; Fang, C.; Wu, E. A.; Meng, Y. S. Interfaces and Interphases in All-Solid-State Batteries with Inorganic Solid Electrolytes. *Chem Rev* **2020**, *120* (14), 6878–6933. https://doi.org/10.1021/acs.chemrev.0c00101.

(227) Zhang, S.; Zeng, Z.; Zhai, W.; Hou, G.; Chen, L.; Ci, L. Bifunctional In Situ Polymerized Interface for Stable LAGP-Based Lithium Metal Batteries. *Adv Mater Interfaces* **2021**, *8* (10), 1–9. https://doi.org/10.1002/admi.202100072.

(228) Zhang, Z.; Zhao, Y.; Chen, S.; Xie, D.; Yao, X.; Cui, P.; Xu, X. An Advanced Construction Strategy of All-Solid-State Lithium Batteries with Excellent Interfacial Compatibility and Ultralong Cycle Life. *J Mater Chem A Mater* **2017**, *5* (32), 16984–16993. https://doi.org/10.1039/c7ta04320a.

(229) Liu, Y.; Li, C.; Li, B.; Song, H.; Cheng, Z.; Chen, M.; He, P.; Zhou, H. Germanium Thin Film Protected Lithium Aluminum Germanium Phosphate for Solid-State Li Batteries. *Adv Energy Mater* **2018**, *8* (16), 1–7. https://doi.org/10.1002/aenm.201702374.

(230) Wang, C.; Bai, G.; Yang, Y.; Liu, X.; Shao, H. Dendrite-Free All-Solid-State Lithium Batteries with Lithium Phosphorous Oxynitride-Modified Lithium Metal Anode and Composite Solid Electrolytes. *Nano Res* **2019**, *12* (1), 217–223. https://doi.org/10.1007/s12274-018-2205-7.

(231) Fortulan, C. A.; Souza, D. P. F. de. Microstructural Evolution of the Al2o3-Zro2 Composite and Its Correlation with Electrical Conductivity. *Materials Research* **1999**, *2* (3), 205–210. https://doi.org/10.1590/s1516-14391999000300016.

(232) Mangani, L. R.; Villevieille, C. Mechanical: Vs. Chemical Stability of Sulphide-Based Solid-State Batteries. Which One Is the Biggest Challenge to Tackle? Overview of Solid-State Batteries and Hybrid Solid State Batteries. *J Mater Chem A Mater* **2020**, *8* (20), 10150–10167. https://doi.org/10.1039/d0ta02984j.

(233) Xiong, S.; Liu, Y.; Jankowski, P.; Liu, Q.; Nitze, F.; Xie, K.; Song, J.; Matic, A. Design of a Multifunctional Interlayer for NASCION-Based Solid-State Li Metal Batteries. *Adv Funct Mater* **2020**, *30* (22). https://doi.org/10.1002/adfm.202001444.

(234) Zhu, Y.; He, X.; Mo, Y. Origin of Outstanding Stability in the Lithium Solid Electrolyte Materials: Insights from Thermodynamic Analyses Based on First-Principles Calculations. *ACS Appl Mater Interfaces* **2015**, *7* (42), 23685–23693. https://doi.org/10.1021/acsami.5b07517.

(235) Xu, X.; Wen, Z.; Wu, X.; Yang, X.; Gu, Z. Lithium Ion-Conducting Glass-Ceramics of Li1.5Al 0.5Ge1.5(PO4)3-XLi2O (X=0.0-0.20) with Good Electrical and Electrochemical Properties. *Journal of the American Ceramic Society* **2007**, *90* (9), 2802–2806. https://doi.org/10.1111/j.1551-2916.2007.01827.x.

(236) Lu, Y.; Zhao, C. Z.; Yuan, H.; Cheng, X. B.; Huang, J. Q.; Zhang, Q. Critical Current Density in Solid-State Lithium Metal Batteries: Mechanism, Influences, and Strategies. *Adv Funct Mater* **2021**, *2009925*, 1–33. https://doi.org/10.1002/adfm.202009925.

(237) Dussart, T.; Rividi, N.; Fialin, M.; Toussaint, G.; Stevens, P.; Laberty-Robert, C. Critical Current Density Limitation of LLZO Solid Electrolyte: Microstructure vs Interface. *J Electrochem Soc* **2021**, *168* (12), 120550. https://doi.org/10.1149/1945-7111/ac44be.

(238) Girard, G. M. A.; Wang, X.; Yunis, R.; MacFarlane, D. R.; Bhattacharyya, A. J.; Forsyth, M.; Howlett, P. C. Sustainable, Dendrite Free Lithium-Metal Electrode Cycling Achieved with Polymer Composite Electrolytes Based on a Poly(Ionic Liquid) Host. *Batter Supercaps* **2019**, *2* (3), 229–239. https://doi.org/10.1002/batt.201800120.

(239) Flatscher, F.; Philipp, M.; Ganschow, S.; Wilkening, H. M. R.; Rettenwander, D. The Natural Critical Current Density Limit for Li7La3Zr2O12garnets. *J Mater Chem A Mater* **2020**, *8* (31), 15782–15788. https://doi.org/10.1039/c9ta14177d.

(240) Wan, M.; Kang, S.; Wang, L.; Lee, H. W.; Zheng, G. W.; Cui, Y.; Sun, Y. Mechanical Rolling Formation of Interpenetrated Lithium Metal/Lithium Tin Alloy Foil for Ultrahigh-Rate Battery Anode. *Nat Commun* **2020**, *11* (1). https://doi.org/10.1038/s41467-020-14550-3.

(241) Bieker, G.; Winter, M.; Bieker, P. Electrochemical in Situ Investigations of SEI and Dendrite Formation on the Lithium Metal Anode. *Physical Chemistry Chemical Physics* **2015**, *17* (14), 8670–8679. https://doi.org/10.1039/c4cp05865h.

(242) Kato, A.; Kowada, H.; Deguchi, M.; Hotehama, C.; Hayashi, A.; Tatsumisago, M. XPS and SEM Analysis between Li/Li3PS4 Interface with Au Thin Film for All-Solid-State Lithium Batteries. *Solid State Ion* **2018**, *322* (April), 1–4. https://doi.org/10.1016/j.ssi.2018.04.011.

(243) Zhu, Y.; He, X.; Mo, Y. Strategies Based on Nitride Materials Chemistry to Stabilize Li Metal Anode. *Advanced Science* **2017**, *4* (8), 1–11. https://doi.org/10.1002/advs.201600517.

(244) Liu, Y.; Xie, K.; Pan, Y.; Li, Y.; Wang, H.; Lu, W.; Zheng, C. LiPON as a Protective Layer on Graphite Anode to Extend the Storage Life of Li-Ion Battery at Elevated Temperature. *Ionics (Kiel)* **2018**, *24* (3), 723–734. https://doi.org/10.1007/s11581-017-2250-3.

(245) Dudney, N. J. Addition of a Thin-Film Inorganic Solid Electrolyte (Lipon) as a Protective Film in Lithium Batteries with a Liquid Electrolyte. *J Power Sources* **2000**, *89* (2), 176–179. https://doi.org/10.1016/S0378-7753(00)00427-4.

(246) Su, H.; Jiang, Z.; Liu, Y.; Li, J.; Gu, C.; Wang, X.; Xia, X.; Tu, J. Recent Progress of Sulfide Electrolytes for All-Solid-State Lithium Batteries. *Energy Materials* **2022**, 1–37. https://doi.org/10.20517/energymater.2022.01.

(247) Su, Z.; Decencière, E.; Nguyen, T. T.; El-Amiry, K.; de Andrade, V.; Franco, A. A.; Demortière, A. Artificial Neural Network Approach for Multiphase Segmentation of Battery Electrode Nano-CT Images. *NPJ Comput Mater* **2022**, *8* (1). https://doi.org/10.1038/s41524-022-00709-7.

(248) Shen, F.; Dixit, M. B.; Xiao, X.; Hatzell, K. B. Effect of Pore Connectivity on Li Dendrite Propagation within LLZO Electrolytes Observed with Synchrotron X-Ray Tomography. *ACS Energy Lett* **2018**, *3* (4), 1056–1061. https://doi.org/10.1021/acsenergylett.8b00249.

(249) Madsen, K. E.; Bassett, K. L.; Ta, K.; Sforzo, B. A.; Matusik, K. E.; Kastengren, A. L.; Gewirth, A. A. Direct Observation of Interfacial Mechanical Failure in Thiophosphate Solid Electrolytes with Operando X-Ray Tomography. *Adv Mater Interfaces* **2020**, *7* (19), 1–12. https://doi.org/10.1002/admi.202000751.

(250) Seitzman, N.; Bird, O. F.; Andrykowski, R.; Robbins, S.; Al-Jassim, M. M.; Pylypenko, S. Operando X-Ray Tomography Imaging of Solid-State Electrolyte Response to Li Evolution under Realistic Operating Conditions. *ACS Appl Energy Mater* **2021**, *4* (2), 1346–1355. https://doi.org/10.1021/acsaem.0c02607.

(251) Seitzman, N.; Guthrey, H.; Sulas, D. B.; Platt, H. A. S.; Al-Jassim, M.; Pylypenko, S. Toward All-Solid-State Lithium Batteries: Three-Dimensional Visualization of Lithium Migration in β-Li 3 PS 4 Ceramic Electrolyte . *J Electrochem Soc* **2018**, *165* (16), A3732–A3737. https://doi.org/10.1149/2.0301816jes.

(252) Sun, F.; Dong, K.; Osenberg, M.; Hilger, A.; Risse, S.; Lu, Y.; Kamm, P. H.; Klaus, M.; Markötter, H.; García-Moreno, F.; Arlt, T.; Manke, I. Visualizing the Morphological and Compositional Evolution of the Interface of InLi-Anode Thio-LISION Electrolyte in an All-Solid-State Li-S Cell by: In Operando Synchrotron X-Ray Tomography and Energy Dispersive Diffraction. *J Mater Chem A Mater* **2018**, *6* (45), 22489–22496. https://doi.org/10.1039/c8ta08821g.

(253) Markowitz, M. M.; Boryta, D. A. Lithium Metal-Gas Reactions. *J Chem Eng Data* **1962**, *7* (4), 586–591. https://doi.org/10.1021/je60015a047.

(254) Vadhva, P.; Hu, J.; Johnson, M. J.; Stocker, R.; Braglia, M.; Brett, D. J. L.; Rettie, A. J. E. Electrochemical Impedance Spectroscopy for All-Solid-State Batteries: Theory, Methods and Future Outlook. *ChemElectroChem* **2021**, *8* (11), 1930–1947. https://doi.org/10.1002/celc.202100108.

(255) Zhao, E.; Ma, F.; Guo, Y.; Jin, Y. Stable LATP/LAGP Double-Layer Solid Electrolyte Prepared: Via a Simple Dry-Pressing Method for Solid State Lithium Ion Batteries. *RSC Adv* **2016**, *6* (95), 92579–92585. https://doi.org/10.1039/c6ra19415j.

(256) Kaboli, S.; Demers, H.; Paolella, A.; Darwiche, A.; Dontigny, M.; Clément, D.; Guerfi, A.; Trudeau, M. L.; Goodenough, J. B.; Zaghib, K. Behavior of Solid Electrolyte in Li-Polymer Battery with NMC Cathode via in-Situ Scanning Electron Microscopy. *Nano Lett* **2020**. https://doi.org/10.1021/acs.nanolett.9b04452.

(257) Tan, D. H. S.; Chen, Y. T.; Yang, H.; Bao, W.; Sreenarayanan, B.; Doux, J. M.; Li, W.; Lu, B.; Ham, S. Y.; Sayahpour, B.; Scharf, J.; Wu, E. A.; Deysher, G.; Han, H. E.; Hah, H. J.; Jeong, H.; Lee, J. B.; Chen, Z.; Meng, Y. S. Carbon-Free High-Loading Silicon Anodes Enabled by Sulfide Solid Electrolytes. *Science (1979)* **2021**, *373* (6562), 1494–1499. https://doi.org/10.1126/science.abg7217.

(258) Paolella, A.; Liu, X.; Daali, A.; Xu, W.; Hwang, I.; Savoie, S.; Girard, G.; Nita, A. G.; Perea, A.; Demers, H.; Zhu, W.; Guerfi, A.; Vijh, A.; Bertoni, G.; Gazzadi, G. C.; Berti, G.; Sun, C.; Ren, Y.; Zaghib, K.; Armand, M.; Kim, C.; Xu, G. L.; Amine, K. Enabling High-Performance NASICON-Based Solid-State Lithium Metal Batteries Towards Practical Conditions. *Adv Funct Mater* **2021**, *31* (30), 1–9. https://doi.org/10.1002/adfm.202102765.

(259) Chen, S.; Zhang, J.; Nie, L.; Hu, X.; Huang, Y.; Yu, Y.; Liu, W. All-Solid-State Batteries with a Limited Lithium Metal Anode at Room Temperature Using a Garnet-Based Electrolyte. *Advanced Materials* **2021**, *33* (1), 1–10. https://doi.org/10.1002/adma.202002325.

(260) Kato, Y.; Hori, S.; Saito, T.; Suzuki, K.; Hirayama, M.; Mitsui, A.; Yonemura, M.; Iba, H.; Kanno, R. High-Power All-Solid-State Batteries Using Sulfide Superionic Conductors. *Nat Energy* **2016**, *1* (4), 1–7. https://doi.org/10.1038/nenergy.2016.30.

(261) He, Y.; Lu, C.; Liu, S.; Zheng, W.; Luo, J. Interfacial Incompatibility and Internal Stresses in All-Solid-State Lithium Ion Batteries. *Adv Energy Mater* **2019**, *9* (36), 1–40. https://doi.org/10.1002/aenm.201901810.

(262) Xu, R. C.; Xia, X. H.; Zhang, S. Z.; Xie, D.; Wang, X. L.; Tu, J. P. Interfacial Challenges and Progress for Inorganic All-Solid-State Lithium Batteries. *Electrochim Acta* **2018**, *284*, 177–187. https://doi.org/10.1016/j.electacta.2018.07.191.

(263) Ruan, Y.; Lu, Y.; Li, Y.; Zheng, C.; Su, J.; Jin, J.; Xiu, T.; Song, Z.; Badding, M. E.; Wen, Z. A 3D Cross-Linking Lithiophilic and Electronically Insulating Interfacial Engineering for Garnet-Type Solid-State Lithium Batteries. *Adv Funct Mater* **2021**, *31* (5), 1–10. https://doi.org/10.1002/adfm.202007815.

(264) Aboulaich, A.; Bouchet, R.; Delaizir, G.; Seznec, V.; Tortet, L.; Morcrette, M.; Rozier, P.; Tarascon, J. M.; Viallet, V.; Dollé, M. A New Approach to Develop Safe All-Inorganic Monolithic Li-Ion Batteries. *Adv Energy Mater* **2011**, *1* (2), 179–183. https://doi.org/10.1002/aenm.201000050.

(265) Delaizir, G.; Viallet, V.; Aboulaich, A.; Bouchet, R.; Tortet, L.; Seznec, V.; Morcrette, M.; Tarascon, J. M.; Rozier, P.; Dollé, M. The Stone Age Revisited: Building a Monolithic

Inorganic Lithium-Ion Battery. *Adv Funct Mater* **2012**, *22* (10), 2140–2147. https://doi.org/10.1002/adfm.201102479.

(266) Deshpande, V.; Doerrer, C.; Dyer, M. S.; El-shinawi, H.; Fleck, N.; Irvine, J. T. S.; Lee, H. J.; Li, G.; Liberti, E.; Mcclelland, I.; Thomas, C. I.; Turrell, S. J.; Vestli, M.; Williams, C. K. Journal of Physics : Energy 2020 Roadmap on Solid-State Batteries. *Journal of Physics: Energy* **2020**, *2* (3), 32008.

(267) Logan, E. R.; Hebecker, H.; Eldesoky, A.; Luscombe, A.; Johnson, M. B.; Dahn, J. R. Performance and Degradation of LiFePO 4 /Graphite Cells: The Impact of Water Contamination and an Evaluation of Common Electrolyte Additives . *J Electrochem Soc* **2020**, *167* (13), 130543. https://doi.org/10.1149/1945-7111/abbbbe.

(268) Wang, C.; Yuan, X.; Tan, H.; Jian, S.; Ma, Z.; Zhao, J.; Wang, X.; Chen, D.; Dong, Y. Three-Dimensional Carbon-Coated Lifepo4 Cathode with Improved Li-Ion Battery Performance. *Coatings* **2021**, *11* (9), 1–11. https://doi.org/10.3390/coatings11091137.

(269) Meesala, Y.; Chen, C. Y.; Jena, A.; Liao, Y. K.; Hu, S. F.; Chang, H.; Liu, R. S. All-Solid-State Li-Ion Battery Using Li1.5Al0.5Ge1.5(PO4)3 As Electrolyte Without Polymer Interfacial Adhesion. *Journal of Physical Chemistry C* **2018**, *122* (26), 14383–14389. https://doi.org/10.1021/acs.jpcc.8b03971.

(270) Peng, C.; Kamiike, Y.; Liang, Y.; Kuroda, K.; Okido, M. Thin-Film NASICON-Type Li1+ XAl XTi2- x(PO4)3 Solid Electrolyte Directly Fabricated on a Graphite Substrate with a Hydrothermal Method Based on Different Al Sources. *ACS Sustain Chem Eng* **2019**, *7* (12), 10751–10762. https://doi.org/10.1021/acssuschemeng.9b01435.

(271) Li, Y.; Chen, X.; Dolocan, A.; Cui, Z.; Xin, S.; Xue, L.; Xu, H.; Park, K.; Goodenough, J. B. Garnet Electrolyte with an Ultralow Interfacial Resistance for Li-Metal Batteries. *J Am Chem Soc* **2018**, *140* (20), 6448–6455. https://doi.org/10.1021/jacs.8b03106.

(272) Du, F.; Zhao, N.; Li, Y.; Chen, C.; Liu, Z.; Guo, X. All Solid State Lithium Batteries Based on Lamellar Garnet-Type Ceramic Electrolytes. *J Power Sources* **2015**, *300*, 24–28. https://doi.org/10.1016/j.jpowsour.2015.09.061.

(273) Zhong, Y.; Xie, Y.; Hwang, S.; Wang, Q.; Cha, J. J.; Su, D.; Wang, H. A Highly Efficient All-Solid-State Lithium/Electrolyte Interface Induced by an Energetic Reaction. *Angewandte Chemie - International Edition* **2020**, *59* (33), 14003–14008. https://doi.org/10.1002/anie.202004477.

(274) Kobayashi, E.; Plashnitsa, L. S.; Doi, T.; Okada, S.; Yamaki, J. I. Electrochemical Properties of Li Symmetric Solid-State Cell with NASICON-Type Solid Electrolyte and Electrodes. *Electrochem commun* **2010**, *12* (7), 894–896. https://doi.org/10.1016/j.elecom.2010.04.014.

(275) Lee, K. J.; Yang, H. J.; Chen, K. C. Mechanical Analysis of the Delamination of Artificial Solid Electrolyte Interface in Lithium-Ion Batteries. *Applications in Engineering Science* **2022**, *9*, 100088. https://doi.org/10.1016/j.apples.2022.100088.

(276) Kim, J.; Kowal, J. A Method for Monitoring State-of-Charge of Lithium-Ion Cells Using Multi-Sine Signal Excitation. *Batteries* **2021**, *7* (4). https://doi.org/10.3390/batteries7040076.

(277) Petrovic, S. *Electrochemistry Crash Course for Engineers*; Springer, 2021. https://doi.org/10.1007/978-3-030-61562-8.

(278) Cronau, M.; Szabo, M.; König, C.; Wassermann, T. B.; Roling, B. How to Measure a Reliable Ionic Conductivity? The Stack Pressure Dilemma of Microcrystalline Sulfide-Based Solid Electrolytes. *ACS Energy Lett* **2021**, *6* (9), 3072–3077. https://doi.org/10.1021/acsenergylett.1c01299.

(279) Secco, R. A.; Rütter, M.; Huang, Y. Pressure-Induced Increase in the Ionic Conductivity of Li, Na, and K Zeolites of Type A. *Technical Physics* **2000**, *45* (11), 1447–1451. https://doi.org/10.1134/1.1325028.

(280) Kaiser, N.; Spannenberger, S.; Schmitt, M.; Cronau, M.; Kato, Y.; Roling, B. Ion Transport Limitations in All-Solid-State Lithium Battery Electrodes Containing a Sulfide-Based

Electrolyte. *J Power Sources* **2018**, *396* (January), 175–181. https://doi.org/10.1016/j.jpowsour.2018.05.095.

(281) Brazier, A.; Dupont, L.; Dantras-Laffont, L.; Kuwata, N.; Kawamura, J.; Tarascon, J. M. First Cross-Section Observation of an All Solid-State Lithium-Ion "Nanobattery" by Transmission Electron Microscopy. *Chemistry of Materials* **2008**, *20* (6), 2352–2359. https://doi.org/10.1021/cm7033933.

(282) Fawey, M. H.; Chakravadhanula, V. S. K.; Munnangi, A. R.; Rongeat, C.; Hahn, H.; Fichtner, M.; Kübel, C. First Results from in Situ Transmission Electron Microscopy Studies of All-Solid-State Fluoride Ion Batteries. *J Power Sources* **2020**, *466* (May), 228283. https://doi.org/10.1016/j.jpowsour.2020.228283.

(283) Xie, Q.; Chen, J.; Xing, L.; Zhou, X.; Ma, Z.; Wu, B.; Lin, Y.; Zhou, H.; Li, W. Revealing the Critical Effect of Solid Electrolyte Interphase on the Deposition and Detriment of Co(Ⅱ) Ions to Graphite Anode. *Journal of Energy Chemistry* **2022**, *69*, 389–396. https://doi.org/10.1016/j.jechem.2021.12.009.

(284) Tu, Q.; Shi, T.; Chakravarthy, S.; Ceder, G. Understanding Metal Propagation in Solid Electrolytes Due to Mixed Ionic-Electronic Conduction. *Matter* **2021**, *4* (10), 3248–3268. https://doi.org/10.1016/j.matt.2021.08.004.

(285) Rauch, E. F.; Véron, M. Automated Crystal Orientation and Phase Mapping in TEM. *Mater Charact* **2014**, *98*, 1–9. https://doi.org/10.1016/j.matchar.2014.08.010.

(286) Chen, X.; Guan, Z.; Chu, F.; Xue, Z.; Wu, F.; Yu, Y. Air-Stable Inorganic Solid-State Electrolytes for High Energy Density Lithium Batteries: Challenges, Strategies, and Prospects. *InfoMat* **2022**, *4* (1), 1–20. https://doi.org/10.1002/inf2.12248.

(287) Wu, J.; Yuan, L.; Zhang, W.; Li, Z.; Xie, X.; Huang, Y. Reducing the Thickness of Solid-State Electrolyte Membranes for High-Energy Lithium Batteries. *Energy Environ Sci* **2021**, *14* (1), 12–36. https://doi.org/10.1039/d0ee02241a.

(288) Janek, J.; Zeier, W. G. A Solid Future for Battery Development. *Nat Energy* **2016**, *1* (9), 1–4. https://doi.org/10.1038/nenergy.2016.141.

(289) O. U. Kudu, T. Famprikis, S. Cretu, B. Porcheron, E. Salager, A. Demortiere, M. Courty, V. Viallet, T. Mercier, B. Fleutot, M-D Braida, C. M. Structural Details in Li3PS4: Variety in Thiophosphate Building Blocks and Correlation to Ion Transport. *Energy Storage Mater* **2022**, *44*, 168–179. https://doi.org/10.1016/j.ensm.2021.10.021.

(290) Kudu, Ö. U.; Famprikis, T.; Fleutot, B.; Braida, M. D.; le Mercier, T.; Islam, M. S.; Masquelier, C. A Review of Structural Properties and Synthesis Methods of Solid Electrolyte Materials in the Li2S − P2S5 Binary System. *J Power Sources* **2018**, *407* (October), 31–43. https://doi.org/10.1016/j.jpowsour.2018.10.037.

(291) Chu, I.-H.; Zhang, M.; Ong, S. P.; Meng, Y. S. Battery Electrodes, Electrolytes, and Their Interfaces. *Handbook of Materials Modeling* **2019**, 1–24. https://doi.org/10.1007/978-3-319-50257-1_96-2.

(292) Wu, X.; Billaud, J.; Jerjen, I.; Marone, F.; Ishihara, Y.; Adachi, M.; Adachi, Y.; Villevieille, C.; Kato, Y. Operando Visualization of Morphological Dynamics in All-Solid-State Batteries. *Adv Energy Mater* **2019**, *9* (34), 1–10. https://doi.org/10.1002/aenm.201901547.

(293) Ke, X.; Wang, Y.; Dai, L.; Yuan, C. Cell Failures of All-Solid-State Lithium Metal Batteries with Inorganic Solid Electrolytes: Lithium Dendrites. *Energy Storage Mater* **2020**, *33* (July), 309–328. https://doi.org/10.1016/j.ensm.2020.07.024.

(294) Jena, A.; Tong, Z.; Bazri, B.; Iputera, K.; Chang, H.; Hu, S. F.; Liu, R. S. In Situ/ Operando Methods of Characterizing All-Solid-State Li-Ion Batteries: Understanding Li-Ion Transport during Cycle. *Journal of Physical Chemistry C* **2021**, *125* (31), 16921–16937. https://doi.org/10.1021/acs.jpcc.1c04771.

(295) Wynn, T. A.; Lee, J. Z.; Banerjee, A.; Meng, Y. S. In Situ and Operando Probing of Solid-Solid Interfaces in Electrochemical Devices. *MRS Bull* **2018**, *43* (10), 740–745. https://doi.org/10.1557/mrs.2018.235.

(296) Yang, Z.; Ong, P.; He, Y.; Wang, L.; Bowden, M. E.; Xu, W.; Droubay, T. C.; Wang, C.; Sushko, P. v; Du, Y. Direct Visualization of Li Dendrite Effect on LiCoO 2 Cathode by In Situ TEM. **2018**, *1803108*, 1–8. https://doi.org/10.1002/smll.201803108.

(297) Li, Z.; Tan, X.; Li, P.; Kalisvaart, P.; Janish, M. T.; Mook, W. M.; Luber, E. J.; Jungjohann, K. L.; Carter, C. B.; Mitlin, D. Coupling in Situ TEM and Ex Situ Analysis to Understand Heterogeneous Sodiation of Antimony. *Nano Lett* **2015**, *15* (10), 6339–6347. https://doi.org/10.1021/acs.nanolett.5b03373.

(298) Bhatia, A.; Cretu, S.; Hallot, M.; Folastre, N.; Berthe, M.; Troadec, D.; Roussel, P.; Pereira-Ramos, J. P.; Baddour-Hadjean, R.; Lethien, C.; Demortière, A. In Situ Liquid Electrochemical TEM Investigation of LiMn1.5Ni0.5O4 Thin Film Cathode for Micro-Battery Applications. *Small Methods* **2022**, *6* (2), 1–13. https://doi.org/10.1002/smtd.202100891.

(299) Liu, X.; Garcia-Mendez, R.; Lupini, A. R.; Cheng, Y.; Hood, Z. D.; Han, F.; Sharafi, A.; Idrobo, J. C.; Dudney, N. J.; Wang, C.; Ma, C.; Sakamoto, J.; Chi, M. Local Electronic Structure Variation Resulting in Li 'Filament' Formation within Solid Electrolytes. *Nat Mater* **2021**, *20* (11), 1485–1490. https://doi.org/10.1038/s41563-021-01019-x.

(300) Zheng, H.; Lu, X.; He, K. In Situ Transmission Electron Microscopy and Artificial Intelligence Enabled Data Analytics for Energy Materials. *Journal of Energy Chemistry* **2022**, *68*, 454–493. https://doi.org/10.1016/j.jechem.2021.12.001.

(301) Huan Tong, Jian Liu, Yi Qiao, X. S. Characteristics of Interface between Solid Electrolyte and Electrode in All-Solid-State Batteries Prepared by Spark Plasma Sintering. *J Power Sources* **2022**, *Volume 521*, 230964. https://doi.org/10.1016/j.jpowsour.2021.230964.

(302) Oh, P.; Lee, H.; Park, S.; Cha, H.; Kim, J.; Cho, J. Improvements to the Overpotential of All-Solid-State Lithium-Ion Batteries during the Past Ten Years. *Adv Energy Mater* **2020**, *10* (24), 1–8. https://doi.org/10.1002/aenm.202000904.

(303) Özdogru, B.; Cha, Y.; Gwalani, B.; Murugesan, V.; Song, M. K.; Çapraz, Ö. Ö. In Situ Probing Potassium-Ion Intercalation-Induced Amorphization in Crystalline Iron Phosphate Cathode Materials. *Nano Lett* **2021**, *21* (18), 7579–7586. https://doi.org/10.1021/acs.nanolett.1c02095.

Abstract English

The increasing request for electric vehicles demands high energy density batteries, wide temperature compatibility and improved safety technology. Solid-state batteries could represent a possible future solution for the current battery technology as they replace the liquid electrolyte which contains flammable organic materials, they offer the possibility to use high voltage cathode materials and opens the possibility to use safely lithium metal as anode resulting in batteries with high energy density.

Solid-state performances improved over the past the past years, but challenges regarding their interfaces, ionic conductivity due to grain boundaries limitations, generation of cracks and dendrites during cycling restrain their performances. To be able to design better solid-state batteries, insights into the nature of the parameters that impede their further development are required.

In this work, various characterization methods were carried out to understand the degradation mechanism of oxide solid-state batteries based on LAGP as solid electrolyte. A combined approach using FIB-SEM tomography, EIS, SEM-EDX, XRD and NMR was used to correlate the morphology and crystal structure of the grain boundaries region with their ionic conductivity properties. We build understanding about the (electro)chemical reactions occurring at the LAGP-metallic lithium interface based on a combination of ex-situ techniques (SEM, TEM, SIMS) and in-situ X-ray micro-computed tomography allowing us to obtain information about kinetics and dynamic processes. Finally, the degradation mechanism of an all-solid-state battery was followed at the nanoscale using in-situ electrochemical STEM where the apparition of cracks and amorphous area within LAGP was observed.

Abstract Français

La demande croissante des véhicules électriques exige des batteries à haute densité d'énergie, une large compatibilité thermique et une technologie de sécurité améliorée. Les batteries tout solides pourraient représenter une possible solution d'avenir par rapport à la technologie actuelle car elles remplacent l'électrolyte liquide qui contient des matériaux organiques inflammables, offrent la possibilité d'utiliser des matériaux de cathode à haute tension et ouvrent la possibilité d'utiliser en toute sécurité le lithium métal comme anode, ce qui donnera des batteries à haute densité d'énergie.

Les performances des batteries tout-solide se sont améliorées au cours des dernières années, mais des limitations concernant leurs interfaces, la conductivité ionique, la génération de fissures et de dendrites lors du cyclage limitent leurs performances. Pour être en mesure de concevoir de meilleures batteries toutes solides, il est nécessaire de mieux comprendre la nature des paramètres qui limite leur développement.

Dans ce travail, diverses méthodes de caractérisation ont été réalisées pour comprendre le mécanisme de dégradation des batteries oxyde toutes solide qui utilisent comme électrolyte solide le LAGP. Une approche qui combine la tomographie FIB-SEM, EIS, SEM-EDX, XRD et RMN a été utilisée pour corréler la morphologie et la structure cristalline de la région des joints de grains avec leurs propriétés de conductivité ionique. Une compréhension profonde des réactions (électro)chimiques produisant à l'interface LAGP-lithium métallique a été réalisé en nous basant sur une combinaison de techniques ex-situ (SEM, TEM, SIMS) et in situ tomographie à rayons X qui nous a permis d'obtenir des informations sur la cinétique et les processus dynamiques. Enfin, le mécanisme de dégradation d'une batterie tout solide a été suivi à l'échelle nanométrique utilisant in situ STEM où l'apparition de fissures et des zones amorphe au sein du LAGP a été observée.